UNIVERSIDADE FEDERAL DO RIO GRANDE

INSTITUTO DE CIÊNCIAS BIOLÓGICAS

PROGRAMA DE PÓS-GRADUAÇÃO EM CIÊNCIAS FISIOLÓGICAS

EFEITOS DE NANOTUBOS DE CARBONO BASEADOS EM MECANISMOS MITOCONDRIAIS E CORRELAÇÕES *IN SILICO* ESTRUTURA-ATIVIDADE

Michael González-Durruthy

Orientador: Prof. Dr. José M. Monserrat

Tese apresentada ao Programa de Pós-Graduação em Ciências Fisiológicas da Universidade Federal do Rio Grande como requisito parcial para a obtenção do Título de Doutor.

Rio Grande, 2018

"Eu nunca vejo o que já foi feito. Eu somente vejo o que ainda falta para ser feito…"

Marie Skłodowska Curie

Agradecimentos

A minha família, por tudo o amor, apoio e incentivo constantes para a realização dos meus sonhos, pela confiança e a força desde distância;

A minha companheira Diana, pela compreensão e paciência, pelo amor, por ser incondicional, por construir juntos nesta caminhada;

A meu Orientador José M. Monserrat, realmente não teria palavras para resumir a amizade, apoio, e convívio incomparáveis nestes quatro anos. Me senti cada dia com muita sorte por isso. Obrigado José, por deixar-me tentar goles olímpicos no terreno da Nanotoxicologia. Também recebam meu sincero agradecimento Laura e Malena;

Aos professores Karina Machado, Adriano Werhli, também ao Vinicius, pela amizade e parceria increível em Nanotoxicologia Computacional, sem dúvida fizeram meu Doutorado 2018 (“a pasta mais Feliz”);

Ao professor Marcos Alexandre Gelesky, Carol, Rudy e funcionários do CEMESUL pela grande ajuda, amizade, parceria e comprometimento com a qualidade dos nossos resultados de caracterização dos nanotubos de carbono;

Aos professores Carlos Curti e Zeki Naal da Faculdade de Ciências Farmacêuticas de Ribeirão Preto Universidade de São Paulo;

Ao professor Humberto González-Díaz pela bela amizade e incrível colaboração na construção dos modelos preditivos Nano-QSAR;

Aos professores Luiz Eduardo Maia Nery e Marta Marques de Souza por dar-me a oportunidade de lutar no Programa de Pós-Graduação em Ciências Fisiológicas pelo apoio desde Cuba para conseguir participar do edital;

Agradecimento especial para Universidade Federal do Rio Grande, ás agências de fomento que viabilizaram a realização do projeto: CAPES/PEC-PG pela bolsa de doutorado, Rede de Nanotoxicologia (MCTI/CNPq) e, ao INCT de Nanomateriais de Carbono pelo suporte financeiro e logístico;

Ao Lauro e Noemi pela amizade e solidariedade por estendermos a mão amiga como família longe de casa.

A Maria Ângela e João pela amizade sincera e incondicional os levo no coração amigos

Ao Juan Zamora Sillero e Isa pela grande amizade e carinho de sempre os levo conmigo

Ao André Peres Koth, grande amigo que a vida me deu nestas terras do Sul, grande abraço irmão;

A todos os professores e colegas do Programa de Pós-Graduação em Ciências Fisiológicas.

Muito obrigado a todos!

Sumário

Lista de abreviaturas

CNT – Nanotubos de carbono (do inglês *carbon nanotubes*)

SWCNT – Nanotubos de carbono de parede única (do inglês *single-walled carbon nanotubes*)

MWCNT – Nanotubos de carbono de paredes múltiplas (do inglês *multi-walled carbon nanotubes*)

ADP – Adenosina 5'-difosfato (do inglês *adenosine 5'-diphosphate*)

ATP – Adenosina 5'-trifosfato (do inglês *adenosine 5'-triphosphate*)

ANT – Translocador de nucleotídeos de adenina (do inglês *adenine nucleotide translocator*)

VDAC – Canal aniônico dependente de voltagem (do inglês *voltage dependent anion channel*)

MPTP – Poro de transição de permeabilidade mitocondrial (do inglês *mitochondrial permeability transition pore*)

CATR – Ácido carboxiatractilosídeo (do inglês carboxyatractiloside acid)

ROS – Espécies reativas de oxigênio (do inglês *reactive oxygen species*)

·OH – Radical hidroxila (do inglês *hydroxyl radical*).

TEM – Microscopia eletrônica de transmissão (do inglês *transmission electron microscopy*)

SEM – Microscópio electrónico de varredura (do inglês *scanning eléctron microscopy*)

FT-IR – Espectroscopia infravermelho por transformada de Fourier (do inglês *Fourier transform infrared spectroscopy*)

MD – Docagem molecular (do inglês *molecular docking*)

VSF – Plataforma de triagem virtual (do inglês virtual screening framework)

FEB – Energia livre de ligação (do inglês *free energy of binding*)

PDB – Banco de dados de proteínas (do inglês *Protein Data Bank*)

Nano (QSAR) – Relação Quantitativa Nanoestrutura-Atividade (do inglês *Nanoparticle Quantitative-Structure-Activity-Relationship*)

Nano (QSPR) – Relação quantitativa nanoestrutura-propriedade (do inglês *Nanoparticle Quantitative-Structure-Property-Relationship*)

PT – Teoria de perturbação (do inglês *Perturbation Theory*)

V_k – Nanodescriptores (do inglês *nanodescriptors*)

DFT – Teoria Funcional da Densidade (do inglês *Density Functional Theory*)

DMSO – Dimetilsulfóxido

EGTA – Ácido etilenglicolamino tetracético (do inglês *ethylene glycol-bis (β-aminoethyl)-N,N,N',N'-tetraacetic acid*)

CCCP – Carbonyl cyanide m-chlorophenyl hydrazine

RLM – Mitocôndrias fígado de ratos (do inglês *rat liver mitochondria*)

SMP – Partículas submitocondriais (do inglês *submitochondrial particles*)

ΔΨ – Potencial de membrana mitocondrial

V3 – Respiração estado 3

V4 – Respiração estado 4

CsA – Ciclosporina A

SG – Gráfico de estrelas (do inglês *Star Graph*)

S2SNet software – Sequência para redes de estrelas (do inglês *sequence to star networks*)

LMR – Regressão linear múltipla (do inglês *Multiple Linear Regression*)

PLS – Regressão parcial por mínimos quadrados (do inglês *Partial Least Squares Regression*)

NN – Redes neurais (do inglês *Neural Networks*)

ANN – Redes neurais artificiais (do inglês *Artificial Neural Networks*)

RF – Árvores aleatórias (do inglês *Random Forest*)

RMSE – Erro da raiz quadrada media (do inglês *Root Mean Square Error*)

Sp – Especificidade (do inglês *specificity*)

Sn – Sensibilidade (do inglês *sensitivity*)

Lista de figuras

Introdução

Resumo

Nanotubos de carbono (CNT, do inglês *carbon nanotubes*) constituem um grupo de nanomateriais de carbono com grande versatilidade devido às suas propriedades físico-químicas singulares (flexibilidade, condutividade, reatividade superficial) e biológicas (seletividade farmacológica e toxicidade mitocondrial). Diferentes tipos de CNT manufaturados (CNT-prístinos, CNT-oxidados) chamam a atenção da comunidade científica sobre suas potenciais aplicações biomédicas orientadas especificamente para o desenvolvimento das chamadas "terapias inteligentes" baseadas em Medicina de Precisão (ex.: Medicina Mitocondrial). Paralelamente, com as perspectivas de aplicação biomédica, se apresentam potenciais riscos toxicológicos para a saúde humana e meio ambiente que precisam ser avaliados cuidadosamente no intuito de compreender melhor as relações benefício/risco dos CNT. Neste contexto, surge a necessidade de contar com metodologias de avaliação fármaco-toxicológicas precisas e rápidas e em consonância com as normas éticas no sentido de reduzir significativamente o uso de animais na experimentação. Neste cenário, a presente tese integra, de forma inédita, abordagens *in sílico/in vitro* para avaliar, correlacionar e predizer interações fármaco-toxicológicas de CNT (CNT-prístinos, CNT-oxidados) com mecanismos mitocondriais através de: **(1)** avaliação experimental de parâmetros bioquímicos chaves da função mitocondrial; **(2)** caracterização de interações utilizando ferramentas teóricas de docagem molecular; **(3)** implementação de ferramentas preditivas Nano-QSAR (do inglês, *Nanoparticles-Quantitative-Structure-Relationships*) para identificar atributos físico-químicos (nanodescritores) de CNT, responsáveis pela modulação de mecanismos mitocondriais (disfunção mitocondrial) envolvidos em diversas doenças crônicas de alta prevalência e mortalidade como: câncer, Alzheimer, Parkinson, epilepsia, diabetes e outras. As evidências *in vitro* mostraram que CNT oxidados (CNT-OH, CNT-COOH) apresentam maior capacidade que os CNT-prístinos para prevenir a disfunção mitocondrial em condições fisiopatológicas experimentalmente induzidas, e que respostas mitotóxicas e/ou mitoprotetoras podem ser eficientemente preditas e correlacionadas *in sílico* através de modelos Nano-QSAR em função de seus atributos estruturais mais relevantes como: diâmetro e tipo de funcionalização. Consistentemente, os resultados de docagem molecular salientam a relação estreita destes atributos com a nanotoxicidade sobre transportadores mitocondriais (para ADP e ATP) responsáveis pela integridade da estrutura bioenergética celular.

Palavras-Chave: Nanotoxicidad mitocondrial, nanotubos de carbono, docagem molecular, Nano-QSAR.

Abstract

Carbon nanotubes (CNT) constitute a group of carbon nanomaterials with great versatility, due to their unique physico-chemical (flexibility, conductivity, surface reactivity) and biological properties (pharmacological selectivity and mitochondrial toxicity). Different types of manufactured CNT (pristine-CNT, oxidized-CNT) draw the attention of the scientific community due to their potential biomedical applications specifically oriented for the development of so-called "*intelligent therapies*" based on Precision Medicine (eg, Mitochondrial Medicine). At the same time, with the perspectives of biomedical applications, potential nano-toxicological hazards to human and environmental health need to be carefully evaluated to better understand the benefit/risk relationships. In this context, there is a need to apply accurate and quick methodologies for pharmacological and toxicological evaluation according to the ethical principles on animal experimentation. Following this idea, the present Thesis integrates, for the first time, *in silico* and *in vitro* models to evaluate, correlate and predict pharmaco-toxicological interactions of aforementioned CNT-family members with key mitochondrial mechanism through: **1)** experimental evaluation of key biochemical parameters of mitochondrial function; **2)** characterization of interactions using theoretical tools like molecular docking; **3)** implementation of predictive tools as Nanoparticles-Quantitative-Structure-Relationships (Nano-QSAR) to identify physical-chemical attributes (nanodescriptors) from CNT-family members involved in the modulation of mitochondrial mechanisms (mitochondrial dysfunction and apoptosis), which are associated to several chronic diseases of high prevalence and mortality as cancer, Alzheimer's disease, Parkinson's disease, epilepsy, diabetes and others. The *in vitro* results show that oxidized-CNT (CNT-OH, CNT-COOH) have a great capacity than their similar CNT-pristine to prevent the mitochondrial dysfunction-induced in pathological conditions. Besides, the mitotoxic and/or mitoprotective responses can be efficiently predicted and correlated with relevant physic-chemical or nanodescriptors (like: diameter, type of functionalization) through *in silico* Nano-QSAR models. Consistently, molecular docking results reveal the close relationship between the aforementioned CNT-nanodescriptors and the mitochondrial channels nanotoxicity-based bioenergetic dysfunction.

Keywords: Mitochondrial nanotoxicity, carbon nanotubes, molecular docking, Nano-QSAR.

1. Introdução

A introdução das novas tecnologias em vários campos da atividade humana tem ganhado um papel cada vez mais importante na sociedade contemporânea. Neste contexto entram as nanotecnologias, como uma nova ferramenta com a capacidade de manipular a matéria na escala atómica e molecular, gerando diversos nanomateriais, cujos principais constituintes têm no mínimo uma dimensão entre 1-100 nanómetros (1-3).

Os trabalhos apresentados por Richard Feynman, Prêmio Nobel de Física em 1965, já chamavam a atenção da comunidade científica com relação ao impacto das nanotecnologias (4). Com os avanços da microscopia de alta resolução e de outras técnicas espectroscópicas, as nanotecnologias tornaram-se nos últimos 10 anos uma das áreas mais relevantes da ciência moderna e da inovação tecnológica, com projeções comerciais estimadas para 2020 em um trilhão de dólares (5).

As aplicações práticas têm sido muito promissórias, refletindo-se na indústria da informação, alimentar (nutracêuticos), têxtil, química e fundamentalmente no campo das ciências biomédicas e farmacêuticas, na produção e síntese de novos candidatos com potencial terapêutico com maior grau especificidade e seletividade por um órgão, tecido, célula ou biomolécula chave, num determinado processo ou mecanismo fisiopatológico; cuja área é atualmente reconhecida como Nanomedicina de precisão (do inglês *Precision Medicine*) (6,7). Paralelamente com as perspectivas de inovação na área biomédica, a nanotecnologia traz potenciais riscos tóxicos à saúde humana e meio ambiente que precisam ser avaliados cuidadosamente, devido à capacidade intrínseca destes produtos de atuar no nível sub-celular e bioquímico, fato associado à redução significativa do tamanho na escala nanométrica (1-100 nm) e grande acessibilidade aos tecidos por ter dimensões comparáveis com as biomoléculas constituintes dos seres vivos (2). Assim, a Nanotoxicologia é uma ciência que surge com a finalidade de predizer/avaliar a potencial toxicidade desses materiais nos seres vivos e ampliar nossa percepção sobre as relações benefício/risco para um uso seguro em Nanomedicina (2,8).

1.1. Nanotubos de carbono: origem e estrutura

Dentre os nanomateriais mais usados estão os nanotubos de carbono (CNT, do inglês *carbon nanotubes*) (9,10). Os CNT são nanoestruturas cilíndricas de carbono que têm a rede hexagonal plana do grafeno (alótropo do carbono com hibridização sp^2) como elemento estrutural

básico (9,10). Os CNT ocorrem naturalmente, com origens geológicas e pirogênicas e são também produzidos antropogenicamente como subprodutos da combustão, de forma não intencional e intencional. Os CNT apresentam um desenho em forma cilíndrica baseado no enrolamento de uma ou mais folhas de grafeno e comprimento na ordem de mícrons (9), assim os podem ser arranjados em: parede única (SWCNT, do inglês *single-walled carbon nanotubes*), duas folhas cilíndricas de grafeno (DWCNT, do inglês *doble-walled carbon nanotubes*), ou de paredes múltiplas (MWCNT, do inglês *multi-walled carbon nanotubes*), quando compostos por duas ou mais folhas de grafeno concêntricas (9) (**Figura 1**).

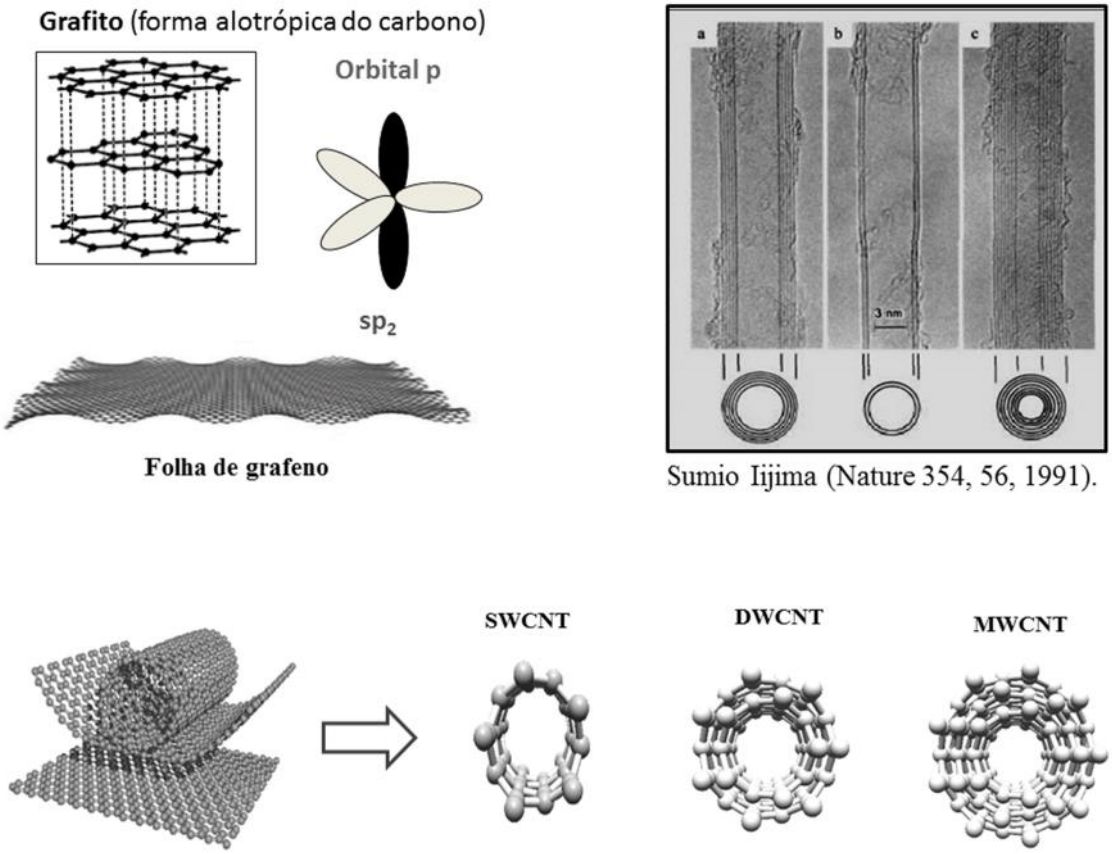

Figura 1. Origem e estrutura de diferentes nanotubos de carbono. (*Adaptada de S. Iijima.* 1991)

Desde o ponto de vista estrutural a maioria das propriedades dos CNT (SWCNT) depende do seu diâmetro (**D**) e "ângulo quiral", também chamado quiralidade ou helicidade (**Φ**). Estes dois parâmetros são definidos pelos dois números inteiros não negativos, denominados índices de Hamada (*n, m*). Conceitualmente, um SWCNT pode ser construído a partir de uma única folha de grafeno enrolada de tal forma, que coincidam dois sítios cristalográficamente equivalentes de sua

rede hexagonal. O vetor **C** chamado “vetor quiral”, define a direção na qual a folha de grafeno é enrolada e a posição relativa dos dois sítios cristalograficamente equivalentes é definido pelos índices de Hamada (*n*, *m*) e vetores unitários da rede hexagonal $\mathbf{a_1}$ e $\mathbf{a_2}$ ($\mathbf{C} = n\mathbf{a_1} + m\mathbf{a_2}$) (11,12). Essa característica determina a estrutura atômica específica dos SWCNT. Assim, um SWCNT é chamado "armchair" se $n = m$ e $\mathbf{\Phi}$=30°, e "zigzag" quando $n > 0$, $m = 0$ e $\mathbf{\Phi} = 0°$. Em todos os outros casos os SWCNT são chamados "quirais" ($n \neq m > 0$ e $0° \leq \mathbf{\Phi} \leq 30°$), (11,12) conforme representado na **Figura 2**.

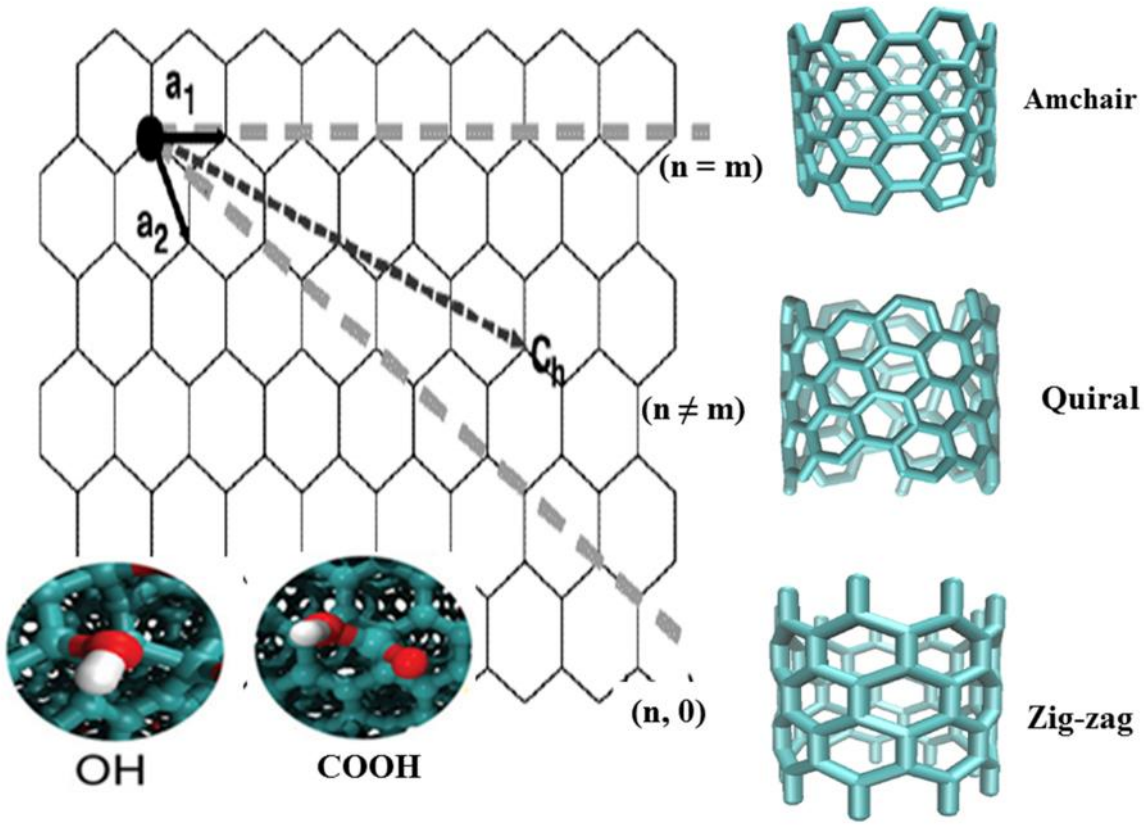

Figura 2. Representação de CNT com diferente geometria estrutural através dos índices de Hamada (n, m) e tipo de oxidação (OH, COOH). (*Adaptada de Hamada*. 1992).

Além disso, em função dos índices (*n*, *m*), um CNT é metálico (propriedades condutoras) quando ($n - m$) = 3q, sendo q um número inteiro, em caso contrário é considerado semicondutor. Todos os SWCNT do tipo “armchair” são metálicos (q = 0), enquanto que os “zigzag” e “quirais” podem ser metálicos ou semicondutores (11-13).

Estes atributos electro-topológicos da estrutura devem ser levados em consideração, já que podem afetar as propriedades de interação dos CNT com os componentes biológicos e

modular respostas no nível bioquímico, quando utilizados nas formas puras ou funcionalizados (oxidação com grupos OH, COOH, por exemplo); as quais podem ser relevantes para induzir toxicidade (citotoxicidade) ou promover respostas terapêuticas citoprotetoras por modificação covalente ou não covalente da superfície dos CNT (1, 2, 7,8).

Atualmente os métodos de funcionalização estão sendo desenvolvidos com o objetivo de melhorar sua biocompatibilidade (reduzir sua nanotoxicidade) e propriedades de solubilidade em solventes aquosos devido ao carácter hidrofóbico dos CNT (14). A funcionalização dos CNT pode ser realizada através de adsorção química e/ou dopagem por modificação não covalente, a qual pode favorecer a incorporação de grupos funcionais de diferentes complexidades com uma ampla variedade de moléculas incluindo: peptídeos, ácidos, aminas, polímeros com alta sensibilidade de detecção e reconhecimento molecular ou utilizados como efetivos carregadores de fármacos de liberação controlada (do inglês *drug delivery*) com propriedades anticancerígenas, antivirais ou antibacterianas (7).

Particularmente, a modificação covalente de CNT através de processos oxidativos com frequência geram grupos hidroxila (OH) e carboxila (COOH) nas pontas e/ou paredes dos CNT, permitindo que possam expressar interessantes propriedades como complexação/quelação de íons potencialmente tóxicos de tipo metálico e não metálico (Ca^{2+}, Fe^{2+}), baseado no aumento significativo da capacidade de adsorção (quimissorção). As funcionalizaçãoes podem também potencializar propriedades antioxidantes frente a determinadas espécies reativas de oxigênio como o radical hidroxila gerado na reação de Fenton-Haber-Weiss e incluso em condições pro-oxidantes induzidas experimentalmente como excesso de peroxido de hidrogênio (15).

1.2. Efeitos de nanotubos de carbono

Em termos gerais, as dimensões das nanopartículas (CNT) podem interferir em processos toxicocinéticos como: absorção, biodistribuição, metabolismo e na excreção nos sistemas biológicos (8).

Ao contrário das micropartículas (carbono amorfo particulado) de maior diâmetro médio, os CNT abaixo de 30 nm podem ter maior acessibilidade e potencial de acumulação nos tecidos e sítios ativos de enzimas chaves. Também podem redistribuir-se a partir do seu sítio de exposição, escapar das defesas fagocíticas normais, ativar respostas imunológicas inflamatórias, modificar a estrutura de proteínas, e com isso afetar a função fisiológica dos tecidos expostos (8). Este fato

deve ser analisado desde o ponto de vista toxicodinâmico; através do estudo de interações com os mecanismos bioquímicos relevantes para a sobrevivência e morte das células. Um dos fatores que deve ser levado em consideração nos estudos de citotoxicidade de CNT relaciona-se a sua habilidade de penetrar as barreiras biológicas através de um processo passivo independente de energia, já que os CNT se difundem através da membrana celular (bicamadas lipídicas das membranas citoplasmáticas e de organelas chaves como lisossomos e mitocôndrias) (8). Assim, os CNT bem dispersos (individualizados) podem atravessar as membranas biológicas no nível celular e subcelular dependendo de sua afinidade determinada pelo coeficiente de partição octanol/agua (Log P) ou entrar diretamente através dos transportadores e canais iônicos e potencialmente induzir diferentes graus de inibição destes, dependendo da concentração, diâmetro e outros atributos geométrico-estruturais, que serão tratados em detalhe mais adiante desde o ponto de vista das relações quantitativas estrutura-atividade (16).

Estudos prévios de citotoxicidade (genotoxicidade) sugerem a existência de interação toxicodinâmica direta entre CNT e proteínas ou enzimas regulatórias relacionadas ao DNA que poderiam levar a danos físicos no material genético. Em adição, a genotoxicidade também tem sido associada com estresse oxidativo, inflamação e alterações na sinalização celular (17, 18). Os catalizadores metálicos usados no processo de síntese de CNT têm sido apontados como a fonte principal de efeitos deletérios sobre diferentes organelas celulares (mitocôndria, lisossomos) (17,18). Apesar de ser relativamente esperado que impurezas metálicas apresentem potencial citotóxico, no caso dos CNT não é possível saber com precisão se os efeitos são devidos a íons (cátions divalentes) liberados desde a superfície das impurezas metálicas ligadas ao carbono. Também pode-se questionar se os efeitos citotóxicos podem ser atenuados pela capacidade dos CNT de adsorver metais na superfície quando funcionalizados (oxidados), fatos estes pelos quais estudos mecanísticos sobre avaliações nanotoxicológicas resultam desafiadores.

1.2.1. Efeitos mitocondriais induzidos por nanotubos de carbono

As mitocôndrias têm sido reconhecidas por seu papel decisivo em todas as células eucariotas, como responsáveis diretas do metabolismo energético (produção de energia na forma de ATP). Numerosos estudos *in vitro* salientam a importância da mitocôndria como organela celular fundamental onde convergem importantes vias de sinalização tanto de morte como de sobrevivência para a célula. Recentemente, a mitocôndria, e em particular o processo de indução

da abertura do poro de transição de permeabilidade mitocondrial (MPTP, do inglês *mitochondrial permeability transition pore*), têm sido relacionados diretamente com a manutenção do estado redox e bioenergético em condições fisiopatológicas (19).

O MPTP é um canal complexo multiproteico não seletivo a diversos solutos e sensível a inibição pela ciclosporina A (CsA). Estruturalmente o MPTP está formado pelo transportador mitocondrial de nucleotídeos de adenina (ADP/ATP) ou (ANT, do inglês *adenine nucleotide traslocase*), o transportador de fosfato mitocondrial (PiC, do inglês *pyrophosphate carrier*), a subunidade F0 da F0F1-ATP-sintase-sensível a inibição da oligomicina A (Oligo A) na membrana interna e o canal aniônico dependente de voltagem (VDAC, do inglês *voltage-dependent anion channel*) presente na membrana externa mitocondrial e sensível às variações do potencial membrana mitocondrial (ψ_m) (19). O MPTP constitui uma ponte de comunicação entre o meio extracelular e a matriz mitocondrial e tem sido associado à disfunção mitocondrial, com alta incidência na epidemiologia molecular de mecanismos fisiopatológicos indutores de doenças como: isquemia cardíaca, neurodegenerativas (Alzheimer, Parkinson, distrofia musculares), hepatotoxicidade induzida e outras (19) conforme representado na **Figura 3**.

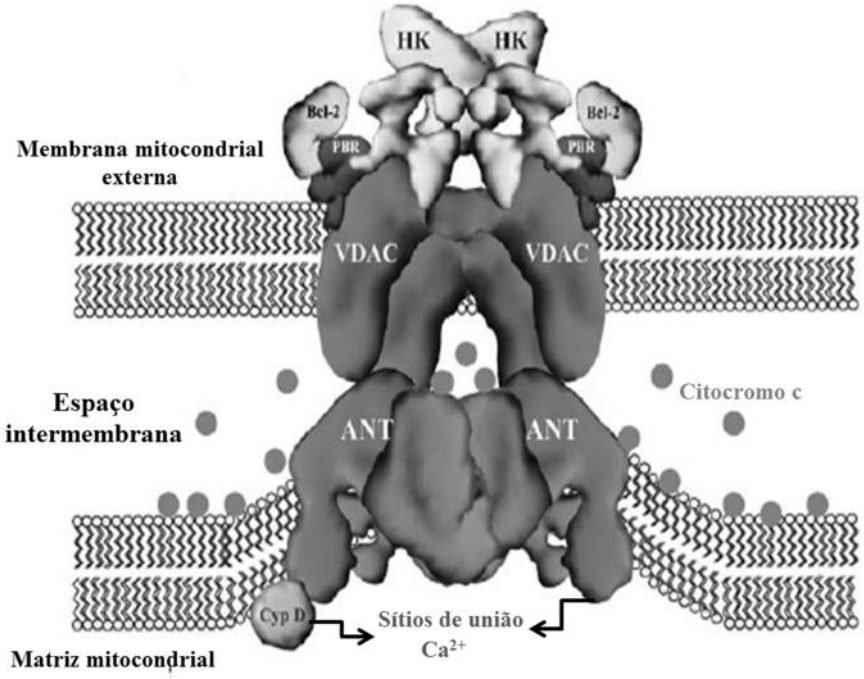

Figura 3. Representação dos componentes moleculares chaves do complexo multiproteico poro de transição de permeabilidade mitocondrial (MPTP). (*Adaptado de P. Bernardi*. 2006). Hexoquinase (HK), ciclofilina D (CypD), receptor benzodiacepínico periférico (PBR), proteína anti-apoptótica reguladora de permeabilidade da membrana mitocondrial externa (Bcl2).

A abertura do MPTP pode ser iniciada nas mitocôndrias frente a diferentes estímulos como: perda da homeostase de Ca^{2+} e posterior sobrecarga intracelular, exposição a cátions divalentes (Fe^{2+}), e condições metabólicas pro-oxidantes como o excesso de peróxido de hidrogênio ou acumulação significativa de espécies reativas de oxigênio (ROS, do inglês *reactive oxygen species*), como o radical hidroxila (•OH) gerado na reação de Fenton-Haber-Weiss na matriz mitocondrial (15, 19).

Este processo seria mediado pela permeabilizacão das mitocôndrias e abertura do MPTP, gerando uma difussão de solutos de até 1,5 kD ao interior da matriz mitocondrial, provocando alterações coloido-osmóticas (inchamento mitocondrial), perda do potencial de membrana da mitocôndria por eventos de desacoplamento da cadeia transportadora de elétrons e a fosforilação oxidativa na F0F1ATP-sintase, acompanhado de redução significativa nos níveis de ATP. Ao mesmo tempo são liberados sinais pro-apoptóticos ao citoplasma como o citocromo *c,* integrante da cadeia transportadora de elétrons, ao citoplasma, moléculas efetoras como caspases 3 e 9, além do fator indutor de apoptose (FIA), considerados mecanismos responsáveis da disfunção mitocondrial (15,19).

A apoptose tem sido considerado em vários estudos como um dos mecanismos fundamentais associados à nanotoxicidade. Por outra parte, é considerado um alvo importante para o tratamento do câncer, durante a progressão de tumores que parecem estar relacionados com alterações na habilidade da célula de experimentar este processo. De fato, diferentes fármacos anticancerígenos atuam através da ativação de vias apoptóticas intrínsecas (mitocondriais). Baseado nos elementos anteriormente mencionados, a Nanomedicina Mitocondrial é uma área nova em rápido crescimento na pesquisa biomédica, que promove o desenvolvimento de novas subdisciplinas como a Nanofarmacologia e Nanotoxicologia Mitocondrial. Neste contexto, o objetivo principal é fornecer plataformas *in vitro* através do uso de modelos de mitocôndrias isoladas de diferentes tecidos, para acessar e manipular os mecanismos mitocondriais, bem como seus componentes proteicos. E importante salientar que os nanomateriais de carbono com alto coeficiente de partição octanol/água (SWCNT, MWCNT) apresentam alto potencial mitocôndrio-trópico (capacidade para atravessar as membranas externa e interna e se acumular seletivamente nas mitocôndrias) (15,19). A presença de nanotubos de carbono próximos à cadeia transportadora de elétrons e pode interromper o fluxo normal de

elétrons nos complexos respiratórios (I, II, III, IV) e afetar o gradiente de prótons (H^+), associado a uma redução incompleta do oxigênio molecular a H_2O e diminuição da síntese de ATP (ADP + Pi), pela ATP-sintase (fosforilação oxidativa ou estado 3 da respiração), que podem induzir abertura do MPTP (19).

Assim, a síntese de nanomateriais de carbono (CNT) orientada para a modulação dos efeitos sobre os mecanismos de indução do MPTP, poderia ser considerada no planejamento racional e avaliação de novos candidatos terapêuticos, biocompatíveis e com grande potencial para modular seletivamente mecanismos mitocondriais de toxicidade ou de mitoproteção a escala manométrica, e, de esta forma contribuir ao desenvolvimento de uma Nanomedicina segura para a saúde humana e o meio ambiente.

1.3. Correlações *in sílico* estrutura-atividade (Nano-QSAR) de nanotubos de carbono

O número e variedade de nanomateriais de carbono (CNT) tem se incrementado desproporcionalmente ao longo da passada década, e as expectativas de vendas até 2020 estima-se que irão superar o trilhão de dólares (5). Atualmente existem no mercado mundial mais de 15 milhões de nanocompostos de diferente natureza, os quais têm sido descobertos ou sintetizados em laboratórios de química-farmacêutica com base em algum procedimento envolvendo nanotecnologias (5). Uma grande quantidade destes nanomateriais de carbono (CNT), em formas puras ou funcionalizados, não tem ainda estudos conclusivos e aplicações definidas para áreas como as ciências biomédicas, farmacologia clínica, indústria agrícola ou de algum outro tipo. Isto é consequência direta do desequilíbrio existente entre a velocidade com que os novos nanomateriais são gerados ou produzidos, em relação à quantidade dos mesmos que são submetidos à rigorosa avaliação do potencial risco tóxico para a saúde humana e meio ambiente, inerente aos sistemas de dimensões nanométricas. A situação é mais crítica levando em consideração que a maioria dos ensaios de farmacologia e toxicologia experimental para nanopartículas é, em geral, muito custosa em termos de infraestrutura, recursos humanos e tempo. Também vale a pena salientar o aspecto ético associado à pesquisa com animais e sua posterior morte ao final da pesquisa. Estes aspectos críticos ainda estão sendo implementados pelos principais órgãos regulatórios como a Organização para o Desenvolvimento e Cooperação Económica (OECD, do inglês *Organization for Economic Cooperation and Development*) e a Organização Internacional para a Estandardização (ISO, do inglês *International Standard*

Organization) (20,21) incluindo novas iniciativas como NanoReg baseada na colaboração multi-laboratórios ao redor do mundo. Que se responsabilizam e reconhecem a importância do desenvolvimento de metodologias de Toxicologia Alternativa, em concordância com o princípio das *3Rs* (do inglês *Reduction, Refinement and Replacement*) (22), que permitam predizer o impacto tóxico das nanopartículas e dar resposta á crescente produção de nanomateriais de diversa natureza.

Neste contexto, a indústria Farmacêutica e Biotecnológica tem desenvolvido novas estratégias para aprimorar o desenho racional de nanomateriais. Assim, os estudos baseados no uso de ferramentas *in sílico* (Nano-QSAR/Nano-QSPR/Nano-QSTR, do inglês *quantitative structure-activity/property/toxicity-relationships for nanoparticles*), são usados como ferramentas preditivas para o descobrimento, otimização de nanomateriais líderes, decodificação quantitativa de atributos estruturais, propriedades físico-químicas relevantes, envolvidas na resposta biológica de nanomateriais de carbono (CNT) (23-27). Os métodos *in silico* de relação quantitativa estrutura- atividade estão baseados numa representação da estrutura molecular das nanopartículas (CNT), através de informação estrutural relevante que se traduz em certos números, denominados nanodescritores moleculares (**D_m**: índices topológicos, índices de Hamada (*n*, *m*), diâmetro, ângulo quiral, massa molecular, número de átomos, condutividade elétrica, grau/tipo de funcionalização, log P, grafo-teóricos, invariantes entrópicas, geometria/dimensão fractal, etc) (23-27), os quais podem ser relacionados com uma atividade biológica específica (**Y**) determinada experimentalmente (**Y_{obs}**: citotoxicidade, citoproteção, indução de ROS, atividade antioxidante) ou calculada teoricamente ($Y_{teórica}$: energia livre de ligação (FEB, do inglês *free energy of binding*) proteína-ligante, constantes de inibição enzimática (K_i)) usando diferentes softwares de bioinformática (Autodock tools, Autodock Vina, etc). Estas relações quantitativas estrutura-atividade podem ser formalmente representadas mediante modelos matemáticos (equação Nano-QSAR) como uma função de regressão linear ou não linear (**Y_{pred}**) de cada um dos n_i-nanodescritores moleculares **D_m** multiplicados por um coeficiente estatísticos ótimos **a_k (a_1, a_2, a_3,..., a_n)** derivados da análise de regressão junto com um termo de erro (**e_0**):

$$Y_{obs} = Y_{pred} + e_0 \qquad (1)$$

$$Y_{pred} = f\left(\sum_{i}^{n} a_k D_m\right) + e_0 \qquad (2)$$

$$Y_{pred} = a_1 D_{m_1} + a_2 D_{m_2} + a_3 D_{m_3} + a_n D_{m_n} + e_0 \qquad (3)$$

Os valores dos $\mathbf{a_k}$ podem ser obtidos estatisticamente dependendo do algoritmo estatístico selecionado (classificação e regressão) para gerar a melhor equação do modelo Nano-QSAR.

Os modelos mais utilizados estão baseados em métodos de regressão (linear ou não linear), particularmente aqueles como regressão linear múltipla (MLR, do inglês *Multiple Linear Regression*) devido à sua simplicidade. Os modelos nano-QSAR baseados em MLR permitem modelar a atividade/propriedade biológica ($\mathbf{Y_{pred}}$) como uma função linear multivariável de nanodescritores moleculares ($\mathbf{D_m}$). Além disso, nas etapas iniciais da descoberta molecular e estudo do mecanismo de ação de novos candidatos terapêuticos, as técnicas lineares aportam suficiente informação da relação quantitativa em termos de probabilidade de que uma determinada molécula apresente atividade associada a um mecanismo em estudo. Adicionalmente os modelos nano-QSAR baseados em algoritmos de classificação, em particular, os métodos de análise de discriminante linear (LDA, do inglês *Linear Discriminant Analysis*) têm a qualidade de ser simples, permitindo a classificação de objetos (nanopartículas) em grupos ou atributos/propriedades predeterminadas (ex: níveis de intensidade de uma atividade em: **1)** inativo, baixo, médio, elevado, ou **2)** no tóxico ou não tóxico).

Um passo decisivo para o sucesso dos estudos Nano-QSAR está associado à interpretação dos modelos gerados e verificação de sua robustez e potencial preditivo devido à escassez de conjuntos de dados abrangentes sobre nanotoxicidade e caracterização físico-química dos nanomateriais. Desta forma as novas ferramentas *in sílico* devem dispor de algoritmos e parâmetros de validação rigorosos, para modelar com sucesso dados relativamente escassos e às vezes de baixa qualidade para quantificar/correlacionar a estrutura/propriedades dos nanomateriais com os efeitos biológicos experimentais ou teoricamente determinados (23-27).

O poder preditivo dos modelos Nano-QSARs pode ser julgado através de vários critérios ou parâmetros de validação estatística (interna e externa), dependendo do método estatístico aplicado (regressão, classificação):

1.3.1. Validação de modelos Nano-QSARs baseado em métodos de regressão:

Validação interna

A validação interna permite julgar a qualidade e ajuste preditivo do modelo nano-QSAR (Y_{pred} vs. Y_{obs}). Neste procedimento os dados são divididos através de diversos procedimentos estatísticos num subconjunto de treinamento ou calibração (75 % das Y_{obs}), que é usado para

obter a equação nano-QSAR e um subconjunto de validação (25% das Y_{obs}), o qual é utilizado para provar o ajuste preditivo do modelo (25). A limitação desta abordagem é a robustez preditiva quando aplicado a um conjunto de dados completamente novo (20,28). Alguns dos parâmetros estatísticos da validação interna são:

- Coeficiente de validação cruzada (LOO-CV, do inglês, *leave-one-out cross-validation*)
- Soma dos quadrados dos resíduos calculados (PRESS, do inglês, *predicted residual sum of squares*).
- Coeficiente de determinação de validação interna (R^2_{train}).
- Coeficiente de determinação de validação interna ajustado (R^2adj).

Validação externa

A validação externa permite julgar a externabilidade (robustez) e/ou poder preditivo do modelo nano-QSAR (23-27). De forma similar, neste procedimento os dados são divididos através de diversos procedimentos estatísticos num subconjunto de treinamento ou calibração (75 % das Y_{obs}), que é usado para o desenvolvimento da equação nano-QSAR e um subconjunto de validação (25% das Y_{obs}), que garante previsibilidade do modelo; através da aplicação da equação nano-QSAR obtida a um conjunto de dados completamente novo (20,28). Alguns dos parâmetros estatísticos usados para fins de validação externa são:

- Coeficientes de validação externa Q^2_{test} (Q^2_{F1}, Q^2_{F2}, Q^2_{F3}), onde F_k: diferentes níveis de validação externa.
- Valores da raiz quadrada do erro médio (RMSE, do inglês, *root mean square error*)
- Erro médio absoluto (MAE, do inglês *mean absolute error*)
- Coeficiente de correlação de concordância (CCC, do inglês *concordance correlation coefficient parameter*).

1.3.2. Validação de modelos Nano-QSARs baseados em classificação estatística:

Parâmetros estatísticos de validação gerais:

- Chi quadrado ($\chi 2$)
- Especificidade (*Sp*)
- Sensibilidade (*Sn*)

1.3.3. Nanodescritores relevantes

Numa análise QSAR tradicional, as características estruturais (descritores moleculares), são utilizadas para caracterizar e quantificar as propriedades físico-químicas das moléculas. Estes

parâmetros estruturais fornecem uma grande variedade de informações valiosas para entender e predizer potenciais relações entre características moleculares e atividade biológica (23-27). Os descritores podem ser determinados experimentalmente ou calculados através de diferentes teorias/métodos semi-empíricos implementados em pacotes de software comerciais. Embora mais de 5000 descritores moleculares tenham sido propostos e calculados para representar a estrutura de moléculas convencionais, a maioria deles é inaplicável para o caso dos nanomateriais ou precisa pelo menos de algum nível de adaptação para ser utilizado em nanoescala (23-27). Uma representação geral dos passos chaves na construção de um modelo Nano-QSAR é apresentada conforme **Figura 4**.

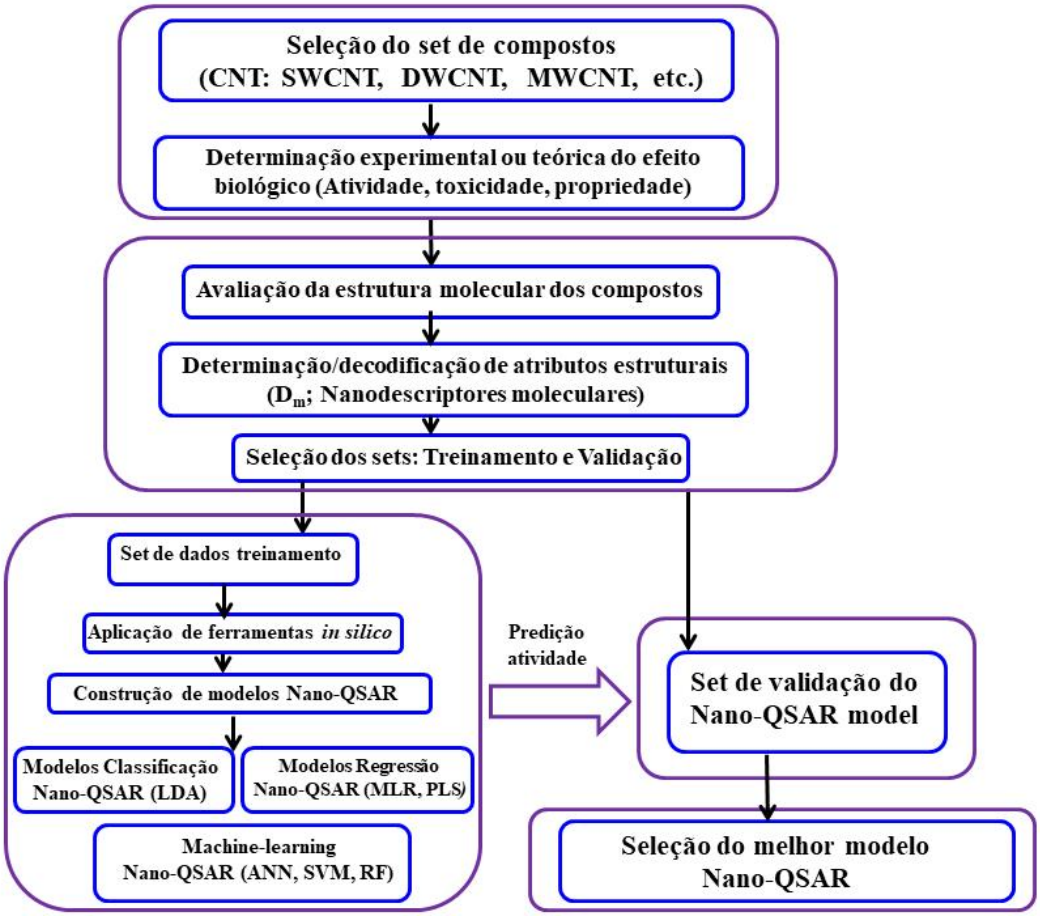

Figura 4. Representação geral para a construção de um modelo Nano-QSAR. (*Adaptação de OECD* 2011).

Os principais problemas associados ao cálculo dos descritores teóricos para os nanosistemas (nanodescritores) são a complexidade e a não uniformidade dos nanomateriais para representar numericamente um determinado atributo físico-químico ou propriedade estrutural relevante.

Alternativamente, parâmetros importantes, como tamanho, forma e carga de superfície, grau de funcionalização, estado de aglomeração, podem ser usados como nanodescritores para o desenvolvimento de modelos nano-QSAR. Os mesmos podem ser medidos por várias técnicas experimentais como: Microscopia Electrónica de Transmissão (TEM), Microscopia Electrónica de Varredura (SEM), Espectroscopia Raman, Espectroscopia infravermelho com transformada de Fourier e outras. A falta de acordo sobre como caracterizar os nanomateriais antes ou durante os ensaios de toxicidade é amplamente reconhecida como um dos principais desafios que devem ser abordados para a aplicação bem sucedida da abordagem *in sílico* nano-QSAR, para representação estrutural de nanomateriais de carbono (CNT-nanodescritores). (20, 21). Neste sentido, grandes esforços têm sido realizados pela comunidade científica internacional no intuito de harmonizar critérios e diretrizes para validar procedimentos *in sílico* de avalição dos efeitos dos nanomateriais, através de normativas implementadas pela OECD, ISO-TC-229 (20, 21), eNanoMapper, NANOREG. Baseando suas atividades na criação de redes de especialistas, grupos de trabalho e grandes bases de dados provenientes de estudos interlaboratoriais, para desta forma modelar a toxicidade de nanomateriais (20, 21).

1.4. Ensaios de Docagem Molecular

No intuito de desenvolver técnicas que permitam avaliar ou inferir a toxicidade de nanomateriais com rapidez e eficiência, tem sido sugerido o uso de abordagens via simulação computacional de processos biofísicos envolvidos na nanotoxicidade de nanopartículas (CNT). Neste contexto, a docagem molecular (*do inglês*, *Molecular Docking*) pode ser definida como uma ferramenta da Biologia Computacional para prever a energia de interação entre duas moléculas, um receptor-alvo (proteina) e um xenobiótico/fármaco (ligante) (29,30). Com esta abordagem teórica pode ser modelada a estabilidade dos complexos formados entre receptor-ligante, testando diferentes conformações e orientações de um ou vários potenciais inibidores num local presumido de ligação (sítio ativo da proteína alvo)), o qual é definido a partir da análise da estrutura tridimensional do receptor alvo (29,30). A docagem molecular é baseada em algoritmos ou funções matemáticas de regressão linear (AutoDock Vina *scoring functions*), que são capazes de gerar um grande número de complexos receptor-ligante, avaliando-os em termos da energia livre de ligação (ΔG_{bind} ou FEB: do inglês *free energy of binding*, expresso em Kcal/mol^{-1}), resultado do balanço crítico entre contribuições que se opõem à complexação

receptor-ligante e aquelas que a favorecem (29,30). A estratégia de busca da melhor conformação/orientação do ligante precisa explorar exaustivamente todas as múltiplas formas de ligação no sítio ativo do receptor alvo, o que inclui tanto a exploração de todos os seis graus de liberdade translacional e rotacional do ligante, quanto os graus de liberdade conformacionais do receptor (29,30). Desta forma, o valor de FEB para representar a estabilidade dos complexos receptor-ligante leva em conta os efeitos hidrofóbicos e termodinâmicos de desolvatação, quando um ligante desloca as moléculas de água do sítio ativo do receptor.

O processo de analisar a interação receptor-ligante não é simples, pois diversas contribuições desempenham papel determinante na afinidade entre moléculas pequenas como os CNT e seus alvos biológicos (mecanismos mitocondriais); o mesmo é influenciado por muitos fatores entrópicos e entálpicos como: **1)** dos complexos proteina-ligante (efeito hidrofóbico ou ΔGw, pontes de hidrogênio $\Delta G_{H\text{-}bond,}$ interações eletrostáticas $\Delta G_{electrost}$, entropia residual ou vibracional $\Delta S_{prot\text{-}ligante}$, interações intermoleculares $\Delta H_{prot\text{-}ligante}$), **2)** do receptor ($\Delta H_{intra}$, $\Delta H_{desolvatação}$, $\Delta S_{translacionais}$, $\Delta S_{conformacionais}$, $\Delta S_{torcionais}$, $\Delta S_{vibracionais}$), e **3)** do ligante (ΔH_{intra}, $\Delta H_{desolvatação}$, $\Delta S_{conformacionais}$, $\Delta S_{torcionais}$, $\Delta S_{vibracionais}$), segundo equações **4** e **5**.

$$FEB_{dock} \approx \Delta G_{bind} = \Delta G_{vdW} + \Delta G_{H-bond} + \Delta G_{electrost} + \Delta G_{\text{int}} \quad \textbf{(4)}$$

$$FEB = \Delta H + \Delta G_{(solvation)} - T\Delta S_{(bind)} \quad \textbf{(5)}$$

Estes parâmetros termodinâmico-biofísicos serão discutidos em detalhe nas próximas secções da tese. A docagem molecular também considera o efeito do ambiente biofísico no receptor em termos de flexibilidade e/ou rigidez parcial ou total da proteina, ligantes co-cristalizados provenientes do processo de cristalografia do receptor os quais devem ser removidos antes da simulação, assim como a distribuição de cargas no ligante. Dessa forma, os algoritmos de docagem molecular precisam inserir aproximações tanto no método de campo de força (Autodock Vina scoring functions), como no método de varredura do espaço conformacional do sítio ativo do receptor e/ou ligante (docagem rígido ou docagem flexível), para minimizar o custo computacional associado a fatores de incerteza entálpicas e entrópicas, os quais são difíceis de prever quando o sistema envolve muitos átomos (29,30). A intenção aqui não é analisar todas as contribuições termodinâmicas descritas acima, mas sim introduzir aquelas sobre as quais o pesquisador possui maior controle e compreensão (interações hidrofóbicas de van der Waals, eletrostáticas, ligações de hidrogênio, dentre outras). Dentro do atual panorama de

desenvolvimento crescente de novos nanomateriais e aplicações em nanotecnologias, a integração de abordagens metodológicas multidisciplinares (*in silico*/*in vitro*) não é somente uma tarefa desafiadora, senão também pertinente diante da complexidade das novas propriedades físico-químicas emergentes da escala nanométrica e que estão criticamente envolvidas na interação com os mecanismos bioquímicos celulares e nanotoxicidade seletiva, os quais ainda precisam ser estudados.

Levando em consideração os elementos anteriormente mencionados, a presente tese foi orientada a partir dos seguintes objetivos:

2. Objetivo geral

Avaliar os efeitos induzidos por uma família de nanotubos de carbono sobre mecanismos mitocondriais chave através da integração de metodologias *in vitro* e *in sílico,* baseadas na predição de relações quantitativas estrutura-atividade.

2.1. Objetivos específicos

- Determinar e predizer os efeitos de CNT (CNT-prístinos, CNT-OH, CNT-COOH) sobre a modulação da abertura do poro transição de permeabilidade mitocondrial (MPTP) induzida por sobrecarga de Ca^{2+}, Fe^{2+} e H_2O_2 através de ensaios *in vitro* utilizando mitocôndrias isoladas de fígado de ratos *Wistar* e modelos *in sílico* Nano-QSAR.
- Caracterizar e predizer interações relevantes de CNT (CNT-prístinos, CNT-OH, CNT-COOH) com proteínas mitocondriais envolvidas na modulação do MPTP como: ANT (proteína translocadora de nucleotídeos de adenina; ADP/ATP) e canal aniônico dependente de voltagem (VDAC) utilizando de docagem molecular e Nano-QSAR (Nano-QSBR).
- Corroborar os resultados *in sílico* de docagem molecular sobre o mecanismo de interação dos CNT (CNT-prístinos, CNT-OH, CNT-COOH) com a ANT através de ensaios bioenergéticos num modelo de ecotoxicologia *in vitro* utilizando mitocôndrias isoladas de hepatopâncreas *litopenaeus vannamei*.
- Determinar e predizer os efeitos de CNT (CNT-prístinos, CNT-OH, CNT-COOH) sobre a inibição da reação de Fenton-Haber-Weiss eletro-induzida por sobrecarga de íons de Fe^{2+} (formação de radical hidroxila $^{\cdot}OH$) na matriz mitocondrial e utilizando modelos preditivos Nano-QSAR.

- Determinar os efeitos induzidos por CNT (CNT-prístinos, CNT-OH, CNT-COOH) sobre parâmetros críticos da função mitocondrial (respiração mitocondrial nos estados V3 e V4, potencial de membrana mitocondrial) *in vitro* e *in silico*.
- Identificação de atributos estruturais (nanodescritores) de CNT (CNT-prístinos, CNT-OH, CNT-COOH) responsáveis pelos efeitos sobre os mecanismos mitocondriais.

Artigo 1: Mitoprotective activity of oxidized carbon nanotubes against mitochondrial swelling induced in multiple experimental conditions and predictions with new expected-value perturbation theory

RSC Advances

PAPER

Cite this: *RSC Adv.*, 2015, **5**, 103229

Mitoprotective activity of oxidized carbon nanotubes against mitochondrial swelling induced in multiple experimental conditions and predictions with new expected-value perturbation theory†

Michael González-Durruthy,*[abcd] Jose Maria Monserrat,[abcd] Luciane C. Alberici,[e] Zeki Naal,[e] Carlos Curti[e] and Humberto González-Díaz*[fg]

Mitochondrial Permeability Transition Pore (MPTP) is involved in neurodegeneration, hepatotoxicity, cardiac necrosis, nervous and muscular dystrophies. We used different experimental protocols to determine the mitoprotective activity (%*P*) of different carbon nanotubes (CNT) against mitochondrial swelling in multiple boundary conditions (b_j). The experimental boundary conditions explored included different sub-sets of combinations of the following factors b_0 = three different mitochondrial swelling assays using the MPT-inductor (Ca^{2+}, Fe^{3+}, H_2O_2) combined or not with a second MPT-inductor and swelling control assays using MPT-inhibitor (CsA, RR, EGTA), b_1 = exposure time (0–600 s), and b_2 = CNT concentrations (0–5 μg ml^{-1}). Other boundary conditions (b_k) changed were the CNT structural parameters b_3 = CNT type (SW, SW + DW, MW), b_4 = CNT functionalization type (H, OH, COOH). We also changed different of CNT like b_5 = molecular weight/functionalization ratio ($^{min}W/^{max}W$) or b_6 = maximal and minimal diameter (D_{min}/D_{max}) as physic-chemical properties (V_k). Next, we employed chemoinformatics ideas to develop a new Perturbation Theory (PT) model able to predict the %*P* of CNT in multiple experimental conditions. We investigated different output functions of the absorbance $'f(\varepsilon_{ij})$ used in PL4/PL5 methods like (ε_{ij}, $1/\varepsilon_{ij}$, $1/\varepsilon_{ij}^2$, or $-\log \varepsilon_{ij}$) as alternative outputs of the model. The inputs are in the form an additive functions with linear/non-linear terms. The first term is a function $^0f(\langle\varepsilon_{ij}\rangle)$ of the average absorbance $\langle\varepsilon_{ij}\rangle$ (expected value) in different assays (b_j). The concentration dependent terms are linear functions of concentration, or hill-shaped curves similar to PL4/PL5 functions (used in dose–response analysis). The CNT structure perturbation terms are linear/non-linear functions of Box–Jenkins operators (ΔV_{kj}). The ΔV_{kj} are moving averages (deviations) of the V_k of the CNT with respect to their expected values $\langle V_{kj}\rangle$. The best model found predicted the values of absorbance (measure of mitoprotective activity *vs.* mitochondrial swelling) with regression coefficient R^2 = 0.997 for >6000 experimental data points (q^2 = 0.994). Last, we used the model to carry out a simulation of the changes on mitoprotective activity for CNT family after one increase of 1–10% of the $^{min}W_i$ and $^{max}D_i$ of CNT.

Received 21st July 2015
Accepted 20th November 2015

DOI: 10.1039/c5ra14435c

www.rsc.org/advances

Introduction

Mitochondrial Permeability Transition (MPT) is associated with a higher permeability of the mitochondrial membranes to metabolites and xenobiotics under a threshold value of MW < 1500 Da due to the opening of MPT pore (MPTP).[1–5] The MPTP is a multi-protein complex that connects the interior and the outer mitochondrial membrane formed by the ADP/ATP carrier or adenine nucleotide translocase (ANT) and the voltage-dependent anion channel (VDAC). Since the discovery of MPTP by Haworth and Hunter in 1979, this biochemical event has been linked to hepatotoxicity, neurodegeneration (Alzheimer, Parkinson), cardiac ischemia, nervous and muscular dystrophies (amyotrophic lateral sclerosis). In these sense, MPTP has been recognized as a critical factor in the cellular responses under

[a]*Institute of Biological Science (ICB), Universidade Federal do Rio Grande (FURG), 90610-000, Porto Alegre, RS, Brazil. E-mail: gonzalezdurruthy.furg@gmail.com*
[b]*ICB-FURG Post-graduate Program Physiological Sciences – Comparative Animal Physiology, Brazil, 90610-000, Porto Alegre, RS, Brazil*
[c]*National Institute of Carbon Nanomaterial Science and Technology, Belo Horizonte, MG, Brazil*
[d]*Nanotoxicology Network (MCTI/CNPq), Environmental and Occupational Nanotoxicology, Rio Grande, RS, Brazil*
[e]*Department of Physic-Chemistry, Faculty of Pharmacy of Ribeirão Preto, University of São Paulo (USP), 14040-903 Ribeirão Preto, SP, Brazil*
[f]*Department of Organic Chemistry II, Faculty of Science and Technology, University of the Basque Country UPV/EHU, 48940, Leioa, Bizkaia, Spain. E-mail: humberto.gonzalezdiaz@ehu.es*
[g]*IKERBASQUE, Basque Foundation for Science, 48011, Bilbao, Bizkaia, Spain*

† Electronic supplementary information (ESI) available. See DOI: 10.1039/c5ra14435c

pathological conditions accompanied of osmotic swelling, leading to increases in volume in the mitochondrial matrix, rupture of the outer mitochondrial membrane by opening of membrane pores in mitochondria, dissipation of the membrane potential, increase of reactive oxygen species (ROS) generation and affects the normal ATP levels. This process is triggered by calcium overload, transition metals in concentrations greater than 5 μM and other pro-oxidant conditions.[2–5] Also can trigger conformational changes in inner mitochondrial membrane proteins; oxidation of thiol groups that form the MPTP and release of pro-apoptotic signals (cytochrome c, caspase 3, caspase 9), which are closely linked to mitochondria dysfunction mechanisms. Following this idea, the search of new chemical structures able to act as MPTP-inhibitors (mitoprotectors) has become a very important goal. The immunosuppressant drug cyclosporine A (CsA)[6] is a one of the best known examples of mitoprotector agent with direct action over this target. Recently research has focused on the effects of structural changes over structure–property relationships of mitoprotectors. For instance, de Faria *et al.*[6] carried out experimental studies of structure-mitoprotective activity relationships on derivatives of phenothiazine. In other recent study it was evaluated the comparative hepatoprotective effects of tocotrienol analogs by different mechanisms including mitoprotective activity.[7]

In this context, the great potential of applications of carbon nanotubes (CNT) has increased the interest with respect to other carbon biomaterials. The lipophilic character based on its high lipid/water partition coefficient and enough access to the mitochondrial membranes could induce cell death or apoptosis mediated by alteration of bioenergetic mechanisms.[7–9] Nevertheless is possible to reduce their toxicity through the chemical oxidation as in the case of SW/MWCNT-OH and/or SW/MWCNT-COOH. In this context, other authors,[8] demonstrated in structure–property relationships studies that the acid-treated and taurine functionalized multi-walled carbon nanotubes (MWCNT) induced differential pulmonary toxicity in mice. Also, Ye *et al.*,[10] examined the mitoprotective effects of multi-wall carbon nanotubes (MWCNT) over osteoclastogenesis in presence of cyclosporine A (CsA) (classical inhibitor of MPTP), rendering MWCNTs as a promising candidate for the treatment of osteoclast-related diseases.

On the other hand,[11] the combination of different methods is of the major interest for the rational design of nanoscale systems like CNT, iron nanoparticles, micelle nanoparticles, *etc.* For this reason, Quantitative Structure–Property/Activity Relationships (QSPR/QSAR) methods may play an important role as enabling or complementary tools to experimentation. Tropsha, Leszczynski, Toropov, Puzyn, Roy, Hopfinger, and others[11–28] have published some of the pioneering works on NQSPR studies of nanoparticles (NQSPR). The main assumption of QSPR/QSAR[29–32] models in general is that similar molecules have similar properties. Consequently, small changes in the structure of the system should correlate linearly with small changes on the values of its properties. Paradoxically, not all similar molecules have similar properties. Very recently, Gonzalez-Díaz *et al.*,[33] formulated a general-purpose PT-QSPR method combining QSPR/QSAR approach and Perturbation Theory (PT) ideas. PT-QSPR models are very useful for the study of complex molecular systems with simultaneous variation of multiple experimental boundary conditions. In fact, González-Díaz H. *et al.* have applied PT-QSPR analysis for the study of chemical reactivity, drug metabolism, vaccine epitopes, metabolic networks, and also micelle nanoparticles. In addition, Luan *et al.*[36] published the first PT-QSPR model for the cytotoxicity of nanoparticles in multiple experimental conditions. Kleandrova *et al.*[37,38] extended the idea to the PT-QSPR studies of ecotoxicity and cytotoxicity of uncoated and coated nanoparticles under different experimental conditions. Last, Speck-Planche *et al.*[39] published the first PT-QSPR model of antibacterial profiles of nanoparticles in multiple experimental conditions.

In this context, it is clear the importance of the development of new mitoprotective drugs studying diverse types of CNT. They may become of the major importance towards both an experimental characterization of CNT in different experimental conditions using a definition of a general model for the prediction of MPT response to different kind of CNT. However, there are no reports of combined experimental and PT-QSPR theoretical studies towards the development of predictive tools for the design of new CNT with mitoprotective activity on MPTP.

In this work, we are going to report the first combined study with experimental–theoretical techniques in this direction. Firstly, we used three different experimental swelling protocols to determine the mitoprotective activity (%P) of different CNT in multiple experimental boundary conditions (b_j). The conditions explored were b_0 = specifications of the biological assay carried out (MPT-inductor: Ca^{2+}, Fe^{2+}, H_2O_2; MPT-inhibitor: CsA, ruthenium red (RR), EGTA, quercetin (Q) and second MPT-inductor: KCN, ascorbic acid or VitC), b_1 = exposure time to CNT, b_2 = CNT concentrations, b_3 = CNT type (SW, SW + DW, MW), b_4 = CNT functionalization type (H, OH, COOH). We also changed different of CNT like b_5 = molecular weight/functionalization ratio ($^{min}W/^{max}W$) or b_6 = maximal and minimal diameter (D_{min}/D_{max}) as physic-chemical properties. Next, we developed a new PT-QSPR model of mitoprotective activity. Last, we used the model to predict the values of %P of CNTs as mitoprotective activity in many different experimental conditions or after structural changes.

Materials and methods

Experimental section

Reagents and solutions. Sucrose, ethylene glycol-bis(β-aminoethyl)-*N*,*N*,*N*′,*N*′-tetraacetic acid (EGTA), $CaCl_2$, KCL, Fe^{2+}–citrate solutions, H_2O_2, ascorbic acid, cyclosporine A (CsA), ruthenium red (RR), potassium succinate (plus 2 μM rotenone), K_2HPO_4, piperazine-*N*′-2-ethanesulfonic acid (Hepes-KOH), quercetin, KCN. All other reagents were commercial products of the highest purity grade available. Pristine-carbon nanotubes, hydroxylated carbon nanotubes (CNT-OH) and carboxylated carbon nanotubes (CNT-COOH) were provided by Cheaptubes Company (http://cheaptubes.com/shortohcnts.htm).

Carbon nanotubes characterization and stock solutions. Transmission Electron Microscope (TEM, Tecnai G2-12 –

SpiritBiotwin FEI – 120 kV) was used to characterize the morphology of pristine and oxidized carbon nanotubes (MWCNT: CNT1; [SWCNT + DWCNT]-OH: CNT2; MWCNT-OH: CNT3, CNT4, CNT5; MWCNT-COOH: CNT6, CNT7, and CNT9; SWCNT-COOH: CNT8) see Fig. 1. In addition, Raman spectra were measured using a Renishaw Micro-Raman Spectroscopy System (Renishaw plc, Wotton-under-Edge, UK) at room temperature at a laser excitation wavelength of 514 nm (2.33 eV). All reactions were quenched to room temperature before Raman spectra were recorded to identify the characteristic peaks in the position of 1580 cm^{-1} (G band of graphite) and the peak in the 1350 cm^{-1} approximately associated to the presence of disorder and/or vacancy defects in the CNT-structure produced by chemical oxidation in the graphite structure (oxidized-CNT with OH and COOH functional groups) as shown in Fig. 2. The content of metallic impurities in all the samples was less than 5%. The proportions of metal impurities were determined by mass variation as a function of temperature using thermogravimetric analysis. The impurities of MWNT and SWNT with diameter (D) < 8 nm (CNTs 1, 2, 8 and 9) including their –OH and –COOH derivatives are the same: Co, Fe, Cr, Mg. For MWNT-OH and -COOH 10–20 nm are Co, Ni, Mg and Al (CNTs 4 and 7). For larger diameter MWNT (30–50 nm), the metallic impurities and its derivatives are Fe, Ni, Cr, Co, Mg (see Table 1 for details). CNTs were dissolved in dimethyl sulfoxide (DMSO: 900 μl) and ultrapure Milli Q water (10 μl) in individual stock solutions at a concentration of 1 mg ml^{-1}. Tip-sonication regime during 5–10 min was used to prevent CNTs agglomeration for MPT-assays carried out at a range of concentrations of 0.5–5 μg ml^{-1}. In this sense, the employed sonication time is known to generate a non-agglomerated suspension in a monodisperse state at concentrations below 100 μg ml^{-1} according to Bergin *et al.* (2010). The sonication power was 9.3 W, with an energy input of 16.7 kJ at 25 °C using a Ultronique/Eco-sonics Q-3.0/40A sonicator. After, samples were stirred for 10–15 min. The resulting diluted suspensions were cooled to room temperature and filtered through a 0.22 μm polycarbonate membrane (Millipore, USA), before exposure to mitochondria suspensions.

Animal welfare. Male *Wistar* rats (4 month-old; approx. 200 g) received food and water *ad libitum*. They were kept in plastic cages with wire tops in a light-controlled room (12 h light–dark cycle) at 22 ± 2 °C before starting the study in accordance with the Guidelines on the Handling and Training of Laboratory Animals published by the Universities Federation for Animal Welfare (1992).

Isolation of rat-liver mitochondria. We used standard differential centrifugation to isolate the mitochondria.[40] Male *Wistar* rats weighing approximately 200 g were euthanized by decapitation; livers (10–15 g) were immediately removed, sliced in medium (50 ml) consisting of 250 mM sucrose, 1 mM ethyleneglycol-bis(β-aminoethyl)-*N*,*N*,*N*′,*N*′-tetraacetic acid (EGTA) and 10 mM HEPES-KOH, pH 7.2, and homogenized three times for 15 s at 1 min intervals using a Potter-Elvehjem homogenizer. Homogenates were centrifuged (580 g, 5 min) and the resulting supernatant further centrifuged (10 300 × g, 10 min). Pellets were then suspended in medium (10 ml) consisting of 250 mM sucrose, 0.3 mM EGTA and 10 mM HEPES-KOH, pH 7.2, and centrifuged (3400 × g, 15 min). The final mitochondrial pellet was suspended in medium (1 ml) consisting of 250 mM sucrose and 10 mM HEPES-KOH, pH 7.2, and used within 3 h. Mitochondrial protein contents were determined by the Biuret reaction.[41]

Standard incubation procedure. Mitochondria isolated were energized with 5 mM potassium succinate (plus 2.5 μM

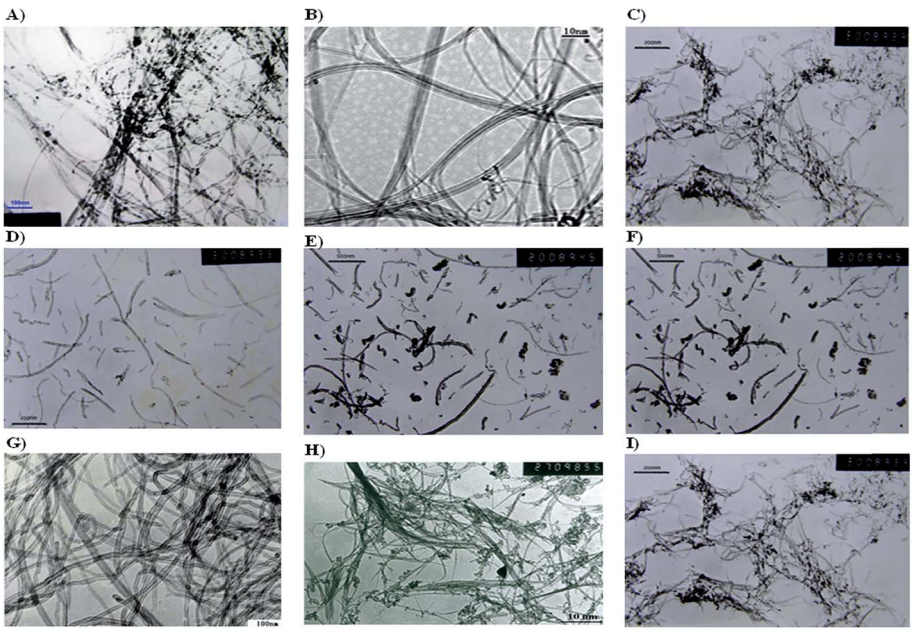

Fig. 1 TEM images of carbon nanotubes used in this study. (a) Pristine-MWCMT [CNT1], (b) SW/DWCNT-OH [CNT2], (c) MWCNT-OH [CNT3], (d) MWCNT-OH [CNT4], (e) MWCNT-OH [CNT5], (f) MWCNT-COOH [CNT6], (g) MWCNT-COOH [CNT7], (h) SWCNT-COOH [CNT8], (i) MWCNT-COOH [CNT9] (TEM, Tecnai G2-12-SpiritBiotwin FEI- 120 kV).

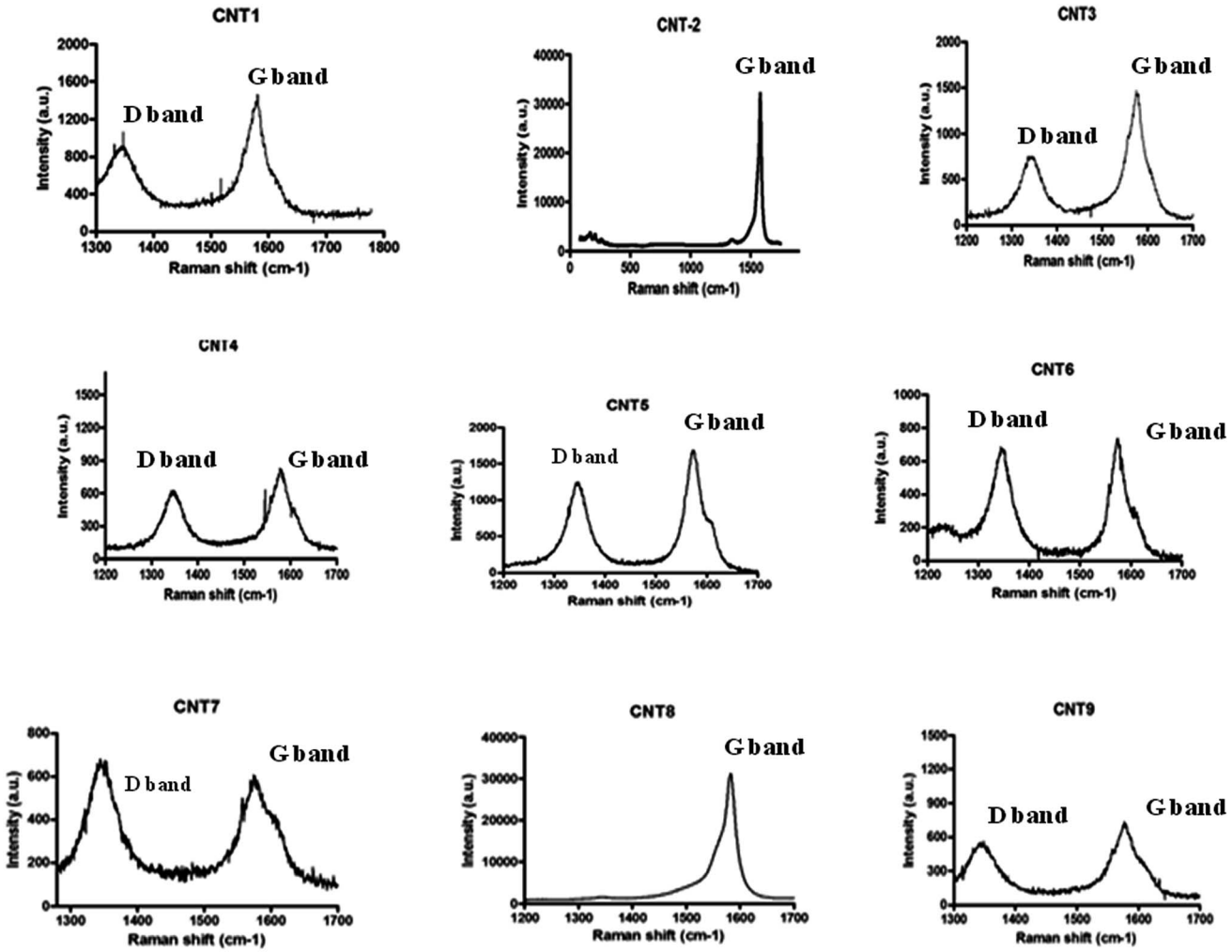

Fig. 2 Raman spectra of carbon nanotubes used in this study. Pristine-MWCMT (CNT1), SW/DWCNT-OH (CNT2), MWCNT-OH (CNT3), MWCNT-OH (CNT4), MWCNT-OH (CNT5), MWCNT-COOH (CNT6), MWCNT-COOH (CNT7), SWCNT-COOH (CNT8), MWCNT-COOH (CNT9) (for more details see Materials and methods).

rotenone) in a standard incubation medium consisting of 125 mM sucrose, 65 mM KCl, 2 mM inorganic phosphate (K_2HPO_4) and 10 mM HEPES-KOH pH 7.4 at 30 °C.[41]

Determinations of MPT induction in different conditions. MPT was measured through monitoring the decrease in apparent absorbance of the mitochondrial suspension

Table 1 Physico-chemical parameters ($^{K}V_i$) of CNT family

CNT properties[a]			W_i (%)		D_i (nm)					
n	Type	Function	min	max	min	max	L_i (μm)	P_i (%)	Mi (% metal)	C_i (S cm^{-1})
1	MWCNT	—	0.9[b]	3.03[b]	8	8	0.5–2	>95	<5	<1.5
2	SW/DWCNT	OH	0	3.96	1	4	0.5–2	>95	<5	<1.5
3	MWCNT	OH	0	3.86	1	8	0.5–2	>95	<5	<1.5
4	MWCNT	OH	3	4	10	20	0.5–2	>95	<5	<1.5
5	MWCNT	OH	1	1.06	30	50	0.5–2	>95	<5	<1.5
6	MWCNT	COOH	0	0.73	30	50	0.5–2	>95	<5	<1.5
7	MWCNT	COOH	3	4	10	20	0.5–2	>95	<5	<1.5
8	SWCNT	COOH	0	2.73	1	4	0.5–2	>95	<5	<1.5
9	MWCNT	COOH	0	3.86	1	8	0.5–2	>95	<5	<1.5

[a] MWCNT = Multiple-Walled, SWCNT = Single-Walled, SW/DWCNT = DWCNT + SWCNT mixture, W_i (%) = functional groups (OH, COOH) carbon atoms ratio (%); the properties of the ith carbon nanotube (CNT) are D_i = CNT outer diameter, L_i = CNT length, P_i = purity, C_i = electric conductivity, Mi = metal impurities.

measured at 540 nm in a Hitachi U-3000 spectrophotometer equipped with magnetic stirring and temperature control (28 °C).[42] Mitochondria were incubated in the standard incubation medium at 1 mg of mitochondrial protein per ml. Before the spectrophotometric MPT-measurements the blanks with CNTs were run to compare with mitochondria exposed to CNT and interferences of carbon nanotubes were not observed at 400–550 nm. MPT was induced by three different experimental conditions: (1) swelling assay induced by Ca^{2+} 20 μM, for this instance, we designed three protocols using different MPT-inhibitors controls as CsA 1 μM a known classic MPT-inhibitor of mitochondrial swelling induced by calcium overload; ruthenium red (RR), 1 μM an specific blocker of mitochondrial calcium uniporter that interferes with Ca^{2+} influx from cytoplasm to mitochondrial matrix and EGTA 100 μM as chelating agent. The combinations tested were: [Ca^{2+} 20 μM]; [Ca^{2+} 20 μM + CsA 1 μM]; [Ca^{2+} 20 μM + RR 1 μM]; [Ca^{2+} 20 μM + EGTA 100 μM] to represent MPT-inhibition (100%) and [Ca^{2+} 20 μM + CNTs]; (2) for swelling assay induced by Fe^{2+} 20 μM were used as MPT-inhibitors control (EGTA 100 μM) and additional control as second MPT-inductors to recreate synergistic action on MPT. Followed this idea it was used (KCN 1 μM: indirect MPT-inductor by inhibition of cytochrome c oxidase associated to ROS-formation; ascorbic acid or VitC 100 μM: a strong reducing agent that induce similarly MPT based in ROS-generation). For this instance, the combinations evaluated were: [Fe^{2+} 20 μM], [Fe^{2+} 20 μM + EGTA 100 μM] (100% of MPT-inhibition), [Fe^{2+} 20 μM + CNTs]. For evaluate the maximum value of MPT-induction induced by iron we performed the following combinations in order to mitotoxic potential: [Fe^{2+} 20 μM + VitC 1 μM + CNTs, 5 μg ml^{-1}] > [Fe^{2+} 20 μM + KCN 1 μM + CNTs, 5 μg ml^{-1}] > [Fe^{2+} 20 μM + CNTs]. Please note that this conditions proposed are propitious to induce mitochondrial permeability transition based in Fenton–Haber–Weiss reaction. (3) Swelling assay induced by H_2O_2 300 μM in this test was used Fe^{2+} 20 μM as second MPT-inductors to recreate synergistic action on MPT based in pro-oxidant conditions (Fenton–Haber–Weiss reaction) and quercetin 50 μM (Q: MPT-inhibitor, known antioxidant, employed as control based in ROS-inhibition that prevent the MPTP-thiols group oxidation associated to MPT-induction in pro-oxidant conditions). The combinations tested were [H_2O_2 300 μM], [H_2O_2 300 μM + quercetin 50 μM] (100% of MPT-inhibition in pro-oxidant conditions), [H_2O_2 300 μM + CsA 1 μM], [H_2O_2 300 μM + CNTs], [H_2O_2 300 μM + Fe^{2+} 20 μM + CNTs, 5 μg ml^{-1}] (100% of MPT-induction in pro-oxidant conditions). These three mitochondrial swelling protocols: (1)

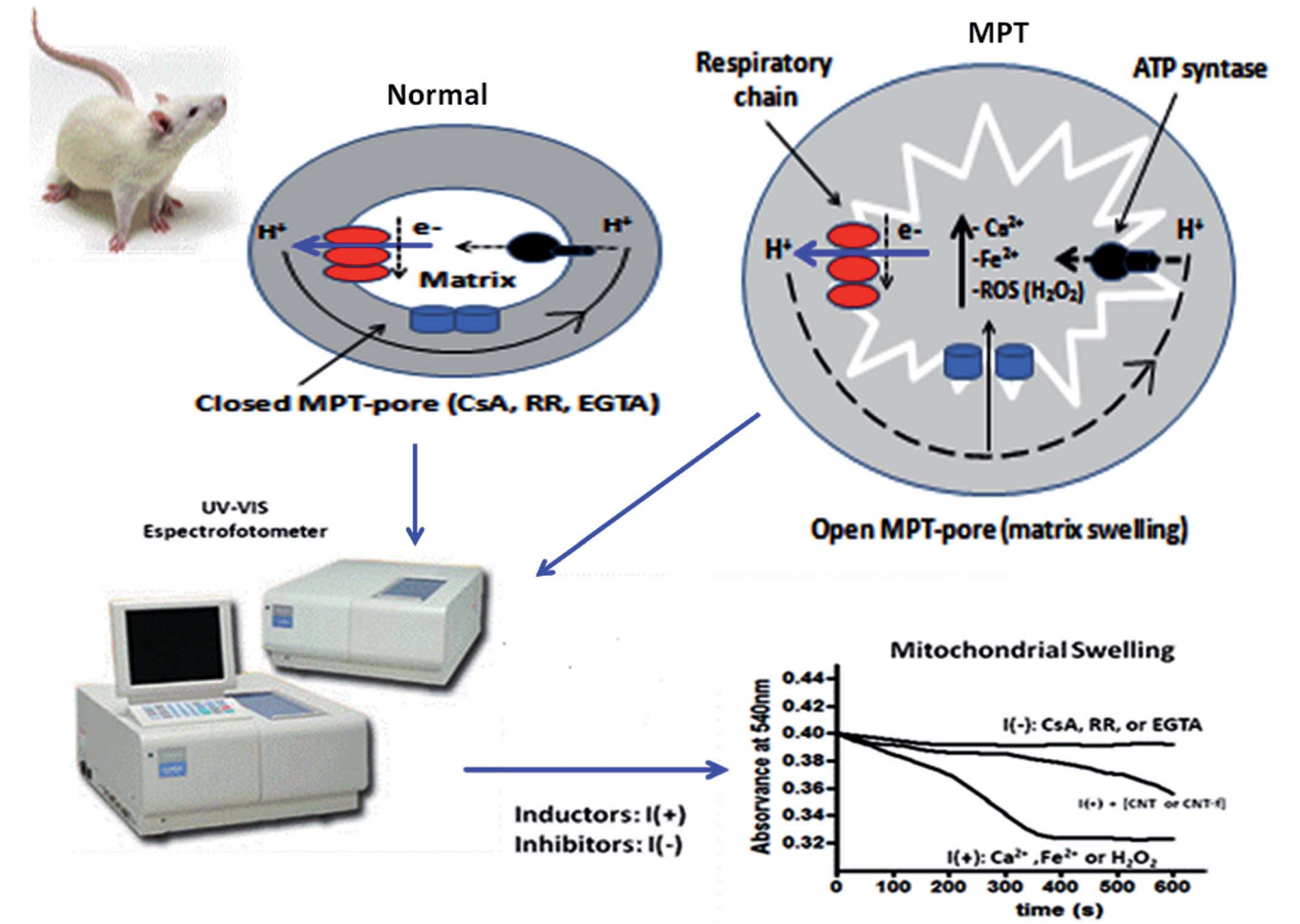

Fig. 3 Workflow of the Experimental section.

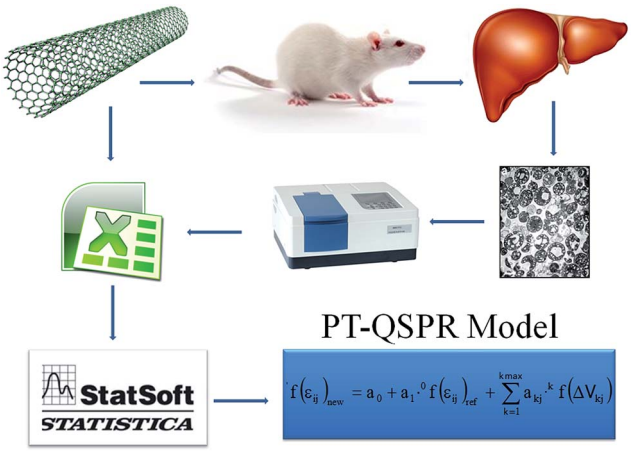

Fig. 4 Workflow used here to seek the PT-QSPR models.

Ca^{2+} 20 μM, (2) Fe^{2+} 20 μM, and (3) H_2O_2 300 μM; were performed in the presence of CNT in different concentrations (0–5 μg ml^{-1}) to investigate in parallel the mechanisms and factors directly or indirectly involved in MPTP-inhibition. All the swelling experiments where the second MPT-inductor is present were performed with the highest concentration (5 μg ml^{-1}) to challenge the mitoprotective potential of CNT.[41,43–48] In addition, we considered other factors as metal impurities. In this context, the maximum expected concentration of metal impurities should be 0.25 μg ml^{-1} (5% of the highest concentration in the CNTs samples) which possess no risk of MPT induction in this low levels.[1–5] In Fig. 3, we illustrate the workflow of this Experimental section.

Microscopy analysis of mitochondrial swelling induction associated to membrane potential. The suspension of isolated rat-liver mitochondria were pre-incubated with a specific mitochondrial dye (JC-1) in 0.2 mg ml^{-1} for 15 min according Reers *et al.*[49] Images were analyzed using a fluorescent microscope (Olympus IX81, Markham, Ontario, Canada) equipped with a DP72 digital camera to study the effects of different mitochondrial swelling assays associated with the loss mitochondrial membrane potential (red to green fluorescent) after incubation with a MPT-inductor (Ca^{2+}, Fe^{2+}, or H_2O_2) and in the presence or the absence of a MPT-inhibitor (CsA, RR, EGTA or one kind of CNT).

Theoretical section

Theoretical details of the PT-NQSPR models. Very recently, Gonzalez-Díaz *et al.*[33] formulated a general-purpose Perturbation Theory (PT) model for Chemoinformatics problems with multiple-boundary experimental conditions. In this work, we are going to re-formulate this theory in order to develop a new type of PT-QSPR models for Nanomaterials (PT-NQSPR models). In Fig. 4, we illustrate the workflow for this theoretical part. Specifically, the new PT-NQSPR models developed here are expected values to predict the effect of different CNT structures in three different MPT induction assays under multiple experimental boundary conditions. The PT-NQSPR model proposed here is an additive equation with linear/non-linear terms expressed in the following form:

$$'f\left(\varepsilon_{ij}\right)_{\text{new}} = e_0 + a_0 \cdot {}^0f\left(\varepsilon_{ij}\right)_{\text{ref}} + \sum_{k=1}^{k\max} a_k \cdot {}^kf\left(\Delta V_{kj}\right) \quad (1)$$

$$'f\left(\varepsilon_{ij}\right)_{\text{new}} = e_0 + a_0 \cdot {}^0f\left(\varepsilon_{ij}\right)_{\text{ref}} + \sum_{k=1}^{k\max} a_k \cdot \left({}^kV_i - \left\langle {}^kV_{ij}\right\rangle\right) \quad (2)$$

We used Multivariate Linear Regression (MLR) and Non-Linear Regression (NLR) algorithms implemented in the software STATISTICA[50] to determine the values of the coefficients (a_k) and other parameters of the model. In our PT-NQSPR model, the output $'f(\varepsilon_{ij})_{\text{new}}$ is a function of the expected absorbance. In the simplest case we use the identity function and $'f(\varepsilon_{ij})_{\text{new}} = {}^{\text{new}}\varepsilon_{ij}$ is equal to the predicted absorbance value under the new sub-set of experimental boundary conditions of reference. Other transformation functions applied to ε_{ij} were: $'f(\varepsilon_{ij}) = 1/\varepsilon_{ij}$, $(1/\varepsilon_{ij})^2$, or $-\log(\varepsilon_{ij})$, see Table 2.

In addition, we are going to consider different sub-sets of input experimental boundary conditions of reference ${}^{\text{ref}}b_j \equiv (b_0, b_1, b_2, b_3 \ldots b_6)$. In the equation we introduced one specific input term to quantify each one of these conditions. The elements of the vectors $\mathbf{v}_i = [{}^0f(\varepsilon_{ij})_{\text{ref}}, {}^1f(\Delta V_{1,j}), \ldots {}^2f(\Delta V_{2,j}), \ldots {}^{k\max}f(\Delta V_{k\max,j})]$ are the inputs of this model.

Table 2 Description of input variables and functions

Coefficient	Input variable	MA	Function ${}^kf$	Function examples	Information
—	—	—	$'f$	$(\varepsilon_{ij})_{\text{new}}$, $1/(\varepsilon_{ij})_{\text{new}}{}^2$, $-\log(\varepsilon_{ij})_{\text{new}}$	Predicted absorbance
e_0	—	—	—	—	Error term
a_0	—	—	${}^0f$	$\langle\varepsilon_{ij}\rangle$	Average of value of absorbance for all CNTs samples for multiple experimental conditions (assay, CNT-type, chemical function, MPT-inductors, MPT-inhibitors)
a_1	t_{ij}	Δt_{ij}	${}^1f$	Δt_{ij} (s), $\exp(-\Delta t_{ij}$ (s))	Exposure time
a_2	c_{ij}	Δc_{ij}	${}^2f$	Δc_{ij} (μg ml^{-1}), $1/(1 + \Delta c_{ij}$ (μg ml^{-1}))	CNT concentration
a_3	${}^{\max}W_i$	ΔW_{ij}	${}^3f$	ΔW_{ij} $(\%)_{\max}$	CNT maximum function/carbon ratio
a_4	${}^{\min}D_i$	ΔD_{ij}	${}^4f$	ΔD_{ij} $(\text{nm})_{\min}$	CNT minimum outer diameter

This first term of this PT-NQSPR model is the function ${}^{0}f(\varepsilon_{ij})_{\text{ref}} = \langle \varepsilon_{ij} \rangle_{\text{new}}$. This function is the average of absorbance value for all CNTs measured under the experimental conditions of the output. It means that we could interpret ${}^{0}f(\varepsilon_{ij})_{\text{new}}$ as the new expected value of absorbance for CNTs measured under the same sub-set of experimental conditions (for a normal distribution).

Following this idea were incorporated the ΔV_{kj} parameters as the second class of terms, which are functions of the Box–Jenkins operators (moving average) used here as perturbation terms ${}^{k}f(\Delta V_{k,j})$. The functions ${}^{k}f$ represent transformations ${}^{k}f(\Delta V_{kj})$ of the moving averages ΔV_{kj} of the original input variables ${}^{k}V_{i}$ for i-th type of CNT in j-th MPT-assay of one specify boundary condition b_{kj}.

The value $\langle V_{kj} \rangle$ is interpreted as the average of the k-th physicochemical properties (${}^{k}V_{ij}$), see the eqn (3):

$$V_{kj} = \frac{1}{n_j}\left(\sum_{i \subset j}^{n_j} {}^{k}V_{ij}\right) \tag{3}$$

This (${}^{k}V_{ij}$) of CNT was used to quantify the effect over the output ${}^{0}f(\varepsilon_{ij})_{\text{new}}$ of perturbations on different experimental boundary conditions (b_j). The following set of conditions are related to the CNT-structure, b_3 = CNT type (SW, SW + DW, MW), b_4 = CNT functionalization type (H, OH, COOH), b_5 = CNT chemical function (OH, COOH, or none) in term of molecular weight/functionalization ratio and b_6 = maximal and minimal diameter ($D_{\min}/D_{\max}$) and for b_0 = multiple experimental boundary conditions. That include the average of the values with the same conditions as mitochondrial swelling assays using the MPT-inductor (Ca^{2+}, Fe^{3+}, H_2O_2, or none) or toxic control $TC_1(+)$, second MPT-inductor (KCN, VitC, or none) or second toxic control $TC_2(+)$, MPT-inhibitors or inhibitor control $IC_1(-)$ (CsA or none) and non-classical MPT-inhibitor control (RR, EGTA, quercetin, or none). Last, included other conditions related to the assay like, solvent (DMSO, or none), replicate sample (Yes, No).

For instance, for exposure time the condition b_1 = exposure time (t_{ij}) of samples corresponding to the i-th CNT used in bj-th MPT-assay. Some of the functions used to transform these variables where: ${}^{1}f(\Delta t_{ij}) = 1/(\Delta t_{ij})$, $\exp(-\Delta t_{ij})$, and the other b_2 = concentration (c_{ij}) of i-th CNT in the j-th assay is ${}^{2}f(\Delta c_{ij}) = 1/\Delta c_{ij}$ or $1/(1 + \Delta c_{ij})$ for CNT concentration. In addition other functions as ${}^{3}f(\Delta W_{ij})$ to molecular weight/functionalization ratio (b_5), ${}^{4}f(\Delta D_{ij})$ for maximal and minimal diameter (b_6) (see Table 2).

Results and discussion

Experimental measure of CNT-MPT modulation in different conditions

The important role of mitochondria to regulate intracellular calcium levels has been associated with several chronic diseases as neurodegenerative diseases, cardiovascular and cancer, which currently have high levels of morbidity and mortality.[51] In this study, we performed three experimental protocols to evaluate the effect of CNT in mitochondrial permeability transition (swelling) induced by different mechanisms, basing each experimental protocol on the causes and factors that trigger this process, as Ca^{2+} overload in the mitochondrial matrix and loss of redox balance under conditions of iron overload and high peroxide production. Under these conditions, the physic-chemicals properties of CNT family were evaluated and linked to their capacity for the inhibition of MPT.[52,53] For this instances the CNT-interferences in spectrophotometric MPT-measurements it were not detected based on the non-existence of the classic UV-visible absorption peaks of mitochondrial redox hemoprotein (408 to 550 nm) as oxidized cytochrome c (Fe^{3+}) at 408 nm and 530 nm and three peaks of reduced cytochrome c (Fe^{2+}) at 415 nm, 520 nm, and 550 nm when we monitored the decrease in absorbance of the mitochondrial suspension measured at 540 nm used to evaluate the mitochondria swelling in the presence of carbon nanotubes as mentioned in Materials and methods section.[52]

At first, we evaluated the effect of CNT family on MPT induced by Ca^{2+} 20 μM, which has been described in many pathological conditions as cancer, neurodegenerative diseases and ischemia-reperfusion processes.[1–3]

In this sense, the selective MPT-modulation with CNT could lead to alternatives for the treatment of cancer and its inhibition may prevent cell and tissue damage associated with a number of diseases. The isolated mitochondria exposed to high calcium concentrations are susceptible to the opening of mitochondrial permeability transition pore, the larger implications of this phenomenon are the diffusion of solutes of up to 1500 Dalton, through the inner mitochondrial membrane, depletion of ATP levels and dissipation of mitochondrial membrane potential as illustrated in Fig. 5. These effects are accompanied by mitochondrial swelling caused by the osmotic difference between the mitochondrial matrix and the extra-mitochondrial medium, followed by outer membrane rupture and release of pro-apoptotic signals (caspases 3 and 9) from the inter-membrane space.[3,4]

Firstly the calcium dependence on MPT was verified by different mechanism, performing teste in the presence of Ca^{2+} (20 μM) with CsA that inhibits the binding of Ca^{2+} to cyclophilin D, in this condition calcium overload produce conformational changes that induce MPT[54] (assay P_1). Also, other non-specific

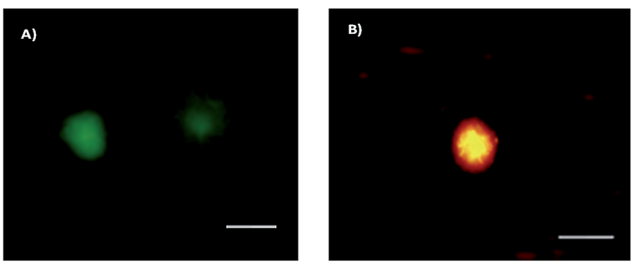

Fig. 5 Isolated rat-liver mitochondria were incubated with a specific mitochondrial dye (JC-1) in 0.2 mg ml^{-1} for 15 min. Show representative fluorescent images of effects on mitochondrial membrane potential for different swelling conditions after exposure with MPT-inductor (Ca^{2+}, Fe^{2+} or H_2O_2) (A) and MPT-inhibitor (CsA, RR, EGTA or CNT-COOH > CNT-OH > pristine-CNT) (B) were examined under a fluorescence microscope (×600 magnification). Scale bars 50 μm.

Table 3 Experimental values of mitochondrial swelling induced by Ca^{2+} for CNT family

CNT[a]						Experimental mitoprotective activity *vs.* Ca^{2+}[b]					
n_i	Type	Function	W_i	D_i	c_{ij}	P_1	N_j	P_2	N_j	P_3	N_j
1	MWCNT	—	3.03[b]	8	0.5	0	42	0	42	0	42
					1	3.5	42	3.4	42	4.1	42
					3	0	42	0	42	0	42
					5	32.3	42	31.2	42	37.8	42
2	SW/DWCNT	OH	3.96	1	0.5	0	21	0	21	0	21
					1	0	21	0	21	0	21
					3	31.9	21	30.7	21	37.3	21
					5	60.7	21	58.5	21	71.0	21
3	MWCNT	OH	3.86	1	0.5	8.3	42	8.0	42	9.8	42
					1	17.3	42	16.7	42	20.3	42
					3	7.3	42	7.1	42	8.6	42
					5	20.2	42	19.5	42	23.7	42
4	MWCNT	OH	4	10	0.5	0	21	0	21	0	21
					1	0	21	0	21	0	21
					3	0	21	0	21	0	21
					5	0	21	0	21	0	21
5	MWCNT	OH	1.06	30	0.5	0	42	0	42	0	42
					1	0	42	0	42	0	42
					3	0	42	0	42	0	42
					5	6.4	42	6.2	42	7.5	42
6	MWCNT	COOH	0.73	30	0.5	10.6	21	10.2	21	12.4	21
					1	0	21	0	21	0	21
					3	0	21	0	21	0	21
					5	0	21	0	21	0	21
7	MWCNT	COOH	4	10	0.5	0	21	0	21	0	21
					1	0	21	0	21	0	21
					3	66.9	21	64.5	21	78.2	21
					5	71.2	21	68.7	21	83.3	21
8	SWCNT	COOH	2.73	1	0.5	0	21	0	21	0	21
					1	0	21	0	21	0	21
					3	22.9	21	22.1	21	26.8	21
					5	67.3	21	64.9	21	78.7	21
9	MWCNT	COOH	3.86	1	0.5	0	21	0	21	0	21
					1	0	21	0	21	0	21
					3	75.9	21	73.2	21	88.8	21
					5	81.4	21	78.5	21	95.2	21
	Groups		W_i	D_i	c_{ij}	e_{ij}	N_j	e_{ij}	N_j	e_{ij}	N_j
	IC + S	Average	2.435	10.25	2.5	0.353	1071	0.353	1071	0.353	1071
		± SD				0.000		0.000		0.000	
	TC + IC + S	Average				0.395	63	0.397	63	0.389	63
		± SD				0.0075		0.001		0.0079	

[a] MWCNT = Multiple-Walled, SWCNT = Single-Walled, SW/WTCNT = MWCNT + SWCNT mixture. [b] Mitoprotective activity, $P(\%) = 100[\varepsilon_{ij}(\text{CNT} + \text{TC} + \text{S})_{obs} - \varepsilon_{ij}(\text{TC} + \text{S})_{obs}]/[\varepsilon_{ij}(\text{IC} + \text{TC} + \text{S})_{obs} - \varepsilon_{ij}(\text{TC} + \text{S})_{obs}]$ and N_j is the number of replicates of the assay. CNT = carbon nanotube, TC = toxic control (MPT-inductor), IC = inhibitor control (MPT-inhibitor), S = solvent. The details of the assays are the following: for toxicity assay P_1 ($a = 1$), TC = Ca^{2+}, IC = CsA, and solvent = DMSO, for assay P_2 ($a = 2$) TC = Ca^{2+}, IC = EGTA and solvent = DMSO; and for assay P_3 ($a = 3$), TC = Ca^{2+}, IC = RR, and solvent = DMSO.

MPT-inhibitors controls were evaluated as EGTA, a calcium chelating agent (assay P_2) and ruthenium red (RR), which interfere in the Ca^{2+} uptake by the mitochondrial uniporter[55] (assay P_3). All these tests were conducted as experimental controls to express the maximum of mitoprotective activity (%P) by different mechanisms.

Swelling assays was performed to study the MPT-effects of CNT family induced by Ca^{2+} 20 μM to find similarities or differences in the pattern of inhibition between CNT family and classic and non-classical MPT-inhibitor controls as showed in Table 3. The results showed low capacity of CNT family to inhibit the MPT induced by Ca^{2+} 20 μM in most cases, when compared with CsA, the main specific inhibitor of MPT pore induced by calcium overload and also using non-specific MPT-inhibitors controls (EGTA 100 μM, RR 1 μM) used as negative control or MPT-inhibitors.[55]

Several aspects must be considered to explain the low and variable MPT inhibition induced by CNT family against mitochondrial Ca^{2+} overload. First, CNT should cross the outer mitochondrial membrane, mitochondrial inter-membrane space, and matrix, process that should be facilitated in virtue of its high lipid partition coefficient/water.[56] However the

modest mitoprotective effects (%*P*) found may be related with certain structural characteristics of CNT family. In this sense, higher %*P* consistent with a decreased of mitochondrial swelling induced by Ca^{2+} was observed for functionalized CNT, following the order CNT-COOH (MWCNT-9, MWCNT-7, SWCNT8, MWCNT-6) > CNT-OH (SWCNT-2, MWCNT-3, MWCNT-5, MWCNT-4) > pristine MWCNT (MWCNT-1). According to the mitoprotective values (%*P*), CNT-9 is the more mitoprotector and CNT-1 is mitotoxic. We suggest a mechanism based in Ca^{2+} adsorption by carboxyl groups (COO^-) of CNT-COOH, which should reduce the free concentration of this divalent ion in the mitochondrial matrix. Chemical adsorption capacity of oxidized CNT has been demonstrated in other nanoQSAR studies using aromatic organic and inorganic MPT inductors.[57] Also for carboxylated-CNT, specifically CNT-7, CNT-8, and CNT-9 it was observed a significant increase of %*P* at higher concentrations (3.0 and 5.0 μg ml^{-1}). The lower %*P* of hydroxylated-CNT compared with their similar carboxylated-CNT could be related with a lower Ca^{2+} adsorption capacity, although higher when compared with similar pristine-CNT, that presented mitotoxic effect.[57]

In this case, the absence of COOH functionalization (MWCNT) could generate mitotoxic effects based in this mechanism and, under this context, the toxicity of carbon nanomaterials should be reduced through the chemical oxidation as in the case of CNT-OH and CNT-COOH according to Zhenbao *et al.*[58] Other possible inhibitory mechanisms could be the interaction of carboxyl groups of carboxylated-CNT with positive NH_2 groups of VDAC and ANT to prevent conformational changes necessary for MPTP components assembly and apoptosis.[59–61] A significant number of studies have demonstrated that MPT-modulation is mediated by conformational changes of VDAC and ANT located on the outer and inner mitochondrial membrane respectively.[61–63]

Next, experiments were performed to study the MPT-effects induced by iron overload for CNT family. Iron overloading has been proposed to cause dissipation of membrane potential and increase of calcium efflux in mitochondria dynamics that are often associated with loss of redox balance, involving oxidation of MPT pore-sulfhydryl groups.[64–66] For this instance were conducted swelling assays in the presence of Fe^{2+} 20 μM. Also it were considered other more aggressive mitotoxic or condition of synergism to enhance the MPT-effects of iron overload combining separately with KCN 1 μM, an inhibitor of mitochondrial complex IV (cytochrome c oxidase) and consequently of the electrons transport chain (assay P_2). Also with ascorbic acid 300 μM, a strong reducing agent that favors the reduction of Fe^{3+} to Fe^{2+} and thus inducing pro-oxidant states (assay P_3).[53,67] Both non-classical MPT inductors and second inductor were used as positive controls to challenge the mitoprotective potential of CNT family to reverse mitochondrial swelling induced by Fe^{2+} 20 μM.[68] Under this protocol, EGTA 100 μM was used as negative control or MPT-inhibitors as show in Table 4.

Mitoprotective activity (%*P*) was higher for carboxylated-CNT and hydroxylated-CNT in comparison with the lowest %*P* of pristine-CNT, more mitotoxic, results that fits with a previous study that reported increased cytotoxicity to pristine CNT in relation to the functionalized-CNT.[69] It is important to note that the %*P* of CNT family was considerably higher to Fe^{2+} swelling than to Ca^{2+} swelling tests. But in both cases the response pattern was similar, according to the functionalization type: CNT-COOH (MWCNT-9, MWCNT-7, SWCNT-8, MWCNT-6) > CNT-OH (SWCNT-2, MWCNT-3, MWCNT-5, MWCNT-4) > pristine-CNT (MWCNT-1). A direct chelation of mitochondrial iron has been suggested as an attractive therapeutic strategy for several clinical disorders involving iron imbalance.[53] In present study, the inhibition of MPT could involve the interaction of the COOH and OH groups of oxidized-CNT with the reduced state (Fe^{2+}) of heme group in the mitochondrial complexes I and III, known to be mitochondrial ROS producers. This interaction should form a coordination complex between the oxidized-CNT and the metallic center, helping to reduce the levels of ferrous ions (Fe^{2+}), preventing Fenton–Haber–Weiss reaction that leads to the generation of hydroxyl radical.[53] Following this idea, we suggest a possible mechanism based on iron coordination by COOH and OH groups of the CNT combined with chemical adsorption mechanisms onto oxidized-MWCNT to reduce the excess in the Fe^{2+} free concentrations, thus preventing mitochondrial swelling in pro-oxidant conditions.[53,58] The *P*% for the MPT-assay using the [Fe^{2+} 20 μM + KCN 1 μM + CNTs, 5 μg ml^{-1}] (P_2) showed a similar behavior to MPT-assay using [Fe^{2+} 20 μM + CNTs, 5 μg ml^{-1}] (P_1) in the order carboxylated-CNT > hydroxylated-CNT > pristine-CNT for mitoprotective activity (%*P*). The evidences suggest therapeutic potential of oxidized nanotubes to reverse the swelling induced by Fe^{2+} overload despite the participation of uncoupling mitochondrial mechanisms as KCN 1 μM, which acts synergistically favoring the opening of MPT-pore. However only carboxylated-CNT (5) and hydroxylated-CNT (2, 3, 6) were able to reverse the pro-oxidant effects generated by iron overload combined with ascorbic acid 300 μM, a strong reducing agent. Also according to the walls number, it was observed higher values of mitoprotection in the order MW-motifs > SW + DW-motif > SW-motifs, these evidences are coherent with studies performed using K562 and HeLa cells cultured in the presence of SWCNT, SWNTs-OH, MWCNT-COOH at concentrations ranging from 1 to 100 μg ml^{-1} based in inhibition of telomerase activity.[59]

Finally, assessments were performed to analyze the potential of CNT family to reverse the MPT induced in pro-oxidant conditions of high mitochondrial H_2O_2 levels as shown in Table 5. It was performed mitochondrial swelling assays in the presence of H_2O_2 300 μM and using a known antioxidant, quercetin 50 μM as negative MPT-control as [H_2O_2 300 μM + quercetin 50 μM] (assay P_1).[70] The same protocol was run taking CsA 1 μM as [H_2O_2 300 μM + CsA 1 μM] a negative additional MPT-control (assay P_2). Also it was performed a mitochondrial swelling assay induced by H_2O_2 300 μM using Fe^{2+} 20 μM to produce MPT-synergism conditions, for this instance the combination [H_2O_2 300 μM + Fe^{2+} 20 μM + CNTs, 5 μg ml^{-1}] (assay P_3) was employed, to intensify the pro-oxidant conditions. In this case it was also used quercetin 50 μM as negative MPT-control of references to find similarities or significant differences in the MPT-modulation based in pro-oxidant induced by H_2O_2 300 μM of CNT family.

Table 4 Experimental values of mitochondrial swelling induced by Fe^{2+} for CNT family

CNT_i[a]						Experimental mitoprotective activity *vs.* Fe^{2+}[b]					
n_i	Type	Function	W_i	D_i	c_{ij}	P_1	N_j	P_2	N_j	P_3	N_j
1	MWCNT	—	3.03[b]	8	0.5	0	14	0	14	0	14
					1	0	14	0	14	0	14
					3	0	16	0	16	0	16
					5	20.3	14	90.8	14	0	14
2	SW/DWCNT	OH	3.96	1	0.5	0	14	0	14	0	14
					1	35.3	14	100	14	0	14
					3	84.8	16	100	16	0	16
					5	100	14	100	14	67.2	14
3	MWCNT	OH	3.86	1	0.5	0	14	42.5	14	0	14
					1	0	14	79.4	14	0	14
					3	93.3	16	100	16	0	16
					5	92.5	14	100	14	0	14
4	MWCNT	OH	4	10	0.5	0	14	0	14	0	14
					1	44.4	14	100	14	0	14
					3	100	16	100	16	0	16
					5	100	14	100	14	10.7	14
5	MWCNT	OH	1.06	30	0.5	0	14	0	14	0	14
					1	0	14	0	14	0	14
					3	0	16	0	16	0	16
					5	6.8	14	30.2	14	0	14
6	MWCNT	COOH	0.73	30	0.5	0	14	68.4	14	0	14
					1	0	14	14.7	14	0	14
					3	0	16	16.9	16	0	16
					5	80.4	14	100	14	0	14
7	MW	COOH	4	10	0.5	12.0	14	53.8	14	0	14
					1	91.0	14	100	14	0	14
					3	100	16	100	16	0	16
					5	100	14	100	14	0	14
8	SWCNT	COOH	2.73	1	0.5	0	14	0	14	0	14
					1	37.6	14	100	14	0	14
					3	90.7	16	100	16	0	16
					5	100	14	100	14	2.3	14
9	MW	COOH	3.86	1	0.5	0	14	0	14	0	14
					1	30.8	14	100	14	0	14
					3	100	16	100	16	0	16
					5	100	14	100	14	24.8	14
	Groups		$\langle W_i \rangle$	$\langle D_i \rangle$	$\langle c_{ij} \rangle$	$\langle e_{ij} \rangle$	N_j	$\langle e_{ij} \rangle$	N_j	$\langle e_{ij} \rangle$	N_j
	IC + S	Average	2.435	10.25	2.5	0.393	189	0.378	189	0.337	126
		± SD				0.000		0.000		0.000	
	TC + IC + S	Average				0.374	781	0.374	781	0.374	781
		± SD				0.003		0.001		0.030	

[a] MWCNT = Multiple-Walled, SWCNT = Single-Walled, SW/WTCNT = MWCNT + SWCNT mixture. [b] Mitoprotective activity, $P(\%) = 100[\varepsilon_{ij}(\text{CNT} + \text{TC} + \text{S})_{obs} - \varepsilon_{ij}(\text{TC} + \text{S})_{obs}]/[\varepsilon_{ij}(\text{IC} + \text{TC} + \text{S})_{obs} - \varepsilon_{ij}(\text{TC} + \text{S})_{obs}]$ and N_j is the number of replicates of the jth assay. CNT = carbon nanotube, TC = toxic control (MPT-inductor), IC = inhibitor control (MPT-inhibitor), S = solvent. The details of the assays are the following: assay P_1 ($a = 1$) $TC_1 = Fe^{2+}$, IC = EGTA and S = DMSO; assay P_2 ($a = 3$), $TC_1 = Fe^{2+}$, TC_2 = KCN, IC = EGTA and solvent = DMSO and assay P_3 ($a = 3$), $TC_1 = Fe^{2+}$, TC_2 = VitC, IC = EGTA and solvent = DMSO.

P% values mitoprotection of CNT family were remarkably high in the swelling assays P_1 and P_2 except for pristine-CNT. The result showed %*P* very similar between CNT-COOH and CNT-OH in the conditions listed above to mitochondrial swelling assays induced by Ca^{2+} and Fe^{2+} at 20 μM. This suggests that OH and COOH functionalization are important to reverse the mitochondrial swelling associated to pro-oxidant conditions.[71] The high %*P* values of functionalized-CNT exhibited a similar pattern of inhibition, when compared with the two controls used quercetin 50 μM (non-specific MPT-inhibitors) and CsA 1 μM (specific MPT-inhibitors), pointing that the inhibition of functionalized-CNT could be associated with the ability to attenuate the loss of redox balance induced by H_2O_2 overload.[51,53]

The mitochondria has an efficient antioxidant defense system, including superoxide dismutase, glutathione peroxidase, glutathione reductase, reduced glutathione, $NAD(P)^+$ and other cofactors. In physiological conditions the mitochondrial superoxide dismutase transforms the superoxide radical ($O_2^{\bullet}$) to the less reactive H_2O_2, which is reduced to H_2O by the action of GSH and glutathione peroxidase.[51]

However, several mito-pathological conditions as peroxide overload (300 μM) reduced the antioxidant defenses and increases oxidative stress by H_2O_2 accumulation, in our study.

Table 5 Experimental values of mitochondrial swelling induced by H_2O_2 for CNT family

CNT[a]						Experimental mitoprotective activity *vs.* H_2O_2[b]					
n_i	Type	Function	W_i	D_i	c_{ij}	P_1	N_j	P_2	N_j	P_3	N_j
1	MWCNT	—	3.03[b]	8	0.5	0	0	0	0	0	0
					1	0	7	0	7	0	7
					3	0	7	0	7	0	7
					5	0	7	100	7	0	7
2	SW/DWCNT	OH	3.96	1	0.5	0	0	0	0	0	0
					1	0	21	65	21	0	21
					3	100	21	80	21	0	21
					5	100	21	81.0	21	72.7	21
3	MWCNT	OH	3.86	1	0.5	0	0	0	0	0	0
					1	100	21	95	21	0	21
					3	100	21	97	21	0	21
					5	100	21	97.5	21	98.0	21
4	MWCNT	OH	4	10	0.5	0	0	0	0	0	0
					1	100	21	51	21	0	21
					3	100	21	97.5	21	0	21
					5	100	21	95.5	21	100	21
5	MWCNT	OH	1.06	30	0.5	0	0	0	0	0	0
					1	100	21	95	21	0	21
					3	100	21	97	21	0	21
					5	100	21	97.5	21	100	21
6	MWCNT	COOH	0.73	30	0.5	0	0	0	0	0	0
					1	100	21	51	21	0	21
					3	100	21	97	21	0	21
					5	100	21	97.5	21	91.0	21
7	MWCNT	COOH	4	10	0.5	0	0	0	0	0	0
					1	100	21	80	21	0	21
					3	100	21	81	21	0	21
					5	100	21	91	21	100	21
8	SWCNT	COOH	2.73	1	0.5	0	0	0	0	0	0
					1	100	21	80	21	0	21
					3	100	21	81	21	0	21
					5	100	21	91	21	90.2	21
9	MWCNT	COOH	3.86	1	0.5	0	0	0	0	0	0
					1	100	21	86	21	0	21
					3	100	21	97	21	0	21
					5	100	21	95.5	21	100	21
	Groups		$\langle W_i \rangle$	$\langle D_i \rangle$	$\langle c_{ij} \rangle$	$\langle e_{ij} \rangle$	N_j	$\langle e_{ij} \rangle$	N_j	$\langle e_{ij} \rangle$	N_j
	IC + S	Average	2.435	10.25	2.5	0.366	175	0.404	175	0.241	105
		± SD				0.000		0.000		0.000	
	TC + IC + S	Average				0.375	525	0.375	525	0.375	525
		± SD				0.0015		0.0068			0.00

[a] MWCNT = Multiple-Walled, SWCNT = Single-Walled, SW/WTCNT = MWCNT + SWCNT mixture. [b] Mitoprotective activity, $P(\%) = 100[\varepsilon_{ij}(\text{CNT} + \text{TC} + \text{S})_{\text{obs}} - \varepsilon_{ij}(\text{TC} + \text{S})_{\text{obs}}]/[\varepsilon_{ij}(\text{IC} + \text{TC} + \text{S})_{\text{obs}} - \varepsilon_{ij}(\text{TC} + \text{S})_{\text{obs}}]$ and N is the number of replicates of the assay. CNT = carbon nanotube, TC = toxic control (MPT-inductor), IC = inhibitor control (MPT-inhibitor), S = solvent. The details of the assays are the following: assay P_1 ($a = 1$) $TC_1 = H_2O_2$, IC = Q and solvent = DMSO; assay P_2 ($a = 2$), $TC_1 = H_2O_2$, IC = CsA, and solvent = DMSO; assay P_3 ($a = 2$), $TC_1 = H_2O_2$, $TC_2 = Fe^{2+}$, IC = Q, and solvent = DMSO.

The presence of Fe^{2+} induces formation of hydroxyl radical ($^{\bullet}OH$) through Fenton–Haber–Weiss reaction involved in the oxidation of thiol groups constituents of MPTP. In the case of assay P_3, only the highest concentration, 5 μg ml^{-1} was able to reverse the mitochondrial swelling induced by pro-oxidant condition[51] similar to quercetin 50 μM.[70–72] The obtained results should contribute for the rational design of novels carbon nanomaterial and point the way to new areas of research as Mitochondrial Nanomedicine,[73,74] based in the effects of carboxylated and hydroxylate carbon nanotubes on mitochondrial permeability transition.

PT-NQSPR model in multiple boundary conditions

In classic response-concentration models, we can use alternative forms of the hill-shaped curve to seek a dose–response equation in order to calculate IC_{50} values.[50] For instance, the software MasterPlex (http://psg.hitachi-solutions.com/masterplex) allows to choose different algorithms such as: 4 parameters logistic (4PL), 5 parameters logistic (5PL), quadratic log–log it, log–log or linear model. The reader can see examples of the use of this software and these algorithms in previous works.[51–55] However, the 4PL and 5PL forms have some drawbacks. Some authors have reported studies towards the search

of alternatives models to these curves. For instance, Liao *et al.* (2009) reported a re-parameterization of 5PL dose–response curve.[75] In any case, almost all of these alternatives fail when we need to account for multiple experimental boundary conditions (b_j). It means that the model fails when we want to predict the response ε_i for the ith compound not only for different concentrations of the compound (c_i) in a single assay. This points to the need of a model able to predict multiple responses ε_{ij} for the same ith compound when we change multiple boundary conditions like b_0 = multiple experimental conditions of j-th MPT-assays, b_2 = different values of concentration c_{ij} for the compound on the different j-th MPT-assays, different exposure time (0–600 s) to the compound $b_1 = t_{ij}$. We can talk here also of different structural or physicochemical properties of the compound under study. For instance, in the case of CNT we consider the CNT type, b_3 = Single-Walled (SW), Multiple-Walled (MW), or mixtures of SW + DW. In these cases, 4PL/5PL and similar models are unable to fit all the data at the same time and we need to seek a different equation for each sub-set of changing boundary conditions b_{kj}. In this work, we propose by the first time a PT-NQSPR model able to account for changes in multiple experimental boundary conditions (b_j). The general formula of this models the following:

$$'f(\varepsilon_{ij})_{\text{new}} = e_0 + a_0 \cdot \langle \varepsilon_{ij} \rangle_{\text{new}} + a_1 \cdot {}^1f(\Delta t_{ij}) + a_2 \cdot {}^2f(\Delta c_{ij}) + a_3 \cdot {}^3f(\Delta W_{ij}) + a_4 \cdot {}^4f(\Delta D_{ij}) \quad (4)$$

$$'f(\varepsilon_{ij})_{\text{new}} = e_0 + a_0 \cdot \langle \varepsilon_{ij} \rangle_{\text{new}} + a_1 \cdot {}^1f(t_i - \langle t_{ij} \rangle) + a_2 \cdot {}^2f(c_i - \langle c_{ij} \rangle) + a_3 \cdot {}^3f(W_i - \langle W_{ij} \rangle) + a_4 \cdot {}^4f(D_i - \langle D_{ij} \rangle) \quad (5)$$

We can compare the equation above with the compact notation presented in the Materials and methods section. In this PT-NQSPR model we can also use (like in 4PL/5PL models) optional weighting schemes for the response variable (output function): $'f(\varepsilon_{ij}) = \varepsilon_{ij}$, $1/\varepsilon_{ij}$, $(1/\varepsilon_{ij})^2$, or $-\log(\varepsilon_{ij})$. We can incorporate different functions ${}^0f = \langle \varepsilon_{ij} \rangle$ of the expected value of ε_{ij} for a sub-set of conditions (*e.g.*, different MPT-assays). We can also use different functions for the input variable; such as: ${}^1f = \Delta t_{ij}$, $1/\Delta t_{ij}$ or $\exp(-\Delta t_i)$ for exposure time, or ${}^2f = \Delta c_i$, $1/\Delta c_i$ or $1/(\Delta c_i)^2$ for CNT concentration. A particular case is when the concentration function takes the classic form of PL4/PL5 models.[76] This equation is represented through a sigmoid curve. The formula below illustrates two examples of alternative models following the eqn (6):

$${}^2f(\Delta c_{ij}) = A + D \cdot \left\{ 1 + \left[\left(\frac{\Delta c_{ij}}{C} \right)^B \right] \right\}^{-E} = {}^2f(\varepsilon_{ij})_{\min} + {}^2f(\varepsilon_{ij})_{\max} \cdot \left\{ 1 + \left[\left(\frac{\Delta c_{ij}}{C} \right)^B \right] \right\}^{-E} \quad (6)$$

The parameters of 4PL/5PL models are: A, B, C, D, and E. A is the value for the minimum asymptote. B is the hill slope. C is the concentration at the inflection point. D is the ε_{ij} for the maximum asymptote. The last parameter E, is present only on 5PL model ($E = 1$ in 4PL model), is the asymmetry factor ($E \neq 1$ for a non-symmetric curve).[76]

PT-NQSTR model for mitoprotective activity of CNTs. The ε_i values are obtained after exposure of the mitochondrial suspension to one volume of 100 μl of CNT at different c_i values. We used physic-chemical parameters of CNTs (V_{kj}) and the values of the Box–Jenkins operators (ΔV_{kj}) of these parameters as inputs of the model in statistical analysis. The best PT-QSPR model found using MLR algorithm and linear operators (functions) of $\Delta V_{k,j}$ was the following:

$$\begin{aligned} {}^{\text{new}}\varepsilon_{\text{ij}} = {} & 1.001191 \cdot \varepsilon_{ij_{\text{new}}} - 0.000066 \cdot \Delta t_{ij}(\text{s}) + 0.002344 \cdot \Delta c_{ij}\ (\mu\text{g ml}^{-1}) \\ & - 0.001191 \cdot \Delta W_{ij}()_{\max} - 0.000688 \cdot \Delta D_{ij}\ (\text{nm})_{\min} + 0.000086, \\ & N = 6045, \quad R^2 = 0.75, F = 2482.1, p < 0.005 \end{aligned} \quad (7)$$

As we mentioned above, in the simplest case the output function $'f(\varepsilon_{ij})_{\text{new}} = {}^{\text{new}}\varepsilon_{ij}$ is the value of absorbance predicted by the linear model under the set of boundary conditions of test of reference. N = number of cases used to train the model, R^2 the determination coefficient, and F the Fisher ratio with the corresponding p-value are the statistical elements used to describe the statistical significance and goodness-of-fit of the model. We can expand the input terms and substitute each symbol $V_k(b_j)$ by the classic symbol of the respective property in order to understand better this equation. The model predicts values of absorbance ${}^{\text{new}}\varepsilon_{ij}$ when assaying the ith CNT in a new

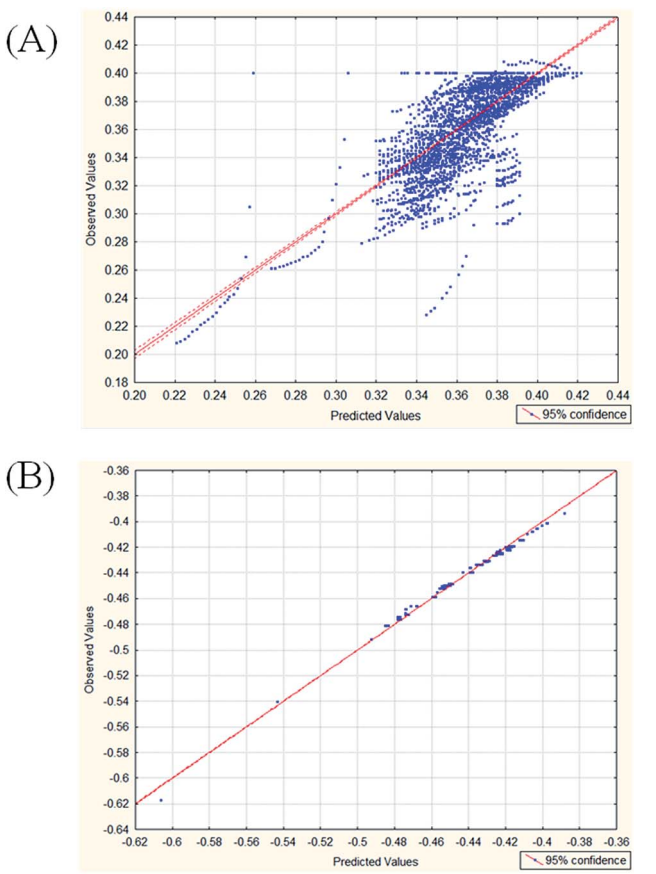

Fig. 6 Observed *vs.* predicted values for models with ${}^0f(\varepsilon_{ij}) = \varepsilon_{ij}$ (A), and (B) ${}^0f(\varepsilon_{ij}) = -\log(\varepsilon_{ij})$.

Table 6 Statistical analysis for alternative PT-NQSPR models developed in this work[a]

Model parameters[b]					Model			
V_k	a_k	s.e.	t	p	Specifications			
a_0	−0.000780	0.003041	−0.26	0.79	**Model 1**			
$\langle\varepsilon_{ij}\rangle^a$	1.002419	0.008302	120.75	0.00	$'f(\varepsilon_{ij})$	$^0f(\varepsilon_{ij})$	$^1f(t_{ij})$	$^2f(c_{ij})$
Δt_{ij}	−0.000066	0.000002	−42.77	0.00	ε_{ij}	$\langle\varepsilon_{ij}\rangle$	Δt_{ij}	Δc_{ij}
Δc_{ij}	0.002395	0.000199	12.02	0.00	R^2	F	p	q^2
$\Delta W_{\max}$	−0.001175	0.000237	−4.97	0.00	0.73	3308.1	<0.05	0.70
$\Delta D_{\min}$	−0.000735	0.000174	−4.21	0.00				
a_0	0.92771	0.000488	−1900.43	0.00	**Model 2**			
$\langle\varepsilon_{ij}\rangle$	−1.33764	0.001332	1003.91	0.00	$'f(\varepsilon_{ij})$	$^0f(\varepsilon_{ij})$	$^1f(t_{ij})$	$^2f(c_{ij})$
Δt_{ij}	0.00001	0.000000	−2.02	0.04	$-\log(\varepsilon_{ij})$	$\langle\varepsilon_{ij}\rangle$	Δt_{ij}	Δc_{ij}
Δc_{ij}	−0.00038	0.000032	11.92	0.00	R^2	F	p	q^2
$\Delta W_{\max}$	−0.00042	0.000038	11.11	0.00	**0.994**	203 384.0	<0.05	**0.994**
$\Delta D_{\min}$	−0.00044	0.000028	15.79	0.00				
a_0	32.5709	0.190990	170.53	0.00	**Model 3**			
$\langle\varepsilon_{ij}\rangle$	−67.6535	0.521307	−129.78	0.00	$'f(\varepsilon_{ij})$	$^0f(\varepsilon_{ij})$	$^1f(t_{ij})$	$^2f(c_{ij})$
Δt_{ij}	0.0035	0.000096	36.33	0.00	$1/(\varepsilon_{ij})^2$	$\langle\varepsilon_{ij}\rangle$	Δt_{ij}	Δc_{ij}
Δc_{ij}	−0.1744	0.012517	−13.93	0.00	R^2	F	p	q^2
$\Delta W_{\max}$	−0.0111	0.014857	−0.75	0.45	0.75	3647.4	<0.005	—
$\Delta D_{\min}$	−0.0295	0.010953	−2.69	0.01				
a_0	6.5064	0.028482	228.44	0.00	**Model 4**			
$\langle\varepsilon_{ij}\rangle$	−10.2097	0.077742	−131.33	0.00	$'f(\varepsilon_{ij})$	$^0f(\varepsilon_{ij})$	$^1f(t_{ij})$	$^2f(c_{ij})$
Δt_{ij}	0.0006	0.000014	39.71	0.00	$1/\varepsilon_{ij}$	$\langle\varepsilon_{ij}\rangle$	Δt_{ij}	Δc_{ij}
Δc_{ij}	−0.0259	0.001867	−13.86	0.00	R^2	F	p	q^2
$\Delta W_{\max}$	0.0027	0.002216	1.20	0.23	0.76	3780.1	<0.05	—
$\Delta D_{\min}$	−0.0003	0.001633	−0.20	0.84				
a_0	0.002922	0.003037	0.96	0.33	**Model 5**			
$\langle\varepsilon_{ij}\rangle$	0.998287	0.008275	120.63	0.00	$'f(\varepsilon_{ij})$	$^0f(\varepsilon_{ij})$	$^1f(t_{ij})$	$^2f(c_{ij})$
Δt_{ij}	−0.000060	0.000002	−39.37	0.00	ε_{ij}	$\langle\varepsilon_{ij}\rangle$	Δt_{ij}	$1/(1+\Delta c_{ij})$
Δc_{ij}	−0.000467	0.000207	−2.25	0.02	R^2	F	p	q^2
$\Delta W_{\max}$	−0.000420	0.000166	−2.53	0.01	0.734	3331.7	<0.05	—
$\Delta D_{\min}$	−0.006490	0.000488	−13.29	0.00				
a_0	−0.927407	0.000494	−1877.49	0.00	**Model 6**			
$\langle\varepsilon_{ij}\rangle$	1.337072	0.001346	993.49	0.00	$'f(\varepsilon_{ij})$	$^0f(\varepsilon_{ij})$	$^1f(t_{ij})$	$^2f(c_{ij})$
Δt_{ij}	0	0	0.47	0.64	$\log(\varepsilon_{ij})$	$\langle\varepsilon_{ij}\rangle$	Δt_{ij}	$1/(1+\Delta c_{ij})$
Δc_{ij}	0.000634	0.000034	18.80	0.00	R^2	F	p	q^2
$\Delta W_{\max}$	0.000539	0.000027	19.96	0.00	0.993	199 112.8	<0.05	—
$\Delta D_{\min}$	−0.000286	0.000079	−3.60	0.00				

[a] $^0f(\varepsilon_{ij})_{\text{ref}} = \langle\varepsilon_{ij}\rangle$ is the average of ε_{ij} (expected value of absorbance) for a given assay carried out under the conditions b_j. [b] Symbols of input variables used. The parameters $\Delta V_{kj} = ({}^kV_i - \langle V_{kj}\rangle)$ are PT operators in form of moving averages, for more details see Materials and methods.

experimental situation (jth set of conditions) given the expected values of reference calculated from the data set. The correlation between the inputs and the answer is statistically significant according to p-error values ($p < 0.005$). The values R^2 are high (75% of variance explained) but, unfortunately, we can observe an important dispersion of data points from the straight line in Fig. 6(A).

We carry out some transformations of output $^0f(\varepsilon_{ij})$ and/or input functions in order to increase the R^2 and decrease the dispersion. The transformation of the output function ε_{ij} were: $'f(\varepsilon_{ij}) = 1/\varepsilon_{ij}$, $(1/\varepsilon_{ij})^2$, or $-\log(\varepsilon_{ij})$. Some of the transformations of the input functions $^kf(\Delta V_{kj})$ were $^1f(\Delta t_{ij}) = 1/(\Delta t_{ij})$, $\exp(-\Delta t_{ij})$ and $^2f(\Delta c_{ij}) = 1/\Delta c_{ij}$ or $1/(1 + \Delta c_{ij})$, between others (see details on Materials and method section). In Table 6 we depict the results obtained after some of these transformations. The transformation of the output function into a logarithmic function have lead to an outstanding increase in the determination coefficient from $R^2 = 0.75$ to $R^2 = 0.994$ (Model 2) with respect to the linear model (Model 1). This result also supposed a notably reduction on the dispersion of data, see Fig. 6(B).

We can note that other transformations of inputs variables like Δc_{ij} and Δt_{ij} do not improved the results of the regression (Models 3 and 4). In particular, the transformation of the Δc_{ij} function into hill-shaped curves of common use in dose-effect studies was not effective (Model 5). In addition, the transformation of both output and input functions at the same time increased the correlation but as a result we obtained a more complex model with loss of statistical significance ($p > 0.05$) for some input variables (Model 6). In closing, the best PT-NQSPR model found here was the one using the negative logarithmic transformation for the output. The model have also a very high validation regression coefficient $q^2 = 0.994$, obtained in Leave-One-Out (LOO) cross-validation. The model equation is the following:

$$^{new}\log(\varepsilon_{ij}) = 1.33764\varepsilon_{ij_{new}} - 0.000001\cdot\Delta t_{ij}(\mathrm{s}) + 0.00381\cdot\Delta c_{ij}\ (\mu g\ ml^{-1}) + 0.000422\cdot\Delta W_{ij}\ (\%)_{max} + 0.000442\cdot\Delta D_{ij}\ (nm)_{min} - 0.927714,\ N = 6045,\ R^2 = 0.994,\ F = 203\ 384.0,\ p < 0.005,\ q^2 = 0.994 \quad (8)$$

We presented the previous equation in a compacted form for the sake of simplicity. However, we want to give also the expanded form of the equation to make easier the understanding of the method. In the following equation, we expanded each moving average term. It can be noted that each term quantifies the deviation (perturbation) of the original variable (t_{ij}, c_{ij}, W_{ij}, or D_{ij}) from its average value ($\langle t_{ij}\rangle$, $\langle c_{ij}\rangle$, $\langle W_{ij}\rangle$, or $\langle D_{ij}\rangle$). In this sense, each moving average term account for the deviation of the original variable from its expected value (the average value).[33–39]

$$^{new}\log(\varepsilon_{ij}) = 1.33764\cdot\varepsilon_{ij_{new}} - 0.000001\cdot(t_{ij} - \langle t_{ij}\rangle) + 0.00381\cdot(c_{ij} - \langle c_{ij}\rangle) + 0.000422\cdot(W_{ij} - \langle W_{ij}\rangle)_{max} + 0.000442\cdot(D_{ij} - \langle D_{ij}\rangle)_{min} - 0.927714,\ N = 6045,\ R^2 = 0.994,\ F = 203\ 384.0,\ p < 0.005,\ q^2 = 0.994 \quad (9)$$

Prediction of mitoprotective activity of CNT in other conditions. We can use the previous PT-QSPR model to carry out a computational simulation of mitoprotection by CNT in other conditions (not measured experimentally). In so doing, we need to substitute three different types of values in the equation. The first is the expected value of absorbance $\langle\varepsilon_{ij}\rangle_{ref}$ for a given subset of experimental conditions or assay (b_{ij}). We also need to substitute the average values of the physic-chemical properties of the CNTs $\langle V_k\rangle$ in these sub-sets of different experimental conditions $\langle V_{kj}\rangle$, see Table 7 (right).

Last, we need to substitute the values V_k for CNTs with different physic-chemical properties not assayed before. In this way, we can obtain new values of absorbance predicted for new CNT with changes in the original physic-chemical properties. Thus we can predict the values of mitoprotection $P(\%)$ using the values of ε_{ij} predicted and the values observed with MPT-inductor or toxic control (TC+) and solvent blank. The equation used was the following $P(\%)_{pred} = 100[\varepsilon_{ij}(CNT + TC + S)_{pred} - \varepsilon_{ij}(TC + S)_{obs}]/[\varepsilon_{ij}(IC + TC + S)_{obs} - \varepsilon_{ij}(TC + S)_{obs}]$.[77,78] In Table 8, we show the prediction of $P(\%)_{pred}$ if we increase at the same time the maximal molecular weight to functionalization ratio ^{max}W and the minimal ^{min}D of the CNT in $x(\%)$ at $t(s) = 600$ seg and $c_{ij} = 2.5\ \mu g\ ml^{-1}$. The effect of dose or concentration (1–5 $\mu g\ ml^{-1}$) influenced poorly the model and, for this reason, an intermediate value (2.5 $\mu g\ ml^{-1}$) was established for the theoretical analysis of CNT-nanodescriptors. This was considered reasonable because it allows the study of the nanostructure–activity relationship and at the same time considers non-agglomeration conditions for simulation of CNT-nanodescriptors in mitochondrial exposure.[18] In this sense the

Table 7 Expected values of variables in different conditions[a]

Experimental conditions					Expected values				
Type	Function	CT_1	CT_2	IC	$\langle\varepsilon_{ij}\rangle$	$\langle V_1\rangle$	$\langle V_2\rangle$	$\langle V_3\rangle$	$\langle V_4\rangle$
MWCNT	NO	Ca^{2+}	NO	NO	0.3528	300	2.38	0	8
SW/DWCNT	OH	Ca^{2+}	NO	NO	0.3528	300	2.38	3.96	1
MWCNT	OH	Ca^{2+}	NO	NO	0.3528	300	2.38	2.97	13.67
MWCNT	COOH	Ca^{2+}	NO	NO	0.3528	300	2.38	2.86	13.67
SWCNT	COOH	Ca^{2+}	NO	NO	0.3528	300	2.38	2.73	1
MWCNT	NO	Fe^{2+}	NO	NO	0.3741	94.14	2.4	0	8
SW/DWCNT	OH	Fe^{2+}	NO	NO	0.3741	94.14	2.4	3.96	1
SW/DWCNT	OH	Fe^{2+}	VitC	NO	0.3361	90	5	3.96	1
MWCNT	OH	Fe^{2+}	NO	NO	0.3741	93.83	2.22	2.83	14.88
MWCNT	OH	Fe^{2+}	VitC	NO	0.3361	90	5	2.97	13.67
MWCNT	COOH	Fe^{2+}	NO	NO	0.3741	94.14	2.4	2.86	13.67
MWCNT	COOH	Fe^{2+}	VitC	NO	0.3361	90	5	2.37	20
SWCNT	COOH	Fe^{2+}	NO	NO	0.3741	94.14	2.4	2.73	1
SWCNT	COOH	Fe^{2+}	VitC	NO	0.3361	90	5	2.73	1
MWCNT	COOH	Fe^{2+}	VitC	NO	0.3479	90	5	3.86	1
SW/DWCNT	OH	H_2O_2	NO	NO	0.3751	300	3	3.96	1
MWCNT	OH	H_2O_2	NO	NO	0.3751	300	3	2.97	13.67
MWCNT	COOH	H_2O_2	NO	NO	0.3751	300	3	2.86	13.67
SWCNT	COOH	H_2O_2	NO	NO	0.3751	300	3	2.73	1
MWCNT	OH	Ca^{2+}	NO	NO	0.3528	300	2.38	2.46	15.5
NO	NO	Fe^{2+}	NO	NO	0.3741	247.5	0	0	0
MWCNT	NO	Fe^{2+}	VitC	NO	0.3361	90	5	0	8
SW/DWCNT	OH	Fe^{2+}	NO	NO	0.3741	94.14	2.4	3.96	1
SW/DWCNT	OH	Fe^{2+}	VitC	NO	0.3361	90	5	3.96	1
MWCNT	OH	Fe^{2+}	NO	NO	0.3741	94.14	2.4	2.97	13.67
MWCNT	COOH	Fe^{2+}	VitC	NO	0.3361	90	5	2.86	13.67

[a] $\langle V_1\rangle = \langle t_{ij}\rangle$ (seg), $\langle V_2\rangle = \langle c_{ij}\rangle$ ($\mu g\ ml^{-1}$), $\langle V_3\rangle = \langle^{max}W_{ij}\rangle$, $\langle V_4\rangle = \langle^{min}D_{ij}\rangle$ (nm).

Table 8 Simulation of $P(\%)_{pred}$ if $^{max}W_i$ and $^{min}D_i$ increase in $x(\%)$ at $t(s) = 600$ and $c(\mu g\ ml^{-1}) = 2.5$

CNT and assay[a]						$x(\%)$ increase of $^{max}W_i$ and $^{min}D_i$[b]			
		CNT structural parameters				0	1	5	10
Assay	CNT	$^{max}W_i$	$^{min}D_i$	Type	Function	P_0 (%)	P_1 (%)	P_5 (%)	P_{10} (%)
Ca^{2+}	1	0	8	MWCNT	H	9.77	10.45	13.14	16.53
	2	3.96	1	SW/DWCNT	OH	7.89	8.51	11.03	14.18
	3	3.86	1	MWCNT	OH	7.82	8.45	10.96	14.12
	4	4	10	MWCNT	OH	13.52	14.21	16.97	20.44
	5	1.06	30	MWCNT	OH	24.28	25.11	28.43	32.60
	6	0.73	30	MWCNT	COOH	24.07	24.90	28.21	32.39
	7	4	10	MWCNT	COOH	13.52	14.21	16.97	20.44
	8	2.73	1	SWCNT	COOH	7.12	7.75	10.26	13.41
	9	3.86	1	MWCNT	COOH	7.82	8.45	10.96	14.12
Fe^{2+}	1	1	8.08	MWCNT	H	37.66	38.63	42.54	47.44
	2	4.96	1.01	SW/DWCNT	OH	34.92	35.83	39.47	44.04
	3	4.86	1.01	MWCNT	OH	34.83	35.74	39.38	43.95
	4	5	10.1	MWCNT	OH	43.08	44.08	48.08	53.10
	5	2.06	30.3	MWCNT	OH	58.67	59.87	64.68	70.72
	6	1.73	30.3	MWCNT	COOH	58.37	59.56	64.37	70.42
	7	5	10.1	MWCNT	COOH	43.08	44.08	48.08	53.10
	8	3.73	1.01	SWCNT	COOH	33.82	34.72	38.36	42.93
	9	4.86	1.01	MWCNT	COOH	34.83	35.74	39.38	43.95
H_2O_2	1	5	8.4	MWCNT	H	0	0.97	5.72	11.68
	2	8.96	1.05	SW/DWCNT	OH	0	0	1.99	7.55
	3	8.86	1.05	MWCNT	OH	0	0	1.88	7.44
	4	9	10.5	MWCNT	OH	6.38	7.59	12.46	18.57
	5	6.06	31.5	MWCNT	OH	25.34	26.80	32.65	40.01
	6	5.73	31.5	MWCNT	COOH	24.97	26.43	32.28	39.63
	7	9	10.5	MWCNT	COOH	6.38	7.59	12.46	18.57
	8	7.73	1.05	SWCNT	COOH	0	0	0.64	6.19
	9	8.86	1.05	MWCNT	COOH	0	0	1.88	7.44

[a] MWCNT = Multiple-Walled, SWCNT = Single-Walled, SW/WTCNT = MWCNT + SWCNT mixture. [b] $P(\%)_{pred} = 100[\varepsilon_{ij}(CNT + TC + S)_{pred} - \varepsilon_{ij}(TC + S)_{obs}]/[\varepsilon_{ij}(IC + TC + S)_{obs} - \varepsilon_{ij}(TC + S)_{obs}]$ is mitoprotective protective activity, CNT = carbon nanotube, TC = toxic control, IC = inhibitor control, S = solvent. Assay details are the following. For toxicity assay 1 ($a = 1$), TC = Ca^{2+}, IC = CsA, and solvent = DMSO. For assay 2 ($a = 2$), TC = Fe^{2+}, IC = EGTA and S = DMSO. For toxicity assay 3 ($a = 3$), TC = H_2O_2, IC = Q, and solvent = DMSO. N is the number of replicas of this assay.

predictions show that $^{min}D_i$ and $^{max}W_i$ are relevant nano-descriptors strongly implicated in the inhibition of mitochondrial permeability transition induced by Ca^{2+}, Fe^{2+}, H_2O_2 for carbon nanotubes. Small increments of $^{min}D_i$ including SWCNT and MWCNT may affect the function of certain proteins and enzymes and induce serious cytotoxic effects at the biochemical and/or sub-cellular level as we assayed in the isolated mitochondria experimental model. Theoretical predictions model the variations of carbon nanotubes diameter ($0\% < {}^{min}D_i < 10\%$) associated with mitochondrial dysfunction (swelling). The results suggest that larger diameters also could act blocking or interfering with the function of carriers and mitochondrial proteins which forms MPTP (like VDAC and ANT) and in this way inhibit apoptosis through deficient MPTP assembly in swelling experimental conditions.

On the other hand the theoretical predictions to increase the functionalization ($0\% < {}^{max}W_i < 10\%$) reveals interesting aspects about the relationship nanostructure–mitoprotective activity (MPT-inhibitors) of oxidized carbon nanotubes family particularly related to motif structure in order (carboxylated-motif) > (hydroxylated-motif) and considering the walls number of CNT (MW-motif) > (SW-motif) in pro-oxidant conditions against mitochondrial swelling in order (swelling assays induced by Fe^{2+}; P_2) > (swelling assay induced by H_2O_2; P_3), suggesting mechanisms based on the inhibition of Fenton–Haber–Weiss reaction.

Conclusions

The prediction of relationships between carbon nanomaterials physic-chemical properties and biological responses, has gained a significant importance to reduce their toxic effects and extend their nanotechnology applications. The structural determinants for mitochondrial mechanisms of functionalized CNTs (oxidized) are remaining poorly understood actually. We found that the CNTs-COOH and CNT-OH were more biocompatibility compared with the *p*-MWCNTs to prevent the mitochondrial dysfunction.

We can use mixed experimental-theoretic methodology to study the effects of different CNT in the modulation of mitochondrial permeability transition pore under the influence of multiple factors. In this context the modulation of mitochondrial physiology through MPTP in experimental swelling condition (Ca^{2+}, Fe^{2+}, H_2O_2 overload) using oxidized CNT can

represent a qualitative advance in the treatment of several chronic diseases (hepatotoxicity, Alzheimer, Parkinson, cardiac ischemia) where MPTP has been directly involved.

Particularly NQSPR perturbation approach used here can contribute to predict nanotoxicological data allowing to infer the effects of new nanomaterials in a short time. Indeed, the derived nano-QSTR perturbation model to mitochondrial swelling provided new insights regarding the typical CNT-nanodescriptors (length, diameter, shape, partition coefficient, chemical functionalization, solubility and Young's modulus) related to mitochondrial responses as therapeutic target at the sub-cellular level, as well as the influence of different experimental conditions under which these physico-chemical properties were evaluated. Finally this *in silico* method allows the prediction of the potential mitoprotective effects of several nanoparticles under conditions not tested in our original database, which could be used to make regulatory decisions, rational design of CNT more selective and less mitotoxic.

Acknowledgements

M. González-Durruthy acknowledges Doctoral fellowship (Post-graduate Students Program PEC-PG No.062/2013) from Brazilian Agencies CAPES-CNPq. J. M. Monserrat is a productivity fellow from CNPq (PQ 307880/2013-3). This study was supported with funds from Brazilian CNPq (Project numbers 552131/2011-3, 479053/2012-0 and 452088/2015-1) given to J. M. Monserrat.

References

1 R. A. Haworth and D. R. Hunter, *Arch. Biochem. Biophys.*, 1979, **195**, 460–467.
2 L. Dong-Wei, H. Huan, L. Bing-Bing, X. Zi-Qiang, J. Feng-Lei and L. Liu, *RSC Adv.*, 2014, **4**, 3913–3919.
3 Z. Jie, Z. Zhi-Qiang, J. Jian-Cheng, Y. Lian, H. Huan, J. Feng-Lei, Y. Xiao-Gang, D. Jie and L. Yi, *Chemosphere*, 2014, **100**, 194–199.
4 G. Jia-ling, W. Man, W. Xuan, Z. Ye-Zhong, J. Feng-Lei, L. Yi and D. Jie, *J. Membr. Biol.*, 2015, **248**, 39–46.
5 X. Cai-Fen, L. Long, C. Xin-You, F. Bo-Qiao, L. Ke-Lin, Q. Cai-Qin and L. Yi, *J. Membr. Biol.*, 2015, **248**, 319–326.
6 P. A. de Faria, F. Bettanin, E. Paredes-Gamero, I. L. de-Mello, T. Nantes and T. Rodrigues, *Toxicology*, 2015, **330**, 44–54.
7 C. T. Tan, T. Y. Saw, C. W. Fong and H. K. Ho, *Redox Biol.*, 2015, **4**, 308–320.
8 A. Shvedova, A. Pietroiusti, B. Fadeel and V. E. Kagan, *Toxicol. Appl. Pharmacol.*, 2012, **261**, 121–133.
9 X. Wang, J. Guo, T. Chen, T. H. Nie, H. Wang, J. Zang, X. Cui and G. Jia, *Toxicol. In Vitro*, 2012, **26**, 799–806.
10 S. Ye, Y. Jiang, H. Zhang, Y. Wang, Y. Wu, Z. Hou and Q. Zhang, *J. Nanosci. Nanotechnol.*, 2012, **12**, 2101–2112.
11 M. Garcia-Fuentes, H. Gonzalez-Diaz and N. Csaba, *Curr. Top. Med. Chem.*, 2014, **14**, 1095–1096.
12 R. Tantra, C. Oksel, T. Puzyn, J. Wang, K. N. Robinson, X. Z. Wang, C. Y. Ma and T. Wilkins, *Nanotoxicology*, 2014, **1**, 1–7.
13 A. Gajewicz, N. Schaeublin, B. Rasulev, S. Hussain, D. Leszczynska, T. Puzyn and J. Leszczynski, *Nanotoxicology*, 2014, **1**, 1–13.
14 S. Kar, A. Gajewicz, T. Puzyn and K. Roy, *Toxicol. In Vitro*, 2014, **28**, 600–606.
15 A. A. Toropov, A. P. Toropova, T. Puzyn, E. Benfenati, G. Gini, D. Leszczynska and J. Leszczynski, *Chemosphere*, 2013, **92**, 31–37.
16 A. A. Toropov, A. P. Toropova, E. Benfenati, G. Gini, T. Puzyn, D. Leszczynska and J. Leszczynski, *Chemosphere*, 2012, **89**, 1098–1102.
17 T. Puzyn, B. Rasulev, A. Gajewicz, X. Hu, T. P. Dasari, A. Michalkova, H. M. Hwang, A. Toropov, D. Leszczynska and J. Leszczynski, *Nat. Nanotechnol.*, 2011, **6**, 175–178.
18 B. D. Shane, S. Zhenyu, S. Philip, H. James and N. C. Jonathan, *J. Phys. Chem. C*, 2010, **114**, 231–237.
19 N. Sizochenko, B. Rasulev, A. Gajewicz, V. Kuzmin, T. Puzyn and J. Leszczynski, *Nanoscale*, 2014, **6**, 13986–13993.
20 R. Carbo-Dorca and E. Besalu, *Environ. Res.*, 2011, **22**, 661–665.
21 C. Y. Shao, S. Z Chen, B. H. Su, Y. J. Tseng, E. X. Esposito and A. J. Hopfinger, *J. Chem. Inf. Model.*, 2013, **53**, 142–158.
22 A. P. Toropova and A. A. Toropov, *Mini–Rev. Med. Chem.*, 2015, **15**, 608–621.
23 A. P. Toropova, A. A Toropov and E. Benfenati, *Environ. Res.*, 2015, **26**, 29–40.
24 C. Oksel, C. Y. Ma and X. Z. Wang, *Environ. Res.*, 2015, **26**, 79–94.
25 M. Shahbazy, M. Kompany-Zareh and M. M. Najafpour, *J. Photochem. Photobiol., B*, 2015, DOI: 10.1016/j.jphotobiol.2014.12.020.
26 A. Gajewicz, M. T. Cronin, B. Rasulev, J. Leszczynski and T. Puzyn, *Nanotechnology*, 2015, **26**, 015701, DOI: 10.1088/0957-4484/26/1/015701.
27 A. P. Toropova, A. A. Toropov, R. Rallo, D. Leszczynska and J. Leszczynski, *Ecotoxicol. Environ. Saf.*, 2015, **112**, 39–45.
28 A. P. Toropova, A. A. Toropov, E. Benfenati, R. Korenstein, D. Leszczynska and J. Leszczynski, *Environ. Sci. Pollut. Res. Int.*, 2015, **22**, 745–757.
29 E. Burello and A. P. Worth, *Wiley Interdiscip. Rev.: Nanomed. Nanobiotechnol.*, 2011, **3**, 298–306.
30 C. Hansch, D. Hoekman, A. Leo, D. Weininger and C. D. Selassie, *Chem. Rev.*, 2002, **102**, 783–812.
31 C. Hansch, A. Kurup, R. Garg and H. Gao, *Chem. Rev.*, 2001, **101**, 619–672.
32 C. Hansch, W. E. Steinmetz, A. J. Leo, S. B. Mekapati, A. Kurup and D. Hoekman, *J. Chem. Inf. Comput. Sci.*, 2003, **43**, 120–125.
33 H. Gonzalez-Diaz, S. Arrasate, A. Gomez-San Juan, N. Sotomayor, E. Lete, L. Besada-Porto and J. M. Ruso, *Curr. Top. Med. Chem.*, 2013, **13**, 1713–1741.
34 H. Gonzalez-Diaz, S. Arrasate, A. G. Juan, N. Sotomayor, E. Lete, A. Speck-Planche, J. M. Ruso, F. Luan and M. Cordeiro, *Curr. Drug Metab.*, 2014, **15**, 470–488.
35 J. Vergara-Galicia, F. J. Prado-Prado and H. Gonzalez-Diaz, *Curr. Drug Metab.*, 2014, **15**, 557–564.

36 F. Luan, V. V. Kleandrova, H. Gonzalez-Diaz, J. M. Ruso, A. Melo, A. Speck-Planche and M. N. Cordeiro, *Nanoscale*, 2014, **6**, 10623–10630.

37 V. V. Kleandrova, F. Luan, H. Gonzalez-Diaz, J. M. Ruso, A. Speck-Planche and M. N. Cordeiro, *Environ. Sci. Technol.*, 2014, **48**, 14686–14694.

38 V. V. Kleandrova, F. Luan, H. Gonzalez-Diaz, J. M. Ruso, A. Melo, A. Speck-Planche and M. N. Cordeiro, *Environ. Int.*, 2014, **73**, 288–294.

39 A. Speck-Planche, V. V. Kleandrova, F. Luan and M. N. Cordeiro, *Nanomedicine*, 2015, **10**, 193–204.

40 P. L. Pedersen, J. W. Greenawalt, B. Reynafarje, J. Hullihen, G. L. Decker, J. W. Soper and E. Bustamente, *Methods Cell Biol.*, 1978, **20**, 411–481.

41 G. L. Pardo-Andreu, Y. Nunez-Figueredo, V. G. Tudella, O. Cuesta-Rubio, F. P Rodrigues, C. R. Pestana, S. A. Uyemura, A. M. Leopoldino, L. C. Alberici and C. Curti, *Toxicol. Appl. Pharmacol.*, 2011, **253**, 282–289.

42 B. V. Chernyak, V. N. Dedov and V. Chernyak, *FEBS Lett.*, 1995, **365**, 75–78.

43 G. L. Pardo-Andreu, R. Delgado, J. A. Velho, C. Curti and A. E. Vercesi, *Arch. Biochem. Biophys.*, 2005, **439**, 184–193.

44 D. Jia-Xin, Z. Guang-Yuan, Y. Qiu-Li-Yang, L. Ran, Y. Lian, C. Jing and L. Yi, *J. Membr. Biol.*, 2013, **246**, 375–381.

45 L. Jia-han, L. Xiao-rong, Z. Yue, T. Fang-fang, Z. Guang-yuan, Y. Qiu-li-yang, J. Feng-lei and L. Yi, *Toxicol. Res.*, 2012, **1**, 137–144.

46 G. L. Pardo-Andreu, R. Delgado, A. J. Nunez-Selles and A. E. Vercesi, *Pharmacol. Res.*, 2006, **53**, 253–260.

47 L. Jiahan, Z. Yue, X. Qi, T. Fangfang, L. Xiaorong, L. Ran, Z. Guangyuan, J. Fenglei and L. Yi, *J. Hazard. Mater.*, 2011, **194**, 440–444.

48 Z. Yue, T. Fangfang, X. Qi, H. Yanjun, L. Jiahan, J. Fenglei and L. Yi, *J. Membr. Biol.*, 2013, **246**, 365–373.

49 M. Reers, T. W. Smith and L. B. Chen, *Biochemistry*, 1991, **30**, 4480–4486.

50 T. Hill and P. Lewicki, *Statistics: Methods and Applications: a Comprehensive Reference for Science, Industry, and Data Mining*, StatSoft, Inc., 2006, p. 832, ISBN: 1884233597.

51 K. Chan, D. Truong, N. Shangari and P. J. O'Brien, *Expert Opin. Drug Metab. Toxicol.*, 2005, **4**, 655–669.

52 M. Xiaowei, Z. Li-Hua, W. Li-Rong, X. Xue, S. Ji-Hong, W. Yan, Z. Guozhang, W. Xia, W. C Paul, G. W. Wayne, Y. Jun-Jie, Z. Kaiyuan and L. Xing-Jie, *ACS Nano*, 2012, **12**, 10486–10496.

53 G. L. Andreu, R. Delgado, J. A. Velho, C. Curti and A. E. Vercesi, *Eur. J. Pharmacol.*, 2005, **513**, 47–55.

54 V. Giorgio, M. E. Soriano, E. Basso, E. Bisetto, G. Lippe, M. A. Forte and P. Bernardi, *Biochim. Biophys. Acta*, 2010, **1797**, 1113–1118.

55 V. M. Figueredo, K. P. Dresdner, A. C. Wolney and A. M. Keller, *Cardiovasc. Res.*, 1991, **25**, 337–342.

56 A. A. Toropov, D. Leszczynska and J. Leszczynski, *Comput. Biol. Chem.*, 2007, **31**, 127–128.

57 H. H. Vilela-Costa, G. F. Lima, L. R. Nacano and C. R. T. Tarley, *Water, Air, Soil Pollut.*, 2011, **217**, 557–565.

58 L. Zhenbao, L. Yanfei and P. Dongming, *J. Biomed. Mater. Res.*, 2015, DOI: 10.1002/jbm.a.35416.

59 C. Yong, Q. Konggang, Z. Chuanqi, W. Li, R. Jinsong, W. Jiasi and Q. Xiaogang, *Nat. Commun.*, 2012, DOI: 10.1038/ncomms2091.

60 A. P. Halestrap and C. Brenner, *Curr. Med. Chem.*, 2003, **10**, 1507–1525.

61 G. J. Gores, C. E. Flarsheim, T. L. Dawson, A. L. Nieminen, B. Herman and J. J. Lemasters, *Biochim. Biophys. Acta*, 2006, **1762**, 181–190.

62 F. Di Lisa, A. Carpi, V. Giorgio and P. Bernardi, *Biochim. Biophys. Acta*, 2011, **1813**, 1316–1322.

63 M. Colombini, *Mol. Cell. Biochem.*, 2004, **256–257**, 107–115.

64 A. Masini, D. Ceccarelli, F. Giovannini, G. Montosi, C. Garuti and A. Pietrangelo, *J. Bioenerg. Biomembr.*, 2000, **32**, 175–182.

65 A. Pietrangelo, G. Montosi, C. Garuti, M. Contri, F. Giovannini, D. Ceccarelli and A. Masini, *J. Bioenerg. Biomembr.*, 2002, **34**, 67–79.

66 U. Rauen, F. Petrat, R. Sustmann and H. Groot, *J. Hepatol.*, 2004, **40**, 607–615.

67 D. Ashton, J. van Reempts and A. Wauquier, *Arch. Pharmacol.*, 1981, **254**, 196–213.

68 G. L. Pardo-Andreu, R. Delgado, A. J. Núñez-Sellés and A. E. Vercesi, *Pharmacol. Res.*, 2006, **53**, 253–260.

69 H. Dumortier, S. Lacotte, G. Pastorin, R. Marega, W. Wu, D. Bonifazi, J. P. Briand, M. Prato, S. Muller and A. Bianco, *Nano Lett.*, 2006, **6**, 1522–1528.

70 A. Toninello, P. Pietrangeli, U. De Marchi, M. Salvi and B. Mondovì, *Biochim. Biophys. Acta*, 2009, **178**, 1425–1432.

71 J. Wang, S. Pingping, B. Yongming, D. Bairui, S. Dandan and L. Yachen, *Toxicol. in Vitro*, 2012, **26**, 32–41.

72 A. Karakoti, S. Singh, J. M. Dowding and S. Seal, *Chem. Soc. Rev.*, 2010, **39**, 4422–4432.

73 A. Albini, V. Mussi, A. Parodi, A. Ventura and E. Principi, *Nanotechnol. Biol. Med.*, 2010, **6**, 277–288.

74 Z. Yang, Y. Zhang, Y. Yang, L. H. Dong, H. Li and C. Wang, *Nanomedicine: Nanotechnology, Biology and Medicine*, 2010, **6**, 427–441.

75 J. J. Liao and R. Liu, *J. Chemom.*, 2009, **23**, 248–253.

76 P. G. Gottschalk and J. R. Dunn, *Anal. Biochem.*, 2005, **343**, 54–65.

77 E. Tenorio-Borroto, F. R. Ramirez, A. Speck-Planche, M. N. Cordeiro, F. Luan and H. Gonzalez-Diaz, *Curr. Drug Metab.*, 2014, **15**, 414–428.

78 E. Tenorio-Borroto, C. G. Peñuelas-Rivas, J. C. Vásquez-Chagoyán, N. Castañedo, F. J. Prado–Prado, X. García-Mera and H. González-Díaz, *Eur. J. Med. Chem.*, 2014, **72**, 206–220.

Artigo 2: Predicting the binding properties of single walled carbon nanotubes (SWCNT) with an ADP/ATP mitochondrial carrier using molecular docking, chemoinformatics, and nano-QSBR Perturbation Theory

RSC Advances

PAPER

Cite this: *RSC Adv.*, 2016, **6**, 58680

Predicting the binding properties of single walled carbon nanotubes (SWCNT) with an ADP/ATP mitochondrial carrier using molecular docking, chemoinformatics, and nano-QSBR perturbation theory†

Michael González-Durruthy,*[ab] Adriano V. Werhli,[cd] Luisa Cornetet,[cd] Karina S. Machado,[cd] Humberto González-Díaz,[ef] Wilson Wasiliesky Jr,[g] Caroline Pires Ruas,[h] Marcos A. Gelesky[h] and José M. Monserrat[ab]

Interactions between the single walled carbon nanotube (SWCNT) family and a mitochondrial ADP/ATP carrier (ANT-1) were evaluated using constitutional (functional groups, number of carbon atoms, *etc.*) and electronic nanodescriptors defined by (*n*, *m*)-Hamada indexes (armchair, zig-zag and chiral). The Free Energy of Binding (FEB) was determined by molecular docking simulation and the results showed that FEB was statistically more negative ($p < 0.05$), following the order SWCNT-COOH > SWCNT-OH > SWCNT, suggesting that polar groups favor the anchorage to ANT-1. In this regard, it was showed that key ANT-1 amino acids (Arg 79, Asn 87, Lys 91, Arg 187, Arg 234 and Arg 279) responsible for ADP-transport were conserved in ANT-1 from different species examined to predict SWCNT interactions, including shrimp *Litopenaeus vannamei* and fish *Danio rerio* commonly employed in ecotoxicology. The SWCNT-ANT-1 inter-atomic distances for the key ANT-1 amino acids were similar to that with carboxyatractyloside, a classical inhibitor of ANT-1. Significant linear relationships between FEB and *n*-Hamada index were found for zig-zag SWCNT and SWCNT-COOH ($R^2 = 0.95$ in both cases). A Perturbation Theory-Nano-Quantitative Structure-Binding Relationship (PT-NQSBR) model was fitted that was able to distinguish between strong (FEB < −14.7 kcal mol^{-1}) and weak (FEB ≥ −14.7 kcal mol^{-1}) SWCNT–ANT-1 interactions. A simple ANT-1-inhibition respiratory assay employing mitochondria suspension from *L. vannamei*, showed good accordance with the predicted model. These results indicate that this methodology can be employed in massive virtual screenings and used for making regulatory decisions in nanotoxicology.

Received 6th April 2016
Accepted 9th June 2016

DOI: 10.1039/c6ra08883j

www.rsc.org/advances

1 Introduction

Nanotechnology has brought great advances to many fields of modern science. Multiple applications of nanomaterials have been found by virtue of their optical, electrical and chemical/biological properties. In this sense, carbon nanotubes (CNTs) are nanomaterials considered for applications in biomedicine because of their flexible structure and possibilities for chemical functionalization.[1,2]

Among the CNTs, single-walled carbon nanotubes (SWCNTs) have rapidly become one of the most widely studied nanomaterials, primarily on the basis that their unique physicochemical properties increase the number of new applications in nanomedicine as active ingredients, supportive substrates and pharmaceutical excipients for the design of versatile drug delivery systems.[1,2]

Given these diverse and important applications, it is expected that the number and variety of manufactured CNTs will

[a]*Instituto de Ciências Biológicas (ICB) – Universidade Federal do Rio Grande-FURG, Cx. P. 474, CEP 96200-970, Rio Grande, RS, Brazil. E-mail: gonzalezdurruthy.furg@gmail.com; Tel: +55 5332935196*

[b]*Programa de Pós-Graduação em Ciências Fisiológicas-Fisiologia Animal Comparada-ICB-FURG, RS, Brazil*

[c]*Centro de Ciências Computacionais (C3) – Universidade Federal do Rio Grande-FURG, RS, Brazil*

[d]*Programa de Pós-Graduação em Computação-C3-FURG, RS, Brazil*

[e]*Department of Organic Chemistry II, Faculty of Science and Technology, University of the Basque Country UPV/EHU, 48940, Leioa, Bizkaia, Spain*

[f]*IKERBASQUE, Basque Foundation for Science, 48011, Bilbao, Bizkaia, Spain*

[g]*Instituto de Oceanografia (IO), FURG, Brazil*

[h]*Programa de Pós-graduação em Química Tecnológica e Ambiental, FURG, Brazil*

† Electronic supplementary information (ESI) available. See DOI: 10.1039/c6ra08883j

increase rapidly over the next years, imposing a need for new methods to quickly test the potential toxicity of these nanomaterials for their safe use in nanotechnologies.[2]

Implementation of *in silico* methods based in Docking Simulation (DS) appears to be an efficient alternative for the prediction of the potential toxicity and environmental impact of CNTs. DS methodology predicts the non-covalent binding of a receptor (usually an enzyme or protein) and a ligand (smaller molecules as SWCNT) at the atomic level.[3] The algorithms defined in DS can test hundreds of thousands of ligand conformations and orientations to find the best receptor-ligand binding affinity by assigning and optimizing a score.[3,4]

In particular, Docking Simulation (DS) coupled to a Virtual Screening Framework (DS-VSF) represents a powerful new technique for the rational design of a SWCNT before its mass production because it allows the computational analysis of a large volume of hypothetical compounds and the selection of the compounds that might have a greater chance of interacting with certain receptors or targets.[5–7] Currently there are no precedents of this methodology applied to the evaluation of potential toxicity of SWCNT.

Some *in vitro* studies have been demonstrated that SWCNTs exert cytotoxicity after their accumulation in the mitochondria matrix and/or by affecting the function of mitochondrial proteins of the inner membrane.[8] Previous *in vitro* research including drugs and environmental pollutants using submitochondrial particles (respiratory chain complexes I, II, III, IV; ADP/ATP translocator, ATP synthase/ATPase) to predict the toxic impact of 92 different xenobiotics showed a strong correlations with the toxicity in human and indicated that the mitochondria are a relevant model for studying the relative toxicity of many xenobiotics.[9] On the other hand, some authors using DS have found that carbon nanomaterials can block different protein channels for the transport of cations, anions and zwitterions, as the CNTs are rich in hydrophobic residues at the catalytic sites, similar to natural toxins and synthetic drugs specific for these channels.[10–13].

A few theoretical works have predicted that the electronic properties of carbon nanotubes depend on both the chirality and diameter, which are both functions of n and m parameters, known as the Hamada indices and defined by wrapping specifies a translation vector of the graphene lattice (chiral vector; C_h). Each CNT topology is usually characterized by these two parameters, thus defining some peculiar symmetries such as armchair ($n = m$), zig-zag ($n > 0$; $m = 0$) and chiral ($n > m > 0$) forms.[14–16] The indexes n and m determine the electronic properties of CNT, which can vary between being metallic and non-metallic. If $(n - m)$ is a multiple of 3, then the CNT exhibits metallic behavior, otherwise the CNT exhibits semiconducting or non-metallic behavior. Furthermore, the presence of OH and COOH covalent functionalization may affect the electrochemical properties and reactivity of the CNT.[14] However, the constitutional and/or electro-topological nanodescriptors of CNT (such as diameter, chirality, and functionalization) have not yet been considered from the point of view of quantitative structure–property/activity relationships (QSPR/QSAR) with respect to their interactions with mitochondrial proteins. This method may play an important role as a predictive tool for the risk assessment of nanomaterials, as indicated by the pioneering works on nano-QSPR studies of nanoparticles (NQSPR) published by Puzyn (2009).[17] In general, the main assumption of QSPR/QSAR models is that similar molecules have similar properties. Consequently, smaller changes in the structure of the system should correlate linearly with smaller changes on the values of its properties. However, not all similar molecules have similar properties. The underlying problem is therefore how to define one *smaller* structural change on a molecular level. The problem is relevant because each type of property, *e.g.*, partition coefficient, reactivity, or metabolism, is expected to depend on another difference. It means that it is necessary to quantify "*smaller*" variations (perturbations) in the molecular structural level that in turn imply a "*smaller*" linear change in the free energy of interaction of the nano-drug with the receptor (or CNT with mitochondrial proteins).[18]

Very recently, Gonzalez-Díaz *et al.* (2013) formulated a general purpose Perturbation Theory (PT) model for chemo-informatics problems with multiple-boundary experimental conditions.[19] This new methodology is potentially useful to carry out Quantitative Structure-Binding Relationships (QSBR) in the context of the present work to predict the interaction of SWCNT with ADP/ATP mitochondrial carrier isoform 1 (ANT-1) in quantitative terms. However, to do so, the method must be adapted for QSBR studies in nanosciences. In this work, it was describe the re-formulation of this model to develop a new type of PT-Nano-QSBR model for nanoparticles (PT-NQSBR models) to be used for *in silico* studies of SWCNT–ANT-1 interactions.

ANT-1 catalyzes the electrogenic ADP^{3-} and ATP^{4-} exchange across the inner mitochondrial membrane. The transporter provides ATP^{4-} efflux into the cytosol in exchange for the entry of ADP^{3-} into the mitochondrial matrix during oxidative phosphorylation, which can be estimated in terms of efficiency as ADP/O ratio. Considering the relationship between the amount of ADP and total amount of oxygen consumed during state III of respiration ADP-dependent. By the other hand, the ADP transport can be specifically inhibited by carboxyatractyloside (CATR), which reduces the ADP affinity. Particularly in the cationic cluster consisting of key amino acids (Arg 79, Asn 87, Lys 91, Arg 187, Asp 231, Arg 234) involved in the ADP-transport through active site of ANT-1.[20,21]

Under several pathophysiological conditions such as cardiomyopathy, Alzheimer disease and lactic acidosis, ANT-1 is a component of the mitochondrial permeability transition pore (PTPM), a multiprotein complex that is directly implicated in apoptosis.[21–23] The induction and/or inhibition of the PTPM-(ANT-1) by SWCNT could represent an attractive therapeutic strategy to induce cytotoxicity and/or cytoprotection based on the modulation of ANT-1 function. In these sense, some potential pre-clinic applications of SWCNT could be considered: (1) death of cancerous cells by conformational changes of ANT-1 associated with the inhibition of ADP transport and mitochondrial swelling, which act as an MPTP-(ANT-1) inducer;[24,25] and (2) as an MPTP-(ANT-1) inhibitor, preventing mitochondrial calcium overload in the calcium binding domain of ANT-1 and the migration of ANT-1 during MPTP-(ANT-1)

assembly in pathophysiological conditions, on the basis that ADP is an inhibitor of MPTP and has an important role in oxidative phosphorylation.[22,26–28]

In present study, it was analyzed how covalent functionalization (–OH and –COOH) and different structural geometries of SWCNT including armchair, chiral and zig-zag forms can act as specific inhibitors of ANT-1. Taking into account the information cited above, the main objective of this study was to evaluate the interactions between SWCNT and ANT-1 using DS-VSF and nano-QSBR-perturbation theory (PT) model to predict the structural attributes of SWCNT involved in the interactions with mitochondrial ADP transport by ANT-1.

2 Materials and methods

2.1. Docking simulation

To analyze the interaction between the ANT-1 protein and various types of carbon nanotubes, it was followed the workflow depicted in Fig. 1. In this methodology, the first step consists of preparing the ANT-1 macromolecule structure file (receptor), which was obtained from the *RCSB Protein Data Bank* (PDB).[28] Before the molecular docking, ANT-1 molecular structures was converted in pdbqt format using the AutoDockTools 4 software for AutoDockVina. The computational algorithm includes the removal of water molecules crystallographic and all the co-crystallized ANT-ligand molecules as carboxyatractyloside (molecular name: CXT, classical inhibitor of the ADP-transport) of the ANT-1 cavity in the PDB structure file and other like cardiolipin (molecular name: CDL, phospholipidic component of mitochondrial outer membrane), 3-laurilamido-*N*-*N*′-dimethylpropylaminoxide (molecular name: LDM), 1,2-diacyl-SN-*glycero*-3-phosphocholine (molecular name: PC1). Also it was performed the addition of hydrogen atoms with appropriate built-in modules to add partial charges, protonation states followed by bond orders assignment and set up rotatable bonds.

In the second step, the SWCNTs-ligands (pristine-SWCNTs or SWCNT-H) structures were carefully modeled taking to account general CNT-nanodescriptors semi-empirical values for [*n*] and [*m*]-Hamada indexes calculated by H. Yorikawa and S. Muramatsu in 1995 (ref. 29) and others CNT-parameters like molecular weight, number of bonds, number of atoms, ratio, diameter, hexagons number/1D unit cell, metallic and/or semiconducting properties.[29] For this instance it was used the software Nanotube Modeler (http://www.jcrystal.com/products/wincnt/) version 1.7.5 registered to one of the authors (J. M. Monserrat). Furthermore, some pristine-SWCNT structures were oxidized either with carboxyl (–COOH) or hydroxyl (–OH) moieties using an advanced semantic chemical editor Avogrado (Version 1.1.1 free software). All the SWCNT-ligands minimization was done using the MOPAC extension for geometry optimization based on the AM1-Hamiltonian method.

An *ad hoc* framework was developed to configure the virtual screening (VS) experiments to evaluate the various parameters. This framework has a web interface in which the user configures the experiment and obtains the respective Python script to automatically perform the VS steps. In the framework interface,

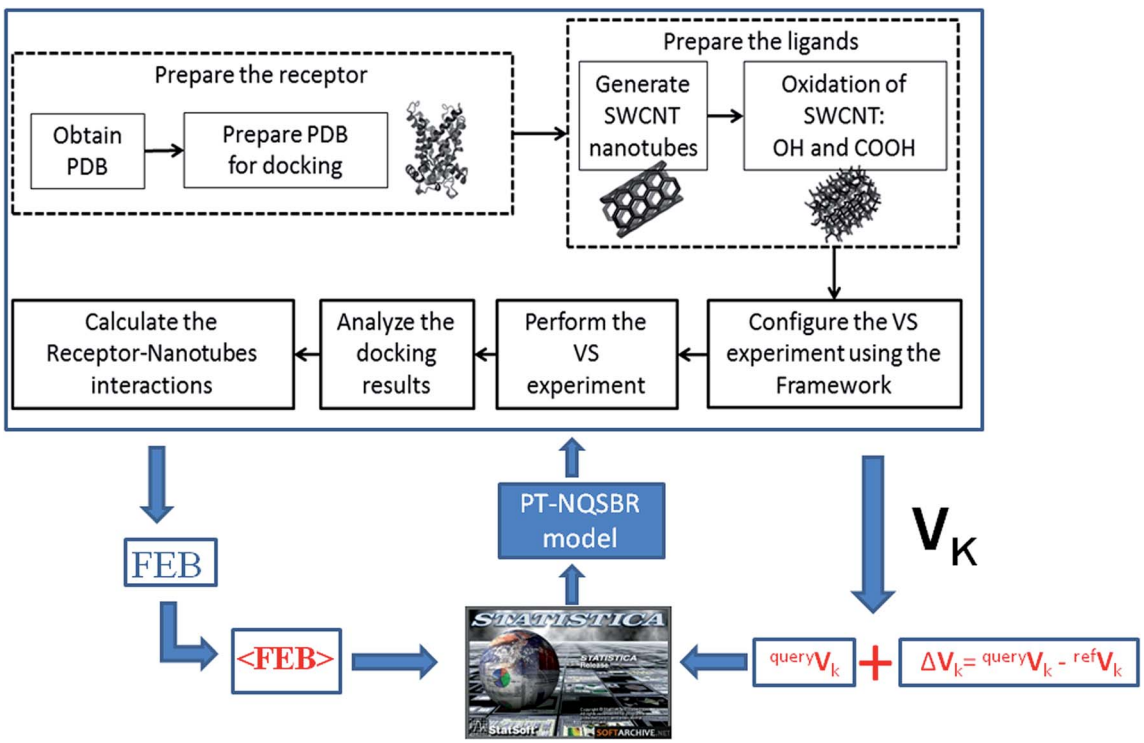

Fig. 1 Methodology employed for performing the virtual screening experiment with carbon nanotubes. PDB: protein data bank (http://www.rcsb.org/pdb/home/home.do). SWCNT: single walled carbon nanotube. VS: virtual screening and general workflow of the PT-NQSBR study of SWCNT–ANT-1 binding affinity.

the user provides information regarding the receptor file (ANT-1) and the folder in which all the nanotubes structures are stored. To evaluate the SWCNTs–ANT-1 *in silico* interactions Autodock Vina rigid docking it was implemented, open source software developed by Trott & Olson (2010) herein the receptor (ANT-1) and ligands (SWCNTs) were considered as a rigid molecules.[30] Following this idea, conformational rigidification favors a significant gain of enthalpy of SWCNT–ANT-1 complexes associated to reduction of SWCNT-intramolecular deformation or vibrational decrease within ANT-1 active site.

In this context, the (SWCNTs–ANT-1) complexes free energy of binding (FEB) were calculated based on the score function which attempt to approximate the standard chemical potentials (ΔG_{bind}). For this instance, the ΔG scoring function used combines the knowledge-based potential and empirical information obtained from experimental affinity measurements. Following this idea, the FEB of SWCNT–ANT-1 complex optimization it was performed with sophisticated gradient and efficient local optimization algorithm of energy based on quasi-Newton method like Broyden–Fletcher–Goldfarb–Shanno (BFGS). In this algorithm, a succession of steps consisting of a mutation and a local optimization are taken, with each step being accepted according to the Metropolis criterion.[30] This theoretical procedure was performed to the receptor binding cavity using Cartesian coordinates for ANT-1 grid box size with the average dimensions of $X = 30$ Å, $Y = 30$ Å, $Z = 30$ Å and the ANT-1 receptor grid box center $X = 18.8$ Å, $Y = 18$ Å, $Z = 32$ Å to evaluate the SWCNT–ANT-1 interaction, considering the CATR-biophysical environment (ANT-1 active site) to evaluate the SWCNT-affinity. Several runs starting from random conformations were performed, and the number of iterations in a run was adapted according to the problem complexity. For this instance an exhaustiveness option of 8 (average accuracy) in each docking calculation was used.[30] The docking output results or FEB values are similarly defined to ΔG_{bind} values for all docked poses according to ΔG energy scoring function with the thermodynamic description represented below:

$$\Delta G_{\text{bind}} \approx \text{FEB} = G_{(\text{SWCNT/ANT-1 complex})} - G_{(\text{ANT-1 receptor})} - G_{(\text{SWCNT})}$$

$$\text{FEB} = \Delta H + \Delta G_{(\text{solvation})} - T\Delta S_{(\text{bind})}$$

$$\text{FEB} = \Delta E_{(\text{MM})} + \Delta G_{(\text{GB})} + \Delta G_{(\text{SA})} - T\Delta S_{(\text{bind})}$$

where $\Delta G = -RT(\ln K_{\text{i}})$, R (gas constant) is 1.98 cal (mol K)$^{-1}$ and K_{i}, represent the predicted inhibition constants at $T = 298.15$ K. $\Delta E_{(\text{MM})}$ is the gas-phase interaction energy between receptor (ANT-1) and ligands (SWCNTs), including the electrostatic and van der Waals interactions; $\Delta G_{(\text{GB})}$ and $\Delta G_{(\text{SA})}$ are the polar and non-polar contributions of desolvation free energy, respectively. $-T\Delta S_{(\text{bind})}$ is the conformational entropy change upon SWCNT binding. Docking was considered as energetically unfavorable when a FEB for SWCNT–ANT-1 complex ≥ 0 kcal mol^{-1} indicating either extremely low or complete absence of binding affinity. Following this criteria only the Gibbs free energy of binding (FEB) were obtained. The remaining default thermodynamic parameters implicit on the ΔG energy scoring function were not analyzed in this study.

The next step was the analysis of the FEB results inter-atomic distances between key amino acids of the receptor (ANT-1) and atoms at the best binding position for ligands (SWCNT).[31–34] It was considered key amino acids those involved in the inhibition of ADP transport by CATR, in way to compare the SWCNT inhibitory potential with this inhibitor.

2.2. Performed docking simulations

For the docking simulations we used, as stated above, the protein ANT-1 from *Bos taurus* (see Section 2.3) as the receptor (PDB ID 1OKC, resolution 2.2 Å) and the following SWCNTs as ligands: armchair, armchair-COOH and armchair-OH (Hamada index $n = m$; 21 nanotubes); chiral, chiral-COOH and chiral-OH (no reflection symmetry; 93 nanotubes); and zig-zag, zig-zag-COOH and zig-zag-OH (Hamada index $m = 0$, $n > 0$; 21 nanotubes). Carboxy-atractiloside (CATR: $C_{31}H_{46}O_{18}S_2$), the classical inhibitor of ANT-1, was used as a control to compare the affinity and/or interactions of SWCNT with ANT-1. For this instance, to analyze the receptor–nanotube interaction, a cutoff value of 7 Å was used.[31] Particularly for the cationic cluster consisting of key amino acids (Arg 79, Asn 87, Lys 91, Arg 187, Asp 231, Arg 234) involved in the ADP transport by ANT-1, *i.e.*, all atoms with distances below this cutoff were considered as interacting atoms. All docking simulations were performed using the default values for Autodock Vina parameters.

2.3. Protein alignments

Sequences of ANT-1 from bull *Bos taurus* (NP_777083.1), human *Homo sapiens* (NP_001142.2), mouse *Mus musculus* (NP_031476.3), rat *Rattus norvegicus* (NP_445967.1), fish *Danio rerio* (NP_999867.1), copepod *Lepeophtheirus salmonis* (ACO12396.1) and shrimp *Litopenaeus vannamei* (AEZ68611.1) were obtained from Gene Bank database (http://www.ncbi.nlm.nih.gov/genbank/). The alignments were performed on-line using the free software ClustalW2 (http://www.ebi.ac.uk/Tools/msa/clustalw2/).

2.4. PT-NQSBR models

In this section it was carried out a chemoinformatics model incorporating the theoretical free energies of binding (FEB) calculated in molecular docking experiments. For this instance, it was described the re-formulation of QSPR approach based on Pertubation Theory (PT) in order to develop a new type of PT-Nano-QSBR model for prospective classification of carbon nanotubes associated to ANT-1-mitotoxicity. The PT-NQSBR model proposed here is an additive equation with non-linear terms expressed in the following form:

$$f(\text{FEB})_{\text{query}} = a_0 f(\text{FEB})_{\text{ref}} + \sum_{k=1}^{k_{\max}} b_k{}^{\text{query}} V_k + \sum_{k=1}^{k_{\max}} c_k \Delta V_k + e_0 \quad (1)$$

$$f(\mathrm{FEB})_{\mathrm{query}} = a_0\langle \mathrm{FEB}\rangle_{\mathrm{query}} + \sum_{k=1}^{k_{\max}} a_k {}^{\mathrm{query}}V_k + \sum_{k=1}^{k_{\max}} b_k [{}^{\mathrm{query}}V_k - {}^{\mathrm{ref}}V_k] + e_0 \quad (2)$$

The first input term is the function $f(\mathrm{FEB})_{\mathrm{ref}} = \langle \mathrm{FEB}\rangle_{\mathrm{query}}$ which is the average value of FEB for all the SWCNT of the same class as query SWCNT. It means that $\langle \mathrm{FEB}\rangle_{\mathrm{query}}$ can be considered as the expected value of FEB for the interaction of a new SWCNT (query SWCNT) with the target protein ANT-1 (assuming a normal distribution). The second class of terms V_k are the values of the structural parameters of the query SWCNT. Last, the difference ($\Delta V_k = {}^{\mathrm{query}}V_k - {}^{\mathrm{ref}}V_k$) quantify the deviations or perturbations (changes, distortions, *etc.*) on the SWCNT-structural parameters ($^{\mathrm{query}}V_k$) of the new SWCNT compared with those of the original reference SWCNT ($^{\mathrm{ref}}V_k$). We can substitute each symbol V_k by the classic symbol of the respective property (SWCNT-nanodescriptors) and expand the input terms in order to understand better this mathematical formalism following the eqn (3) and (4):

$$f(\mathrm{FEB})_{\mathrm{query}} = a_0\langle \mathrm{FEB}\rangle_{\mathrm{query}} + \sum_{k=1}^{k_{\max}} a_k m_{\mathrm{query}} + \sum_{k=1}^{k_{\max}} b_k n_{\mathrm{query}} + \sum_{k=1}^{k_{\max}} c_k[\Delta M_{\mathrm{w}}] + \sum_{k=1}^{k_{\max}} d_k[\Delta N_{\mathrm{a}}] + e_0 \quad (3)$$

$$f(\mathrm{FEB})_{\mathrm{query}} = a_0\langle \mathrm{FEB}\rangle_{\mathrm{query}} + \sum_{k=1}^{k_{\max}} a_k m_{\mathrm{query}} + \sum_{k=1}^{k_{\max}} b_k n_{\mathrm{query}} + \sum_{k=1}^{k_{\max}} c_k \left[M_{\mathrm{w}_{\mathrm{query}}} - M_{\mathrm{w}_{\mathrm{ref}}}\right] + \sum_{k=1}^{k_{\max}} d_k \left[N_{\mathrm{a}_{\mathrm{query}}} - N_{\mathrm{a}_{\mathrm{ref}}}\right] + e_0 \quad (4)$$

Refers to Table 1 to see more details of the employed model. It was used the Linear Discriminant Analysis (LDA) forward-stepwise algorithms implemented in the software STATISTICA to fit the values of the parameters (a_0, a_k, b_k, c_k, d_k and e_0) and other parameters of the model. In the PT-NQSBR model, the output $f(\mathrm{FEB})_{\mathrm{query}}$ is a function of the value of FEB for the new SWCNT-structure which contains the CNT-nanodescriptors (Hamada index n and m, diameter, molecular weight, number of atoms). Following this idea, it is important to note that the SWCNT-diameter as a relevant nanodescriptor on the prediction of the $f(\mathrm{FEB})_{\mathrm{query}}$ it was considered in our chemo-informatics model through Hamada index n and m, because this structural parameter has a strong and direct proportionality relationship with the different geometry configurations of SWCNT evaluated as referred in the Section 2.2 according to eqn (5):

$$d_{\mathrm{SWCNT}(n,\ m)} = 0.783\sqrt{n^2 + nm + m^2} \quad (5)$$

In Fig. 1, it is depicted the workflow for this theoretical process. These PT-NQSBR models should predict the probability of interaction of the CNT structures with a target protein (ANT-1 in this case).

Table 1 Variables used as input for the nano-QSBR model. CNTs stands for carbon nanotubes

Nano-QSBR model input variables	CNTs-nanodescriptors details (V_k)
$\langle \mathrm{FEB}\rangle_{\mathrm{query}}$	FEB-expected value for a CNT of the same type than the query
m_{query}	m Hamada index values for $\mathrm{CNT}_{\mathrm{query}}$
n_{query}	n Hamada index values for $\mathrm{CNT}_{\mathrm{query}}$
$\Delta M_{\mathrm{w}} = M_{\mathrm{w}_{\mathrm{query}}} - M_{\mathrm{w}_{\mathrm{ref}}}$	Difference in molecular weight (M_{w}) between the query and reference CNT
$\Delta N_{\mathrm{a}} = N_{\mathrm{a}_{\mathrm{query}}} - N_{\mathrm{a}_{\mathrm{ref}}}$	Difference in number of atoms (N_{a}) between the query and reference CNT

2.5. Statistical analysis

Mean free energy binding (FEB) from the various carbon nanotubes were compared through two-way analysis of variance in which the factors were CNT functionalization (–H, –OH and –COOH) and geometry (chiral, armchair and zig-zag). Previously, normality and variance homogeneity assumptions were verified. Pairwise comparisons were performed using the Newman–Keuls *post hoc* test. Quantitative structure–affinity relationships were evaluated through the use of stepwise multiple regressions considering the SWCNT-1–ANT-1 complex FEB values as the dependent variable and several CNT quantitative nanodescriptors (n, m, chiral angle, molecular weight and diameter) as independent variables. In all cases, the significance level was fixed at 0.05.

2.6. Experimental measure of oxygen consumption of isolated mitochondria from shrimp *Litopenaeus vannamei* exposed to carbon nanotubes

Taking account the importance of developing of alternative methods in nanotoxicology and in order to corroborated the *in silico* evidences it was performed a rapid and simple respiratory biochemical experiment, considering the ANT-1 mitochondrial physiology using one of the species considered in the docking analysis (the shrimp *Litopenaeus vannamei*). In this regard, mitochondria from hepatopancreas of *Litopenaeus vannamei* were isolated by standard differential centrifugation.[35,36] For this instances adult *L. vannamei* shrimp weighing 30 ± 1 g were acclimatized to laboratory conditions for 8 days in marine water at 28 °C, 35 ppt salinity, constant aeration at 6 mg O_2 per L, and commercial food was supplied twice a day. All procedures performed with *L. vannamei* were carried out are in accordance with the *Code of Ethics of the World Medical Association* (*Declaration of Helsinki*) for animal experiments. After acclimation, seven shrimp were euthanized by decapitation. Hepatopancreas were immediately removed, sliced in medium (50 mL) consisting of 250 mM sucrose, 1 mM ethyleneglycol-bis(β-aminoethyl)-*N*,*N*,*N*′,*N*′-tetraacetic acid (EGTA) and 10 mM HEPES-KOH, pH 7.2, and homogenized three times for 15 s at 1 min intervals using a Potter–Elvehjem homogenizer. Homogenates were

centrifuged (580 × *g*, 5 min at 4 °C) and the resulting supernatant further centrifuged (10 300 × *g*, 10 min at 4 °C). Pellets were then suspended in medium (10 mL) consisting of 250 mM sucrose, 0.3 mM EGTA and 10 mM HEPES-KOH, pH 7.2, and centrifuged (3400 × *g*, 15 min at 4 °C). The final mitochondrial pellet was suspended in medium (1 mL) consisting of 250 mM sucrose and 10 mM HEPES-KOH, pH 7.2, and used within 3 h. Mitochondrial protein contents were determined by the Biuret reaction.[35,36]

Continuous-monitoring of oxygen consumption in mitochondrial suspensions was polarographically determined with a Clark-type electrode (Oxygraph System Hansatech Instrumens) in a 2 mL glass chamber equipped with a magnetic stirrer. Isolated mitochondria (1 mg protein per mL) from hepatopancreas were energized with 5 mM potassium succinate (plus 2.5 μM rotenone) in a standard incubation medium consisting of 125 mM sucrose, 65 mM KCl, 2 mM inorganic phosphate (K_2HPO_4) and 10 mM HEPES-KOH pH 7.4 at 20 °C in standard respiration medium. The experimental approach was calibrated using the oxygen content of air saturated medium.[35,36]

It were performed respiration protocols using three types of multi-walled carbon nanotubes MWCNT which were formed by 3 concentric tubes with distance of 0.34 nm between each wall and semiconducting behavior (conductivity = 100 S cm^{-1}). The outer diameter of $D_{max} = 7.6 \pm 1.5$ Å for the three CNT-samples were similar to maximum diameter of zig-zag-SWCNTs (D_{max} = 7.051 Å) used in the molecular docking experiments. The final concentration was 5 μg mL^{-1} in all cases.

Before the respiratory assays MWCNTs were dissolved in dimethyl sulfoxide (DMSO: 900 μL) and ultrapure Milli Q water (100 μL), to prepare individual stock suspensions at a concentration of 1 mg mL^{-1}. In order to prevent CNTs agglomeration for the oxygen consumption assays, it was employed tip-sonication regime during 5–10 min to generate a non-agglomerated suspension or monodisperse state for these CNT-samples. The sonication power was 9.3 W, with an energy input of 16.7 kJ at 25 °C using a Ultronique/Eco-sonics Q-3.0/40A sonicator. After, samples were stirred for 10–15 min. The resulting diluted suspensions were cooled to room temperature and filtered through a 0.22 μm polycarbonate membrane (Millipore, USA), before exposure to mitochondria suspensions at a final concentration of 5 μg mL^{-1}.

Mitochondria (Mit) total oxygen consumption was calculated as the difference between oxygen concentration of respiration medium (Resp med) at time 0 and oxygen concentration at the end of the measurement (300 s). This allowed the estimation of % ADP-transport inhibition considering oxygen consumption of treatment (3) (see below) as 100%. For this instance, it were performed several combinations of treatments in order to evaluate the ANT-1 inhibition as following: (1) Resp med (blank control), (2) Resp med + Mit, (3) Resp med + Mit + ADP, (4) Resp med + Mit + ADP + CATR, (5) Resp med + Mit + ADP + MWCNT-(H), (6) Resp med + Mit + ADP + MWCNT-OH, and (7) Resp med + Mit + ADP + MWCNT-COOH. CATR refers for carboxyatractyloside, the specific inhibitor of ANT-1. A final concentration of 1 μM of the inhibitor was employed in the assays. For the whole assays, two different experiments with two different mitochondrial suspensions of *L. vannamei* were performed.

2.7. Identification of (COOH and OH)-moieties of carbon nanotubes by Fourier transforms infrared spectroscopy (FT-IR)

FT-IR spectra of carbon nanotubes samples from ANT-1 respiratory biochemical test (MWCNT, MWCNT-OH, MWCNT-COOH) were performed in the range 4000 to 400 cm^{-1} using IR spectrophotometer (Shimadzu PRESTIGE-21) with Fourier transform infrared spectroscopy for the analytical identification of the functional group attached on the surface of the CNTs (OH, COOH). Each CNT-samples were analyzed in solid state by diffuse reflectance. For data processing, the Microcal Origin 5.0 software was used. All spectra were base line corrected and vector normalized. The scan number was set at 45 and the spectral resolution at 4 cm^{-1}. See in details in Fig. 2 of the molecular FT-IR signatures.

3 Results and discussion

The use of computational tools has been recommended and recognized by major regulatory agencies including the Organization for Economic Cooperation and Development (OECD, 2009) and the International Organization for Standardization (ISO/TC 229, 2011) based on the importance of developing alternative methods in nanotoxicology.[38,39] In accordance with this idea, the prediction of the relationships between the physico-chemical properties and the biological responses to carbon nanomaterials is now considered of paramount importance. A large number of studies in nano-scale systems have emphasized the importance of combining advanced experimental data with theoretical models that can distinguish among various atomic configurations. In this sense, computational algorithms can be effective tools to relate the biological effects with complex descriptors of carbon nanomaterials that are not easy to analyze experimentally.[40] In the present study, it was evaluated the relationships between the structural and geometric properties of a family of SWCNT in order to identify sites potentially suitable for the ANT-1 interactions. Firstly, the influence of CNT-geometry/chiral configuration and type of oxidation was considered. The FEB values were compared for different families of SWCNT (SWCNT, SWCNT-COOH, SWCNT-OH). As shown in Fig. 3, more negative FEB values, which represent higher affinity for the interaction with ANT-1, followed the order SWCNT-COOH > SWCNT-OH > SWCNT ≈ carboxy-atractiloside (CATR, classical inhibitor of ANT-1).

Taking into account that according to Pebay-Peyroula *et al.* (2003),[37] the protein ANT-1 has dimensions of 20 and 40 Å for diameter and depth, respectively, it is expected that these are the maximum dimension limits that would allow interaction of a CNT with the protein. In fact, the diameters of the CNT assayed in the docking analysis ranged from 2.35 to 12.21 Å and in all cases the length was 10 Å. Note that Pebay-Peyroula *et al.* (2003) determined that the depth of the cavity for ADP binding is 10 Å. Thus, under the experimental conditions employed

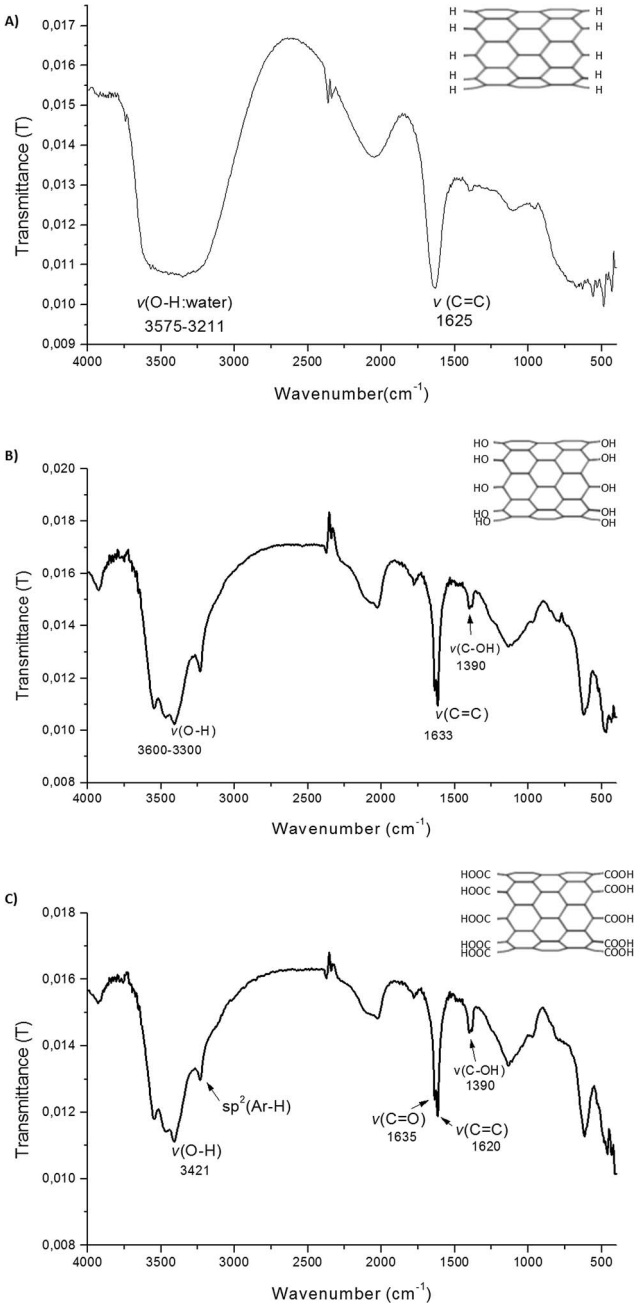

Fig. 2 Fourier-transformed infrared (FT-IR) spectrum of CNT-samples (MWCNT, MWCNT-OH, MWCNT-COOH) are depicted. (A) For MWCNT sample, the water OH-linkages peaks appear as a broad band between 3575 and 3211 cm^{-1} and C=C stretch defined by the peak at 1625 cm^{-1}. (B) For MWCNT-OH, three phenol (OH)-linkages peaks appear as a broad band from 3600 to 3300 cm^{-1} and C=C stretch at 1633 cm^{-1}. Also additional stretching frequency is observed at 1390 cm^{-1} for C-OH. (C) The MWCNT-COOH spectrum is characterized by a broad band at 3421 cm^{-1} due to the stretching mode of the OH groups of carboxyl acid. Carbonyl groups of carboxyl acid C=O stretch at 1635 cm^{-1} as well as the C=C stretch at 1620 cm^{-1} and the C-OH stretch at 1390 cm^{-1}. In addition, it was depicted the small peak for sp^2-aromatic hydrogen Ar-H above 3000 cm^{-1}. In all cases, peaks marked ν refers to stretching mode.

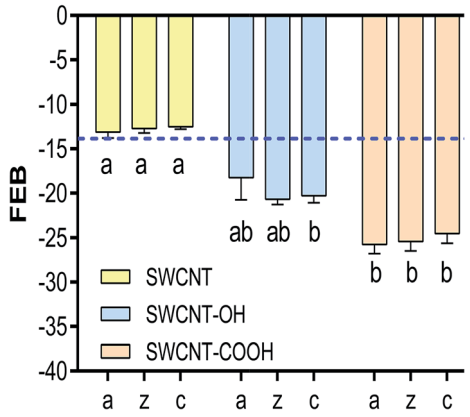

Fig. 3 Free energy binding (FEB, in kcal mol^{-1}) of adenine nucleotide translocase (ANT-1) with pristine, hydroxylated and carboxylated carbon nanotubes (SWCNT, SWCNT-OH and SWCNT-COOH, respectively). Each value is expressed in terms of the mean ± 1 error standard. Similar letters indicate the absence of significant differences ($p > 0.05$) between the different carbon nanotubes. Carbon nanotubes with different forms of chirality were considered: armchair (a), zig-zag (z) and chiral (c). The dotted blue line represents the FEB value determined for the specific inhibitor carboxyatractyloside. In all cases the results were obtained using docking simulations (see Material and methods for details).

here, there were no steric constraints for the interaction of CNT with the catalytic site of ANT-1.[37]

The results showed interesting aspects regarding the potential for SWCNT to modulate the activity of ANT-1, indicating that the employed theoretical procedure can be considered for the rational design of carbon nanomaterials with higher affinity and specificity for ANT-1. The carboxylate (COO^-)-moieties of SWCNT-COOH may be important for electrostatic interactions at the internal ANT-1 hydrophobic pocket, which is formed by five cationic arginine residues (Arg 79, Arg 187, Arg 231, Arg 234, and Arg 279). This observation highlights the importance of hydrophobic residues, particularly arginine rich regions, to form stable complex with SWCNT as has been suggested by Park *et al.* (2003) for studies of the molecular docking between SWCNT and K^+-channels.[12] Pebay-Peyroula *et al.* (2003) considered the COOH-moiety to be a toxicophore important for the ADP transport inhibition by carboxyatractyloside (CATR).[37] In contrast, the presence of the OH-moiety of CATR is considered to be a low affinity descriptor for the ANT-1 interaction.[20,37]

It seems reasonable to propose that the COOH-moiety of SWCNT-COOH can establish stable complexes of salt bridges with ANT-1, similar to the COO^- group of CATR. In this way, deprotonated SWCNT-COO^- could disrupt the association of the ADP^{3-} anion with the positive amines of Arg or Lys residues present at the bottom of ANT-1 cavity. The same authors indicated that the carboxyl groups of CATR bind primarily to residues Arg 79, Asn 87, Lys 91, Arg 187, Arg 231 and Arg 234 at the active site of bovine ANT-1. These interactions showed an electrostatic attraction, which explains the high efficiency of this inhibitor to induce mitotoxic responses through the significant reduction of phosphorylation efficiency (ADP/O

ratio) and ATP synthesis. According to the FEB values obtained for the CATR or SWCNT interactions with ANT-1, the following order of affinity can be postulated: ANT-1–CATR complex ~ ANT-1–SWCNT pristine (armchair, zig-zag and chiral) ~ ANT-1–SWCNT-OH (armchair and zig-zag) < ANT-1–SWCNT-OH (chiral) ~ ANT-1–SWCNT-COOH (armchair, zig-zag and chiral) (Fig. 3). These *in silico* evidences suggest that SWCNT have great potential to exert drastic effects in the same biophysical environment as that affected by the specific inhibitor CATR, increasing the likelihood of inducing mitochondrial toxicity.

In this context, single walled carbon nanotubes can induce mitotoxicity through the modulation of the ADP/ATP transport in diseases such as cancer through the induction of the mitochondrial permeability transition pore (MPTP), mitochondrial dysfunction and apoptosis, in which ANT-1 is an important player on the cell bioenergetics triggering of the MPTP-(ANT-1) in pathophysiological circumstances.[24,25,27,41]

As mentioned in the Introduction section, ANT-1 plays an important role in maintaining the cellular redox potential and phosphorylation efficiency (ADP/O ratio), explaining its wide distribution in all eukaryotic species. In particular, the key amino acids (Arg 79, Asn 87, Lys 91, Arg 187, Asp 231, Arg 234) involved in the ADP transport by ANT-1 were shown to be fully conserved in all the species analyzed (*Bos taurus*, *Mus musculus*, *Rattus norvegicus*, *Danio rerio*, *Lepeophtheirus salmonis*, *Litopenaeus vannamei*, and *Homo sapiens*).[28] In this way it was possible to extrapolate SWCNT affinity to ANT-1 from *Bos taurus* employed in this study to different animal species. To evaluate the coincidence of the key amino acids of ANT-1 involved in the interactions with the families of SWCNT (SWCNT, SWCNT-COOH, SWCNT-OH) in ANT-1 (Table 2), the ANT-1 sequence from bull *Bos taurus* (NP_777083.1) was aligned with the homologous sequences from other relevant species to extrapolate the interactions and/or potential toxicity of SWCNT based on comparison with the classical inhibitor of ANT-1 (carboxyatractiloside, CATR), proposed as control to compare the affinity (FEB). As shown in Fig. 4, these amino acids are fully conserved in all species analyzed.

Furthermore, the inter-atomic distance values between SWCNT and the key amino acids (Arg 79, Asn 87, Lys 91, Arg 187, Asp 231, Arg 234) for binding to ANT-1 are, in most of the cases tested, very similar to the critical values for the interactions of the same amino acids with the classical inhibitor of ANT-1 (carboxyatractiloside, CATR) crystallographycally determined by Pebay-Peyroula *et al.*, 2003.[37] This was true particularly for Arg 79, Asn 87, Lys 91, Arg 187, which are known to be directly involved in the inhibition of ADP-transport (Table 2).[37] In ESI S4† it can be found the 3D structural alignment of ANT-1 from different species (Fig. S4†) as well as the root-mean-square deviation of atomic positions (RMSD) (Table S4a†) and the FEB values after performing rigid docking simulations (Table S4b†) that showed no significant differences ($p > 0.05$) between species.

The analysis presented in this study should provide relevant information about biochemical models used for the evaluation of the interactions of CNT with ANT-1. In particular, this methodology may be used to understand the inhibitory mechanism and to infer a "binding site common substrate" with a location for interaction similar to that of the carbon nanotubes. This would permit extrapolation of the interactions and/or potential toxicity induced by the family of SWCNTs on ANT-1 independently of the phylogenetic position of evaluated species.

Consistent with our goal, the results obtained for the electro-topological properties (diameter-chirality, and functionalization) and the ANT-1 affinity (FEB) relationship indicated that the chiral index *n* is a relevant electro-topological descriptor to predict the interaction of some carbon nanotubes (zig-zag SWCNT and zig-zag SWCNT-COOH) with ANT-1. In this sense the correlation between electro-topological nano-descriptors and affinity (FEB) by ANT-1 was determined. When the influence of the various geometric configurations of SWCNT on the affinity to ANT-1 were analyzed, the chiral index *n* for the zig-zag carbon nanotubes (pristine and carboxylated) was shown to have an excellent linear correlation ($R^2 = 0.95$) with FEB ($p < 0.05$; Fig. 5a and b). In contrast to these results, a low R^2 (0.65) was observed for the linear relationship between FEB and *n* in zig-zag SWCNT-OH (Fig. 5c). The two dimensional (2D)-contour plot analysis to the FEB values for SWCNT, SWCNT-COOH and SWCNT-OH are depicted in the Fig. 5e and f to show that from both Hamada index, only *n* was relevant to describe SWCNT–ANT-1 interaction.

On the other hand, the chiral index *m* does not seem to be a relevant descriptor of SWCNT–ANT-1 interactions, given the lack of significant correlation ($p > 0.05$) with the FEB values for the three geometric configurations of SWCNT studied (zig-zag, armchair, chiral) and for all functional groups evaluated

Table 2 Comparison between inter-atomic distances for ANT-1 specific inhibitor or carboxy-atractiloside (CATR)–ANT-1 (critical residues to ADP-transport) *versus* inter-atomic distances of three different pristine single walled carbon nanotubes (SWCNT) tested as ANT-1 ligands: a (armchair), c (chiral) and z (zig-zag). The numbers between brackets indicate the Hamada indices (*n*, *m*). All distances are expressed in angstroms (Å). The distances for CATR were obtained from Pebay-Peyroula *et al.* (2003)[37]

Amino acids	CATR distance	a-SWCNT (9, 9) distance	c-SWCNT (5, 4) distance	z-SWCNT (9, 0) distance
Arg 79	2.65	3.81	9.90	2.30
Asn 87	3.12	8.50	2.90	3.80
Lys 91	2.73	3.60	2.44	2.51
Arg 187	3.0	5.02	8.77	3.06
Asp 231	3.0	15.40	20.10	10.60
Arg 234	3.0	5.30	10.70	7.80

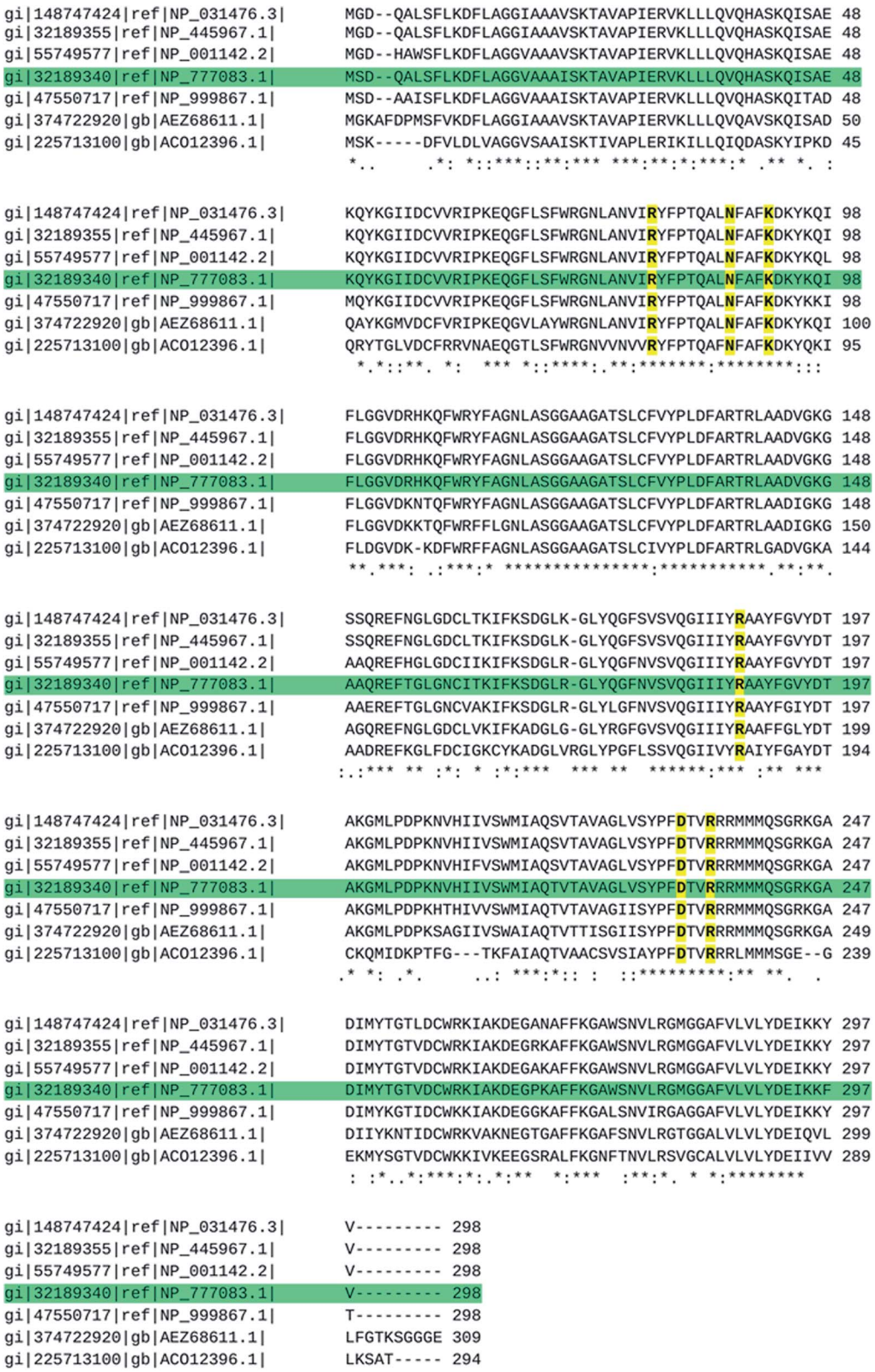

Fig. 4 Alignment of the ANT-1 sequences from bull *Bos taurus* (NP_777083.1), human *Homo sapiens* (NP_001142.2), mouse *Mus musculus* (NP_031476.3), rat *Rattus norvegicus* (NP_445967.1), fish *Danio rerio* (NP_999867.1), copepod *Lepeophtheirus salmonis* (ACO12396.1), and shrimp *Litopenaeus vannamei* (AEZ68611.1). The sequence of *B. taurus* is shown in green and the key amino acids known to interact with the ANT-1 inhibitor carboxyatractiloside are highlighted in yellow (also see Table 1).

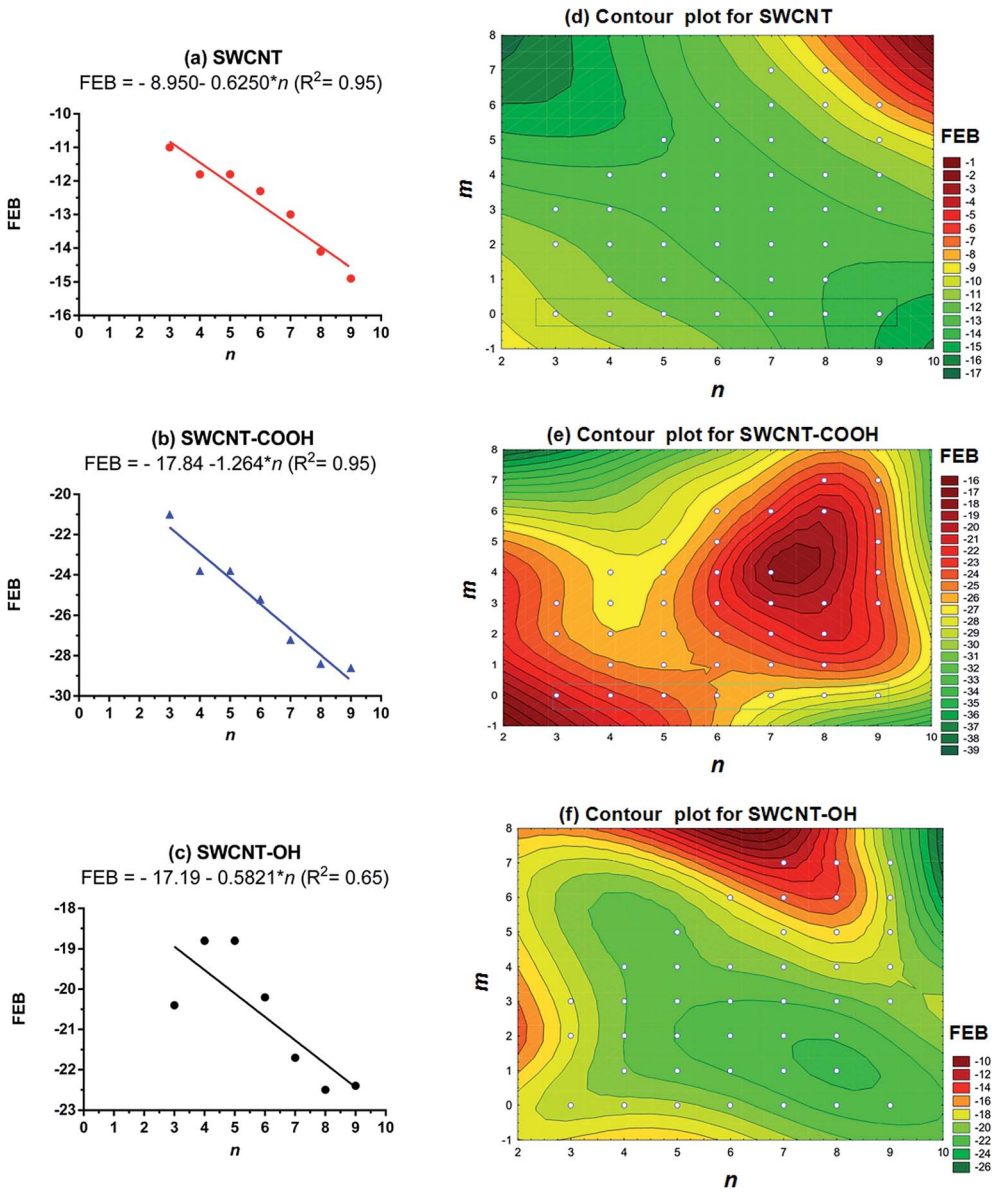

Fig. 5 Linear relationships between free energy binding (FEB, in kcal mol^{-1}) and the *n*-Hamada index for zig-zag ($n > 0$, $m = 0$) carbon nanotubes. (a) Pristine carbon nanotubes (SWCNT), (b) carboxylated carbon nanotubes (SWCNT-COOH), (c) hydroxylated carbon nanotubes (SWCNTs-OH). For (a)–(c), the best linear model is included at the top of each figure, together with the determination coefficient (R^2). In (d)–(f) are depicted the two dimensional 2D-contour plot analysis of FEB values as function of *n* and *m* for SWCNT, SWCNT-COOH and SWCNT-OH, respectively.

(hydrogen, carboxyl and hydroxyl groups) (see Table S1 of ESI S1†). Chirality has been widely used to describe the metallic and/or semiconducting properties, specifically for pristine SWCNT with zig-zag geometry, according to Pumera (2010).[42] Also it is known that *n* index is proportional to the carbon nanotube diameter.[15] As shown in Fig. 6, a higher diameter could induce partial or total distortions in the key amino acids within the active site of ANT-1 resulting in decreased FEB values and increased inhibition of the ADP transport by ANT-1 (see ESI S3† to see the results of the docking experiments used to construct Fig. 6). In addition, we performed control simulations with some examples of zig-zag SWCNT (3.0; 6.0; 9.0) tested, using flexible docking considering the cationic cluster formed by the arginine residues (Arg 79, Arg 187, Arg 231, Arg 234, and Arg 279) of the ANT-1 active site as flexible residues, and the FEB values obtained were very similar (not significant differences; $p > 0.05$) to FEB values from rigid docking simulation when these computational procedures were compared (see Table S2a in ESI 2†). Furthermore, it was verified that a high increase of the exhaustiveness of simulation from 8 to 100 keeping the same FEB results. The modification of the mentioned docking parameters (receptor flexibility and exhaustiveness) only increase the simulation time (see Table S2b in ESI 2†).

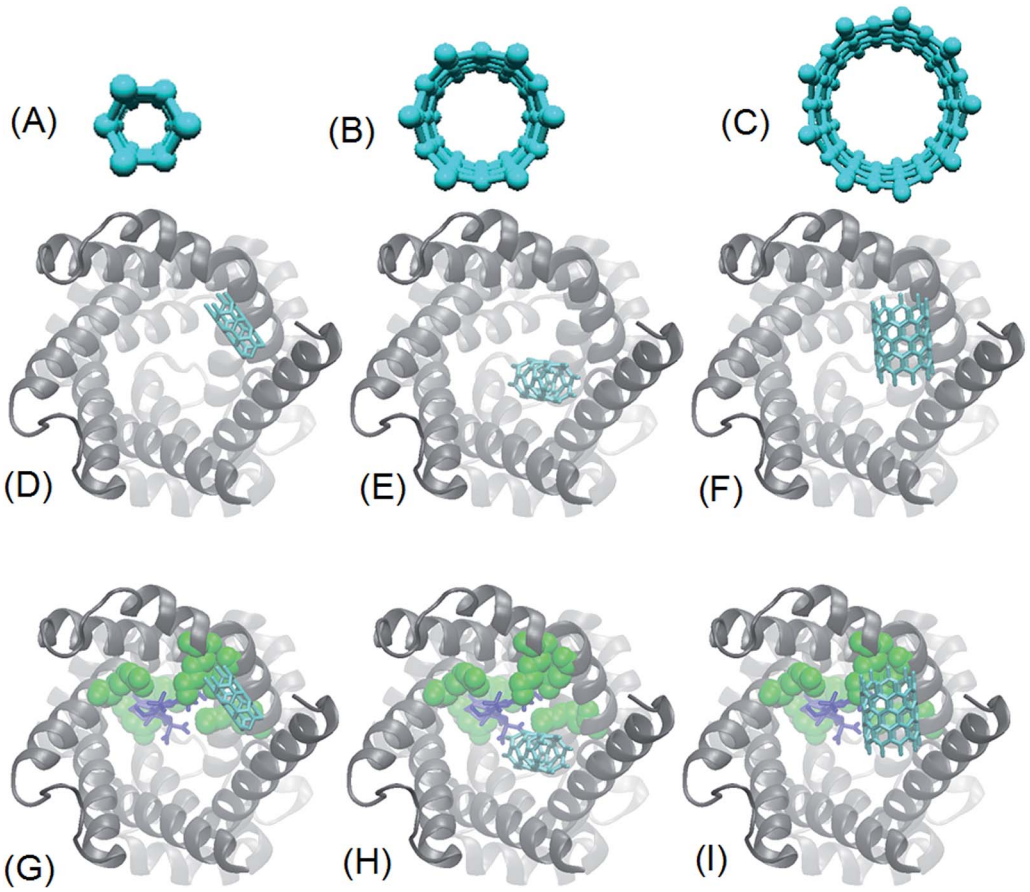

Fig. 6 Images of zig-zag SWCNT with different zig-zag chirality (3, 0); (6, 0); (9, 0) showing the proportional increase in the diameters (2.350; 4.701; and 7.051 Å, respectively) (A–C). Interactions of CNT with bovine ANT-1 protein after docking analysis (D–F). Localization of the zig-zag SWCNT (light blue) and carboxyatractiloside (dark blue) in the same biophysical environment with respect to the key amino acids of the active site in ANT-1 (green) (G–I).

It has been reported that the zig-zag nanotubes are good conductors (similar to metals) or are semiconducting when n is a multiple of 3.[15] Some theoretical studies have shown the existence of symmetry in the distribution of electric charges in the zig-zag SWCNT. In this case, the CNT maintain almost constant charges in the walls and great charge variation at the tips, a phenomenon called "edge effects", that only appear in semiconducting zig-zag topologies of SWCNTs.[43] This electronic feature may play an important role in the interactions of zig-zag SWCNTs with several channel proteins, including ANT-1. In this sense the "edge effects" has not been reported for metallic-armchair SWCNT, wherein the cycloparaphenylene aromatics system of the extreme carbon nanotubes are closed and without tips charge variation. In the case of zig-zag SWCNT-COOH, the high correlation with n could also include the presence of COOH groups that lead to more negative FEB values as shown in Fig. 5. The low correlation ($R^2 = 0.65$) between n and FEB for zig-zag SWCNT-OH indicates that the presence of the OH group is not a good nanodescriptor and suggests that OH-functionalization could modify their electronic properties, reducing the influence of the chiral index n in the interaction energy (FEB) with ANT-1.

Experimentally it has been found that the covalent sidewall functionalization generates sp^3 carbon sites in the CNT, which disrupt the band-to-band transitions of π electrons and cause loss of the novel properties of CNT including their high conductivity and remarkable mechanical properties. Other factors associated with loss of chirality is the presence of defects produced by functionalization of the sidewall including vacancies or pentagon–heptagon pairs (Stone–Wales defects) associated with full or partial covalent functionalization of SWCNT with OH and COOH (Charlier *et al.*, 2002).[14] Recently the use of computational tools focused to theoretical quantitative analysis have been extended to address pharmacological and/or toxicological properties of multiple xenobiotics in biological complex systems, including the interactions at the nanoscale range. In the last years, several articles have been published in the emerging field of Nano-QSAR studies of nanoparticles (NQSAR).[17,18,44,45] In this sense, new chemoinformatics ideas based in PT-QSPR models are very useful for the study of complex molecular systems with simultaneous variation of multiple experimental boundary conditions. In present study, the LDA method was used to seek a PT-QSPR approach (PT-NQSBR) for the prediction of SWCNT–ANT-1 binding

interactions. The PT-NQSBR equation infers the binding of a query SWNCT using the expected values free energy of binding for this type of SWCNT and structural parameters of SWCNT of reference as input. The output of the model is the scoring function $f(\mathrm{FEB})_{\mathrm{query}}$ of the value of the FEB for the mentioned query SWCNT or new SWCNT. The scoring function $f(\mathrm{FEB})_{\mathrm{query}}$ increases for higher values of probability of binding with FEB <-14.7 kcal mol^{-1}. The cutoff value (-14.7 kcal mol^{-1}) represents the FEB value for the interaction of CATR with ANT-1 (calculated in this work, see Fig. 3). The best equation found is indicated below, where M_{w} stands for molecular weight, N_{a} for number of atoms and n and m are Hamada index.

$$f(\mathrm{FEB})_{\mathrm{query}} = -6.5656 - 0.3728\mathrm{FEB}_{\mathrm{query}} - 0.0532m_{\mathrm{query}} - 0.0518n_{\mathrm{query}} - 0.0004\left[M_{\mathrm{w_{query}}} - M_{\mathrm{w_{ref}}}\right] - 0.0035\left[N_{\mathrm{a_{query}}} - N_{\mathrm{a_{ref}}}\right]$$
$$N_{\mathrm{total}} = 18225 \quad \chi^2 = 17603.14 \quad p < 0.005 \qquad (6)$$

This equation is able discriminate the SWCNTs that bind strongly to ANT-1 (FEB < -14.7 kcal mol^{-1}) from those with weak binding (FEB ≥ -14.7 kcal mol^{-1}). The equation showed very high values of accuracy, specificity, and sensitivity in the range of 86.5–99.5% in both the training and external validation series (Table 3). The first input variable of reference is the expected value of $f(\mathrm{FEB})_{\mathrm{ref}} = \langle \mathrm{FEB} \rangle_{\mathrm{new}}$ (average value of FEB) for all SWCNT of the same type as the query SWCNT. The values of $\langle \mathrm{FEB} \rangle_{\mathrm{new}}$ for different types (I, II, III, and IV) of SWCNT are shown in Table 4. The other input variables are the structural variables (m_{query}, n_{query}, $M_{\mathrm{w_{query}}}$, and $N_{\mathrm{a_{query}}}$) for the query SWCNT and the structural variables for the reference SWCNT ($M_{\mathrm{w_{ref}}}$, and $N_{\mathrm{a_{ref}}}$).

The model showed a remarkable efficiency (see Table 3) for the correct classification of different forms of SWCNT having strong or weak binding to ANT-1, showing its potential application in the prediction of nanomaterial–protein interactions. The values of accuracy, specificity, and sensitivity obtained with this LDA model are similar to those obtained with other PT-NQSAR models reported by other authors for the toxicity and ecotoxicity of nanoparticles. For instance, Luan *et al.* (2014) published a PT-NQSAR model that described the cytotoxicity of nanoparticles in multiple experimental conditions.[46] Kleandrova *et al.* (2014) extended the use of PT-NQSPR to studies of the ecotoxicity and cytotoxicity of uncoated and coated nanoparticles under different experimental conditions[47,48] Please note that, as depicted in Fig. 1, the estimated PT-NQSBR model can be employed as a prospective tool or pre-screening filter to SWCNT structure-assigned with predicted low or high affinity to mitochondrial channels like ANT-1 prior to docking experiments.

In order to validate the *in silico* evidences, experiments were performed with mitochondria isolated from hepatopancreas of shrimp *Litopenaeus vannamei*. The profile of oxygen consumption increment after ADP addition (state 3 of respiration-ADP dependent, compare black with red trace). A mild inhibition was registered with CATR (20%, blue light trace in Fig. 7). Maximum inhibition of state 3 of respiration-ADP dependent (26%) was registered with MWCNT-COOH (light green, Fig. 7), a result that fits with the more negative FEB values obtained for this kind of nanotube in the docking experiments (Fig. 3). Taking to account that the oxidative phosphorylation by ATP-synthase is depending of ADP/ATP equilibrium concentrations and the important role of ANT-1 in the ATP-transport to cytosol in physiological normoxic conditions, the *in vitro* results

Table 4 Average values of parameters for different types of pristine and oxidized-SWCNTs. $\langle \mathrm{FEB} \rangle$ and $\langle M_{\mathrm{w}} \rangle$ represent, respectively, the mean value of free binding energy (FEB, in kcal mol^{-1}) according to ANT-1 interaction and the molecular weight for each nanotube type. Type and funct. indicate if the SWCNTs are pristine (–H) or functionalized (–COOH or –OH)

Class	$\langle \mathrm{FEB} \rangle$	$\langle M_{\mathrm{w}} \rangle$	Type	Funct.	Conductivity
I	−12.3	1127.9	Pristine	H	Metallic-SWCNT Semi-metallic-SWCNT
II	−12.7	1096.1	Pristine	H	Semi-conducting-SWCNT
III	−24.6	4778.5	Oxidized	COOH	No conducting properties
IV	−19.9	3507.1	Oxidized	OH	No conducting properties

Table 3 Results of the LDA analysis using a PT-QSBR model that discriminates SWCNT strong binding interactions (FEB < -14.7 kcal mol^{-1}) from SWCNT weak interactions (FEB ≥ -14.7 kcal mol^{-1}) to protein ANT-1. The data in the table indicate the statistical parameters (stat. param.) for specificity, sensitivity and accuracy for both the training data set (for model estimation) and the validation data set (for model evaluation). In each case, the numbers of cases correctly or incorrectly classified are indicated in the table. FEB stands for Free Binding Energy

			Observed values	
Training	Statistical parameter		$(\mathrm{FEB} \geq -14.7)_{\mathrm{pred}}$	$(\mathrm{FEB} < -14.7)_{\mathrm{pred}}$
$(\mathrm{FEB} \geq -14.7)_{\mathrm{obs}}$	Specificity	86.59%	4560	706
$(\mathrm{FEB} < -14.7)_{\mathrm{obs}}$	Sensitivity	99.64%	30	8373
Total	Accuracy	94.62%		
Validation				
$(\mathrm{FEB} \geq -14.7)_{\mathrm{obs}}$	Specificity	86.55%	1518	236
$(\mathrm{FEB} < -14.7)_{\mathrm{obs}}$	Sensitivity	99.50%	14	2788
Total	Accuracy	94.51%		

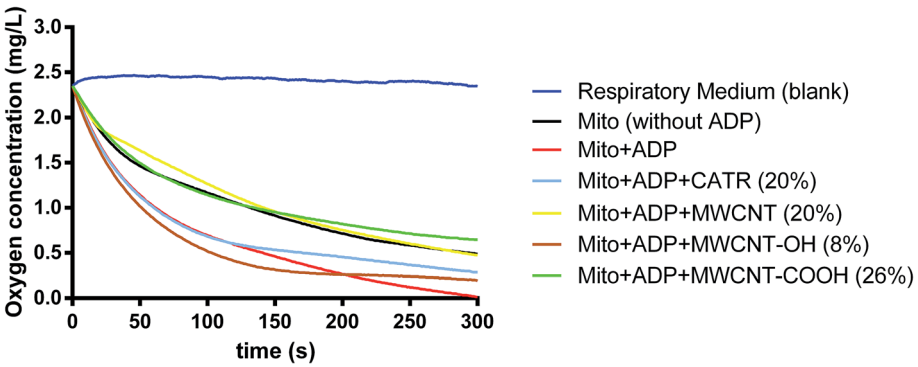

Fig. 7 Profiles of mitochondrial oxygen consumption of isolated mitochondria from shrimp *Litopenaeus vannamei* after ADP addition (state 3 of respiration-ADP dependent), compare black (minimum) with red (maximum) trace. A mild inhibition was registered with carboxyatractiloside (CATR) (20%, blue light trace). MWCNT-COOH (light green) induced maximum inhibition of state 3 of respiration-ADP dependent (26%), followed by MWCNT-pristin (20%; yellow trace) and by MWCNT-OH (8%; brown trace).

suggest potential toxicity for shrimp mitochondria. The results of this case study suggest that the severity of inhibition of the mitochondrial ADP-transport, should depend primarily of the CNT-electronic nanodescriptors as type of functionalization (H, OH, COOH) considering the following order according to the severity of state 3 inhibition: MWCNT-COOH (26%) > MWCNT-(H) (20%) > MWCNT-OH (8%).

Recent experimental evidences using oxidized-CNT porin have show the high potential of carboxylated-SWCNT as synthetic analogues of biological membrane channels with high efficiency and selectivity for transporting ions and molecules.[53,54] In this regard carboxylated-CNTs can spontaneously insert into cellular and mitochondrial membrane lipid bilayers to form channels that exhibit a unitary conductance of 70–100 picosiemens under physiological conditions and at the same time the negative charge of (COO^-)-moiety of carboxylated-CNT could create electrostatic barrier for the anions passage like ADP^{3-} through the positive amines of Arg or Lys residues present at the bottom of ANT-1 cavity as mentioned above.[37,53]

According to *in silico* and experimental physiological results, the CNT-functionalization type (COOH > H > OH) can be considered a relevant CNT-nanodescriptor to explains the ANT-1 biochemical interactions in this context. By the other hand, ANT-1 may be used as a good model for theoretical binding studies because of their special electrostatics properties due to the accumulation of positively charged residues near the binding site that are similar to other cellular and sub-cellular molecular carriers and in this way address structure-relationship studies for new carbon nanomaterials.[49–53]

4 Conclusions

The presence of zig-zag topology and COOH functionalization are geometric and toxicophoric SWCNT-nanodescriptors useful to describe their interactions with ANT-1. In terms of FEB, the interactions based on these SWCNT-nanodescriptors were shown to be stronger than the specific ANT-1 inhibitor carboxyatractiloside. However, some geometric and electronic properties as armchair configuration, chirality and OH functionalization of SWCNT are uncorrelated with the ANT-1 affinity. The use of the Docking Simulation with Virtual Screening Framework combined with new concepts of Nano-QSBR-Perturbation Theory opens several avenues for exploring the SWCNT biological interaction (protein channels nanotoxicity) and their toxicodynamic properties on mitochondrial bioenergetics through ADP transport modulation, which have not been described in the literature currently for any carbon nanomaterial. In this sense, the knowledge of the SWCNT structural requirements involved in the ANT-1-interactions contributes to the rational design of novel carbon nanomaterials with higher benefit/risk relationships, adding to the development of new emerging areas such as nanomedicine, computational nanotoxicology and comparative mitochondrial physiology. Finally, these *in silico* evidences open a gate for the use of chemo-informatics tools linked to experimental biochemical models for making regulatory decisions in nanotoxicology, allowing the prediction/assessment of human health impact and environment risks.

Acknowledgements

J. M. Monserrat and W. Wasiliesky Jr are productivity fellows from CNPq (process number PQ 307880/2013-3 and PQ 310993/2013-0). Part of this study was supported with funds of CNPq (Projects numbers 552131/2011-3 and 452088/2015-1) given to J. M. Monserrat. K. Machado acknowledges the support from CNPq (Process number 477462/2013-8). M. González-Durruthy receives a Doctoral fellowship (PEC-PG Program-Edital 062/2013) from Brazilian Agencies CAPES and CNPq. Authors would like to acknowledge the support from CEMESUL-FURG for logistical support in carbon nanotubes characterization. J. M. Monserrat dedicates this study to the memory of A. J. Monserrat for all the years of kindness and friendship.

References

1 M. Foldvari and M. Bagonluri, *Nanomedicine*, 2008, **4**, 183–200.

2 A. A. Shvedova, A. Pietroiusti, B. Fadeel and V. E. Kagan, *Toxicol. Appl. Pharmacol.*, 2012, **261**, 121–133.
3 M. Rarey, B. Kramer, T. Lengauer and G. Klebe, *Curr. Opin. Struct. Biol.*, 1996, **6**, 402–406.
4 X. Y. Meng, H. X. Zhang, M. Mezei and M. Cui, *Curr. Comput.-Aided Drug Des.*, 2011, **7**, 146–157.
5 T. Cheng, Q. Li, Z. Zhou, Y. Wang and S. H. Bryant, *AAPS J.*, 2012, **14**, 133–214.
6 K. R. Valasani, G. Hu, M. O. Chaney and S. S. Yan, *J. Chem. Inf. Model.*, ACS Publications, 2014, vol. 54, pp. 902–912.
7 B. Q. Wei, W. A. Baase, L. H. Weaver, B. W. Matthews and B. K. Shoichet, *Nature*, 2004, **432**, 862–865.
8 X. Wang, *Toxicol. In Vitro*, 2012, **26**, 799–806.
9 L. M. Knobeloch, G. A. Blondin and J. M. Harkin, *Arch. Environ. Contam. Toxicol.*, 1990, **44**, 661–668.
10 K. Banchhor, A. Patel, J. Choubey and M. K. Verma, *International Journal of Computer Applications*, 2013, **1**, 40–46.
11 M. Calvaresi and F. Zerbetto, *ACS Nano*, 2009, **4**, 2283–2299.
12 K. H. Park, M. Chhowalla, Z. Iqbal and F. Sesti, *J. Biol. Chem.*, 2003, **278**, 50212–50216.
13 G. Zuo, Q. Huang, G. Wei, Z. Zhou and H. Fang, *ACS Nano*, 2010, **4**, 7508–7514.
14 J. C. Charlier, *Acc. Chem. Res.*, 2002, **3**, 1063–1069.
15 N. Hamada, S. Sawada and A. Oshiyama, *Phys. Rev. Lett.*, 1992, **68**, 1579–1581.
16 R. Saito, M. Fujita, G. Dresselhaus and M. S. Dresselhaus, *Appl. Phys. Lett.*, 1992, **60**, 2204–2206.
17 T. Puzyn, D. Leszczynska and J. Leszczynski, *Small*, 2009, **5**, 2494–2509.
18 R. Tantra, C. Oksel, T. Puzyn, J. Wang, K. N. Robinson, X. Z. Wang, C. Y. Ma and T. Wilkins, *Nanotoxicology*, 2014, **1**, 1–7.
19 H. Gonzalez-Díaz, S. Arrasate, A. Gomez-San Juan, N. Sotomayor, E. Lete, L. Besada-Porto and J. M. Ruso, *Curr. Top. Med. Chem.*, 2013, **13**, 1713–1741.
20 F. Dehez and E. Pebay-Peyroula, *J. Am. Chem. Soc.*, 2008, **130**, 12725–12733.
21 Y. Wang and E. Tajkhorshid, *Proc. Natl. Acad. Sci. U. S. A.*, 2008, **105**, 9598–9603.
22 K. A. Manuel, *J. Cell Biol.*, 1999, **147**, 1493–1501.
23 F. Palmieri and L. Pierri, *FEBS Lett.*, 2010, **584**, 1931–1939.
24 T. Kato, *Nanotoxicology*, 2013, **7**, 452–461.
25 C. R. Pestana, C. H. Silva, A. S. Uyemura, A. C. Santos and C. Curti, *J. Biol.*, 2010, **42**, 329–335.
26 F. Di Lisa, A. Carpi, V. Giorgio and P. Bernardi, *Biochim. Biophys. Acta*, 2011, **1813**, 1316–1322.
27 S. George, T. Xia, R. Rallo, Y. Zhao, Z. Ji, S. Lin, X. Wang, H. Zhang and B. France, *ACS Nano*, 2007, **5**, 1805–1817.
28 H. M. Berman, J. Westbrook, Z. Feng, G. Gilliland, T. N. Bhat, H. Weissig, I. N. Shindyalov and P. E. Bourne, *Nucleic Acids Res.*, 2000, **28**, 235–242.
29 H. Yorikawa and S. Muramatsu, *Phys. Rev.*, 1995, **B52**, 2723.
30 O. Trott and A. J. Olson, *J. Comput. Chem.*, 2010, **31**, 455–461.
31 C. H. Da Silveira, *Proteins*, 2009, **74**, 727–743.
32 T. J. Ewing, S. Makino, A. G. Skillman and I. D. Kuntz, *J. Comput.-Aided Mol. Des.*, 2001, **15**, 411–428.
33 J. J. Irwin, T. Sterling, M. M. Mysinger, E. S. Bolstad and R. G. Coleman, *J. Chem. Inf. Model.*, 2012, **52**, 1757–1768.
34 M. L. Verdonk, J. C. Cole, M. J. Hartshorn, C. W. Murray and R. D. Taylor, *Proteins*, 2003, **52**, 609–623.
35 O. Martinez-Cruz, F. Garcia-Carreño, A. Robles-Romo, A. Varela-Romero and A. Muhlia-Almazan, *J. Bioenerg. Biomembr.*, 2011, **43**, 119–133.
36 L. R. Jimenez-Gutierrez, S. Uribe-Carvajal, A. Sanchez-Paz, C. Chimeo and A. Muhlia-Almazan, *J. Bioenerg. Biomembr.*, 2014, **46**, 189–196.
37 E. Pebay-Peyroula, C. Dahout-Gonzalez, R. Kahn, V. Trézéguet, G. J. Lauquin and G. Brandolin, *Nature*, 2003, **426**, 39–44.
38 OECD Principles for the validation, for regulatory porposes of (Quantitative) Structure Activity Relationship Model, http://www.oecd.org/, accessed 9/03/2016.
39 ISO/TC 229, *Nanotechnology*, 2011, 1–11, Draft 4.
40 X. R. Xia, N. A. Monteiro-Riviere and J. E. Riviere, *Nat. Nanotechnol.*, 2010, **5**, 671–674.
41 S. Das, R. Wong, N. Rajapakse, E. Murphy and C. Steenbergen, *Circ. Res.*, 2008, **103**, 983–991.
42 M. Pumera, *Chem. Soc. Rev.*, 2010, **39**, 4146–4157.
43 F. Buonocore, F. Trani, D. Ninno, A. Di Matteo, G. Cantele and G. Iadonisi, *J. Nanotechnol.*, 2008, **19**, 025711.
44 S. Kar, A. Gajewicz, T. Puzyn and K. Roy, *Toxicol. In Vitro*, 2014, **28**, 600–606.
45 T. Puzyn, B. Rasulev, A. Gajewicz, X. Hu, T. P. Dasari, A. Michalkova, H. M. Hwang, A. Toropov, D. Leszczynska and J. Leszczynski, *Nat. Nanotechnol.*, 2011, **6**, 175–178.
46 F. Luan, V. V. Kleandrova, H. Gonzalez-Diaz, J. M. Ruso, A. Melo, A. Speck-Planche and M. N. Cordeiro, *Nanoscale*, 2014, **6**, 10623–10630.
47 V. V. Kleandrova, F. Luan, H. Gonzalez-Diaz, J. M. Ruso, A. Speck-Planche and M. N. Cordeiro, *Environ. Sci. Technol.*, 2014, **48**, 14686–14694.
48 L. Feng, V. V. Kleandrova, H. González-Díaz, J. M. Ruso, A. Melo, A. Speck-Planche and M. N. Cordeiro, *Nanoscale*, 2014, **6**, 10623–10630.
49 R. Riccio, H. Aquila and M. Klingenberg, *FEBS Lett.*, 1975, **56**, 133–138.
50 M. Klingenberg, *Biochim. Biophys. Acta*, 2008, **1778**, 1978–2021.
51 A. J. Robinson and E. R. Kunji, *Proc. Natl. Acad. Sci. U. S. A.*, 2006, **103**, 2617–2622.
52 Z. Yang, Y. Zhang, Y. Yang, L. Sun, L. Han, H. Li and C. Wang, *Nanomedicine*, 2010, **6**, 427–441.
53 S. Shityakov and C. Förster, *Int. J. Comput. Biol. Drug Des.*, 2013, **6**, 351–352.
54 J. Geng, K. Kim, J. Zhang, A. Escalada, R. Tunuguntla and L. R. Comolli, *Nature*, 2014, **514**, 612–615.

Artigo 3: QSPR/QSAR-based Perturbation Theory approach and mechanistic electrochemical assays on carbon nanotubes with optimal properties against mitochondrial Fenton reaction experimentally induced by Fe^{2+}-overload

Carbon 115 (2017) 312–330

Contents lists available at ScienceDirect

Carbon

journal homepage: www.elsevier.com/locate/carbon

QSPR/QSAR-based Perturbation Theory approach and mechanistic electrochemical assays on carbon nanotubes with optimal properties against mitochondrial Fenton reaction experimentally induced by Fe^{2+}-overload

Michael González-Durruthy [a, b, c, d, *], Micheli Castro [a, b], Silvana Manske Nunes [a, b], Juliane Ventura-Lima [a, b, c, d], Luciane C. Alberici [e], Zeki Naal [e], David T. Atique-Sawazaki [e], Carlos Curti [e], Caroline Pires Ruas [f], Marcos A. Gelesky [f], Kunal Roy [g], Humberto González-Díaz [h, i, **], José M. Monserrat [a, b, c, d, ***]

[a] Institute of Biological Sciences (ICB), Universidade Federal do Rio Grande - FURG, 96270-900, Rio Grande, RS, Brazil
[b] ICB-FURG Post-Graduate Program in Physiological Sciences, 96270-900, Rio Grande, RS, Brazil
[c] National Institute of Carbon Nanomaterial Science and Technology, Belo Horizonte, MG, Brazil
[d] Nanotoxicology Network (MCTI/CNPq), Rio Grande, RS, Brazil
[e] Department of Physic-Chemistry, College of Pharmacy of Ribeirão Preto, University of São Paulo (USP), 14040-903, Ribeirão Preto, SP, Brazil
[f] Post-Graduate Program in Technological and Environmental Chemistry, 96270-900, Rio Grande, RS, Brazil
[g] Drug Theoretics and Cheminformatics Lab, Division of Medicinal and Pharmaceutical Chemistry, Department of Pharmaceutical Technology, Jadavpur University, Kolkata, 700 032, India
[h] Department of Organic Chemistry II, College of Science and Technology, University of the Basque Country UPV/EHU, 48940, Leioa, Bizkaia, Spain
[i] IKERBASQUE, Basque Foundation for Science, 48011, Bilbao, Bizkaia, Spain

ARTICLE INFO

Article history:
Received 29 October 2016
Received in revised form
15 December 2016
Accepted 1 January 2017
Available online 9 January 2017

Keywords:
Carbon nanotubes
Mitoprotective
Fenton reaction
Dose-response models
Perturbation Theory
QSPR/QSAR

ABSTRACT

In the present study, different *in vitro* and electrochemical protocols were employed to determine the mitoprotective properties of carbon nanotubes family (pristine-CNT, oxidized-CNT) based on free radical scavenging ability against the most aggressive reactive oxygen species (ROS) as hydroxyl radical (·OH) formed by Fenton-Haber-Weiss reaction, which was experimentally induced on isolated rat-liver mitochondria through Fe^{2+} ions overload. The results suggest that the mitochondrial Fenton-inhibition response involves a significant reduction of (·OH) concentration linked to iron-complexing ability of CNT-family, following the order: carboxylated-CNT > pristine-CNT ~ hydroxylated-CNT, without affecting the electrochemical mitochondrial membrane potential in Fe^{2+}-overloaded mitochondria.

Besides, a new *in silico* dose-response QSPR-model was applied suggesting reliability for the CNT-dose-effect series predictions towards the mitochondrial Fenton ROS-inhibition with excellent linear behavior on the training set (R^2 = 0.901; $R^2(adj.)$ = 0.901; $Q^2(LOO\text{-}CV)$ = 0.901) and test set (Q^2_{F1} = 0.9008; Q^2_{F2} = 0.9008; Q^2_{F3} = 0.9009; *MAE* = 21.213) for internal and external validation respectively, with $p < 0.05$ for all regression coefficient for > 70,000 data points. Lastly, these experimental and theoretical evidences open a gate to the rational design of novel carbon nanomaterials toward mitochondrial nanomedicine based redox-targeting as an alternative of treatment of several chronic diseases where pathological Fenton-reaction mechanisms have been directly involved.

* Corresponding author. Institute of Biological Sciences (ICB), Universidade Federal do Rio Grande -FURG, 96270-900, Rio Grande, RS, Brazil.
** Corresponding author. Department of Organic Chemistry II, College of Science and Technology, University of the Basque Country UPV/EHU, 48940, Leioa, Bizkaia, Spain.
*** Corresponding author. Institute of Biological Sciences (ICB), Universidade Federal do Rio Grande -FURG, 96270-900, Rio Grande, RS, Brazil.
E-mail addresses: gonzalezdurruthy.furg@gmail.com (M. González-Durruthy), humberto.gonzalezdiaz@ehu.es (H. González-Díaz), josemmonserrat@pq.cnpq.br (J.M. Monserrat).

http://dx.doi.org/10.1016/j.carbon.2017.01.002
0008-6223/

1. Introduction

The mitochondrial dysfunction associated to oxidative stress conditions is emerging as an important pathophysiological factor in a large number of neurodegenerative (Alzheimer, Parkinson), cardiovascular diseases and the most aggressive phenotypes of cancer. The mechanism appears to involve the catalytic role of iron, the most abundant metal in the human body (approximately 4 g in normal adult humans), which exists in two ways: non-chelatable iron that mainly acts as a co-factor for relevant proteins such as the main mitochondrial ROS-generated respiratory complexes (I, III) and chelatable iron as free ferrous (Fe^{2+}) [1]. Under certain physiopathological conditions, like Fe^{2+} overload, mitochondria rapidly accumulates ferrous ions via mitochondrial (Ca^{2+}, Fe^{2+}) uniporter-sensitive to ruthenium red (RR) [2,3]. Fe^{2+} ions in mitochondrial matrix when combined with hydrogen peroxide (H_2O_2) from a radical superoxide anion ($O_2^{\bullet -}$) catalytic-dismutation through superoxide dismutase enzyme (Mn-SOD), can induce the reactive oxygen species (ROS) formation as hydroxyl ($\cdot OH$) radical, considered the most aggressive oxygen radical formed through Fenton-Haber-Weiss reaction, which is strongly associated to significant weakness of antioxidant defense system, dissipation of mitochondrial membrane potential and events like ferroptosis, an iron-dependent form of non-apoptotic cell death [1]. Some of the mechanisms of mitotoxicity through Fenton pro-oxidant conditions include mitochondrial permeability transition pore-iron dependent (MPTP), a key event for the induction of pathological conditions [2–5].

Carbon nanotubes (CNT) have rapidly become one of the most widely studied nanomaterials, essentially for their unique physicochemical and biological properties that increase new applications in nanomedicine as active principles and pharmaceutical excipients of drug delivery systems [5]. Under this context, new mitoprotective therapies based on free radical scavenging activity using CNT, grant more selectivity and efficacy as therapeutic strategies for several pathologies.

On the other hand, the induction of reactive oxygen species has been considered in several studies as one of the main mechanisms implicated in CNT nanotoxicity [6]. In fact, some *in vitro* studies have shown that CNT can be more cytotoxic after its accumulation in the mitochondrial matrix [6].

However, it is possible to reduce CNT cytotoxicity through covalent functionalization on CNT-tips or CNT-walls through chemical oxidation as in the case of oxidized-CNT (hydroxylated-SW/MWCNT and/or carboxylated-SW/MWCNT). The interaction of hydroxyl and/or carboxyl-motifs with the porphyrin-metal centers (Fe^{2+}/Fe^{3+}) of mitochondrial complex can form stable unions wherein the ligand acquires a new redox center that mimics antioxidant enzymes such as superoxide dismutase, thus eliciting mitoprotective effects. In this regard, it has been recognized that these oxidized-motifs (OH, COOH) have potential ability to chelate metals ions (as Fe^{2+}) in iron overload pro-oxidant condition. In addition, oxidized-motifs (OH, COOH) are more easily detoxified by redox multienzymatic cellular mechanisms, including horseradish peroxidase (HRP) and hydrogen peroxide (H_2O_2) [7–9]. Latest works published have shown that ROS (as •OH-hydroxyl radical) can interact with pristine-MWCNT and carboxylated-MWCNT inducing layer-by-layer carbon nanotube-degradation in the presence of HRP and H_2O_2 (by hydroxylation and carboxylation associated to several oxygen functionalized-defects generated in the tips and walls graphitic-structure) [9]. But in this context, it is important to note that new groups generated as oxidized-motifs (OH, COOH) retain their potential ability to chelate metals ions (as Fe^{2+}) in iron overload pro-oxidant condition.

The potential biomedical applications of CNT have increased the interest in comparison to other carbon nanomaterials [9]. Recent work using pristine and oxidized multi walled carbon nanotubes on human liver cell line L02 showed evidence of ameliorated cytotoxicity related to oxidative stress reduction for MWCNT-COOH (cytoprotective effect) when compared with similar pristine-MWCNT, which induced oxidative stress, membrane damage, cell cycle arrestment at G0/G1, caspase-8 activation and L02 apoptosis increase [10]. Other studies published by Lucente-Schultz et al. (2009) [11] showed that SWCNT and ultrashort SWCNTs (US-SWCNTs) induce little acute cytotoxic response or no deleterious effect in human renal epitelial and HepG2 liver cells, suggesting oxygen radical absorbance capacity (ORAC assay) associated to SWCNT-functionalization with phenolic antioxidant derivatives. Following this idea, Ye She-Fang et al. (2009) [12] showed that the pre-treatment of adenocarcinomic human alveolar basal epithelial cells (A549 cells) with antioxidants prior to adding MWCNTs decreased ROS production and abrogated expression of IL-8 mRNA.

In this sense, very interesting works on free radical scavenging ability of pristine and oxidized carbon nanotubes have been performed by Galano et al. (2008)[13], using semi-empirical methods based on Functional Density Theory (DFT), suggesting that the CNT-free radical scavenging activity is particularly important for hydroxyl-Fenton radical ($\cdot OH$) and others, according to the type of functionalization present at the order oxidized-CNT (carboxylated-CNT > hydroxilated-CNT) > pristine-CNT [12–16].

According to this idea, electrochemical tools based on cyclic voltammetry (CV) have been applied efficiently in mechanistic studies of redox process like electro-induced Fenton-Haber-Weiss reactions [17,18]. These techniques can be useful particularly when combined with chemical-biological assays due to their accuracy to elucidate ROS-mechanism based in chemical reaction induced by electron transfer, which involves electrocatalytic processes as addition and/or dissociation of ligand by immobilization/coordination with metallic center as possible mitochondrial redox effects of CNT [19,20]. According to this idea, electrocatalized biochemical processes as Fenton reaction considers that the thermodynamic free energy variations to ligand-metalic centers is proportional to the current (I(μA)) and the potential difference (ΔE (V)) in the redox biochemical processes [21–23].

The discovery and development of new carbon nanomaterials is a complex and expensive process in terms of time and money. Thereby, the novel quantitative structure-activity relationship paradigm (QSAR), in the nanoscience context, has become an important tool for the nanomaterials optimization with less impact on health and environment [24]. Herein, one important step in QSAR/QSPR is to express structural features in a quantitative way which is not always straightforward [25–28]. In this sense, quantitative structure-property relationships (QSPR model) can be seen as a function that predicts the structure of a single or complex systems using parameters that numerically describe its properties. To this end, Gonzalez-Díaz et al. (2013) [26], formulated a general-purpose PT-QSPR method combining QSPR/QSAR approach and Perturbation Theory (PT). PT-QSPR models are very useful for the study of complex molecular systems with simultaneous multiple experimental boundary conditions. In fact, González-Díaz et al. (2013) [26] have applied PT-QSPR analysis in studies dealing with chemical reactivity, drug metabolism, immunotoxicity assays, metabolic networks, metal nanoparticles and also CNT. Toropova et al. (2016) [29] published a Nano-QSAR model to address the genotoxicity of pristine multi-walled carbon nanotubes in multiple experimental conditions. Recently, González-Durruthy et al. (2015) [30] using a PT-NanoQSPR approach was able to predict the inhibition of mitochondrial swelling (MPTP-mitoprotective activity) induced by oxidized CNT in multiple experimental conditions. Their results suggested that oxidized-CNT could modulate the

mitochondrial ROS-production involved in mitochondrial dysfunction [30].

The main assumption of QSAR/QSPR models in general is that similar molecules have similar properties. Consequently, small changes ("*perturbations*") in the structural system should correlate linearly with small changes on the values of their properties (biological activities). In this regard, QSPR-perturbation approaches start knowing the exact solution of a problem (for instance a physic-chemical or biological property) and continue adding small terms to predict a solution to a related problem without a known exact solution [31–34].

In this context, currently there are no precedents for the application of this methodology combining experimental methods in isolated rat-liver mitochondria, chemo-informatics ideas to predict the potential therapeutic effects of CNT as ROS-mitoprotective agents through the inhibition of Fenton reaction and mechanistic explanations based on electrochemical assays.

Taking into account the facts aforementioned, the purpose of this study was to evaluate and predict the potential of CNT-family as radical scavengers against the most deleterious reactive oxygen species like hydroxyl free radical (·OH) formed by Fenton-Haber-Weiss reaction experimentally induced by Fe^{2+} ions overload on isolated rat-liver mitochondria (RLM). This biochemical/pharmacodynamic endpoint can be experimentally measured as arbitrary fluorescence unit (or AFU %) and modeled applying new chemoinformatic concepts on QSPR/QSAR-Perturbation Theory approaches as a function of CNT-functionalization, CNT-diameter and also optimal experimental conditions of exposure like CNT-concentration and exposure time. This model can be regarded as a generalized model for making predictions of free radical scavenging ability of other functionalized CNTs with different physical (such as diameter) and experimental (such as CNT concentration and exposure time) specifications not used in model development, thus aiding in design of new functionalized CNTs of potential therapeutic benefit. The acceptability and applicability of the QSPR/QSAR models for such prediction purposes have been statistically judged using different internal and external validation tests.

2. Experimental

2.1. Sample preparation

2.1.1. Reagents and solutions

Sucrose, ethylene-glycol-bis (β-aminoethyl)-N,N,N′,N′-tetra-acetic acid (EGTA), $Fe(NH4)_2(SO4)_2 \times 6H_2O$, $[Fe_2(citrate)_2]^{2-}$ solutions with 1:2 iron–citrate ratio, $FeSO_4$, Triazine, KCL, H_2O_2 solution in water, 30–32 wt%, semiconductor grade, 99.999% trace metals basis, sodium citrate ($Na_3C_6H_5O_7$), potassium succinate (plus 2 μM rotenone), K_2HPO_4, piperazine-N-2-ethanesulfonic acid (Hepes), Amplex Red (10-acetyl-3,7-dihydroxyphenoxazine sensitive fluorescent probe for H_2O_2 from Invitrogen), horseradish peroxidase (HPR, Sigma), carbonyl cyanide 3-chlorophenylhydrazone (CCCP) stock solution of 1 mM, chloroacetic acid solution + KCL 1 M, $Fe(NO_3)_3$-Na_2H_2EDTA to form [Fe^{3+}/EDTA] equimolar mixture solution (0.4 mM) (1:1), Biuret reagent, safranine O; 5,5′,6,6′-tetrachloro-1,1′,3,3′-tetraethyl-benzimidazolcarbocyanine iodide (JC-1 probe), calcium green stock solution of 150 nm. All other reagents were commercial products of the highest purity grade available. Carbon nanotubes like pristine-CNT (CNT1) and hydroxylated-CNT (CNT-OH: CNT2; CNT3, CNT4, CNT5) and carboxylated-COOH (CNT-COOH: CNT6, CNT7, CNT8, CNT9) with very low conductivity and semi-metallic properties were provided by Cheaptubes Company (http://cheaptubes.com/shortohcnts.htm) (see Table 1 for details).

For ROS-mitochondrial assays CNT was dispersed in dimethyl sulfoxide (DMSO: 900 μL) and ultrapure Milli Q water (100 μL) in individual stock suspensions at concentration of 1 mg/ml [35].

2.1.2. Carbon nanotubes characterization

Transmission Electron Microscope (TEM, Tecnai G2-12 - SpiritBiotwin FEI - 120 kV) was employed to characterize the morphology of pristine and oxidized carbon nanotubes (see in Fig. 1).

CNTs were synthesized by CCVD and purified/functionalized using a concentrated acid mixture of H_2SO_4:HNO_3 mixed (2:1). The pristine and oxidized multi-walled carbon nanotubes were formed by 3 concentric tubes with distance of ~0.34 nm between each wall. The content of metallic impurities in all the samples was less than 1%. The proportions of CNT-metal impurities were determined by using energy dispersive x-ray (EDS) analysis. The metal impurities of MWNT and SWNT with diameter (D) <8 nm (CNTs 1, 2, 8 and 9) including their −OH and −COOH derivatives are the same: Co, Al, Cr. For MWNT-OH and −COOH with diameter between 10 and 20 nm (CNTs 4 and 7) are Si and Al. For larger diameter MWNT (30–50 nm) (CNTs 5 and 6), the metallic impurities and their derivatives are Al, Si. For more details see Supporting Information (S1) about EDS characterization. For the final concentrations range employed in present study (0.5–5 μg/ml) and with the aim of preventing CNT-agglomeration for ROS-assays, it was employed tip-sonication regime during 5–10 min that prevents the CNT-exfoliation into individual CNT. In this sense, the employed sonication time is known to generate a non-agglomerated suspension in a monodisperse state at concentrations below 100 μg/ml according to Bergin et al. (2010) [34–36]. The sonication power was 9.3 W, with an energy input of 16.7 kJ at 25 °C using a Ultronique/Eco-sonics Q-3.0/40A sonicator. Afterwards, samples were stirred for 10–15 min. The resulting diluted suspensions were cooled to room temperature and filtered through a 0.22 μm polycarbonate membrane (Millipore, USA), before exposure to mitochondria suspensions.

2.2. Animal welfare

Male *Wistar* rats (4-month-old; approx. 150 g.) received food and water *ad libitum*. They were kept in plastic cages with wire tops in a light-controlled room (12:12 h light–dark cycle) at 22 ± 3 °C before starting the study in accordance with the animal care and experimental procedures based on the Directive 2010/63/EU of the European Parliament and of the Council on the protection of animals used for scientific purposes, and were also approved by the Animal Care and Use Committee of the School of Pharmaceutical Sciences of Ribeirão Preto (CEUA-FCFRP) (license and registration Number: 01.0263.2014).

2.3. Isolation of rat-liver mitochondria (RLM)

Mitochondria were isolated throughstandard differential centrifugation [35]. Male *Wistar* rats weighing approximately 150 g were euthanized by decapitation; livers (10–15 g) were immediately removed, sliced in medium (50 ml) consisting 250 mM of sucrose, 1 mM of ethyleneglycol-bis (β-aminoethyl)-N,N,N′,N′-tetraacetic acid (EGTA) and 10 mM of HEPES-KOH, pH 7.2, and homogenized three times for 15 s at 1 min intervals using a Potter-Elvehjem homogenizer. Mitochondria were isolated by standard differential centrifugation. For this purpose, homogenates were centrifuged (580×*g*, 5 min at 4 °C) and the resulting supernatant further centrifuged (10300×*g*, 10 min at 4 °C). Pellets were then suspended in medium (10 ml) consisting of 250 mM sucrose, 0.3 mM of EGTA and 10 mM of HEPES-KOH, pH 7.2, and centrifuged again (3400×*g*, 15 min 4 °C). The final mitochondrial pellet was suspended in medium (1 ml) consisting of 250 mM sucrose and

Table 1
Physic-chemical parameters ($^{i}V_k$) of CNT family.

CNT Properties			W_i (%)		D_i(nm)		L_i (μm)	P_i (%)	C_i S cm^{-1}
n	Type	Function	min	max	min	max			
1	MWCNT	–	–	–	8	8	0.5–2	>95	<1.5
2	Mixed-SW/DWCNT	OH	0	3.96	1	4	0.5–2	>95	<1.5
3	MWCNT	OH	0	3.86	1	8	0.5–2	>95	<1.5
4	MWCNT	OH	3	4	10	20	0.5–2	>95	<1.5
5	MWCNT	OH	1	1.06	30	50	0.5–2	>95	<1.5
6	MWCNT	COOH	0	0.73	30	50	0.5–2	>95	<1.5
7	MWCNT	COOH	3	4	10	20	0.5–2	>95	<1.5
8	SWCNT	COOH	0	2.73	1	4	0.5–2	>95	<1.5
9	MWCNT	COOH	0	3.86	1	8	0.5–2	>95	<1.5

MWCNT = Multiple-Walled, SWCNT = Single-Walled, SW/DWCNT = DWCNT + SWCNT mixture, W_i(%) = Functional groups(OH, COOH)/carbon atoms ratio (%); the properties of the ith Carbon Nanotube (CNT) are D_i = CNT outer diameter, L_i = CNT Length, P_i = Purity, C_i = Electric conductivity.

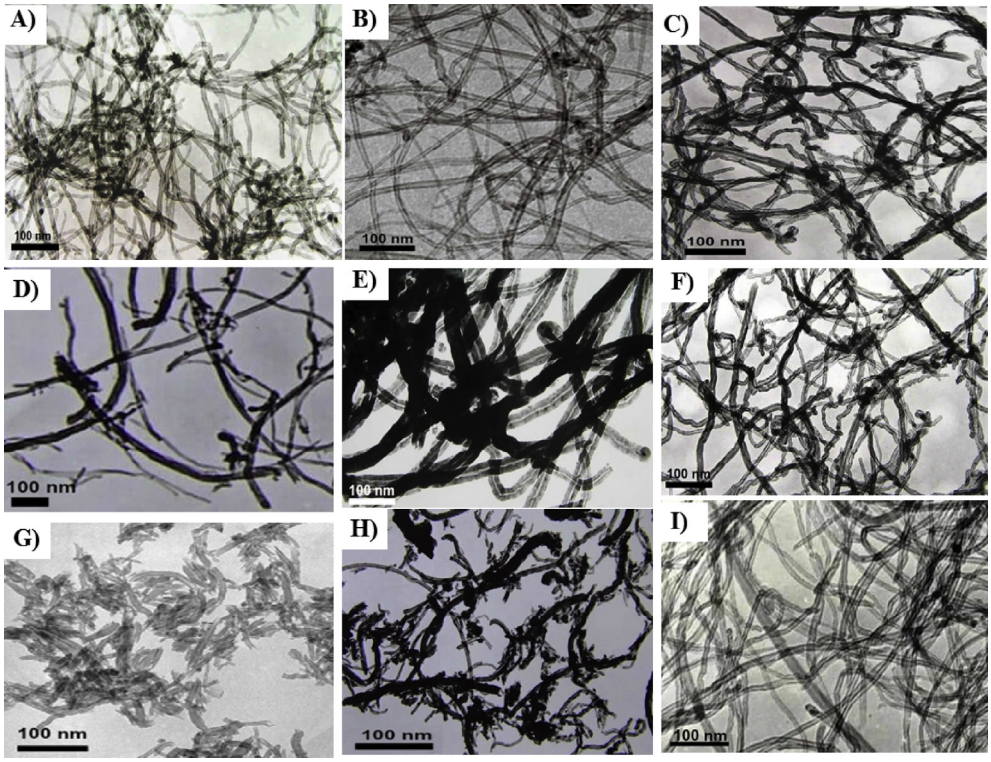

Fig. 1. TEM images of carbon nanotubes used in this study: (A) Pristine-MWCMT (CNT1), (B) SW/DWCNT-OH (CNT2), (C) MWCNT-OH (CNT3), (D) MWCNT-OH (CNT4), (E) MWCNT-OH (CNT5), (F) MWCNT-COOH (CNT6), (G) MWCNT-COOH (CNT7), (H) SWCNT-COOH (CNT8), (I) MWCNT-COOH (CNT9). (A colour version of this figure can be viewed online.)

10 mM of HEPES-KOH, pH 7.2, and used within 3 h. Mitochondrial proteins content (>90%) was determined by the Biuret reaction.

2.4. Standard incubation procedure

Mitochondria liver isolated were energized with 5 mM of potassium succinate (plus 2.5 μM of rotenone) in a standard incubation medium consisting of 125 mM of sucrose, 65 of mM KCl, 2 mM of inorganic phosphate (K_2HPO_4) and 10 mM of HEPES-KOH pH 7.4 at 30 °C [35].

2.5. Determination of mitochondrial H_2O_2-production

The influence of CNT-family on mitochondrial H_2O_2-generation was measured using the Amplex Red Assay for H_2O_2 (Molecular Probes, Eugene, OR). This assay was considered important because the generation of H_2O_2 and the factors associated to the increase of their concentration, are directly involved in the Fenton reaction induction with consequent hydroxyl free radical generation in the presence of Fe^{2+} overload. For this purpose, 1 mg of isolated rat-liver mitochondria were incubated in 1 ml of standard incubation medium and the mitochondria (1 mg of protein/ml) supplemented with 50 μM of Amplex red (a derivative from 10-acetyl-3,7-dihydroxyphenoxazine), which is employed as a specific probe for the measurement of mitochondrial H_2O_2-production based on the reaction with H_2O_2 with 1:1 stoichiometic ratios catalyzed through horseradish peroxidase (HRP) 0.025 μM (mU/ml) to form the colored and highly fluorescent compound resorufin through Amplex red oxidation via two one-electron oxidation with continuous stirring at 37 °C.

Fluorescence of oxidized Amplex red probe (Resorufin) was measured in a Model Hitachi F-4010 spectrofluorimeter (Tokyo, Japan) equipped with a thermostatic cuvette holder and magnetic stirrer at 563/587 nm (slits 5/5 nm) excitation/emission wavelength

pairs, respectively and obtained as arbitrary fluorescence units (*AFU*). In this sense the quantity of mitochondria protein isolated (>90%) was determined through Biuret method. This procedure is very important because the contamination of mitochondrial preparation with cytosolic structures such as peroxisomes, fragments of broken mitochondria can significantly interfere with ROS measurements [35–39]. Previously the spectrofluometric ROS-measurements, it was performed the blanks with each CNT in order to compare with mitochondria exposed to CNT. In this sense, the presence of Stern-Volmer quenching fluorescent processes associated to carbon nanotubes UV–visible optical interferences was not detected at 500–590 nm, according to their semi-metallic properties [20]. Here, it was performed a genuine Fenton reaction-induced model using mitochondrial suspension exposure of an iron chelate $[Fe_2(citrate)_2]^{2-}$ to Fe^{2+} exposure. Sodium citrate ($Na_3C_6H_5O_7$) has been used by its potent chelating activity with a variety of metals as iron $[Fe_2(citrate)_2]^{2-}$ it was prepared with $Fe(NH4)_2(SO4)_2 \times 6H_2O$ which is soluble at neutral pH and a potent catalyst of Fenton reaction with 2–3 free iron (Fe^{2+})-ligands. In this sense, the optimal ferrous ions experimental concentration was established at 20 μM for all biochemical assays to study the Fenton chemistry, considering that the physiological concentration is 0.5 μM in order to reproduce mitochondrial ferrous overloading condition [38,39]. It is important to note that at the time of the exposure to isolated mitochondria suspensions for spectrofluorometric measurement of AFU (Fenton ROS-inhibition), each CNT-sample was added under continuous stirring by using magnetic stirrer cuvettes which favors optimal exposure conditions according to monodisperse state and prevents spontaneous agglomeration in CNT-sample dispersions.

The experimental protocols were performed using five Fenton reaction-induced experimental assays: **(1)** mitochondrial control groups in the absence, **(2)** in the presence of Fe^{2+}: citrate (1:2) at concentration of 20 μM as positive control for the induction of Fenton-Haber-Weiss reactions, **(3)** mitochondrial exposed to Fe^{2+}: citrate (20 μM) + CNT-family (0; 0.5; 3; and 5 μg/ml); and **(4)** mitochondrial exposed to DMSO(CNT-solvent) as negative control. Lastly it was estimated the relative free radical scavenging activity against Fenton reaction of the studied CNT-family which has been assigned through comparisons with assay **(5)** using mitochondrial exposed to Fe^{2+}/citrate 20 μM + Quercetin 50 μM as control or reference to establish the maximum of free radical scavenging activity against Fe^{2+} electro-induced Fenton reaction, due to its well recognized antioxidant properties and iron(II)-complexing ability [39]. Also we considered other factors such as the presence of metal impurities (iron impurities) into CNTs-tested. In this context, the maximum expected concentration of CNT-metal impurities mentioned above should be 0.05 μg/ml (<1% of the highest concentration in the CNTs samples) which possess no risk of Fenton ROS-induction in this lower levels of iron impurities [37–39]. Herein the % AFU-values decreasing is equivalent to CNT-ROS-inhibition ability. The work-flow of this experimental section it illustrated in Fig. 2.

2.6. Theoretical details of the QSPR-model

In this section we carried out a chemoinformatics study of the experimental results obtained in the Fenton ROS-*in vitro* assays. For this purpose, in classic dose-response models we can use alternative forms of the Hill curve to seek an equation in order to calculate IC_{50} values [40]. For instance, the software MasterPlex (http://psg.hitachi-solutions.com/masterplex) allows to choose different algorithms such as: 4 parameters logistic (4PL), 5 parameters logistic (5PL), quadratic log-log, log-log or linear model. However, the 4PL and 5PL forms have some drawbacks. Some authors have reported studies towards the search of alternatives models to these models. For instance, Liao et al. (2009) [41] reported a re-parameterization of 5PL dose-response curve. In any case, almost all of these alternatives fail when we need to account for multiple experimental boundary conditions. It means that the model fails when we want to predict the ROS-response (AFU_i) for the ith CNT not only for different concentrations of the CNT in a single ROS-assay. This points to the need of a model able to predict Fenton multiple dose-response series (AFU_i) for the same ith CNT when we change experimental boundary conditions (c_{kj}) like c_0 = ROS-assays with Fenton-Haber-Weiss inductor or positive control (Fe^{2+}:citrate; 20 μM); free radical scavenge control test with Fe^{2+}:citrate 20 μM + Quercetin (50 μM), c_1 = different CNT-times of exposure (t_i), c_2 = different values of CNT-concentration (c_i) and c_3 = CNT-structural parameters like type of nanotube (SWCNT, SW/DWCNT, or MWCNT), type of functionalization (H, OH, COOH), W_i = molecular weight/functionalization carbon ratio (W_{min}, W_{max}), D_i = maximal and/or minimal diameter (D_{min}, D_{max}) in the different j-th ROS-*in vitro* assay.

It is possible also to mention here the different structural or physicochemical properties of the CNTs-family under study. In these cases, 4PL/5PL and similar models are unable to fit all the data at the same time and we need to look for a different equation for each sub-set of Fenton experimental boundary conditions c_{kj}.

For this purpose, in the present work we propose for the first time a Dose-Response Perturbation Theory Model able to account for changes in multiple experimental boundary conditions (c_{kj}) for the CNT-family Fenton-effects assessment. In addition to the strategy used for choosing the most adequate CNT-nanodescriptors, the principle of parsimony was applied. This means that the best model must be selected by considering the highest statistical quality and the lowest number of parameters (experimental boundary condition and CNT-nanodescriptors). For this instance, the mathematical formalism adapted to work is presented in the following way:

$$'f\left(AFU_{ij}\right)_{pred} = a_0 \cdot {}^0f\left(AFU_{ij}\right)_{expected} + \sum_{k=1}^{kmax} a_k \cdot {}^kf\left(V_{kj}\right) + e_0 \quad (1)$$

$$'f\left(AFU_{ij}\right)_{pred} = a_0 \cdot {}^0f\left(AFU_{ij}\right)_{expected} + a_1 \cdot {}^1f\left(\Delta t_{ij}\right) + a_2 \cdot {}^2f\left(\Delta c_{ij}\right) + a_3 \cdot {}^3f\left(\Delta W_{ij}\right) + a_4 \cdot {}^4f\left(\Delta D_{ij}\right) + e_0 \quad (2)$$

For this theoretical model, we can also use (like in 4PL/5PL models) optional weighting schemes for the response variable (output function): $'f(AFU_{ij}) = AFU_{ij}$, $1/AFU_{ij}$, $(1/AFU_{ij})$ [2], or $-\log(AFU_{ij})$ to minimize the error (e_0). We can incorporate different functions ${}^0f(AFU_{ij}) = \langle AFU_{ij} \rangle$ of the expected value of AFU_{ij} for a subset of conditions (e.g., different ROS-*in vitro* assays). The ${}^0f(AFU_{ij})_{expected}$ function is the average value of fluorescence for all CNT-structure measured under the experimental boundary conditions of the *AUF*-output. It means that we could interpret ${}^0f(AFU_{ij})_{expected}$ as the *AFU*-expected value of fluorescence (AFU_i) for a particular CNT-type (pristine-CNT_i, hydroxylated-CNT_i, carboxylated-CNT_i) measured under the same sub-set of *j*-th experimental conditions (for a normal distribution) which allows to quantify the Box-Jenking operators (moving average) of the first experimental condition c_0 = ROS-assays by using Fenton-Haber-Weiss inductor (Fe^{2+}:citrate) and after the co-exposure to CNT-type. We can also use different functions for the input variable; such as: ${}^1f = \Delta t_{ij}$, $1/\Delta t_{ij}$ or $\exp(-\Delta t_{ij})$ for exposure time, or ${}^2f = \Delta c_{ij}$, $1/\Delta c_{ij}$ or $1/(\Delta c_{ij})$ [2] for CNT concentration. A particular case is when the concentration function takes the classic form of PL4/PL5 models [41]. This

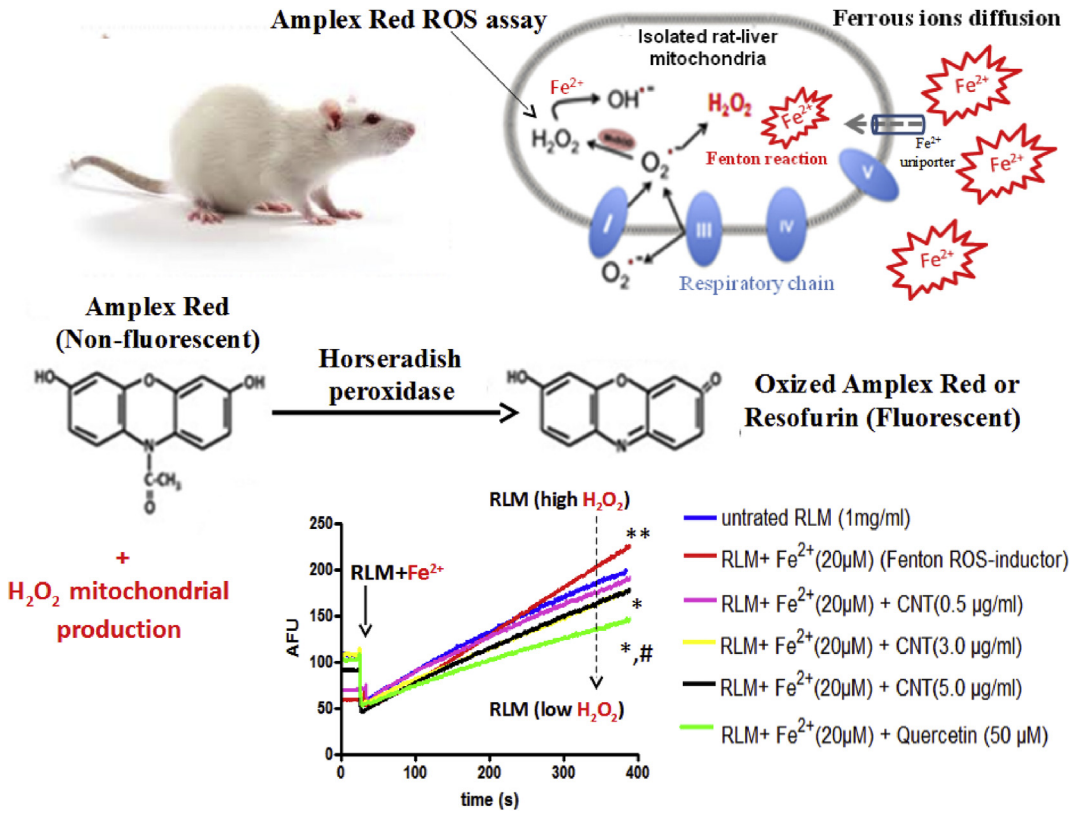

Fig. 2. Experimental workflow of Fenton ROS-inhibition assays. (A colour version of this figure can be viewed online.)

equation is represented through a sigmoid curve. The formula below illustrates two examples of alternative models (**3**) and (**4**) according to the following equations ((3) and (4)):

$$^{2}f(AFU_{ij}) = A + D\cdot\left\{1+\left[\left(\frac{\Delta c_{ij}}{C}\right)^{B}\right]\right\}^{-E} = {}^{2}f(AFU_{ij})_{min} + {}^{2}f(AFU_{ij})_{max}\cdot\left\{1+\left[\left(\frac{\Delta c_{ij}}{C}\right)^{B}\right]\right\}^{-E} \quad (3)$$

$$^{2}f\left[1/(AFU_{ij})^{2}\right] = A + D\cdot\left\{1+\left[\left(\frac{1}{C(\Delta c_{ij})^{2}}\right)^{B}\right]\right\}^{-E} = {}^{2}f(\mathrm{AFU_{ij}})_{min} + {}^{2}f(\mathrm{AFU_{ij}})_{max}\cdot\left\{1+\left[\left(\frac{1}{C(\Delta c_{ij})^{2}}\right)^{B}\right]\right\}^{-E} \quad (4)$$

The parameters of 4PL/5PL models are: A, B, C, D, and E. A is the value for the minimum asymptote. B is the Hill slope. C is the concentration at the inflection point (or IC_{50}-ROS-values). D is the AFU_{ij} for the maximum asymptote or free radical scavenging response against Fenton-Haber-Weiss reaction experimentally induced (Fe^{2+}:citrate 20 μM + Quercetin 50 μM). The last parameter E, present on *5PL* model (E = 1 in 4PL model), is the asymmetry factor (E ≠ 1 for a non-symmetric curve) [41]. The workflow for this theoretical model is showed in Fig. 3.

Specifically, the computational model developed here are *AFU*-expected values to predict the effect of different CNT-structures on mitochondrial ROS-inhibition mediated by Fenton-Haber-Weiss reaction and we could interpret this as the expected value of AFU for a CNT in this experimental condition (j^{th}-ROS assay).

We used Multivariate Linear Regression (MLR) algorithms implemented in the software STATISTICA to determine the values of the equation optimal coefficients a_k (a_0,a_1,a_2,a_3,a_4) and e_0 to represent the error or independent term of the QSPR-model using statistical descriptors as the determination coefficient (R^2), the leave-one-out-cross validation (CV-LOO) as internal validation parameters, the Fisher F ratio with the corresponding probability of error or *p-level* (p) [40]. In our dose-response QSPR-model, the output $'f(AFU_{ij})_{pred}$ is a function of the value of fluorescence (AFU_{ij}). In the simplest case we use the identity function and $'f(AFU_{ij})_{pred} = (AFUij)_{pred}$ is equal to the fluorescence value in the new sub-set of experimental boundary conditions of reference $(AFU_{ij})_{ref}$ (or *AFU*-expected value). Other transformation functions applied to AFU_{ij} were: $'f(AFU_{ij}) = 1/AFU_{ij}$, $(1/AFU_{ij})^2$, or $-\log(AFU_{ij})$.

In addition, it was considered different sub-sets of input ROS-experimental conditions according to the ontology $^{ref}c_j \equiv (c_0, c_1, c_2, c_3 \ldots c_k)$ of reference (or boundary conditions, c_{kj}). In the equation we introduced one specific input term to quantify each one of these conditions. All data were processed in an Excel file; the functions ^{k}f represent transformations $^{k}f(\Delta V_{k,j})$ of the moving averages or Box-Jenkins operators ($\Delta V_{k,j}$) of the original input variables ($^{i}V_k$) for *i*-th type of CNT_i in *j*-th Fenton ROS-assay of one specify experimental boundary condition c_{kj}. The CNT-parameters ΔV_{kj} (or moving averages CNT-nanodescriptors) are useful to quantify the output $^{0}f(AFU_{ij})_{expected}$ of perturbations on different experimental conditions (c_{kj}) like $\Delta V_k(c_j) = (^{i}V_k - \langle V_k(c_j)\rangle)$. The n_j is the number of experimental entries for condition $^{ref}c_j$ according to the total number of experimental entries measured in this work (n_j-

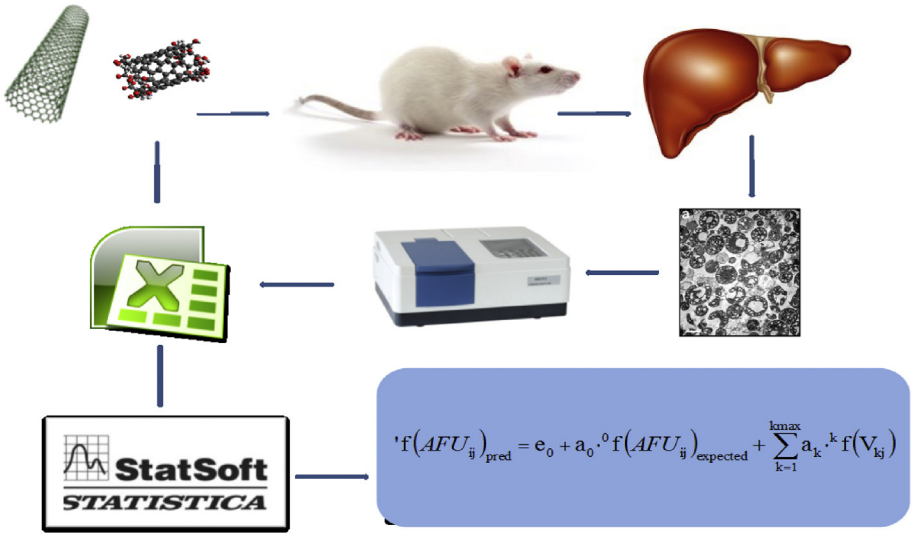

Fig. 3. Theoretical workflow to seek the Dose-Response Perturbation Theory Model. (A colour version of this figure can be viewed online.)

total).

The $\langle V_k(c_j)\rangle$ value can be interpreted as the average (or mean) for all the *k*-th physicochemical properties of CNTs-tested, according to the equation (5):

$$\langle V_k(c_j)\rangle = \frac{1}{n_j}\left(\sum_{i\subset c_j}^{n_j} {}^{i}V_{kj}\right) \tag{5}$$

The elements of the vectors $\mathbf{v}_i = [{}^{0}f(\mathrm{AFU_{ij}})_{\mathrm{expected}}, {}^{1}f(\Delta V_{1,j}), \ldots {}^{2}f(\Delta V_{2,j}), \ldots, {}^{\mathrm{kmax}}f(\Delta V_{\mathrm{kmax},j})]$ are the inputs of this model according to equation (6), whereas the terms are expanded like ${}^{k}f(\Delta V_{kj}) = {}^{i}V_k - \langle V_k(c_j)\rangle$ as follows:

$$\begin{aligned} {}'f(\mathrm{AFU_{ij}})_{pred} = {} & a_0\cdot\langle \mathrm{AFU_{ij}}\rangle_{\mathrm{expected}} + a_1\cdot{}^{1}f(t_i - \langle t_{ij}\rangle) + a_2\cdot{}^{2}f(c_i \\ & - \langle c_{ij}\rangle) + a_3\cdot{}^{3}f(W_i - \langle W_{ij}\rangle) + a_4\cdot{}^{4}f(D_i \\ & - \langle D_{ij}\rangle) + e_0 \end{aligned} \tag{6}$$

We can compare Eq. (6), with Eqs. (1) and (2) presented above in the compact notation. This *in silico* model has two types of input terms.

The first term is the function ${}^{0}f(AFU_{ij})_{\mathrm{expected}} = \langle AFU_{ij}\rangle_{\mathrm{new}}$ (or AFU_{ij}-expected values) which is the average value of fluorescence (AFU_i) for all CNT-structure measured under the experimental boundary conditions (j-th) of the output as mentioned above. The second class of terms ($\Delta V_{k,j}$) parameters were incorporated to represent the ${}^{k}f(\Delta V_{k,j})$-functions of the Box-Jenkins operators (moving averages) used here as Fenton-experimental perturbation terms (see Table 2).

For instance, the condition c_2 = concentration of *i*-th CNT in the *j*-th Fenton-ROS assay and the other is c_1 = time (t_i) of exposition of samples used in *j*-th ROS-assay corresponding to the *i*-th CNT. Some of the functions used to transform these variables where: ${}^{1}f(\Delta t_{ij}) = 1/(\Delta t_{ij})$, $\exp(-\Delta t_{ij})$, for exposure time and ${}^{2}f(\Delta c_{ij}) = 1/\Delta c_{ij}$ or $1/(1 + \Delta c_{ij})$ for CNT concentration. The following set of conditions are related to the physic-chemical nanodescriptors or CNT-structure parameters (c_3) for the *j*-th Fenton-ROS *in vitro* assay like ${}^{3}f(\Delta W_{ij})$ to molecular weight/functionalization carbon ratio and ${}^{4}f(\Delta D_{ij})$ for maximal and minimal diameter. Last, we also included other conditions related to the Fenton ROS-assay (c_0) like Solvent (DMSO, or none) and replicate sample (Yes, No). It is very important to note that internal validation parameters (R^2, Q^2 (*LOO-CV*)) aforementioned consider only the carbon nanotubes tested belonging to the same set of experimental boundary condition. As a consequence, one cannot assess the predictive potential of the developed QSPR-model when it has been employed to predict a completely new set of carbon nanotubes taking into account that, in many cases truly external data points like modulation of Fenton-Haber-Weiss mechanisms induced by carbon nanotubes are currently unavailable for prediction purposes. In this case, the original data set carbon nanotubes can be divided into training and test sets, allowing external validation [27,40]. Following this idea, it was divided the data points into a training set composed of 58,410 data points and a test set of 19,461 data points. For this division every fourth data point of a particular CNT type was taken into the training set. Herein we had a total of 77,871 data points with *AUF* values for the mitochondria Fenton ROS-inhibition at different exposure time for nine types of CNTs (this information can be found in the Supporting Information S2 and S3 as raw data in .xls format). The training set was used for model development while the test set was used solely for validation of the developed model. Stepwise multiple regression analysis with an objective function as $'f(AFU_{ij})$ (or F-to- enter = 4 and F-to-remove = 3.9) [40].

For developing a statistically acceptable QSPR-model and testing its predictive ability through external validation among the considered predictors were c(ug/ml), t(seg), W_{min}(%), D_{max}(nm), $AFU(\%)_{\mathrm{expected}}$ and considering the Fenton response *AFU* at time 0 s ($AFU_{t=0}$). These last two predictors were derived by taking the Box-Jenkins moving averages of the *AFU*-values and the $AFU_{t=0}$ for each CNT-type considering the training set only (see Table 2) and different conventional external validation parameters (Q^2_{F1}, Q^2_{F2}, Q^2_{F3}, CCC, R^2_m) were used [40].

The CNT-structural parameters and experimental boundary conditions relationships (concentration and time), involved in the Fenton inhibition response (*AFU*) were expressed below as ($\leftrightarrow$) symbol to explain the different contribution on the biological effects.

2.7. Continuous-monitoring of mitochondrial membrane potential (Ψ_m) linked to fluorescence microscopy analysis

The influence of CNT-family on the mitochondrial membrane potential was performed on the basis of mitochondrial retention of

Table 2
Description of CNT-input variables ($^{i}V_k$), Box-Jenkins operators (ΔV_{kj}) and functions (^{k}f) to seek the QSPR-model.

Optimal coefficients	($^{i}V_k$)	ΔV_{kj}	^{k}f	Function examples	Interpretation
–	–	–	$'f$	$(AFU_{ij})_{pred}$, $1/[(AFU_{ij})_{pred}]^2$, $-\log(AFU_{ij})_{pred}$	Predicted fluorescence
a_0	–	–	^{0}f	$\langle AFU_{ij}\rangle$	Average of value of fluorescence (or AFU- expected values) for all CNTs samples for multiple experimental conditions (ROS-assay, CNT-type, chemical function, Fenton-inductors.
a_1	t_i	Δt_{ij}	^{1}f	$\Delta t_{ij(s)}$, $\exp[-\Delta t_{ij}(s)]$	Exposure time.
a_2	c_i	Δc_{ij}	^{2}f	$\Delta c_{ij}(\mu g/ml)$, $1/[1+\Delta c_{ij}(\mu g/ml)]$	CNT concentration.
a_3	$W_{i\ (min)}$	ΔW_{ij}	^{3}f	$\Delta W_{ij\ min}$ (%)	CNT minimun function/carbon ratio.
a_4	$D_{i(max)}$	ΔD_{ij}	^{4}f	$\Delta D_{ij\ max}$ (nm)	CNT maximum outer diameter.
a_5	–	–	^{0}f	$AFU_{t=0\ (s)}$	*AFU* value at time 0 s.
e_0	–	–	–	–	Error term.

the fluorescent cationic probe safranine O using model F-4010 Hitachi spectrofluorimeter at excitation and emission wavelengths of 495 and 586 nm, respectively, with a slit width of 5 nm. Relative changes in membrane potential (Ψ_m) were expressed as arbitrary fluorescence units (*AFU*) [42].

For this purpose, the mitochondria (1 mg of protein/ml) were incubated in 2 ml of standard medium consisting of 125 of mM sucrose, 65 mM of KCl, 2 mM of inorganic phosphate and 10 mM of HEPES-KOH pH 7.4 at 30 °C. supplemented with 2 μM of Safranin O and individual CNT-sample (5 μg/ml) in the presence of Fe^{2+}:citrate 20 μM. When mitochondrial potential was established, Fe^{2+}:citrate 20 μM or Fe^{2+}:citrate 20 μM + CNT was added to the medium during 120 s to identify the Ψ_m-dissipation to compare with untreated mitochondria and mitochondrial exposed to (negative control, CNT-solvent). At the final of mitochondrial potential scanning (600 s), carbonyl cyanide 3-chlorophenylhydrazone (CCCP 1 μM; classic mitochondrial uncoupler) was added to obtain the maximum of Ψ_m-dissipation in the experiment.

Then the RLM suspensions were pre-incubated with a specific mitochondrial membrane potential probe as 5, 5′, 6, 6′-tetrachloro-1, 1′, 3, 3′-tetraethyl-benzimidazolcarbocyanine iodide (JC-1) in 0.2 mg/ml for 15 min according to Reers et al. (1991) [43] JC-1 is widely used in apoptosis studies to monitor mitochondrial health. JC-1 dye exhibits potential-dependent accumulation in mitochondria, indicated by a fluorescence emission shift from green (~529 nm) to red (~590 nm). To this end, mitochondrial depolarization was indicated by decreasing the red/green fluorescence intensity ratio. The potential-sensitive color shift is due to concentration-dependent formation of red fluorescent JC-1 aggregates. Fluorescent images were analyzed using a fluorescence microscope (Olympus IX81, Markham, Ontario, Canada) equipped with a DP72 digital camera to study the effects on mitochondrial membrane potential induced by pro-oxidant redox conditions after incubation with Fenton-inductor Fe^{2+}: citrate 20 μM, with iron–citrate ratio of (1:2)Next red:green fluorescent intensity ratios for JC-1 mitochondrial membrane potential probe of carbon nanotubes from CNT1 to CNT9 at maximum concentration of 5 μg/ml in Fe^{2+}-overloaded mitochondria were calculated.

2.8. Continuous-monitoring of mitochondrial iron (Fe^{2+}) uptake

The influence of CNT-family on the mitochondrial ferrous (Fe^{2+}) ions influx trough mitochondrial (Ca^{2+}, Fe^{2+}) uniporter was evaluated by using 5 μM calcein-free acid (Molecular Probes, OR, USA) [2]. Calcein does not penetrate into the mitochondria locating itself in the reaction medium Calcein fluorescence (495-nm excitation/515-nm emission wavelength pair) was measured at 37 °C. After collection of base-line fluorescence, CNT-interferences were not detected according to similar criteria as mentioned above for the H_2O_2-formation assays. For starting the mitochondrial iron (Fe^{2+}) influx measurements, $FeSO_4$ (20 μM) was added, and the fluorescence measured for 100 s Fe^{2+} binds to calcein in 1:1 ratio resulting in quenching of calcein fluorescence [2–4]. Then the mitochondrial ferrous (Fe^{2+}) ions influx was observed between 30 and 60 s after incubation with $FeSO_4$ 20 μM through the rapid decline on the extra-mitochondrial calcein fluorescence intensity, which was expressed as arbitrary fluorescence units (AFU).

2.9. Statistical procedures for the mitochondrial assays

Analysis of variance (ANOVA) followed by a post hoc Newman–Keuls multiple comparison test to determine statistical differences between experimental groups was performed. All mitochondrial tests were performed at least three times in triplicate. Differences were considered statistically significant at a probability lower than 5% ($p < 0.05$). Normality and variance homogeneity were verified using Shapiro–Wilks and Levene tests, respectively, before using ANOVA analysis. In all cases, significance level was set in 5%.

2.10. Electrochemical assays

Electrochemical assays for each CNT sample (5 μg/ml) were carried out with a BAS CV-27 potentiostat (BAS Bioanalytical Systems, West Lafayette, IN) and registered on an Omnigraphic XY recorder (Houston Instruments, Houston, TX). For these purposes, a stock solution of H_2O_2 (2.4 mM) was dissolved in H_2O containing a mixture of stock solution with chloroacetic acid/KCL of 0.1 M as the supporting electrolyte. Solution of Fe^{3+}-EDTA (0.4 mM) was obtained from a stock solution of equimolar mixture of $Fe(NO_3)_3$ and Na_2H_2EDTA with a final volume and concentration of 5.0 ml and 0.4 mM, respectively. Each sample was deoxygenated with argon for 15 min before measurement. Cyclic voltammetry was conducted at a potential sweep rate of 100 mV s^{-1} in 5 ml of phosphate buffer pH 7.2. The reproducibility of the potential peaks voltammetry was about ±0.01 V. CNT samples were used from individual stock suspensions at a concentration of 1 mg/ml.

A conventional electrochemical cell with three electrodes was employed. A glassy carbon electrode with geometric area of 0.0314 cm^2 was used as working electrode. It was polished prior to use with 1 μL of alumina water suspension 1 mM and rinsed thoroughly with water and acetone. A platinum wire was used as counter electrode and all potentials were referred to a potassium chloride saturated silver/silver chloride electrode [Ag/AgCl/KCl(sat)] without regard for the liquid junction potential.

For the electrocatalytic Fenton-Haber-Weiss reaction, the

methods reported by Laine F et al. (2009) [18] were used. Several electrochemical assays (cyclic voltammograms) were measured as intensity I (μA) versus voltage [E(V) vs. Ag/(AgCL)]. Before the CNT-electrochemical studies, different control assays were performed with the aim of optimizing the experimental conditions to evaluate the redox responses of the CNT-samples as: **a)** chloroacetic acid solution + KCl 1 M; **b)** chloroacetic acid solution + H_2O_2 2.4 mM; **c)** chloroacetic acid solution + DMSO 100 mM (CNT-vehicle); and **d)** chloroacetic acid solution + oxidized-CNTs (5 μg/ml). These assays were run in order to discard the presence of faradaic peaks (cathodic and/or anodic redox processes) or possible interference associated to CNT-metallic impurities. Next, three voltametric experiments were performed to evaluate the influence on the Fenton chemistry for each type of nanotube using supporting eletrolyte according to: **1)** Fe^{3+}-EDTA complex; **2)** Fe^{3+}-EDTA + hydrogen peroxide (H_2O_2); and **3)** Fe^{3+}-EDTA + H_2O_2 + oxidized-CNTs (5 μg/ml). All assays were performed in the absence of oxygen. For this purpose, each sample was deoxygenated with argon for 15 min before electrochemical measurement. When the potential was scanned, the inert gas was kept on the surface of the solution to ensure that any oxidation reaction was not initiated by oxygen.

Cyclic voltammograms were recorded in triplicate at a window potential (- 0.4 to 0.4 V) similar to window potential observed in mitochondrial redox complexes (I and III) of the respiratory chain, which are the main sources of mitochondrial ROS-formation in physiopathological conditions [3,4].

2.11. Determination of ferrous ions (Fe^{2+}) chelating activity

The carbon nanotubes chelating ability of ferrous ions was estimated using the method of Dinis et al. (1994) with small modifications [44]. According to this protocol, triazine can form a blue complex with Fe^{2+}, which can be spectrophotometrically measured at 570 nm. In the presence of chelating agents, the complex formation is impaired, resulting in a decrease in the blue color generation. Therefore, the color reduction allows an estimation of the metal chelating activity of the co-existing potential chelator [44]. Lower absorbance indicates higher metal chelating activity and vice versa. Indeed, the metal chelation is an important antioxidant property according to results obtained by Kehrer (2000) [45]. For this instance, was assessed the CNT-ability to compete with triazine for ferrous ions (Fe^{2+}) in the solution in order to evaluate the potential of Fe^{2+}-chelating. Before all spectrophotometric chelating measurements, the blanks with each CNT were run and interferences absorbance peaks of CNT were not observed at 400–600 nm[20], a result that ensured that colorimetric measurements at 570 nm were reliable. Firstly, it was determined the absorbance of the control group, containing triazine-Fe^{2+} complex in the presence of DMSO (CNT-solvent), a condition that represents the free Fe^{2+} or non-chelated ferrous ions. Also, EDTA (0.4 mM) was employed as positive control, in order to get an estimate of 100% of Fe^{2+} chelating activity. Then, Fe^{2+} chelating activity was determined in the presence of different concentration of CNT (0.5; 1; 3; and 5 μg/mL) from a CNT-stock suspension in the solution of 2 mM $FeSO_4$. The reaction was initiated throughthe addition of 5 mM of triazine and the total volume was adjusted to 2 mL with water. Next, the mixture was shaken vigorously and left at room temperature for ten minutes followed by spectrofotometric measurement at 570 nm. Data of chelanting activity on ferrous ion (Fe^{2+}) by carbon nanotubes were expressed as the mean ± 1 standard deviation (SD). Differences between the experimental groups were evaluated using one-way ANOVA followed by the post hoc Newman–Keuls multiple comparison test when appropriate. All tests were performed at least three times in triplicate. Differences were considered statistically significant at a probability of less than 5% ($p < 0.05$). Normality and variance homogeneity were verified using Shapiro–Wilks and Levene tests, respectively, before using ANOVA analysis. In all cases, a significance level of 5% was employed.

3. Results and discussion

3.1. Effects of CNT-family on mitochondrial ROS levels

The experimental values of ROS-inhibition [ROS_i (%)] for the different CNTs determined in the concentration range of 0–5 μg/ml are shown in Table 3. In order to evaluate the mitochondrial H_2O_2 production, the Amplex Red assay in the presence of Fe^{2+} 20 μM, as classical Fenton-Haber-Weiss-ROS-inductor, was used to induce a mitochondrial pro-oxidant condition. The CNT potential interference in this method was not detected. In this regard, it is important to note that de-bundled semiconducting carbon nanotubes as the CNT-family tested, are known to exhibit the first van Hove absorption peak (E_{11}) in the near-infrared region (800–2500 nm) [20], which does not compromise in any sense, the mitochondrial Fenton *in vitro* measurements (AFU or ROS-inhibition response) performed at 563/587 nm of excitation/emission, respectively as mentioned in Materials and methods section.

In the present study relationship between CNT-concentration, CNT-time of exposure, CNT-functional groups (OH, COOH) and CNT-diameter toward mitochondria Fenton inhibition-targeted like [ROS_i (%)] was analyzed and compared with quercetin to obtain a maximum free radical scavenging activity [39]. The obtained results presented the following order: quercetin (antioxidant positive control) > CNT-COOH (MWCNT-9, MWCNT-7, MWCNT-6, SWCNT-8) > CNT-OH (SWCNT-2, MWCNT-5, MWCNT-3, MWCNT-4) ~ pristine-CNT (MWCNT-1).

3.2. Interpretation of QSPR-Perturbation model

The predictive QSPR-model obtained in the present work is a canonical generalization of the pharmacodynamics problems of dose-response, addressed to assess the effects of CNTs on the inhibition of mitochondrial ROS-production in Fenton chemical pro-oxidant conditions. Next, the AFU_i-values were obtained after exposure of the rat-liver mitochondrial sample as ROS-target to one volume of 100 μL of CNT at different c_i values. It was employed CNT-physic-chemical parameters (^iV_k), were used as inputs for statistical model development as was shown in Table 2. The endpoint (response variable) used in the QSPR/QSAR analyses is a predictive function of the percent of arbitrary fluorescence unit ($f(AFU_{ij}$ %)) which means the free radical scavenging ability against mitochondrial Fenton reaction induced by Fe^{2+}-overload (AUF_i (%) = ROS_i(%) or % Fenton ROS-inhibition) obtained from experimental dataset as a function of CNT-functionalization, CNT-diameter and also optimal experimental conditions of exposure like CNT-concentration and exposure time according to Eq. (7). This approach allows to evaluate and predict the influence of multiple experimental conditions in Fenton radical scavenging ability.

This QSPR/QSAR-model can be regarded as a generalized model for making predictions of •OH-hydroxyl free radical scavenging ability of other functionalized CNTs with different physical (such as diameter) and experimental (such as CNT concentration and exposure time) specifications not used in model development thus aiding in design of new functionalized CNTs of potential therapeutic benefit. The acceptability and applicability of Eq. (7) for such prediction purposes have been statistically judged in quantitative terms using different internal and external validation parameters according to the best quantitative structure–activity relationship models (QSAR-model) obtained is represented by Eq. (7):

Table 3
Experimental Fenton ROS-inhibition values (ROS_i%) for CNT family.

[a]n_i	[a]CNT type	[a]Function	[a]W_i	[a]D_i	[a]c_i	[b]ROS_i(%)	N_j
1	MWCNT	–	3.03[b]	8	0.5	0	42
					1	3.5	42
					3	15.6	42
					5	32.3	42
2	SW/DWCNT	OH	3.96	1	0.5	0	21
					1	0	21
					3	31.9	21
					5	60.7	21
3	MWCNT	OH	3.86	1	0.5	7.3	42
					1	8.3	42
					3	17.3	42
					5	20.2	42
4	MWCNT	OH	4	10	0.5	0	21
					1	6.2	21
					3	13.4	21
					5	17.2	21
5	MWCNT	OH	1.06	30	0.5	0	42
					1	6.4	42
					3	21.1	42
					5	24.1	42
6	MWCNT	COOH	0.73	30	0.5	10.6	21
					1	14.7	21
					3	30.2	21
					5	68.4	21
7	MWCNT	COOH	4	10	0.5	2.9	21
					1	53.8	21
					3	66.9	21
					5	71.2	21
8	SWCNT	COOH	2.73	1	0.5	0	21
					1	0	21
					3	22.9	21
					5	56.3	21
9	MWCNT	COOH	3.86	1	0.5	0	21
					1	22.1	21
					3	75.9	21
					5	81.4	21
Control	Quercetin				50	100	21
		Groups	⟨W_i⟩	⟨D_i⟩	⟨c_{ij}⟩	ROS_i(%)	N_j
		Average ± S.D.	2.435	10.25	2.5	0.353 ± 0.06802	1071

[a]MWCNT = Multiple-Walled, SWCNT = Single-Walled, SW/DWCNT = DWCNT + SWCNT mixture. Percent of arbitrary fluorescence unit or [b]AUF_i (%) = [b]Fenton ROS-inhibition = [b]ROS_i(%) = 100*[$AFU_{cnt} - AFU_{solvent}$]/[$AFU_{Quercetin\text{-}control} - AFU_{solvent}$] where CNT = carbon nanotubes or Fe^{2+}:citrate (Fenton-inductor), Solvent = DMSO or H_2O from Fe^{2+}:citrate solution; $AFU_{Quercetin\text{-}control}$ (Free radical scavenge-mitochondrial control with Fe^{2+}-complexing ability) [52] and N_j is the number of replicates of the Fenton ROS-assay.

$$\begin{aligned} AFU_{ij}(\%)_{pred} &=' f(AFU_{ij}) \\ &= 0.332(\pm 0.0153)AFU_{ij}(\%)_{expected} \\ &\quad - 1.46(\pm 0.0567)c_{ij}(\mu g/ml) \\ &\quad + 0.195(\pm 0.0003)t_{ij}(s) \\ &\quad - 1.03(\pm 0.0826)W_{ij}\min(\%) \\ &\quad - 0.163(\pm 0.0063)D_{ij}(nm)_{max} \\ &\quad + 0.287(\pm 0.0086)AFU_{t=0} + 10.51(\pm 2.555) \end{aligned} \quad (7)$$

3.2.1. Training set statistics (internal validation parameters)

$N = 58410$, $F = 88394.64$ (df 5, 58403), $s = 25.2042$; $R^2 = 0.901$; $R^2(adj.) = 0.901$; $Q^2(LOO\text{-}CV) = 0.901$; SEE = 25.2042; $PRESS = 37109229$.

3.2.2. Test set statistics (external validation parameters)

$N = 19461$, $Q^2_{F1} = 0.9008$; $Q^2_{F2} = 0.9008$; $Q^2_{F3} = 0.9009$; $MAE = 21.213$; Scaled Avg. $R^2_m = 0.8608$, Scaled Delta $R^2_m = 0.0796$; CCC = 0.9478.

Quality of prediction (based on MAE criteria): Moderate.

Please note that the standard errors of each regression coefficient of the predictive QSPR-model represented by Equation (7) are shown in parenthesis. All the regression coefficients are significant at $p < 0.05$ while the model shows 90.1% explained variance and 90.1% predicted variance based on the training set data. In order to provide an example of numeric simulation about the potential applicability based on Eq. (7) for such prediction purposes on free radical scavenging ability against mitochondrial Fenton reaction induced by Fe^{2+}-overload in different experimental conditions it was represented the following Eq. (8); to check, each parameters of the model see the Supporting Information S2 and S3 as raw data in .xls format).:

$$\begin{aligned} AFU_{ij}(\%)_{pred} &=' f(AFU_{ij}) \\ &= 0.332(142\%) - 1.46(2.5\mu g/ml) + 0.195(600s) \\ &\quad - 1.03(2\%) - 0.163(5nm) + 0.287(33.67)_{t=0} \\ &\quad + 10.51 = 177.79\% \end{aligned} \quad (8)$$

As we mentioned above, in the simplest case the output function $^1f(AFU_{ij})_{pred}$ represents the fluorescence predicted value ($AFU_{ij}(\%)_{pred}$) by the linear model under the set of boundary conditions of test of reference. Overall behavior of observed vs. predicted values for each CNT dose-effect series it was depicted (Fig. 4).

The general model predicts an excellent linear behavior for different dose-effect series according to alternative models represented above by the equation (3) and (4) for the different CNT with different diameters $(D_i)_{max}$ and chemical functions $(W_i)_{min}$, etc.

3.3. Effects of CNT-family on mitochondrial membrane potential (Ψ_m)

In this regard Fig. 5 (a) shows graphically that the CNT-family does not affect the electrochemical mitochondrial membrane potential, despite of the presence of pro-oxidant experimental conditions induced by Fenton initiator (Fe^{2+}/citrate 20 μM). The fluorescence units (means ± SEM at 120 s) were of 22.10 ± 3.72 for the mitochondria from Fe^{2+}/citrate + CNT treatment at 5 μg/ml (CNT-lines: CNT1 to CNT9) *versus*. 54.8 ± 2.13 for the mitochondria from Fe^{2+}/citrate-treated treatment (Fenton-inductor, green line) and 120.64 ± 4.14 for CCCP (which was added at the final of the mitochondrial potential scanning during 600 s for all Ψ_m-experiments). This value of response (120.64 ± 4.14) was similar even if CCCP (1 μM) was added at 120 s, attest to its strong uncoupling properties associated to Ψ_m-dissipation. Statistically significant differences ($p < 0.05$) were found between mitochondria from Fe^{2+} (20 μM)-treatment (green line) and for mitochondria from Fe^{2+} (20 μM) + CNT (5 μg/ml) treatment (CNT-lines: CNT1 to CNT9) at 120 s.

In addition, these evidences were similarly reinforced by the (Ψ_m) results with mitochondrial membrane potential dye (JC-1) probe, allowing the identification of healthy and dysfunctional mitochondria. In this regard it was not observed the presence of miptotic J-monomers (green fluorescent) for mitochondria exposed to from Fe^{2+} (20 μM) + CNT (5 μg/ml) when compared with mitochondria treated with Fe^{2+} (20 μM) and mitochondria exposed to Fe^{2+} (20 μM) + CCCP in the fluorescence microscopy analysis. See details in Fig. 5(b–g). Also it was estimated the red: green fluorescent intensity ratio for all the experiments performed and it was confirmed the absence of significant statistical differences ($p > 0.05$) for RLM exposed to Fe^{2+} (20 μM) + CNT (5 μg/ml) compared with untreated-RLM, treated-RLM with ruthenium red

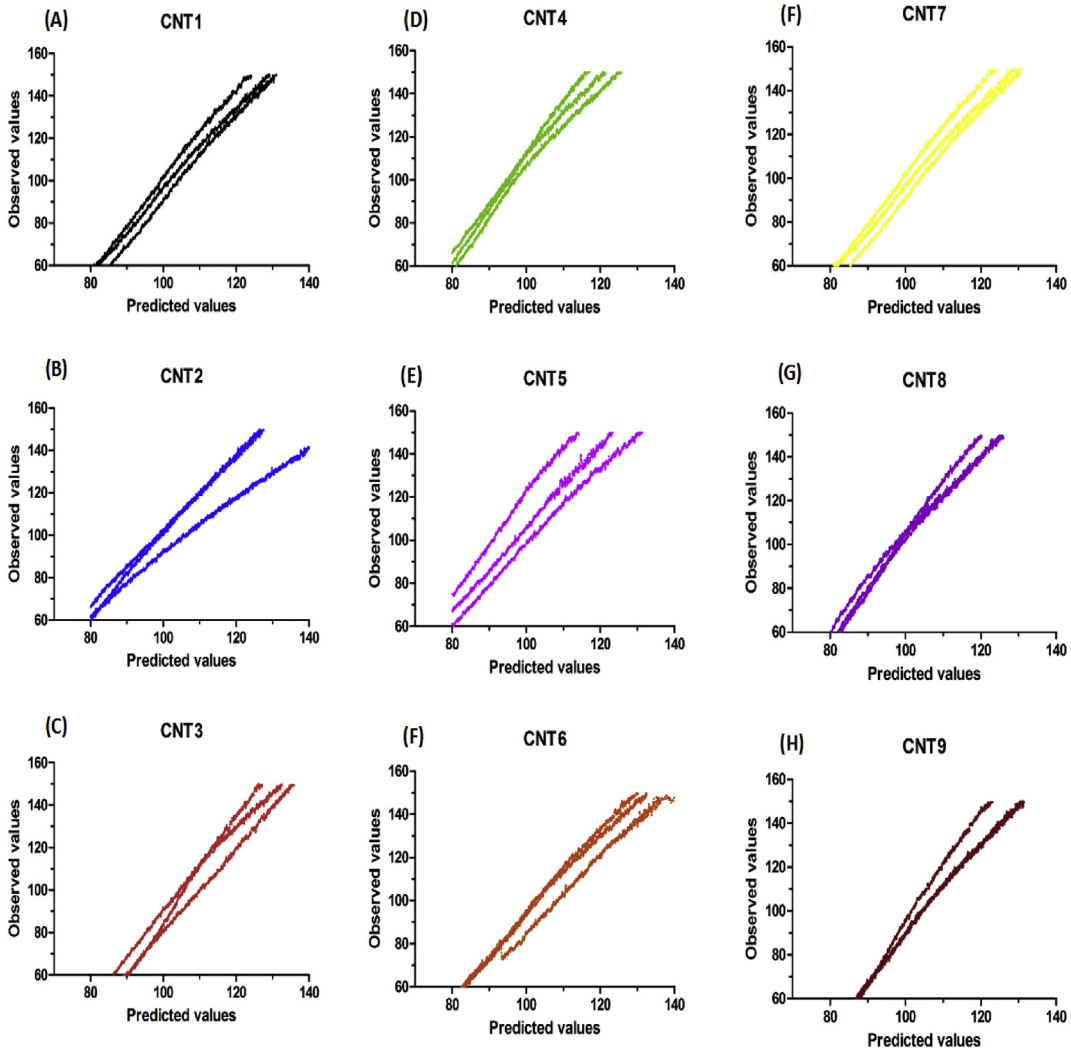

Fig. 4. Observed vs. predicted *AFU*-values obtained for each CNTs dose-response series with the QSPR-model. (A colour version of this figure can be viewed online.)

and DMSO-treated mitochondria (J-aggregates):dysfunctional mitochondria (miptotic J-monomers) rate. At the same time, it was observed marked significant statistical differences ($p < 0.05$) when compared with treated-RLM from Fe^{2+} and CCCP + Fe^{2+}, which are closely associated with loss of mitochondrial membrane potential. See in details in Fig. 5h.

3.4. Electrochemical evidences on Fenton reaction inhibition by CNT-family

The general mechanism of Fenton chemistry is represented by the sequence of coupled redox reactions as depicted below:

Electrochemical Mediated Fenton Reaction:

$$[Fe^{3+}EDTA]^{+} + e^{-} \leftrightarrow [Fe^{2+}EDTA]^{+} \quad (9)$$

$$[Fe^{2+}EDTA]^{+} + H_2O_2 \rightarrow [Fe^{3+}EDTA]^{+} + {}^{\bullet}OH \text{ (hydroxyl radical)} + HO^{-} \quad (10)$$

Firstly, the cyclic voltammograms are shown for the controls experiments in the absence of Fe^{2+}/EDTA. To this end, it was shown that non-associated redox peaks to ($Fe^{2+}{}_{red} \leftrightarrow Fe^{3+}{}_{ox}$), can be related to H_2O_2 catalytic reduction mediated by Fe^{3+}/EDTA. In addition, it was discarded the influence of possible interferences or Fenton redox processes by CNT-metal impurities (Cr, Co or Fe) and other types of carbon particles or amorphous carbonaceous impurities, since it was observed the absence of Faraday process (cathodic and anodic peaks) in the control electrochemical assays as depicted by Fig. 6A (above), where it can be verified the absence of redox peaks.

Next, it was performed three electrochemical experiments according to Fenton chemistry for each type of nanotube based on the sequence of the following electrochemical reactions: **(1)** Fe^{3+}-EDTA complex; **(2)** Fe^{3+}-EDTA + hydrogen peroxide (H_2O_2); and **(3)** Fe^{3+}-EDTA + H_2O_2 + oxidized-CNT (5 μg/ml) in order to evaluate the hypothesis of Fe^{2+} chelation as a possible mechanism for the CNT scavenging activity, the electrochemical Fenton-Harbor-Weiss assays were performed as shown in Fig. 6B (below).

Each graphic shows an individual electrochemical assay (cyclic voltammogram) performed for each carbon nanotubes of the present study in Fig. 6B. In all the cases depicted, the black line shows a cyclic voltammogram of Fe^{3+} EDTA/Fe^{2+} EDTA obtained from a scan to the negative potentials and the oxidation process in the reverse scan, this redox process can be represented by equation (9). The blue line shows a voltammetric behavior of Fe^{3+}-EDTA in presence of 8 mM H_2O_2. It can be seen that cathodic current has

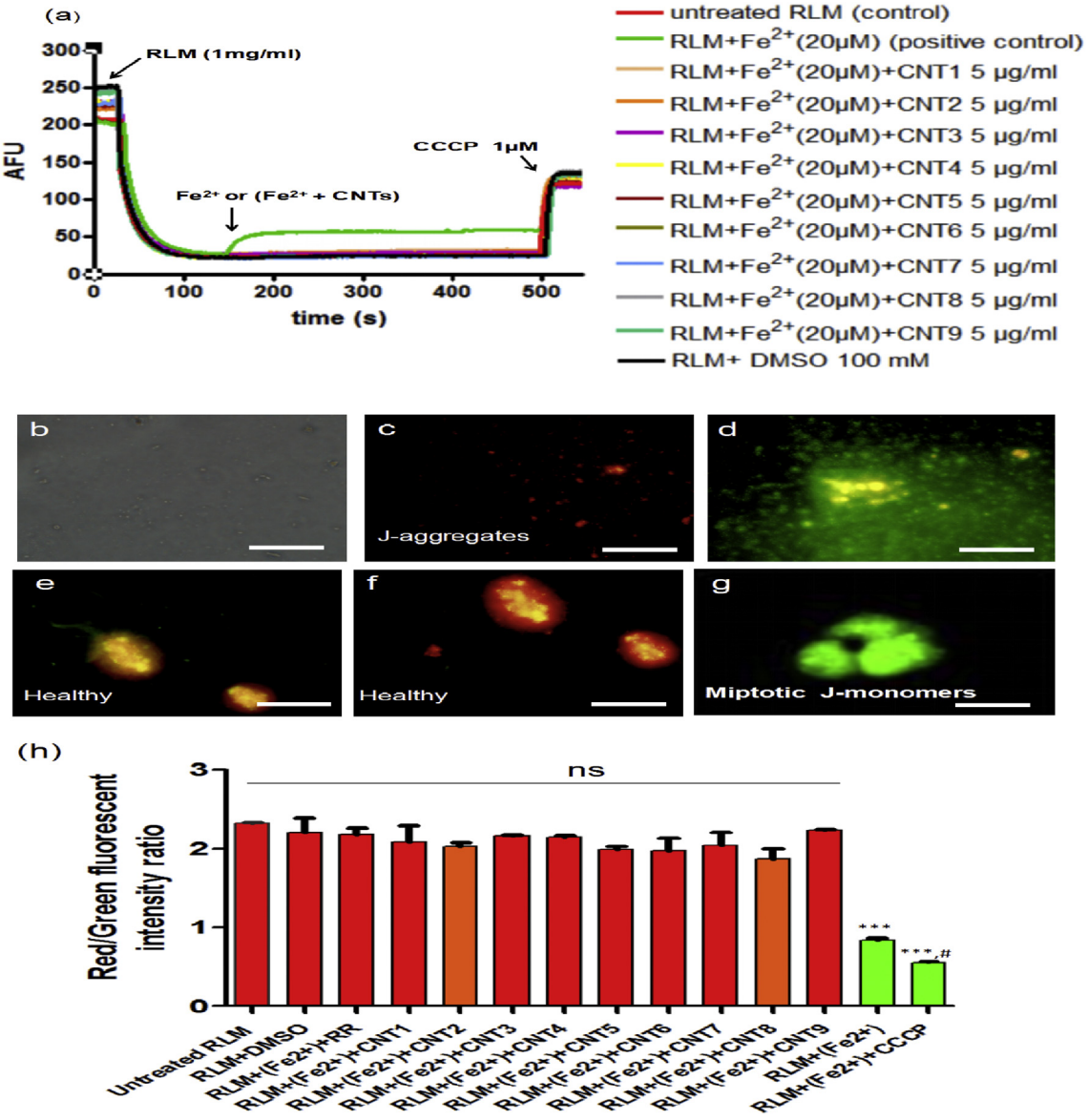

Fig. 5. (a) Graphic behavior of effects on dissipation of mitochondrial membrane potential (Ψm) induced by Fenton-inductor (Fe^{2+}/citrate 20 μM) expressed as arbitrary fluorescence units (AFU) vs. time (s). Experimental conditions are described under Materials and Methods section. Different treatments are depicted: mitochondria control (untreated RLM, red line), mitochondria from DMSO-treated rats (black line), mitochondria from Fe^{2+}/citrate-treated rats (green line, positive control) and mitochondria from Fe^{2+}/citrate + CNTs-treated rats at concentration 5 μg/ml (remaining colored lines). RLM (1 mg/ml), Fe^{2+}/citrate complex and Fe^{2+}/citrate + CNTs, and CCCP (1 μM) were added where indicated by the arrows. Results are representative of three experiments. Below, isolated rat-liver mitochondria were incubated with a specific mitochondrial dye (JC-1) in 0.1 mg/ml for 15 min. Show details of representative fluorescent images of effects on mitochondrial membrane potential (Ψm) for different controls and CNT-treatments. (b) Bright field mitochondria from untreated rats, (c) mitochondria from untreated rats (control), (d) Mitochondria from Fe^{2+}/citrate-treated rats (positive control) show miptotic J-monomers (green), (e) mitochondria from DMSO-treated rats without Fe^{2+}/citrate (only CNT-solvent, negative control) show healthy mitochondria or J-aggregates (pseudocolored red), (f) Mitochondria from Fe^{2+}/citrate + CNTs(5 μg/ml) or Fe^{2+}/citrate + RR 1 μM treated rats inducing mitoprotective activity after incubations with Fenton-inductor (Fe^{2+} 20 μM) show healthy mitochondria or J-aggregates (red to pseudocolored red), (g) Mitochondria from CCCP + Fe^{2+}/citrate -treated rats show miptotic J-monomers (green) were examined under a fluorescence microscope (x 600 magnification). Scale bars 50 μm. (h) Overall red: green fluorescent intensity ratios for JC-1 mitochondrial membrane potential probe of carbon nanotubes from CNT1 to CNT9 at maximum concentration of 5 μg/ml in Fe^{2+}-overloaded mitochondria (RLM + Fe^{2+}+CNT-family). Also are depicted the results of mitochondria control (untreated RLM), mitochondria from DMSO-treated rats without Fe^{2+}/citrate (RLM + DMSO), mitochondria from Fe^{2+}/citrate + RR 1 μM (RLM + Fe^{2+} + RR), mitochondria from Fe^{2+}/citrate-treated rats (RLM + Fe^{2+}) and Mitochondria from CCCP 1 μM + Fe^{2+}/citrate -treated rats (RLM + Fe^{2+} + CCCP). Experimental data are presented as the mean ± S.E of the fluorescent intensity ratio values to represent the J-aggregates and J-monomers measured using excitation/emission wavelengths of 535/595 nm and 485/535 nm, respectively (n = 3). To denote the absence of statistical differences (ns or $p > 0.05$) it was used to compare with mitochondrial control, DMSO (CNT-solvent) or RR (Ca^{2+}, Fe^{2+} uniporter classical inhibitor) and ***$p < 0.001$ to statistical differences between positive control (Fe^{2+} or CCCP) are represent by # symbol. (A colour version of this figure can be viewed online.)

its intensity increased noticeably, followed by absence of anodic current. This electrochemical behavior is due to the catalytic behavior of Fenton reaction as depicted by the equation (10). For this purpose, the addition of CNT represented by the red line for all cyclic voltammograms, significantly inhibits this catalytic process, according to the following order: oxidized carbon nanotubes > pristine carbon nanotubes, more in details: carboxylated-MWCNT-6(30–50 nm) > hydroxilated-MWCNT-5 (30–50 nm) > MWCNT-1 (8 nm) > carboxylated-SWCNT-8 (4 nm) > carboxylated-MWCNT-7 (10–20 nm) > carboxylated-

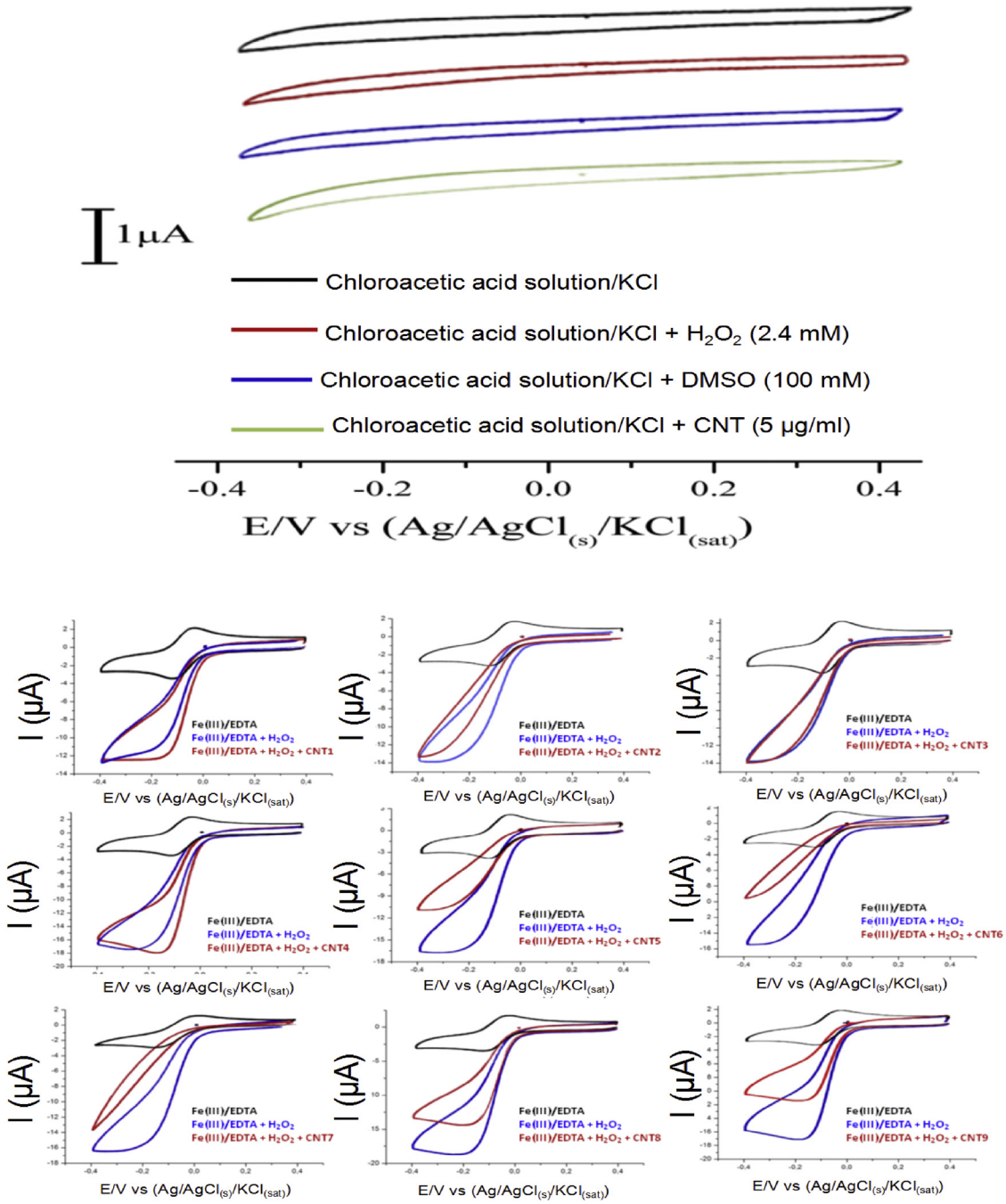

Fig. 6. A. Representative cyclic voltammogram controls for chloroacetic acid solutions and KCL (100 mM) supporting electrolyte (black line), in the presence of hydrogen peroxide (H_2O_2, red line), dimethyl sulfoxide solution (DMSO or CNT-solvent, blue line); CNTs (CNT1-CNT9) at 5 µg/ml (green line). Each experimental condition is representative of 3 individual experiments. B cyclic voltammograms of each carbon nanotubes tested are represented by three eletrochemical profiles of redox processes according to following sequence: the Fe^{3+}/EDTA solution showing the faradaic peaks to ($Fe^{2+}{}_{red} \leftrightarrow Fe^{3+}{}_{ox}$) (black line), Fenton-Haber-Weiss reaction electro-induced by Fe^{2+} ions from Fe^{3+}/EDTA solution in the presence of hydrogen peroxide (H_2O_2, blue line); inhibition of cathodic peak current values [Ipc (µA)] of Fenton-Haber-Weiss reaction in the presence of carbon nanotubes at 5 µg/ml (red line). Scan rate it was 100 mV/s measured from 0.4 to −0.4 V, using a glassy carbon electrode (area = 0.0314 cm^2). Please note that all cyclic voltammograms were scanned including negative ranges (−0.4–0.4 V) similar to recognized window potential of mitochondrial complexes (I and III) of the respiratory chain, which are the main sources of mitochondrial ROS-formation (•OH-hydroxyl free radical) in physiopathological conditions (Fenton-Haber-Weiss reaction) as tested. Typical examples are shown. Each experimental condition is representative of 3 individual experiments, for experimental details see Materials and Methods. (A colour version of this figure can be viewed online.)

MWCNT-9 (1–8 nm), what can be observed throughthe decrease of cathodic current. On the other hand, the hydroxylated-CNTs (SW/DWCNT-2, MWCNT-4, MWCNT-3) exhibit lower or non-activity against Fenton reaction.

Electrochemical results of Fenton inhibition reaction for carbon nanotubes are illustrated regarding the percent of inhibition to the cathodic peak current values (Ipc (µA)) in Table 4.

It is recognized that (Ipc(µA)) is directly proportional to the concentration of reduced species (hydroxyl free radical). In this contex, only the CNT-Fenton inhibition (hydroxyl free radical attenuating ability) as a function of (Ipc (µA)) was estimated following the equation (9):

$$I_{pc} = \left[100 - \frac{I_{pc}[(Fe^{2+}/EDTA) + H_2O_2 + CNT]}{I_{pc}[(Fe^{2+}/EDTA) + H_2O_2]}\right] \times 100 \quad (11)$$

Based on these evidences, the CNT-family exhibits the potential ability to act as hydroxyl(·OH)-free radical scavenger based in the inhibition of Fenton chemistry according to the CNT-type functionalization. Particularly to oxidized-CNT (MWCNT-6 > MWCNT-5 with diameter range (30–50 nm) when compared with pristine-CNT (MWCNT-1) with d = 8 nm. Taking into account the ·OH-free radical scavenging based on the inhibition of Fenton chemistry associated to CNT with smaller diameter ranges (1–20 nm), the Fenton chemistry inhibition presents low % Ipc values following the order carboxylated-SWCNT-8 (1–4 nm) > carboxylated-MWCNT-7 (10–20 nm) > carboxylated-MWCNT-9 (1–8 nm) > hydroxylated-SW/DWCNT-2 (1–4 nm) > hydroxylated-MWCNT-4(10–20 nm) > hydroxylated-MWCNT-3 (1–8 nm), which do not show ability to inhibit the Fenton-reaction, and instead of suggesting synergistic effect on the Fenton-reaction mechanism induced in this electrochemical assay. On the other hand, the slips observed for the cathodic peak potential values (Epc (V)) in the presence of carbon nanotubes for the experiments **(3)** like Fe^{3+}-EDTA + H_2O_2 + oxidized-CNT (5 μg/ml) showed less relevance to explain the inhibition of Fenton reaction in most of the cases that used this voltammetric cyclic study. However, the difference for the cathodic peak current values (Ipc (μA)) were unambiguously defined when compared with Fe^{3+}-EDTA + H_2O_2 in the absence of carbon nanotubes used as control experiments.

3.5. Effects of CNT-family on the Fe^{2+} chelating activity

The complexing effect of ferrous ions (Fe^{2+}) by CNTs and the controls were measured according to the method of Dinis et al. (1994) [44]. The members of CNT-family interfered with the formation of ferrous (Fe^{2+})-triazine complex, suggesting that CNTs are capable of capturing ferrous ion before their interaction with triazine in most of the cases. Performing a general analysis, it is possible to observe that CNT-family showed an excellent ability to chelate the ferrous ions at lower concentrations than 1 μg/ml, and the values were statistically significant ($p < 0.05$) when compared with the control treatment using DMSO (CNT-solvent) (Fig. 7).

The chelation ability followed this order: carboxylated-SWCNT-8 (d = 4 nm) > carboxylated-MWCNT-9 (d = 8 nm) > carboxylated-MWCNT-7 (d = 10–20 nm)>carboxylated-MWCNT-6 (d = 30–50 nm) > hydroxylated-MWCNT-5 (d = 30–50 nm). Similarly, hydroxylated-MWCNT-3 (d = 8 nm) > hydroxylated-SW/DWCNT-2 (d = 1–4 nm) > MWCNT-1 (d = 8 nm) > hidroxylated-MWCNT-4 (d = 10–20 nm) showed ability to chelate the ferrous ions at lower concentrations than 0.5 μg/ml, with statistically significant differences ($p < 0.05$) related to control experiment (DMSO), showing the same pattern of response in the sense of decrease of nanotube diameter, but for this instance it was not observed a concentration dependence for the ferrous ion chelating activity. Also it should be emphasized that for higher concentration than 3 μg/ml, the complexing activity on ferrous ion (Fe^{2+}) for CNT with diameter lower than 8 nm, the Fe^{2+} ions immobilization reached the maximum value, similar to positive control EDTA (0.4 mM), used as reference of maximum Fe^{2+} chelating response, with statistically significant differences ($p < 0.05$) related to control experiment (DMSO).

3.6. Effects of CNT-family on mitochondrial iron (Fe^{2+}) uptake

This assay provided mechanistic information regarding the potential of CNT-ability to inhibit the mitochondrial iron (Fe^{2+}) uptake. The results showed that all the members of CNT-family did not interferewith Fe^{2+}-translocation from extra-mitochondrial medium to mitochondrial matrix in Fe^{2+} 20 μM overload conditions. No significant statistical differences were registered ($p > 0.05$) when compared with untreated mitochondria suspensions. However, for mitochondria treated with ruthenium a (Ca^{2+}, Fe^{2+})-uniporter classical inhibitor (positive control), significant statistical differences ($p < 0.05$) were detected when compared with control group (Fig. 8).

4. General discussion

The important role of mitochondria to regulate intracellular ROS levels has been extensively characterized and associated with several chronic diseases as neurodegenerative diseases, cardiovascular and cancer, which currently have high levels of morbidity and mortality [1]. In this study, we performed biochemical and redox electrochemical protocols to evaluate the properties of different carbon nanotubes on mitochondrial Fenton reaction under physiophatological conditions of iron overload and high peroxide production.

In this sense, several aspects must be considered to explain the ability of carbon nanotubes (oxidized-CNT) to inhibit mitochondrial ROS-formation. First, CNT should cross the outer mitochondrial membrane, inter-membrane space and mitochondrial matrix [7], this ability could be dependent on its octanol/water partition coefficient and CNT-electronical properties [28].

The evidences suggest a CNT-hydroxyl free radical scavenging ability mediated by CNT-(Fe^{2+})-complexing ability and suggest that it removes Fe^{2+} from the citrate complex because Fe^{2+} is directly involved in the formation of •OH radical through Fenton-Haber-Weiss-reactions. Following this idea, the Fenton inhibition responses obtained are strongly dependent on the relevant structural parameters (CNT-nanodescriptors).

Table 4
Percent of inhibition of electrocatalyzed Fenton reaction for CNT-family.

CNT-Properties			Wi (%)		Di (nm)		Cathodic peak current values Ipc (μA)		
n	Type	Function	min	max	min	max	Ipc (Fe3 + EDTA + H2O2)	Ipc (Fe3 + EDTA + H2O2+CNT)	Ipc inhibition (%)
1	MWCNT	H	0.9	3	8	8	−17.2	−11.5	41.01
2	SW/DWCNT	OH	0	4	1	4	−14	−13.5	4.67
3	MWCNT	OH	0	3.9	1	8	−14	−14.1	0,00
4	MWCNT	OH	3	4	10	20	−18.5	−17.5	3.45
5	MWCNT	OH	1	1.1	30	50	−16.5	−11	43.31
6	MWCNT	COOH	0	0.7	30	50	−15.5	−9.6	46.83
7	MWCNT	COOH	3	4	10	20	−16.5	−13.7	20.74
8	SWCNT	COOH	0	2.7	1	4	−18.5	−14.5	28.1
9	MWCNT	COOH	0	3.9	1	8	−12.6	−11.6	10.99
10	DMSO	no	no	no	no	no	−17	−17	0,00

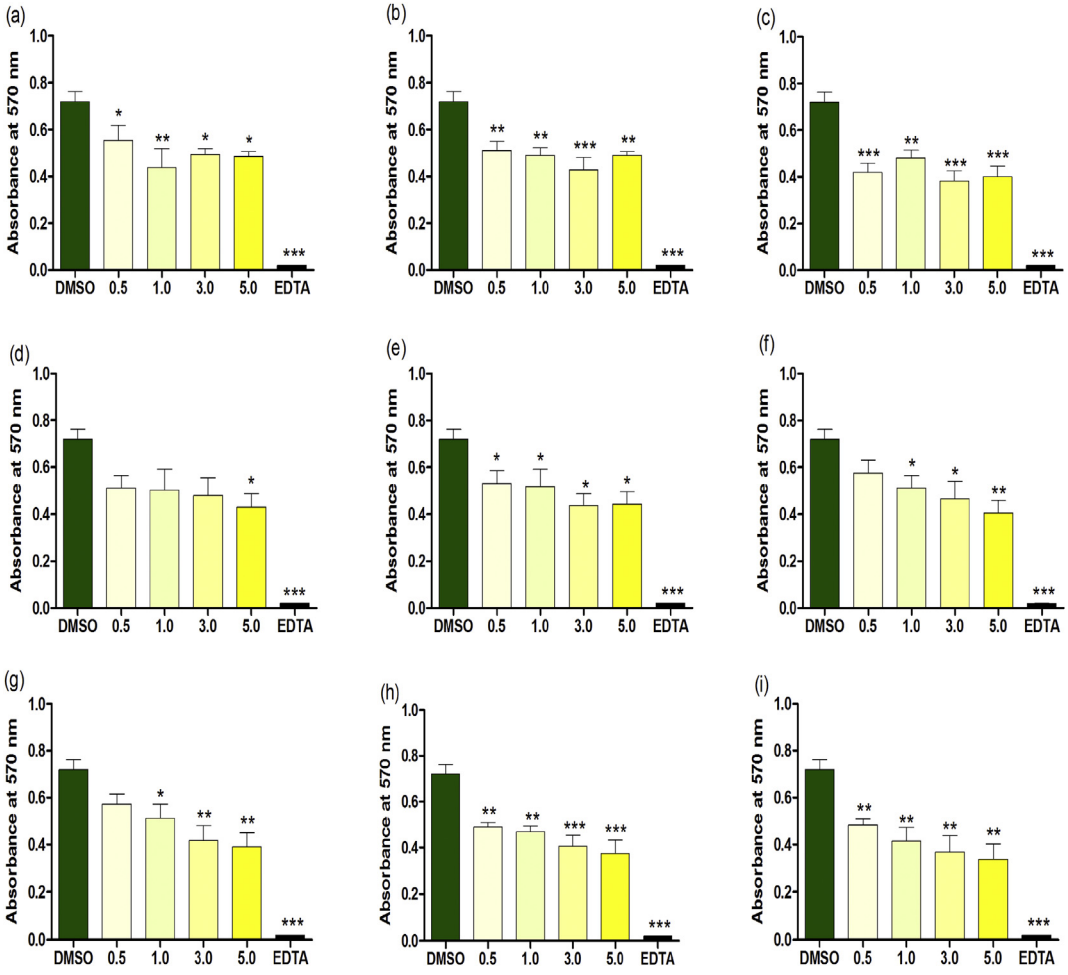

Fig. 7. Ferrous ion (Fe^{2+}) chelating activity of carbon nanotubes from CNT1 to CNT9 (a–i) at different concentrations (0.5, 1.0, 3.0 and 5 μg/ml) and EDTA (0.4 mM) control test used to indicate 100% to Fe^{2+} chelating activity. Experimental data are presented as the mean ± S.E of the absorbance values at 570 nm (n = 3). *: $p < 0.05$; **: $p < 0.01$; and ***: $p < 0.001$, compared with DMSO control (CNT-solvent or negative control) to express the Fe^{2+} ions non-chelating activity. (A colour version of this figure can be viewed online.)

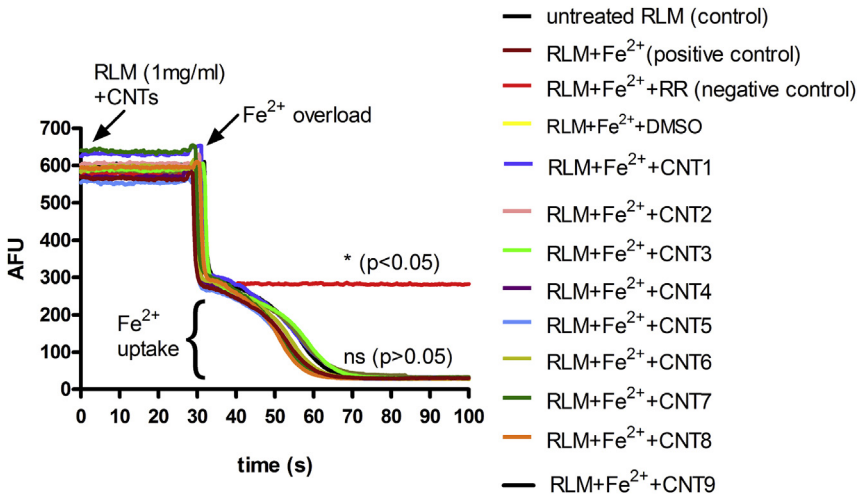

Fig. 8. Effects of CNT-family on mitochondrial Fe^{2+} ion uptake through (Ca^{2+}, Fe^{2+})-uniporter in RLM (1 mg/ml). Show that all the members of CNT-family (RLM from Fe^{2+} 20 μM + CNTs 5 μg/ml treated, colored CNT-lines: CNT1 to CNT9) not interfere with mitochondrial Fe^{2+}-influx. Significant statistical differences were not observed (ns) when compared with untreated-RLM and also with RLM from DMSO-treated (yellow line) between 30 and 100 s of mitochondrial Fe^{2+}-overexposure at 20 μM. RLM from ruthenium red (RR)-treated (red line) show marked significant statistical differences ($p < 0.05$) related to untreated-RLM and RLM from DMSO-treated (yellow line) between 30 and 100 s of mitochondrial Fe^{2+}-overexposure. Each CNTs and Fe^{2+} were added where indicated by the arrows. Results are representative of three experiments with different mitochondrial preparations. *Significantly different from control (untreated-RLM) at $p < 0.05$. (A colour version of this figure can be viewed online.)

The results obtained using the isolated liver-rat mitochondria *in vitro* model are consistent with the results of the recent work published by Zhenbao Liu et al. (2015) [8] using pristine and oxidized multi walled carbon nanotubes on human liver cell line L02, which reinforce the potential relevance for Nanomedicine. In addition, the results are consistent with *in silico* evidences obtained by Galano et al. (2010)[13], using semi-empirical methods based on Functional Density Theory (DFT), which suggests that the CNT-free radical scavenging activity is particularly increased for hydroxyl-Fenton radical (·OH), following a pattern of CNT-functionalization as oxidized-CNT (carboxylated-CNTs > hydroxilated-CNTs) > pristine-CNTs as mentioned in the Introduction of this work [13–17]. According to this idea, the use of computational tools has been recommended and recognized by the major regulatory agencies including the Organization for Economic Cooperation and Development (OECD, 2013) [46] and the International Organization for Standardization (ISO/TC 229, 2011) [47] based on the importance of developing alternative methods to evaluate the performance-related properties of new drugs (nanoparticles) toward therapeutic potential and nano-risks [46–48]. In this regard, very recently Gonzalez-Díaz et al. (2013) [26] formulated a general-purpose Perturbation Theory (PT) model for Chemoinformatics problems with multiple-boundary experimental conditions. In the present study the CNT-nanodescriptors, like CNT-minimum function/carbon ratio ($\%W_{min}$), CNT-maximum outer diameter (D_{max}), and experimental conditions as CNT-concentration (c_i) and time (t_i) expressed good linear correlation performance with the Fenton inhibition response for the *in silico* model performed with the experimental results obtained from H_2O_2-formation assays.

We identified three important relationships to explain the Fenton inhibition response by carbon nanotubes tested, which involve original input variables ${}^{i}V_k$ (CNT-nanodescriptors) and experimental boundary conditions mentioned above: **1)** CNT-function/carbon ratio, maximum outer diameter and time of exposure ($Wi_{min,}$ Di_{max} ↔ t_i) relationships; **2)** CNT-concentration-time of exposure (c_i ↔ t_i) relationships; and **3)** CNT-concentration, CNT-function/carbon ratio and maximum outer diameter (c_i ↔ $Wi_{min,}$ Di_{max}) relationships. For the first ($Wi_{min,}$ Di_{max} ↔ t_i)-relationship, the type of CNT-function/carbon ratio and/or relative position of these functional groups in the tips or sides of the oxidized-CNTs (Wi_{min} (%)) can increase proportionally the (·OH)-free radical scavenging activity according to the following order: carboxylated-CNT > hydroxylated-CNT ~ pristine-CNT; assuming that ·OH-radicals interactions with CNTs-structure take place at the most CNT-reactive sites as it has been suggested recently by Galano (2010) [6]. An increase of the CNT-functionalization [$W_{i\ min}$(%)] is able to increase the value of the Fenton inhibition response according to the observed and predicted values (AFU-outputs results) of the theoretical model. It has been recognized that CNT-covalent functionalization can generate different vacancies as adatom and Stones-Wales defects formed by rotating a C-C bond by 90° in the sidewalls of CNT-structure with loss of sp^2-carbon hybridization [13]. Moderate or partial oxidation is associated to the presence of point defects in the carbon lattice of CNT and, in this regard, it is predicted an increase of their free-radical scavenging activity probably involving C-atoms with dangling bonds which is expected to cause a larger increase of CNT reactivity toward free radicals than the Stones-Wales and vacancy defects without C-atoms with dangling bonds [13]. Carbon nanotubes covalently functionalized (oxidized-CNT) with point defects are also expected to have such ROS inhibitory activity, probably to a larger extent than the pristine carbon nanotubes. Particularly, the CNT-covalent functionalization through introduction of OH and COOH groups like the ones used in the present study is commonly associated with Stone-Wales point defect according to Galano (2010) [13]. This kind of CNT could increase the effect on the (•OH)-free-radical scavenging activity through interaction of hydroxyl radical on the CNTs walls and the formation of strong (•OH)-Fenton radical-oxidized-CNTs adducts [14–16]. It is known that the formation of new chemical bond is a time-dependent process and, in this regard, taking into account the exposure time (t_i) it is suggested the generation of a transient charge transfer complex between Fe^{2+} and the oxidized-CNT that should accelerate Fe^{2+} oxidation and formation of a more stable Fe^{3+}–oxidized-CNT complex, unable to participate in Fenton–Haber–Weiss reactions [18].

Regarding the CNT-concentration-time of exposure (c_i ↔ t_i) relationships, the experimental concentration to CNT (or carbon nanotubes dosimetry), is a significant endpoint to address biochemical target studies, particularly *in vitro* systems. In this context, the redox effects observed in mitochondria depend on the CNT-concentration and duration of exposure to a fixed level of response for a given endpoint, according to dose/time-response models based on the Haber's rule (law of toxicity) [49,50]. Following this criteria, the CNT-induced Fenton response (nanotoxicity) is a function of (c_i↔t_i) relationships. This issue should always be examined exhaustively regading the CNT-nanodescriptors (nanoparticle diameter, type of functionalization) and concentration captured by the biological model (isolated rat liver mitochondria). The CNT-properties are expected to significantly affect mitochondrial dose-uptake, but are largely ignored in the conduct of *in vitro* pharmacological studies for CNT. Herein the (c_i ↔ t_i) relationship for the dose-response linear QSPR-model found is consistent with studies performed by Miller et al. (2000) [49] suggesting that the experimental conditions c_i and t_i have a relevant influence.

For the relationship CNT-concentration, CNT-function/carbon ratio and maximum outer diameter (c_i ↔ $W_{i\ min,}$ $D_{i\ max}$), a high level of hydrophilic group functionalization on CNT can significantly reduce the CNT-partition coefficient lipid/water and consequently their solubility. Also, this should decrease the ability to internalize in the mitochondrial membranes, and the efficiency as ROS-scavenger regarding the biophysical environment in which it occurs (mitochondrial matrix) [19]. In the present study, the linear QSPR-model found expresses a good condition for modeling the mitochondrial ROS-inhibition (Fenton reaction) when considered the factors involved on the first relationship ($Wi_{min,}$ Di_{max} ↔ t_i). The predictive linear QSPR-model represented by equation (7) shows that the standard error for all the regression coefficients are significant at $p < 0.05$ while the model shows 90.1% explained variance and 90.1% predicted variance based on the training set data. The high value of the variance ratio F suggests stability of the regression coefficients while the low error (s) value indicates the goodness of fit. Different conventional external validation metrics (Q^2_{F1}, Q^2_{F2}, Q^2_{F3}, CCC, R^2_m) computed from the prediction for the test set show acceptable values suggesting the reliability of predictions from the QSPR-model. The external validation parameters (Q^2_{F1}, Q^2_{F2}, Q^2_{F3}, CCC, R^2_m) are valuable criteria of the predictive potential of a QSAR/QSPR model according to the literature: a model has predictive potential if their values exceed the predetermined value of 0.5 [40]. The application of the recently suggested MAE based criteria [27] after converting the response range and error value into log units showed that the predictions are of moderate quality [27,40]. It is straightforward to realize that the general model predicts linear behavior for different dose-effect series according to alternative models represented above by the equation (3) and (4) for the different CNT with different diameters, chemical functions and concentrations.

In addition, it was observed that CNT-family tested did not induce dissipation of mitochondrial membrane potential (Ψm) at the maximum concentration of 5 μg/ml in the presence of Fe^{2+} as

Fenton initiator for the two mitochondrial membrane potential tests applied (safranine O and JC-1) (see details in Fig. 5). In the presence of mitochondrial Fe^{2+}-overexposure, all CNTs tested were able to keep the Ψm avoiding the miptotic J-monomers formation, which are characteristic of mitochondrial dysfunction processes associated to ROS-increment and other pathological conditions, like induction of mitochondrial permeability transition pore (MPTP)-iron dependent. All these data indicate an unambiguous mitoprotection effect when compared to the strong uncoupling effects verified for the mitochondria from Fe^{2+} and CCCP treatments as shown (Fig. 5d and g). Consistent with this idea, the results obtained for the red: green fluorescence intensity ratio suggest that CNT can act preventing the dissipation of the mitochondrial electrochemical potential gradient (Ψm) which has been described as an early event in apoptosis (ferroptosis) [1].

According to recent experimental evidences obtained by González-Durruthy et al. (2015) [30], oxidized single and multi walled carbon nanotubes can act as mitoprotective agents based on their ability to prevent the mitochondrial permeability transition pore (MPTP) induced in strongest pro-oxidant conditions using Fe^{2+} ions overload with ascorbic acid 100 μM (a strong reducing agent) and H_2O_2 to generate hydroxyl free radical from Fenton-Haber-Weiss reaction experimentally induced in the context of mitochondrial swelling assays [30]. Therefore, the evidences suggest potential biomedical relevance of oxidized-CNT family, pointing that the ROS-inhibition could be associated with the CNT-ability to attenuate the loss of redox balance induced by the physiophatological concentration of ·OH radical [22].

Multi-walled carbon nanotubes have exhibited good electronic relation with redox proteins. It is also known the involvement of iron on free radicals production in several chronic diseases through induction of oxidative stress. Besides, the reduced metals such as Fe^{2+} can catalyze the production of Fenton hydroxyl radicals through the decomposition of preformed lipid hydroperoxides [10].

For this purpose, it was reproduced an electrochemical study published by Laine and Cheng (2009) [18] in order to measure the oxidized-CNT ability for the inhibition of Fenton reaction [18]. To this end, cyclic voltammograms for all CNT were recorded at a window potential (- 0.4 to 0.4 V), similar to a potential window observed in mitochondrial redox complexes (I and III) of the respiratory chain, which are the main sources of mitochondrial ROS generation.

In this regard we suggest that the weak Fenton inhibition response obtained for hydroxylated-CNT compared with carboxylated-CNT ≈ pristine-CNT (MWCNT-1) is consistent with its chemical structure (hydroxyl covalent functionalization). In this sense, the OH-oxidation of C=C double bonds can create sp^3 sites that do not offer the adjacent conjugated structure necessary for free radical resonance stabilization. For this reason, OH-moieties are not expected to exhibit strong antioxidant activity based on the results of electrochemical assays. In addition, the only source of phenolic groups (aromatic hydroxyl sites) would be at the hydroxyl-CNT tips, which could mimic to a lesser extent the free radical scavenging ability from poliphenolic systems present in antioxidants like quercetin. However, in hydroxylated-CNT most of OH-moieties must be non-phenolic, which is consistent with a low H-donor antioxidant activity towards hydroxyl radical scavenging effect [51].

Also the decrease of the catalytic process (cathodic peak current inhibition) observed in the cyclic voltammetric analysis may have occurred through two logical paths: first, a direct decomposition of H_2O_2 used in the Fenton-generation of hydroxyl radical by the presence of the carboxylated-CNT. According to Voitko et al. (2011) [52], the hydrogen peroxide decomposition kinetics process is inextricably linked to the surface chemistry, number, type of functional groups and ability to trap and deactivate free radicals (hydroxyl-Fenton radical). The second option is the chelation of the catalyst Fe^{2+}EDTA or ferrous ions complexation by carboxylated-CNT to form a Fe^{2+}-oxidized-CNT complex unable to participate in Fenton–Haber–Weiss reactions [18,52]. Curiously for pristine-CNT(MWCNT) it has been demonstrated that in aqueous suspension it does not generate oxygen free radicals in the presence of H_2O_2. On the contrary, it was observed that MWCNTs exhibit a remarkable free radical scavenging ability, when in contact with an external source of hydroxyl or superoxide radicals, suggesting that the walls of MWCNTs can act as oxygen free-radicals sponges for multiple ·OH radicals on the carbon lattice [14–17]. Taking into account the results of Fe^{2+} ions chelating activity, this mechanism seems to have a crucial role on the inhibition of Fenton chemistry and the potential therapeutic as hydroxyl-free radical scavenging of CNT-family tested. Because it is well recognized that elemental metal species such as ferrous iron (Fe^{2+}) can facilitate the hydroxyl free radical generation and lipid peroxidation, therefore the ability of oxidized CNT to chelate iron in its reduced state can be a relevant antioxidant capability by retarding metal-catalyzed oxidation [44,45]. Even though ferric ions Fe^{3+} also produce oxygen radicals from peroxides, the rate is tenfold lower than that of ferrous Fe^{2+} [38].

It is also known that the covalent functionalization of carbon nanotubes (hydroxylation, carboxylation) can activate small molecules and increase the scope of their use. In particular, metal porphyrins such as mitochondrial complexes can display strong π-stacking interactions for the case of pristine-MWCNT sidewalls or through immobilization of iron center by oxidized-MWCNT [53], which allows their stable binding and consequently their use in the oxygen reduction [54–56].

In the context of the present study, the oxidized-CNT/iron (Fe^{3+}) porphyrin formed complexes might exhibit catalytic properties towards the complete oxygen reduction reaction to H_2O from the H_2O_2 and in this way avoid the Fenton reaction in the presence of external high concentration of Fe^{2+} ions as shown in the experimental ROS assays using horseradish peroxidase, a classical enzyme to detect H_2O_2 [56,57]. Following this idea, a direct complexation of mitochondrial iron (as Fe^{2+}) has been suggested as an attractive therapeutic strategy for several clinical disorders involving ROS-imbalance and iron overload [58]. The evidences obtained in the present study suggests that the inhibition of mitochondrial ROS-formation experimentally induced by Fenton reaction could involve the electrostatics binding interaction of the COO^- groups of oxidized-CNT with the reduced state (Fe^{2+}) of metallic heme-centers in the mitochondrial complexes (I and III, known to be mitochondrial ROS producers). Nevertheless, for the only pristine-CNT tested, the non-substituted rings present an extensive π-conjugated system, also could favor iron (Fe^{2+})-chelation.

The mitochondrial iron Fe^{2+} uptake has been recognized as relevant mechanism involved in mitochondrial permeability transition pore (MPTP) when present in non-physiological concentrations. The study of the influence of CNT-family on the mitochondrial Fe^{2+} ions influx was performed to verify the hypothesis of a potential pharmacodynamics inhibition of mitochondrial (Ca^{2+}, Fe^{2+}) uniporter by the CNT assayed. In this sense, this divalent cation channel was able to retain its physiological function for all CNT-tested at their maximum concentration (5 μg/ml). This characteristic was observed by Geng et al. (2014) [59] using oxidized-CNT porin, showing the potential of carboxylated-SWCNT as efficient synthetic analogues of biological membrane channels. According to the mentioned authors, carboxylated-CNT can spontaneously insert into cellular and mitochondrial membrane lipid bilayers to form channels (CNT-porin), which exhibit high selectivity for ion transport and unitary conductance of 70–100 pS without affecting membrane functionality [59]. Based

on these criteria, we suggest that the negative charge of (COO^-)-moiety of carboxylated-CNT could favor the mitochondrial ferrous cations passage. In addition, we must take into account that the natural biophysical environment of Fenton-Haber-Weiss reaction is located in the mitochondrial matrix. This fact is consistent with the results obtained for JC-1 mitochondrial membrane potential probe in the presence of Fe^{2+} and CNT, where the miptotic J-monomers formation and its attenuation occur spatially in the mitochondrial matrix. Mitoprotective activity of carbon nanotubes family (oxidized-CNT > pristine-CNT) towards Fenton free radical scavenging activity, from a temporal point of view occurs after approximately 30–60 s of the iron (Fe^{2+}) uptake by the mitochondrial (Ca^{2+}, Fe^{2+}) uniporter.

Finally, considering the potential CNT-biomedical applications, the carboxyl-groups (oxidized-CNT) and other structural parameters as π-conjugated aromatic network (pristine-MWCNT) could be considered as a relevant CNT-redox moieties or free radical scavenger-pharmacophores to address the potential activity of CNT against Fenton reaction based on the Fe^{2+} complexing activity [13–15,58]. Also, the electrochemical results suggest that the CNT diameter could influence in the inhibition of Fenton catalytic process based on the modulation of Fe^{2+}-CNT side wall electron transfer [8,15]. This relation has been observed by Chenguo Hu et al. (2005) [60] and it was explained above in the theoretical model.

The obtained results open several pathways to assess the risk-benefit relationships to study the exposure to manufactured carbon nanomaterials and can contribute to the rational design of new CNT with potential significance in nanomedicine.

5. Conclusion

Mixed experimental-theoretical methodologies were used to study the effects of different CNT on the Fenton radical scavenging ability against Fenton-Haber-Weiss reaction experimentally induced by Fe^{2+} overload. The pertinent properties of CNT (oxidized-CNT) towards mitochondrial redox mechanisms are still poorly understood nowadays. Our results suggest that the CNT ability to inhibit the electrocatalytic Fenton reaction in Fe^{2+} overload pro-oxidant condition, depends primarily on the structural parameters such as CNT-functionalization, CNT-diameter and also optimal experimental conditions of exposure like CNT-concentration and exposure time, according to the results of the theoretical QSPR-model. Other essential conclusions from this work is that carboxylated-CNT are better than their pristine and hydroxylated CNT analogues to inhibit the electrocatalytic formation of hydroxyl Fenton radical associated to their Fe^{2+} ions complexing ability and also in concentration dependent manner. However, it should be emphasized that the good relationship biocompatibility/nanotoxicity for the best carbon nanotubes (carboxylated-CNTs) against Fenton reaction mechanism is not limited to the presence of carboxylic groups but also to exposure experimental conditions.

According to the experimental and theoretical results, mitochondrial redox effects could be useful for the prediction of new CNT-endpoints (or CNT-pharmacophores) toward Fenton free-radical scavenger ability, including carbon nanotubes not tested in our original database. Finally, the present work can contribute for the rational design of novel carbon nanomaterials and opening new opportunities to emergent areas of research as Mitochondrial Nanomedicine as alternative for the treatment of several chronic diseases (hepatotoxicity, Alzheimer, Parkinson, cancer, etc.) where pathological Fenton-reaction mechanisms have been directly involved.

Acknowledgements

M. González-Durruthy acknowledges Doctoral fellowship (Postgraduate Students Program PEC-PG No. 062/2013) from Brazilian Agencies CAPES-CNPq. Furthermore M. González-Durruthy thanks Professor PhD Alla P. Toropova from the IRCCS-Istituto di Ricerche Farmacologiche “Mario Negri” for her valuable contribution to the review of this work. J.M. Monserrat is a productivity fellow from CNPq. M. González-Durruthy and José M. Monserrat are part of the Nanotoxicology Network from CNPq (Project number 552131/2011-3) entitled “Nanotoxicologia ocupacional e ambiental: subsídios científicos para estabelecer marcos regulatórios e avaliação de riscos”) given to J.M. Monserrat. J.M. Monserrat also acknowledges funds CNPq (Project 452088/2015-1). Authors would like to acknowledge the support from CEMESUL-FURG for logistical support in carbon nanotubes characterization.

Appendix A. Supplementary data

Supplementary data related to this article can be found at http://dx.doi.org/10.1016/j.carbon.2017.01.002.

References

[1] S.J. Dixon, K.M. Lemberg, M.R. Lamprecht, R. Skouta, E.M. Zaitsev, C.E. Gleason, et al., Ferroptosis: an iron-dependent form of non-apoptotic cell death, Cell 149 (2012) 1060–1072.
[2] A.L. Nieminen, J. Schwartz, H.I. Hung, E.R. Blocker, M. Gooz, J.J. Lemasters, Mitoferrin-2 (MFRN2) regulates the electrogenic mitochondrial calcium uniporter and interacts physically with MCU, Biophys. J. 106 (2014) 581–582.
[3] A. Uchiyama, J.S. Kim, K. Kon, H. Jaeschke, K. Ikejima, S. Watanabe, et al., Translocation of iron from lysosomes into mitochondria is a key event during oxidative stress-induced hepatocellular injury, Hepatol 48 (2008) 1644–1654.
[4] S. Kumfu, S. Chattipakorn, S. Fucharoen, N. Chattipakorn, Mitochondrial calcium uniporter blocker prevents cardiac mitochondrial dysfunction induced by iron overload in thalassemic mice, Biometals 25 (2012) 1167–1175.
[5] M. Prato, K. Kostarelos, A. Bianco, Functionalized carbon nanotubes in drug design and discovery, Acc. Chem. Res. 41 (2008) 60–68.
[6] A. Galano, Carbon nanotubes: promising agents against free radicals, Nanoscale 2 (2010) 373–380.
[7] Z. Yang, Y. Zhang, Y. Yang, L. Sun, D. Han, H. Li, C. Wang, Pharmacological and toxicological target organelles and safe use of single-walled carbon nanotubes as drug carriers in treating Alzheimer disease, Nanomed Nanotechnol. Biol. Med. 6 (2010) 427–441.
[8] D. Elgrabli, W. Dachraoui, C. Ménard-Moyon, X.J. Liu, D. Begin, S. Begin-Colin, A. Bianco, F. Gazeau, D. Alloyeau, Carbon nanotube degradation in macrophages: live nanoscale monitoring and understanding of biological pathway, ACS Nano 9 (2015) 10113–10124.
[9] Y. Zhao, B.L. Allen, A. Star, Enzymatic degradation of multiwalled carbon nanotubes, J. Phys. Chem. A 115 (2011) 9536–9544.
[10] Z. Liu, Y. Liu, D. Peng, Carboxylation of multiwalled carbon nanotube attenuated the cytotoxicity by limiting the oxidative stress initiated cell membrane integrity damage, cell cycle arrestment, and death receptor mediated apoptotic pathway, J. Biomed. Mat. Res. A 103 (2015) 2770–2777.
[11] R.M. Lucente-Schultz, V.C. Moore, A.D. Leonard, B.K. Price, D.V. Kosynkin, M. Lu, et al., Antioxidant single walled carbon nanotubes, J. Am. Chem. Soc. 131 (2009) 3934–3941.
[12] S.F. Ye, Y.H. Wu, Z.Q. Hou, Q.Q. Zhang, ROS and NF-kappaB are involved in upregulation of IL-8 in A549 cells exposed to multi-walled carbon nanotubes, Biochem. Biophys. Res. Comm. 379 (2009) 643–648.
[13] A. Galano, M. Francisco-Marquez, A. Martinez, Influence of point defects on the free radical scavenging capability of single-walled carbon nanotubes, J. Phys. Chem. C 114 (2010) 8302–8308.
[14] M. Francisco-Marquez, A. Galano, A. Martinez, On the free radical scavenging capability of carboxylated single-walled carbon nanotubes, J. Phys. Chem. C 114 (2010) 6363–6370.
[15] A. Galano, Influence of diameter, Length, and chirality of single-walled carbon nanotubes on their free radical scavenging capability, J. Phys. Chem. C 113 (2009) 18487–18491.
[16] A. Martinez, A. Galano, Free radical scavenging activity of ultra short single walled carbon nanotubes with different structures through electron transfer reactions, J. Phys. Chem. C 114 (2010) 8184–8191.
[17] A. Martínez, M. Francisco-Marquez, A. Galano, Effect of different functional groups on the free radical scavenging capability of single-walled carbon nanotubes, J. Phys. Chem. C 114 (2010) 14734–14739.
[18] F. Laine, I.F. Cheng, Analysis of hydrogen peroxide and an organic hydroperoxide via the electrocatalytic Fenton reaction, Microchem. J. 91 (2009) 78–81.

[19] X. Ma, L.H. Zhang, L.R. Wang, X. Xue, J.H. Sun, Y. Wu, et al., Single-walled carbon nanotubes alter cytochrome C electron transfer and modulate mitochondrial function, ACS Nano 6 (2012) 10486–10496.
[20] S.M. Bachilo, M.S. Strano, C. Kittrell, R.H. Hauge, R.E. Smalley, R.B. Weisman, Structure-assigned optical spectra of single-walled carbon nanotubes, Science 298 (2002) 2361–2365.
[21] J.D. Rush, W.H. Koppenol, Reactions of Fe(II)-ATP and Fe(II)-citrate complexes with t-butyl hydroperoxide and cumyl hydroperoxide, FEBS Lett. 275 (1990) 114–116.
[22] S. Toyokuni, Iron-induced carcinogenesis: the role of redox regulation, Free Radic. Biol. Med. 20 (1996) 553–566.
[23] M.J. Zhao, L. Jung, Kinetics of the competitive degradation of the oxyribose and other molecules by hydroxyl radicals produced by the Fenton reaction in the presence of ascorbic acid, Free Radic. Res. 23 (1995) 229–243.
[24] K.D. Welch, T.Z. Davies, S.D. Aust, Iron autoxidation and free radical generation: effects of buffer, ligands and chelators, Arch. Biochem. Biophys. 397 (2002) 360–369.
[25] A.A. Toropov, A.P. Toropova, Quasi-QSAR for mutagenic potential of multi-walled carbon-nanotubes, Chemosphere 124 (2015) 40–46.
[26] H. González-Díaz, S. Arrasate, A. Gómez-San Juan, N. Sotomayor, E. Lete, L. Besada-Porto, et al., General theory for multiple input-output perturbations in complex molecular systems. 1. Linear QSPR electronegativity models in Physical,Organic, and medicinal chemistry, Curr. Top. Med. Chem. 13 (2013) 1713–1741.
[27] K. Roy, R.N. Das, P. Ambure, R.B. Aher, Be aware of error measures. Further studies on validation of predictive QSAR models, Chemom. Intell. Lab. Sys. 152 (2016) 18–33.
[28] A.A. Toropov, D. Leszczynska, J. Leszczynski, Predicting water solubility and octanol water partition coefficient for carbon nanotubes based on the chiral vector, Comput. Biol. Chem. 31 (2007) 127–128.
[29] A.P. Toropova, A.A. Toropov, R. Rallo, D. Leszczynska, J. Leszczynski, Nano-QSAR: genotoxicity of multi-walled carbon nanotubes, Int. J. Environ. Res. 10 (2016) 59–64.
[30] M. González-Durruthy, J.M. Monserrat, L.C. Alberici, Z. Naal, C. Curti, H. González-Díaz, Mitoprotective activity of oxidized carbon nanotubes against mitochondrial swelling induced in multiple experimental conditions and predictions with new expected-value perturbation theory, RSC Adv. 5 (2015) 103229–103245.
[31] H. Poincaré, Sur le probléme des trois corps et les eéquations de la dynamique, Ac Mathem. 13 (1890) 1–270.
[32] E.L. Bouzarth, A. Brooks, R. Camassa, H. Jing, T.J. Leiterman, R.M. McLaughlin, Epicyclic orbits in a viscous fluid about a precessing rod: theory and experiments at the micro- and macro-scales, Phys. Rev. E 76 (2007) 016313.
[33] H.T. Ham, Y.S. Choi, I.J. Chung, An explanation of dispersion states of single-walled carbon nanotubes in solvents and aqueous surfactant solutions using solubility parameters, J. Colloid Interface Sci. 286 (2005) 216–223.
[34] S.D. Bergin, Z. Sun, P. Streich, J. Hamilton, J.N. Coleman, New solvents for nanotubes: approaching the dispersibility of surfactants, J. Phys. Chem. C 114 (2010) 231–237.
[35] P.L. Pedersen, J.W. Greenawalt, B. Reynafarje, J. Hullihen, G.L. Decker, J.W. Soper, Preparation and characterization of mitochondria and submitochondrial particles of rat liver and liver derived tissues, Meth. Cell Biol. 20 (1978) 411–481.
[36] A.A. Starkov, Measurement of mitochondrial ROS production, Meth Mol. Biol. 648 (2010) 245–255.
[37] S. Toyokuni, Iron as a target of chemoprevention for longevity in humans, Free Radic.Res. 45 (2011) 906–917.
[38] A. Kuban-Jankowska, M. Gorska, L. Jaremko, M. Jaremko, J.A. Tuszynski, M. Wozniak, The physiological concentration of ferrous iron(II) alters the inhibitory effect of hydrogen peroxide on CD45, LAR and PTP1B phosphatases, BioMetals 28 (2015) 975–985.
[39] M. Leopoldini, N. Russo, S. Chiodo, M. Toscano, Iron chelation by the antioxidant flavonoid quercetin, J. Agric. Food Chem. 54 (2006) 6343–6351.
[40] K. Roy, S. Kar, R.N. Das, Cap7 Understanding the Basics of QSAR for Applications in Pharmaceutical Sciences and Risk Assessment, first ed., Academic Press, 2015, pp. 233–239.
[41] J.J. Liao, R. Liu, Re-parameterrization of five-parameter logistic function, J. Chemomet. 23 (2009) 248–253.
[42] K.E. Åkerman, M.K. Wikström, Safranine as a probe of the mitochondrial membrane potential, FEBS Lett. 68 (1976) 191–197.
[43] M. Reers, T.W. Smith, L.B. Chen, J-aggregate formation of a carbocyanine as a quantitative fluorescent indicator of membrane potential, Biochem. 30 (1991) 4480–4486.
[44] T.C. Dinis, V.M. Madeira, L.M. Almeida, Action of phenolic derivates (acetoaminophen, salycilate, and 5-aminosalycilate) as inhibitors of membrane lipid peroxidation and as peroxyl radical scavengers, Arch. Biochem. Biophys. 315 (1994) 161–169.
[45] J.P. Kehrer, The Haber–Weiss reaction and mechanisms of toxicity, Toxicol 149 (2000) 43–50.
[46] OECD Principles for the validation, for regulatory purposes of (Quantitative) Structure Activity Relationship Model. http:www.oecd.org/ (Accessed 9 March 2016).
[47] ISO/TC 229 Nanotech., (2011).
[48] M. Foldvari, M. Bagonluri, Carbon nanotubes as functional excipients for nanomedicines: I. pharmaceutical properties, Nanomed Nanotechnol. Biol. Med. 4 (2008) 173–182. DPharmSci.
[49] F.J. Miller, P.M. Schlosser, D.B. Janszen, Haber's rule: a special case in a family of curves relating concentration and duration of exposure to a fixed level of response for a given endpoint, Toxicol. Appl. Pharmacol. 149 (2000) 21–34.
[50] K. Chan, D. Truong, N. Shangari, O'Brien, Drugs-induced mitochondrial toxicity, Expert Opin. Drug Metab. Toxicol. 4 (2005) 655–669.
[51] Y. Qiu, Z. Wang, A.C. Owens, I. Kulaots, Y. Chen, A.B. Kane, R.H. Hurt, Antioxidant chemistry of graphene-based materials and its role in oxidation protection technology, Nanoscale 6 (2014) 11744–11755.
[52] K.V. Voitko, R.L.D. Whitby, V.M. Gun'ko, O.M. Bakalinska, M.T. Kartel, K. Laszlo, et al., Morphological and chemical features of nano and macroscale carbons affecting hydrogen peroxide decomposition in aqueous media, J. Colloid Interface Sci. (2011), http://dx.doi.org/10.1016/j.jcis.2011.05.048.
[53] K. Elouarzaki, A.L. Goff, M. Holzinger, J. Thery, S. Cosnier, Electrocatalytic oxidation of glucose by rhodium porphyrin-functionalized MWCNT electrodes: application to fully molecular catalyst-based glucose/O_2 fuel cell, J. Am. Chem. Soc. 134 (2012) 14078–14085.
[54] I. Hijazi, T. Bourgeteau, R. Cornut, A. Morozan, A. Filoramo, J. Leroy, et al., Carbon nanotubes-templated sintesis of covalent porphyrin network for oxygen reduction reaction, J. Am. Chem. Soc. 136 (2014) 6348–6354.
[55] A. Morozan, S. Campidelli, A. Filoramo, B. Jousselme, S. Palacin, Catalytic activity of cobalt and iron phthalocyanines or porphyrins supported on different carbón nanotubes towards oxygen reduction reaction, Carbon 49 (2011) 4839–4847.
[56] R. Cao, R. Thapa, H. Kim, X. Xu, M.G. Kim, Q. Li, et al., Promotion of oxygen reduction by a bio-inspired tethered iron phthalocyanine carbon-based catalyst, Nat. Commun. 4 (2013) 2076.
[57] B. Reuillard, S. Gentil, M. Carrière, A.L. Goff, S. Cosnier, Biomimetic versus enzymatic high-potential electrocatalytic reduction of hydrogen peroxide on a functionalized carbon nanotube electrode, Chem. Sci. 6 (2015) 5139–5143.
[58] G.L. Pardo-Andreu, T.R. Delgado, J.A. Velho, C. Curti, A.E. Vercesi, Iron complexing activity of mangiferin, a naturally occurring glucosylxanthone, inhibits mitocondrial lipid peroxidation induced by Fe^{2+}-citrate, Eur. J. Pharmacol. 513 (2005) 47–55.
[59] J. Geng, K. Kim, J. Zhang, A. Escalada, R. Tunuguntla, L.R. Comolli, et al., Stochastic transport through carbon nanotubes in lipid bilayers and live cell membranes, Nature 514 (2014) 612–615.
[60] C. Hu, Y. Zhang, G. Bao, Y. Zhang, M. Liu, Z.L. Wang, Diameter-dependent voltammetric properties of carbon nanotubes, Chem. Phys. Lett. 418 (2005) 520–525.

Artigo 4: Decrypting Strong and Weak Single-Walled Carbon Nanotubes Interactions with Mitochondrial Voltage-Dependent Anion Channels Using Molecular Docking and Perturbation Theory

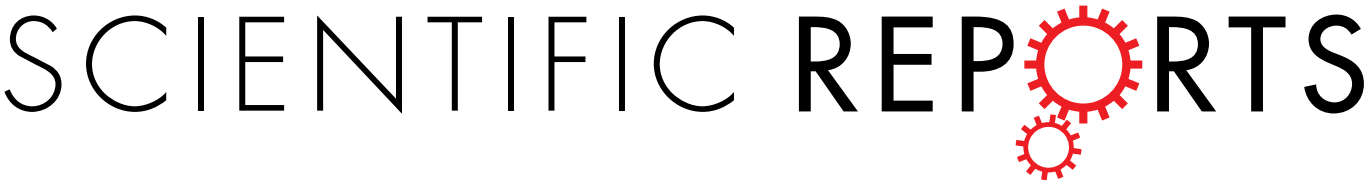

OPEN

Received: 2 June 2017
Accepted: 25 September 2017
Published online: 16 October 2017

Decrypting Strong and Weak Single-Walled Carbon Nanotubes Interactions with Mitochondrial Voltage-Dependent Anion Channels Using Molecular Docking and Perturbation Theory

Michael González-Durruthy[1], Adriano V. Werhli[2], Vinicius Seus[2], Karina S. Machado[2], Alejandro Pazos[3,4], Cristian R. Munteanu[4], Humberto González-Díaz[5,6] & José M. Monserrat[1]

The current molecular docking study provided the Free Energy of Binding (FEB) for the interaction (nanotoxicity) between VDAC mitochondrial channels of three species (VDAC1-*Mus musculus*, VDAC1-*Homo sapiens*, VDAC2-*Danio rerio*) with SWCNT-H, SWCNT-OH, SWCNT-COOH carbon nanotubes. The general results showed that the FEB values were statistically more negative ($p < 0.05$) in the following order: (SWCNT-VDAC2-*Danio rerio*) > (SWCNT-VDAC1-*Mus musculus*) > (SWCNT-VDAC1-*Homo sapiens*) > (ATP-VDAC). More negative FEB values for SWCNT-COOH and OH were found in VDAC2-*Danio rerio* when compared with VDAC1-*Mus musculus* and VDAC1-*Homo sapiens* ($p < 0.05$). In addition, *a* significant correlation ($0.66 > r^2 > 0.97$) was observed between *n*-Hamada index and VDAC nanotoxicity (or FEB) for the zigzag topologies of SWCNT-COOH and SWCNT-OH. Predictive Nanoparticles-Quantitative-Structure Binding-Relationship models (nano-QSBR) for strong and weak SWCNT-VDAC docking interactions were performed using Perturbation Theory, regression and classification models. Thus, 405 SWCNT-VDAC interactions were predicted using a nano-PT-QSBR classifications model with high accuracy, specificity, and sensitivity (73–98%) in training and validation series, and a maximum AUROC value of 0.978. In addition, the best regression model was obtained with Random Forest (R^2 of 0.833, RMSE of 0.0844), suggesting an excellent potential to predict SWCNT-VDAC channel nanotoxicity. All study data are available at https://doi.org/10.6084/m9.figshare.4802320.v2.

VDAC is the most abundant and highly conserved channel-protein in outer mitochondrial membrane of cells from all eukaryotic kingdoms including human (*Homo sapiens*). VDAC is the main communication route between this organelle and cytosol, generating the mitochondrial membrane potential, sucrose exchange, mitochondrial [Ca^{2+}] dynamics and ATP-efflux between these two cellular compartments[1–4]. Besides, VDAC is an

[1]Institute of Biological Sciences (ICB)- Federal University of Rio Grande - FURG, Postgraduate Program in Physiological Sciences, Cx. P. 474, CEP 96200-970, Rio Grande, RS, Brazil. [2]Center of Computational Sciences (C3)- Federal University of Rio Grande - FURG, Cx. P. 474, CEP 96200-970, Rio Grande, RS, Brazil. [3]Biomedical Research Institute of A Coruña (INIBIC), University Hospital Complex of A Coruña (CHUAC), A Coruña, 15006, Spain. [4]RNASA-IMEDIR, Computer Science Faculty, University of A Coruña, Campus de Elviña s/n, 15071, A Coruña, Spain. [5]Department of Organic Chemistry II, University of the Basque Country UPV/EHU, 48940, Leioa, Spain. [6]IKERBASQUE, Basque Foundation for Science, 48011, Bilbao, Spain. Correspondence and requests for materials should be addressed to M.G.-D. (email: gonzalezdurruthy.furg@gmail.com)

essential component of the induced-structure of mitochondrial permeability transition pore (MPTP-VDAC), a multi-protein complex that is directly involved in mitochondrial dysfunction (apoptosis)[5–9].

Carbon nanotubes (CNT) are nanomaterials considered for biomedical applications due to their flexible nature and versatility for chemical functionalization/oxidation (e.g. OH, COOH)[10,11]. More specifically, single-walled carbon nanotubes (SWCNT) have rapidly become one of the most widely studied nanomaterials, based on their unique physico-chemical properties that allow their potential use in new nanomedicine applications like pharmaceutical excipients for the design of several drug delivery systems[10,11].

The VDAC channel inhibition by SWCNT could be an attractive therapeutic strategy to induce mitotoxicity based on specific VDAC-modulation. Following this idea, the chemo-informatics tools based on Docking Simulation (DS)[12] appears to be an efficient strategy for the potential nanotoxicity prediction and SWCNT environmental impact. The use of Docking Simulation coupled to a Virtual Screening Framework (DS-VSF)[12,13] is a powerful new platform for the rational design of a new SWCNT before its mass production, allowing for the computational interaction analysis of a large volume of SWCNT designs with key molecular targets[14,15]. Several *in vitro* studies have demonstrated that SWCNTs exert their cytotoxicity mechanism after their accumulation in the mitochondria matrix[16,17].

In this context, chemoinformatics algorithms may be also very useful to predict carbon nanomaterial structure-activity relationships (QSAR models). Specifically, the term Quantitative Structure-Binding Relationships (QSBR) model is used for ligand-protein interactions. In the particular case of Nanoparticles we can talk about Nano-QSAR (NQSAR) or Nano-QSBR (NQSBR) models, by analogy. In general, these NQSAR/NQSBR models use as input physico-chemical properties of nanoparticles (nanodescriptors) to predict their biological activity, toxicity, and/or target-binding affinity[18–29]. The main assumption of classic QSAR algorithms in general form is that the similar structures (ligands) have similar properties. Consequently, small structural changes ("perturbations") should correlate linearly with small changes in the values of their properties biological (endpoints). NQSAR/NQSBR models based on Perturbation Theory use as a first parameter the value of an exact solution to the problem. This first parameter represents a known value of biological property used as reference value (or an expected value of this endpoint). After that, the PT-NQSAR model add small corrections (functions of nanodescriptors for one specific case) to predict a solution to a related problem[18,30–32]. In principle, there is a large variety of data analysis techniques that have proven to be effective in QSAR/QSBR modeling in general (including NQSAR and PT-NQSAR models). Examples of these techniques are: Linear Discriminant Analysis (LDA), Neural Networks (NN), Random Forest (RF), *etc*.[33–38]. Last, we should note that, NQSAR/NQSBR algorithms should have the ability of feature selection (FS) to exclude redundant nanodescriptors before NQSAR model building[39,40]. Specifically, (*n*, *m*)-Hamada indices (related to SWCNT-chiral topology and SWCNT-diameter) may become interesting candidates to input variables in NQSAR/NQSBR studies[18]. The electro-topological and constitutional SWCNT nanodescriptors for pristine SWCNT and oxidized SWCNT (SWCNT-OH, SWCNT-COOH), based on the information of SWCNT-periodic properties[41–45], have not yet been considered from the perspective of NQSAR with respect to their relevant interactions with mitochondrial channels, such as voltage-dependent anion channel (VDAC).

In this context, the main objective of this study was to evaluate *in silico* interactions (or mitochondrial channel nanotoxicity) between pristine and oxidized SWCNT and VDAC from different species (VDAC1-*Mus musculus*, VDAC1-*Homo sapiens*, and VDAC2-*Danio rerio*) using DS-VSF Chemoinformatic tools. These models are expected to be able to predict the strength of SWCNT-interaction and to quantify the structural requirements of SWCNT family governing the strong or weak SWCNT-VDAC interactions. In this sense, after docking studies we developed a new PT-NQSBR model using as input SWCNT-structural properties (Hamada indices, *etc*.) and *Free Energy of Binding* (*FEB* values), obtained after DS to perform a PT-NQSBR model based on LDA technique. LDA was implemented because it allows explaining the linear relationship between the input variables (SWCNT-structural properties) and 'nanotoxicological endpoint' (FEB values). To verify potential errors in the linear relationship hypothesis on SWCNT nanodescriptors/VDAC channel nanotoxicity, new non-linear classification and regression models were proposed. These non-linear PT-NQSBR models are based on machine learning algorithms implemented on Weka and RRegrs (R package)[33–38]. The present work could pave the way for the use of chemo-informatics tools based on SWCNT-ligand and mitotarget docking interactions for making regulatory decisions in Nanotoxicology, allowing the prediction of potential human health impact and environment risks.

Results and Discussion

Mechanistic interpretation of molecular docking results. The present work evaluated the relationships between all the semi-empirical geometric and physico-chemical SWCNT-nanodescriptors inspired by their periodic properties[41–46] and FEB values from the different SWCNT-VDAC complexes formed. Herein, FEB-mean values of the SWCNT-VDAC complexes were significantly negative ($p < 0.05$) when compared with FEB-mean values of the ATP-VDAC complexes, following a higher binding stability for SWCNT-VDAC complexes formed like FEB (SWCNT-VDAC2-*Danio rerio* complexes) > FEB (SWCNT-VDAC1-*Mus musculus* complexes) > FEB (SWCNT-VDAC1-*Homo sapiens* complexes) in all cases. Nevertheless, higher values of oxidized SWCNT interactions for FEB (SWCNT-COOH > SWCNT-OH) were found in VDAC2-*Danio rerio* when compared to VDAC1-*Homo sapiens* and VDAC1-*Mus musculus* ($p < 0.05$) (Fig. 1).

According to the evidence obtained by Hiller *et al*.[47] the VDAC channel diameter of wall-to-wall is ~34–38 Å, the maximum dimension limits being those allowing SWCNT-interaction with the VDAC-binding active site. Indeed, the assayed SWCNT diameters oscillated from 2.35 to 12.21 Å in the DS and, in all cases, the length was 10 Å, meaning that under the *in silico* conditions employed here, there were no steric constraints for the SWCNT-VDAC interaction with the VDAC-catalytic site. However, in general, a high proximity of the SWCNT family members with the voltage-sensing N-terminal α segment was observed, which is interesting because it explains the toxicodynamic mechanisms based on SWCNT properties and interatomic distances to key

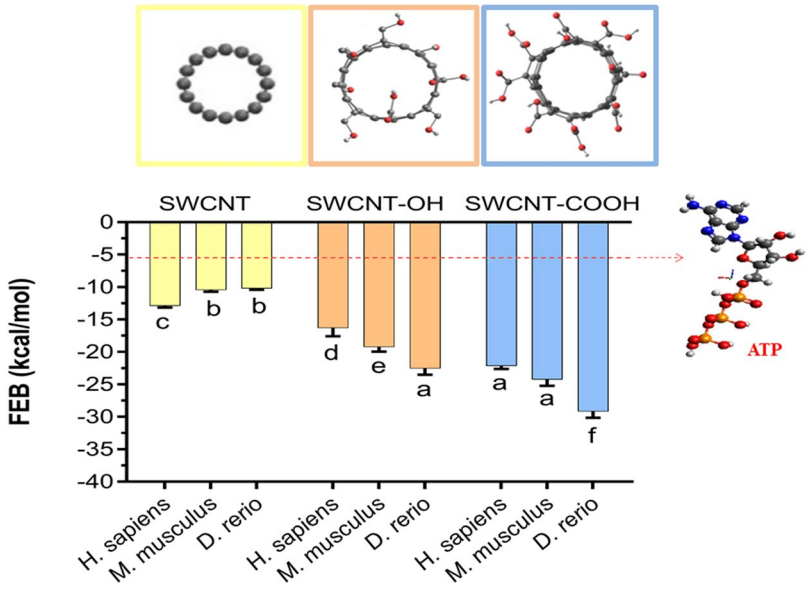

Figure 1. Free energy binding (FEB, in kcal mol^{-1}) of mitochondrial voltage-dependent anion channel (VDAC) with pristine, hydroxylated and carboxylated single-walled carbon nanotubes (SWCNT, SWCNT-OH and SWCNT-COOH, respectively). Each FEB-value is expressed in terms of the mean ±1 error standard (n = 14–93) from the different SWCNT-VDAC complexes evaluated. Equal letters indicate the absence of significant differences ($p > 0.05$) between the different single-walled carbon nanotubes. The dotted red line represents the average FEB value (−5.6 ± 1 Kcal/mol) determined for the adenosine triphosphate (ATP), a natural substrate of the VDAC channel from the three different species like VDAC1-*Homo sapiens* (PDB ID: 2JK4, Resolution 4.1 Å), VDAC1-*Mus musculus* (PDB ID:3EMN, Resolution 2.3 Å), VDAC2-*Danio rerio* (PDB ID:4BUM, Resolution 2.8 Å) used as control. In all cases, the results were obtained using docking simulations (see Methods for details).

VDAC-functional and regulatory residues. The oxidized SWCNT-moieties (COO^- and OH) could be relevant for electrostatic interactions with the VDAC hydrophobic binding active site formed by cationic residues (arginine and lysine) closely involved in the each of the phases of mitochondrial ATP-transportation[1]. Moreover, the FEB docking results obtained for the electro-topological SWCNT-properties (diameter-chiral topology and functionalization) and the VDAC-affinity relationship suggest that the Hamada index *n* is a valuable SWCNT nanodescriptor, able to predict the SWCNT-VDAC interactions in zigzag SWCNT topologies ($n > 0$; $m = 0$) based on the determination coefficient (R^2). In this regard, a significant linear correlation ($0.66 \leq R^2 \leq 0.97$; $p < 0.05$) was observed between *n* and FEB for all zigzag SWCNT topologies. However, theR^2 between *n* and FEB varied for different CNT-types, following the order: SWCNT-COOH > SWCNT-OH > SWCNT (Fig. 2). Particularly, the affinity of zigzag SWCNT based on R^2 takes high values according to VDAC-interspecies criteria following the order VDAC1-*Mus musculus* ($0.78 \leq R^2 \leq 0.96$), VDAC2-*Danio rerio* ($0.58 \leq R^2 \leq 0.96$) and VDAC1-*Homo sapiens* ($0.66 \leq R^2 \leq 0.75$).

On the other hand, the *m*-Hamada index does not seem to be an important nanodescriptor of SWCNT-VDAC interactions, since a lack of significant correlation ($p > 0.05$) with the FEB values was observed for the three SWCNT-topologies (zigzag, armchair, and chiral), for all the SWCNT-functional groups (H, OH, and COOH) considered and considering the VDAC-channels from different species see Figshare[48] (Fig. SM01).

VDAC-active binding site residues (Arg 15, Arg 163, Arg 218, Lys 12, Lys 20, Lys 109, Lys 113, Lys 115, Lys 161, Lys174, Lys 256) that are involved in the ATP-transport have been shown to be fully-conserved in all the species considered (Fig. 3).

In this sense, a "common binding site substrate" can be proposed for ATP-VDAC interaction in the same biophysical environment to that where the SWCNT-family members were tested by DS with VDAC channel. This would support extrapolation criteria of the potential VDAC-nanotoxicity induced by SWCNT (SWCNT-H, SWCNT-OH, SWCNT-COOH) from any species assayed to other eukaryotic species not tested, independently of their phylogenetic location.

It is important to note that to avoid obtaining false positives on flexible-docking interactions (SWCNT-VDAC-channels) it was verified the absence of restricted-flexibility for each VDAC-residues from the three VDAC.pdb x-ray structures (PDB ID: 3EMN, 4BUM, and 2JK4) through Ramachandran plots. All the possible conformations of each VDAC-residue is defined by the torsion values of the dihedral angles (Psi) and (Phi) around the C_{alfa} of the peptide-bond of the VDAC-residues and can be represented by Ramachandran plot. For this instance, allowed torsion values of Ψ (Psi) versus Φ (Phi) of a given VDAC-residue are found within the contour lines of the Ramachandran plot (Ramachandran favored). Otherwise, is considered as disallowed and the torsion values of dihedral angles Ψ (psi) versus Φ (phi) appear outside of the Ramachandran contour line (Ramachandran outliers). Note that the VDAC-active binding site residues (Arg15, Arg163, Arg218, Lys12, Lys20,

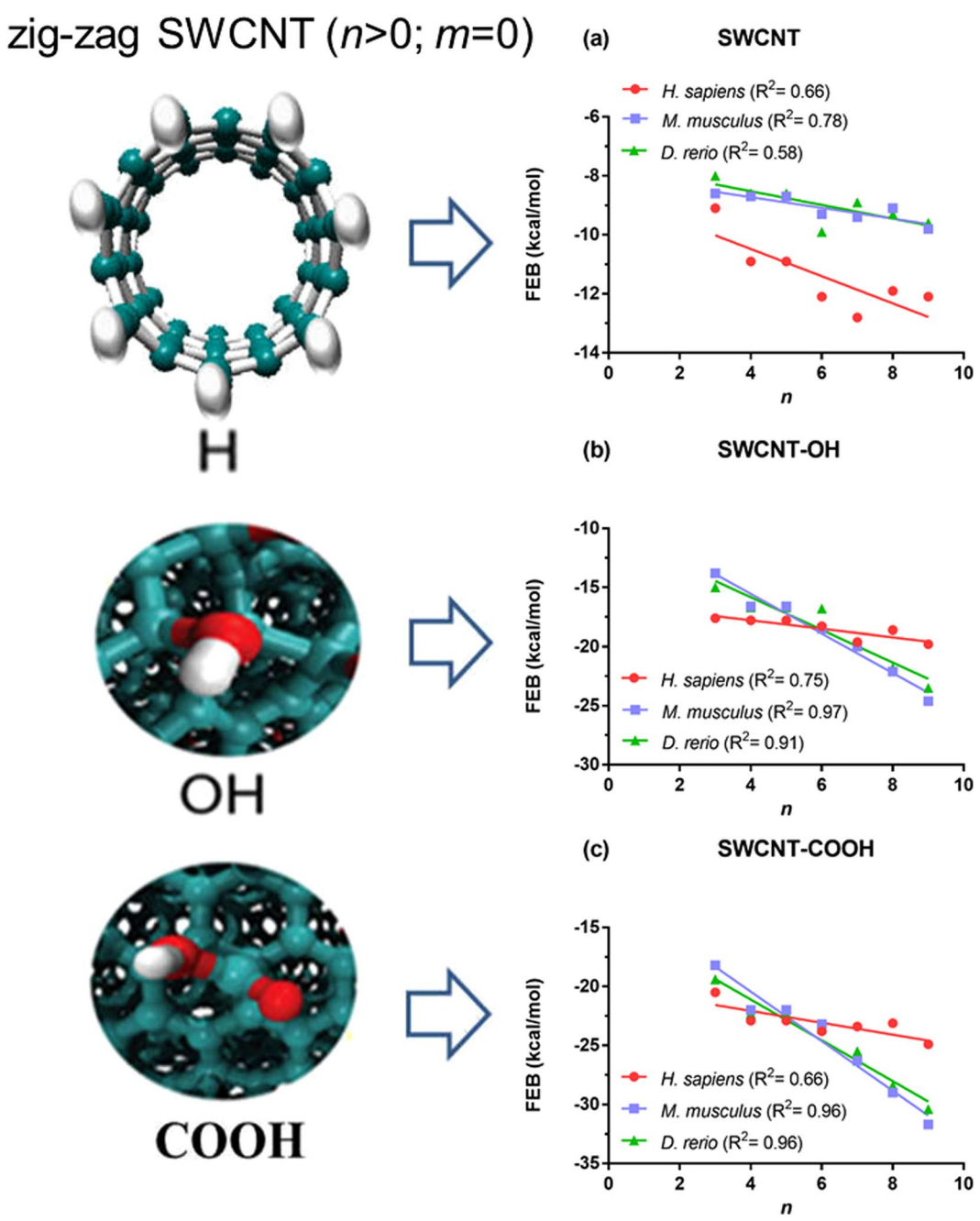

Figure 2. Linear relationships between free energy binding (FEB, in kcal mol^{-1}) and the *n*-Hamada index for zigzag single-walled carbon nanotubes ($n > 0$, $m = 0$) regarding the VDAC channels from different species (mouse: *Mus musculus*, zebrafish: *Danio rerio*, human: *Homo sapiens*). (**a**) Pristine carbon nanotubes (SWCNT), (**b**) hydroxylated carbon nanotubes (SWCNT-OH), (**c**) carboxylated carbon nanotubes (SWCNTs-COOH). For all relationships, the determination coefficient (R^2) is included.

Lys109, Lys113, Lys115, Lys161, Lys174, Lys256) of the VDAC-cavity domain of the voltage-sensing N-terminal α-helix and also for VDAC- phosphorylation binding site regulatory residues (Ser13, Ser43, Ser102, Ser104, Ser240, Ser57, Ser215, Tyr225) considered as flexible in the docking study were not identified as Ramachandran outliers[49–51] (Fig. 4).

It should be pointed out that the identified Ramachandran outliers were not key residues for ATP-transport and phosphorylation (showed in Fig. 3)[49–51].

In silico results for the Euclidean SWCNT-interatomic distance values (**Å**) relative to ATP-VDAC active binding site residues used R code letter for arginine (R15, R163, R218), K code letter for lysine (K12, K20, K109, K113, K115, K161, K174, K256) and E code letter for glutamate (E280). For most of the SWCNT analyzed, the inter atomic distances for the SWCNT-VDAC interaction with the amino acid residues cited above were very similar or, in some cases, lower than the interatomic distance of these residues for the ATP-VDAC interaction (Fig. 5).

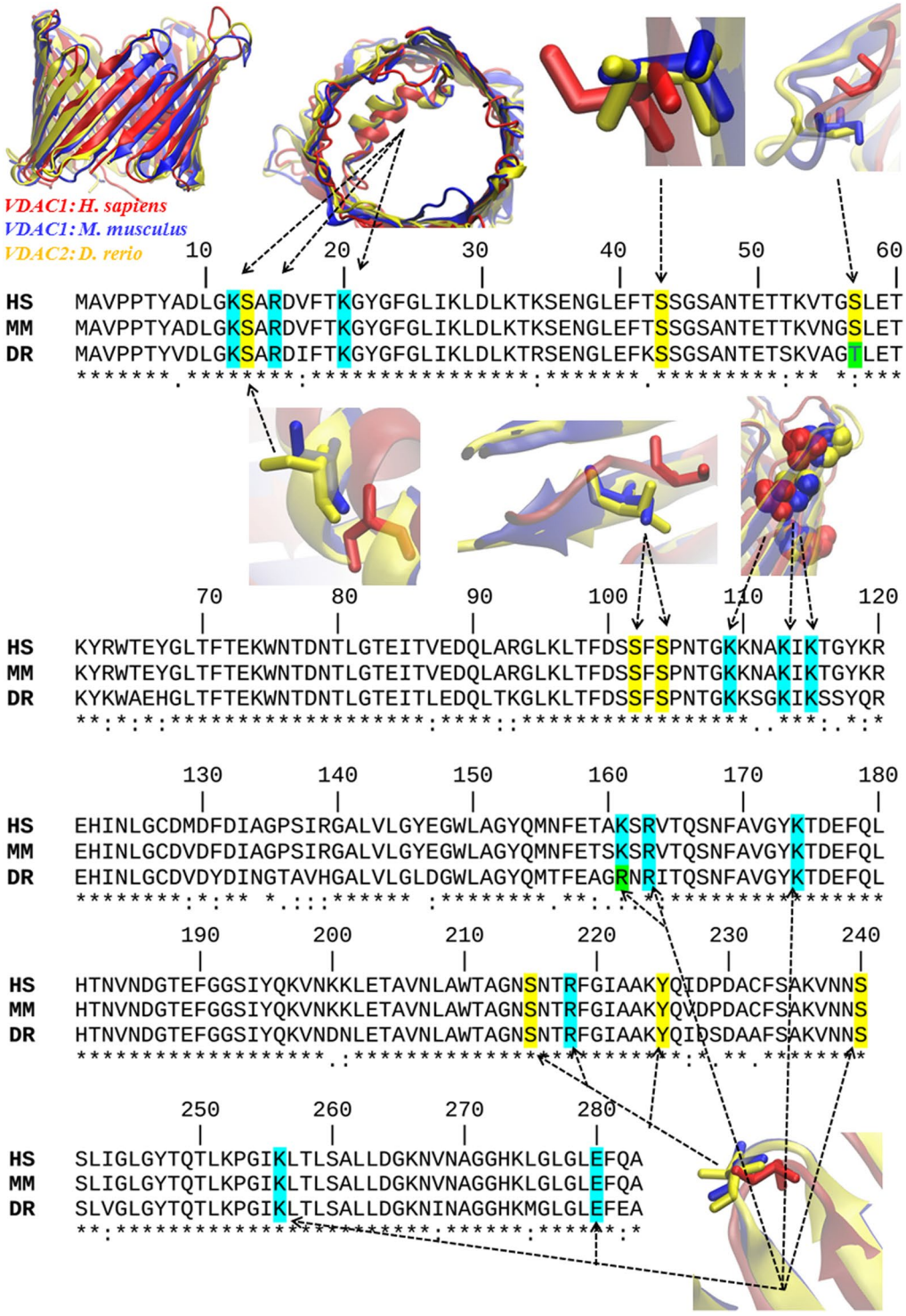

Figure 3. Primary sequence alignment with the position of VDAC-active binding site residues for the ATP transport. The figure includes details of 3D VDAC alignment of amino acid residues known to be phosphorylated (in yellow) (REF) and of the ATP transport (light blue). Note the high homology for VDAC critical residues both for ATP transport and phosphorylation. The alignment was performed for the three analyzed species: VDAC1-*Homo sapiens* (HS), VDAC1-*Mus musculus* (MM) and VDAC2-*Danio rerio* (DR). Note that in the case of residue lysine (K161), it is replaced by the basic residue arginine (R) with a similar ability to that of ATP transport, and the regulatory residue serine (S57) is replaced by tyrosine (T57) with the same ability to be phosphorylated in VDAC2-*D. rerio* (light green).

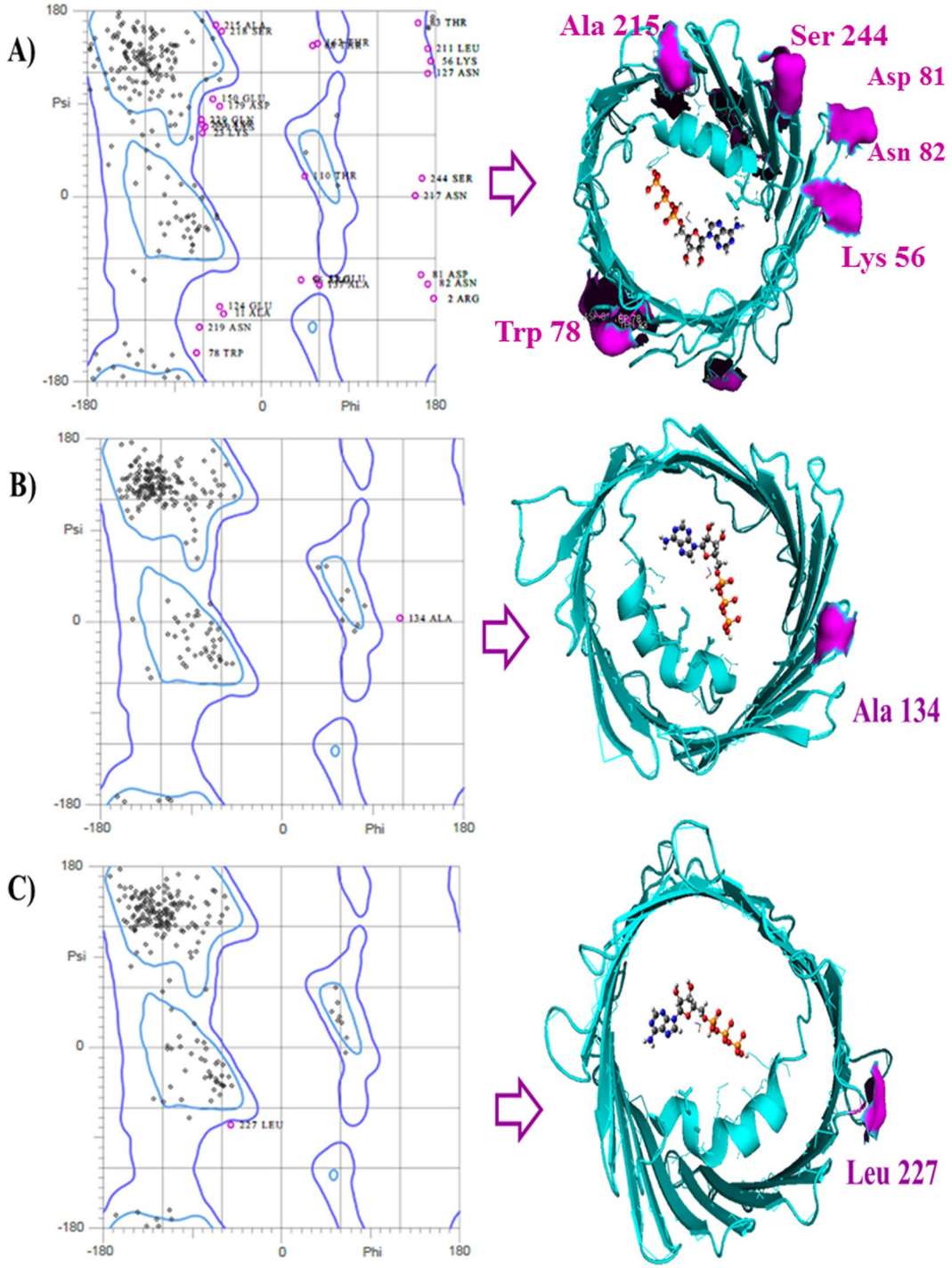

Figure 4. Representation of Ramachandran diagrams (general cases) (left) and spatial distribution of Ramachandran outliers in each VDAC.pdb x-ray structure analyzed (right). Figure shows the similar patterns of the VDAC geometry based on all the possible combinations of dihedral angles of torsion Ψ (Psi) versus Φ (Phi) of the each amino acid residues of VDAC of the different species analyzed: VDAC1-*Homo sapiens* PDB ID: 2JK4 resolution 4.1 Å (**A**); VDAC1-*Mus musculus* PDB ID:3EMN resolution 2.3 Å (**B**), and VDAC2-*Danio rerio* PDB ID:4BUM resolution 2.8 Å (**C**). The stereochemical spatial distribution of the Ramachandran outlier residues (marked in violet) in each VDAC.pdb x-ray structure analyzed (right) confirms that these residues do not belong to the ATP-VDAC active binding site of the VDAC pore domain of the voltage-sensing N-terminal α-helix on the polypeptide formed by the basic residues (Lys12, Lys20, Lys109, Lys113, Lys115, Lys161, Lys174, Lys256).

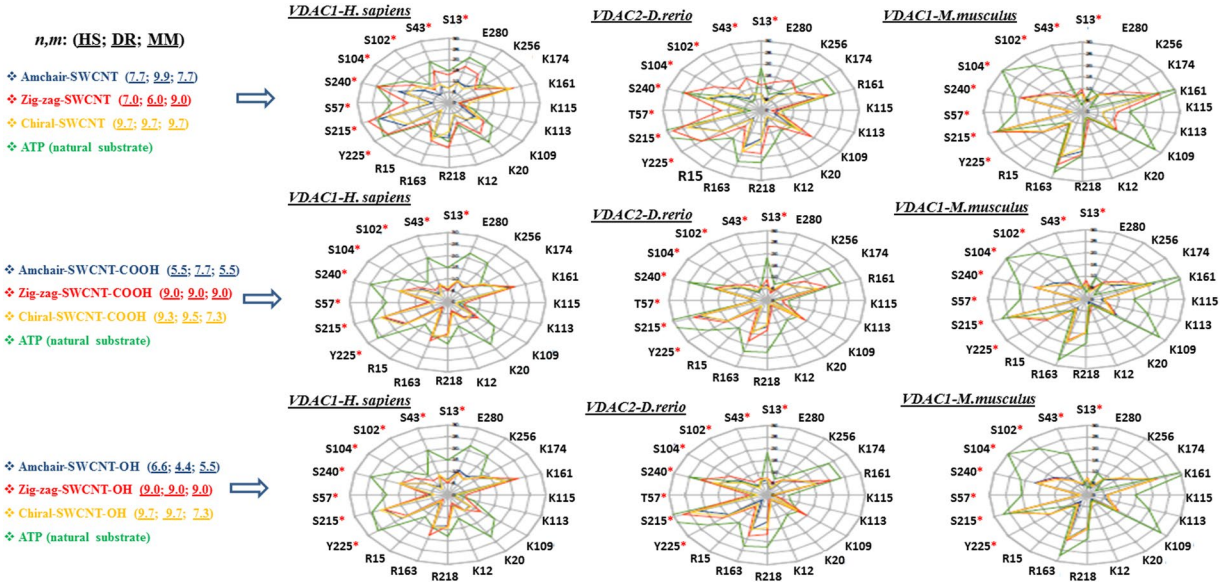

Figure 5. Radar plots showing the relative interatomic distances (scale: 0, 5, 10, 15, 20, 25, and 30 Å) of SWCNT family member (pristine-SWCNT, SWCNT-OH, SWCNT-COOH) with different *n*, *m*-Hamada index for the most negative FEB value results based on the final position after SWCNT-VDAC docking simulations for the three VDAC channels (HS: *Homo sapiens*; DR: *Danio rerio*; MM: *Mus musculus*). The amino acid residues of ATP-VDAC active binding site are marked with R for arginine (R15, R163, R218); K for lysine (K12, K20, K109, K113, K115, K161, K174, K256) and E for glutamate (E280). Red asterisks (*) show VDAC-phosphorylation binding site experimentally determined residues[9]: *S code for serine (*S13, *S43, *S102, *S104, *S240, *S57, *S215) and *Y code for tyrosine (*Y225). Radar plots show that the relative interatomic distances (Å) for SWCNT members with different geometric configurations such as armchair (blue line), zigzag (red line), chiral (orange line) and different types of SWCNT oxidation (OH, COOH) are similar and, in some cases, lower than ATP-relative interatomic distances (green line) used as control.

The atoms-proximity (C, O, H atoms) for each SWCNT-type to key binding residue atoms of VDAC-channels (for the ATP-transport and VDAC-phosphorylation binding site residues) could offer relevant information about VDAC physiological function. Interatomic distances lower than 7 Å imply a high probability of interaction in terms of free energy of binding and low probability of obtaining false contacts[52,53] (Fig. 6).

Considering the docking results the SWCNT-VDAC-interactions (VDAC-channel nanotoxicity) it should be reasonable to hypothesize that the deprotonated SWCNT-COO^- moiety of SWCNT-COOH should disrupt the association of the ATP^{4-} anion (phosphate tail) with the positively charged ε-amino group (N^+ primary amines) of Arg15 or Lys residues (Lys12, Lys20) present at the bottom of the VDAC cavity in the three species studied by forming stable complexes of salt bridges.

Moreover, the presence of pristine SWCNT and oxidized SWCNT in the cavity of the VDAC pore could cause a partial or total narrowing in the VDAC-active site, and thus affect the VDAC conductance through weakness of the function of Lys256 and Glu280, which are associated with electrostatic stabilization of the ATP^{4-} with Arg 15-(N^+) during the ATP passage through formation of hydrogen bonds in the voltage-sensing N-terminal α-helical segment. Potential SWCNT-interactions (H-bond) with Arg15 and other important positive residues, such as Lys113 and Lys115 in the VDAC-binding active site, could alter the rate of ATP-dissociation from the helix. This happens when the adenosine ring is released and ATP passes to Lys12, Lys20, and Lys109 on the N-terminal α-helix segment via Lys174 on the β-barrel wall, which is considered a limiting step in the ATP-efflux when the Euclidean $SWCNT_i$-$VDAC_j$ interatomic distance $d_{ij} \leq 7$Å[52–54]. It is important to note that interatomic distance values relative to VDAC-phosphorylation binding site residues (Ser13) associated to regulation of ATP-efflux in VDAC-pore exhibit values of $d_{ij} \leq 5$ Å for all the SWCNT-types tested.

Phosphorylation is an important mechanism involved in mitochondrial signaling pathways[9,55,56]. Then, these potential biochemical events could explain the difference observed for FEB-values (of SWCNT-VDAC complexes formed) and could still be viewed as a friend or a foe depending on the toxicological condition considered[57] like the presence of zigzag SWCNT topologies with high *n* Hamada index. Besides, a recognized phenomenon of "edge effects", which only appears in semiconducting zigzag SWCNT topologies, plays an important role in the mitochondrial channel nanotoxicity of zigzag SWCNTs[18]. The "edge effects" were not observed for metallic-armchair SWCNT, wherein the cycloparaphenylene aromatic system of the SWCNT-extremes were closed and without tips charge variation[18,58].

Perturbation Theory Modeling and Mechanistic interpretation. Herein, a PT-NQSBR approach for the prediction of SWCNT-VDAC docking free energy of binding (FEB values) was applied. The output of the PT-NQSBR model is the scoring function $f(\text{FEB})_{\text{query}}$ (or $f(\text{FEB}_{ij})_{\text{calc}}$) of the FEB value for the query SWCNT. The

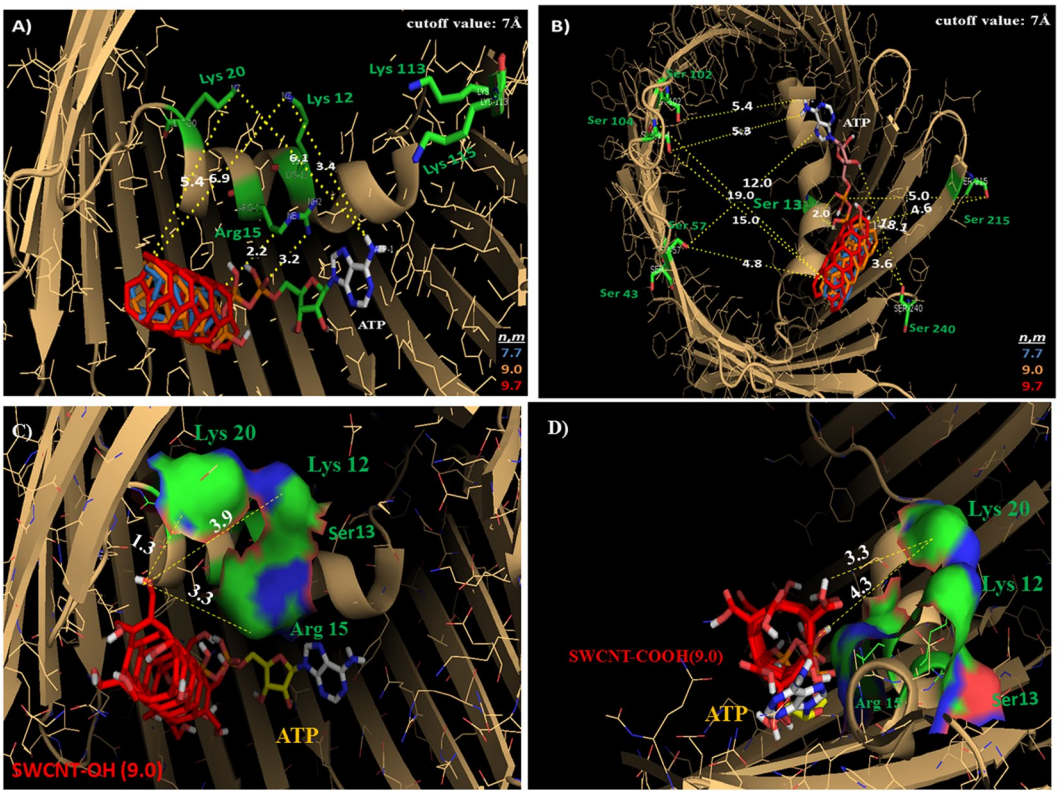

Figure 6. (**A**) Cartoon representation of the docking results in VDAC1-*Mus musculus* showing the calculated lower interatomic distances (d_{ij} cutoff value ≤ 7 Å) represented by yellow dashed lines for overlapping pristine-SWCNT with different *n*,*m*-Hamada indexes such as SWCNT (7.7) (blue), SWCNT (9.0) (orange), SWCNT (9.7) (red) compared to ATP (natural substrate of VDAC) from the supercritical ATP-VDAC active binding site residues (Lys 20; Lys 12; Arg 15). (**B**) Supercritical VDAC phosphorylation binding site regulatory residue (Ser 13) located in the VDAC pore domain of the voltage-sensing N-terminal α-helix show the calculated lower interatomic distances ($d_{ij} < 2$ Å) for overlapping pristine-SWCNT with different *n*,*m*-Hamada indexes such as SWCNT (7.7) (blue), SWCNT (9.0) (orange), SWCNT (9.7) (red) compared to ATP. (**C** and **D**) The calculated lower interatomic distances ($d_{ij} \leq 5$ Å) from the supercritical ATP-VDAC active binding site residues (Lys 20; Lys 12; Arg 15) and also from the phosphorylation regulatory residue (Ser 13) on zigzag oxidized SWCNT members, such as SWCNT-OH (9.0) and SWCNT-COOH (9.0) compared to ATP in the VDAC voltage sensing pore domain, depicted as van der Waals surface (red is acidic, blue is basic). All docking images were designed using open-source Pymol 1.7.x. This pattern is representative of the remaining cases, as shown previously in the radar plots.

scoring function $f(FEB_{ij})_{calc}$ increases for higher values of probability of binding, with FEB < -5.6 kcal/mol as a cutoff value that represents the FEB value for the ATP-VDAC interaction calculated in this work (see Fig. 1). The best NQSBR model found is shown below, according the following equation (1):

$$\begin{aligned} f(FEB_{ij})_{calc} &= 0.044984 \cdot f(FEB_{ij})_{expected} + 0.124831 \cdot V_{01} \\ &\quad + 0.386548 \cdot V_{11} + 0.004531 \cdot V_{14} - 0.519378 \\ N_{total} &= 405 \quad \chi^2 = 206.47 \quad p < 0.005 \end{aligned} \tag{1}$$

This equation is able to discriminate between the SWCNTs that bind strongly to VDAC (FEB < -5.6 kcal/mol) and those with a weak binding site (FEB ≥ -5.6 kcal/mol), only by including the FEB-expected value ($f(FEB_{ij})_{expected}$), *n*-Hamada index (V01), C_h-Chiral vector (V11), and the semi-empirical radial breathing mode V_{RBM} (V14). This LDA model has values of accuracy, specificity, and sensitivity in the range of 73.0–94.7% for the training series, and in the range of 78.0–98.0% for the external validation series (Table 1).

These results obtained with the LDA-NQSBR model support the hypothesis of a linear relationship for the strength of SWCNT-VDAC interactions based on the input variables (SWCNT nanodescriptors) and the output variables $f(FEB_{ij})_{calc}$ (Table 2).

However, both linear and non-linear Artificial Neural Networks (ANN) analyses were carried out to calculate the Receiver Operating Characteristic (ROC) curves and obtain more evidence to support the linear hypothesis of SWCNT-VDAC interactions. The ROC analysis may also contribute to discard more extreme alternatives, such as the non-linear hypothesis or the random classification[59], due to the large number of SWCNT-nanodescriptors used. In fact, the ROC graph shows high values of the area under the ROC curve (AUROC) of ≈0.9 in training

Data subset	Statistical		Observed values	
Training	Parameter	%	$(FEB \geq -5.6)_{calc}$	$(FEB < -5.6)_{calc}$
$(FEB \geq -5.6)_{obs}$	Specificity	73.0	111	41
$(FEB < -5.6)_{obs}$	Sensitivity	94.7	8	144
Total	Accuracy	83.9		
Validation			$(FEB \geq -5.6)_{calc}$	$(FEB < -5.6)_{calc}$
$(FEB \geq -5.6)_{obs}$	Specificity	78.0	39	11
$(FEB < -5.6)_{obs}$	Sensitivity	98.0	1	50
Total	Accuracy	88.1		

Table 1. Results of the LDA analysis using a PT-QSBR model that discriminates between SWCNT strong binding interactions (FEB < −5.6 kcal/mol) and SWCT weak interactions (FEB ≥ −5.6 kcal/mol) with VDAC. The data in the table show the statistical parameters (Stat. Param.) for specificity, sensitivity, and accuracy for both the training dataset (for model estimation) and the validation dataset (for model evaluation). In each case, the numbers of cases correctly or incorrectly classified are mentioned in the table. FEB stands for Free Binding Energy.

Species	SWCNT type	SWCNT function	Mitochondrial Channel	<FEB>
Danio rerio	Pristine	H	VDAC2	−10.20
	oxidized	COOH	VDAC2	−29.06
	oxidized	OH	VDAC2	−22.80
Mus musculus	Pristine	H	VDAC1	−10.44
	oxidized	COOH	VDAC1	−20.63
	oxidized	OH	VDAC1	−17.44
Homo sapiens	Pristine	H	VDAC1	−12.87
	oxidized	COOH	VDAC1	−5.44
	oxidized	OH	VDAC1	−17.11

Table 2. Expected values of free energy of binding (FEB, in kcal/mol) of SWCNT-VDAC interaction.

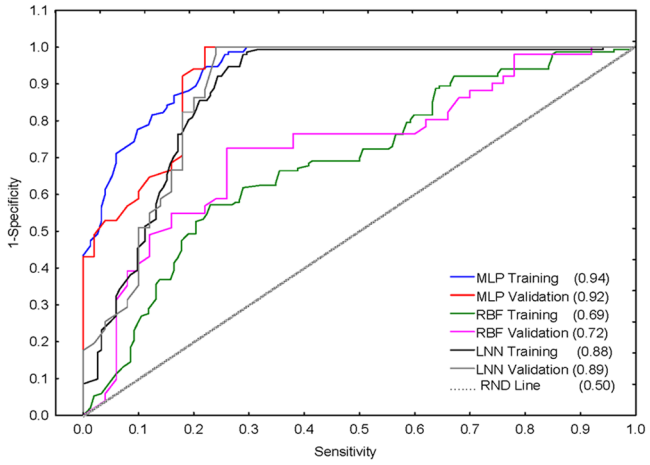

Figure 7. Results of the ROC curve analysis. Training and validation sets of the statistical parameters are represented by the area under receiver operating characteristic curve (AUROC) according to multiple layer perceptron (MLP), radial basis function (RBF) and linear neural network (LNN). The AUROC values are presented in brackets.

and validation series for the Linear Neural Network (LNN) model with the same input variables used in the LDA NQSBR model (Fig. 7).

These values are notably higher than the expected values of AUROC = 0.5, typical of a random classification. The non-linear model corresponding to a Multiple Layer Perceptron (MLP) has also a very high AUROC = 0.92 to 0.94, but the values of accuracy, specificity, and sensitivity (in the range of 80.9–84.2%) are not higher than those for the LDA and LNN linear models. Finally, the Radial Basis Function (RBF) topology shows also notably

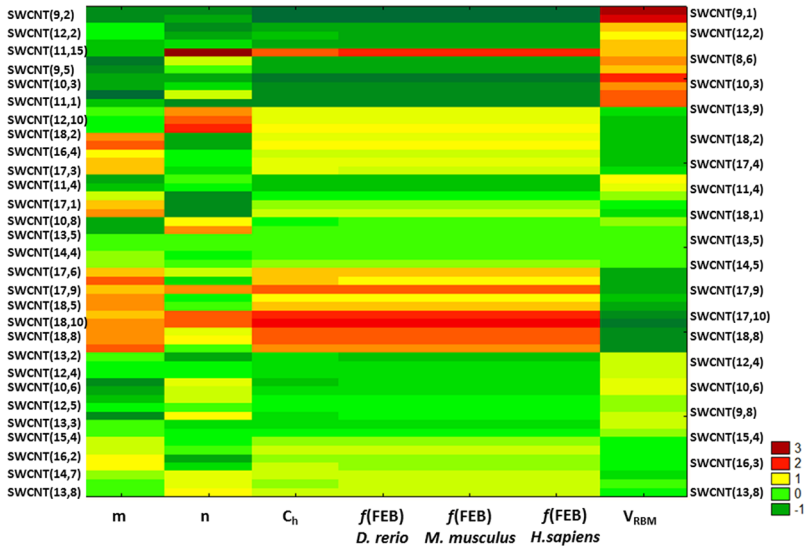

Figure 8. Two Way Joining Cluster (TWJC) analyses for the validation prediction of VDAC nanotoxicity of pristine SWCNTs using an external dataset (SM02.xlsx)[44,60] by applying the obtained LDA classification NQSBR model. Each y-axis describes a vector of the elements corresponding to pristine SWCNT (y_i) in individual layers. x-axis represents the main clusters of parameters from x_n row vectors used to predict the VDAC channel nanotoxicity for individual pristine SWCNT (x_i), such as *n*: Hamada index, Ch: Chiral vector, V_{RBM}: Radial Breathing Mode (cm^{-1}) and expected *f*(FEB), as predictive function of free energy of binding used to classify strong and weak SWCNT-VDAC interactions in different species. The *m*-Hamada index was included in the TWJC analysis, but no correlation was observed in the performed NQSBR model for this SWCNT geometric parameter. Code numbers for SWCNT-VDAC interactions: very strong = 3; strong = 2; moderate = 1; and weak = −1. The results for the three species (zebrafish, *D. rerio*; mouse, *M. musculus*; and human, *H. sapiens*) are shown.

lower AUROC ≈ 0.7 values in the training and validation datasets. Overall, the ROC curve analysis supports our selection of a linear hypothesis to predict the SWCNT-VDAC interaction represented by the LDA model. *Vide infra* in the Materials and Methods section. To verify the results obtained with the LDA classification NQSBR model from the external dataset, the empirical physico-chemical parameter of pristine SWCNT was used, not tested in our original dataset obtained by Bachilo (2002)[44].

The multiple factors involved in VDAC channel nanotoxicity were represented based on the SWCNT-nanodescriptors using Two Way Joining Cluster (TWJC) (Fig. 8) from the external dataset available in Figshare[48] (Table SM02).

A detailed analysis of the two-way contingency table with heat map contributes to verify the VDAC-affinity levels between similar clusters of relevant SWCNT-nanodescriptors. Particularly, the cluster obtained from x_n row vectors for *n*-Hamada index, Ch-Chiral vector, V_{RBM} and expected *f*(FEB) is consistent with the theoretical evidences obtained by the linear NQSBR model based on the classification power of strong and weak SWCNT-VDAC interactions, following the heat map intensity of the contingency table from pristine SWCNT (y_i) in individual layers.

Futhermore, to explain SWCNT-VDAC interactions based on non-linear relationships classification and regression approaches using feature selection (FS) based on QSAR/QSPR non-linear algorithms were efficiently implemented. This procedure allowed eliminating redundant SWCNT-nanodescriptors that could cause a poor predictive potential and generalization of the results, as mentioned in the introduction of this work.

In this sense, J48 model could be used to filter SWCNT-nanodescriptors of new mitochondrial channel interactions based on V_{RBM} (V14), *n*-Hamada index (V01) and FEB-expected value see Figshare[48] (Fig. SM03-A and Fig. SM03-B).

The results of this decision tree (J48 model) are consistent with our goal and have previously been verified in the linear NQSBR model. The V_{RBM} is a low frequency mode observed in the SWCNT-Raman spectrum linked to the CNT chiral-index assignments and it has a direct influence on the SWCNT-diameter (V06). Particularly, the *n*-Hamada chirality-index (V01) has a relevant meaning from the biophysical point of view to predict the SWCNT-VDAC interactions. This is because the *n*-Hamada index has a direct proportionality and strong linear relationship with the SWCNT-diameter (V06) following equation (2):

$$d_{SWCNT(n,m)} = 0.783\sqrt{n^2 + nm + m^2} \quad (2)$$

Note that this relationship also applies for zig-zag topology SWCNT, where $m = 0$, which showed the most negative FEB-values (Kcal/mol). The average cavity-diameter wall-to-wall from the three VDAC-channel studied (VDAC1-*Homo sapiens*, VDAC1-*Mus musculus*, and VDAC2-*Danio rerio*) is about ~34–38 Å and these

dimensions should the maximum to allow interaction with SWCNT. As mentioned previously this was in fact the case since the assayed SWCNT presented diameters raging from 2.35 to 12.21 Å.

We strongly suggest that SWCNT tested could cause partial or total distortions in the VDAC-active site affecting the ATP-efflux and/or modulate potential post-translational modifications in VDAC phosphorylation binding-site residues for large *n*-Hamada index (high SWCNT diameter) directly influencing the strength of interactions (more negatives FEB values) of the formed SWCNT-VDAC complexes available in Figshare[48] (Fig. SM01).

The results based on the FS1 dataset are in general slightly better than the Pool dataset with all SWCNT nanodescriptors. Thus, Random Forest and K Star model were the best classifiers of SWCNT nanotoxicity on VDAC with the same TPR of 0.916, but AUROC of 0.978 and 0.968 see Figshare[48] (Table SM04 and Table SM04-1).

FS3 dataset was used to decrease the dimensionality of the full dataset (Pool) by transforming the 19 dimensions based on SWCNT nanodescriptors into only 8 Principal Components to identify an optimal subset of SWCNT nanodescriptors that best map a relationship between structure and VDAC nanotoxicity see Figshare[48] (Table SM04).

The Random Forest and Multilayer Perceptron are the best classifiers for SWCNT-VDAC interactions. The maximum AUROC/TPR was lower than FS0, FS1, FS2, with values of only 0.956/0.872. OneR model pointed to SWCNT molecular weight (V02) as an important SWCNT nanodescriptor see Figshare[48] (Table SM04), SWCNT-molecular weight was not identified as a relevant SWCNT-nanodescriptor in the previous LDA NQSBR model. However, an increased SWCNT-molecular mass could be associated with a proportional increase in SWCNT diameter (V06). This affected the FEB values through potential steric collisions of the SWCNT-atoms with key binding site residues atoms near to N-terminal α-helical segment in the VDAC channels. Similarly, the FEBexp and SWCNT-molecular weight (V02) were used in FS4 dataset with a minimal dataset of SWCNT nanodescriptors. The Random Forest model demonstrated a similar performance by using FS1 and FS2 dataset of SWCNT nanodescriptors (AUROC = 0.978, TPR = 0.919). J48 classifier model was performed as a simple set of rules using only V02 and FEBexp with good performance for the predictive classification with AUROC of 0.897 and TPR of 0.889: SWCNT with molecular mass $\leq$ 2337 g/mol will have weak SWCNT-VDAC interactions, SWCNT with molecular mass = 2,337–6,245 g/mol and FEBexp ≤ -29.1 Kcal/mol will have strong SWCNT-VDAC interactions see Figshare[48] (Fig. SM03-A and Fig. SM03-B).

In general, a better performance of the predictive classification model is obtained for the non-linear Random Forest model when all 19 SWCNT-nanodescriptors are used (Pool dataset) with an AUROC value of 0.973 and true positive rate (TPR) of 0.916. In this case, the MLP classifier (1 hidden layer with 19 neurons = number of SWCNT nanodescriptors (19) + no. of classes (2)) is better than the one used for the FS0 dataset (AUROC of 0.970 and TPR of 0.904) see Figshare[48] (Table SM04 and Table SM04-1).

The last predictive test included additional categorical information, such as SWCNT Electroconductivity (metallic, semimetallic, semiconducting), SWCNT type (pristine SWCNT, oxidized SWCNT), SWCNT function (H, OH, COOH), VDAC isoform (VDAC1, VDAC2) and species (*Mus musculus*, *Homo sapiens* and *Danio rerio*) using Weka classifiers see details in Figshare[48] (Table SM04 and Table SM04-1). Thus, by the addition of these categorical information to the Pool dataset with REPTree method, we obtained good prediction with AUROC/TPR/FPR = 0.926/0.889/0.111 (FPR = false positive rate). The classifier chooses only the information of FEBexp, *n*-Hamada index of the SWCNT (V01), SWCNT Molecular Weight (V02), SWCNT No. Bonds (V03), SWCNT Radio Rt (V05), SWCNT Nanotube diameter (V06), and species. Simple rules could be decrypted to predict the SWCNT-VDAC interaction from the plot: if V03 $<$ 202 or if V03 $\geq$ 202 and V02 $<$ 2,772 (g/mol) see Figshare[48] (Fig. SM05-A). According to the species type, the SWCNT-VDAC interaction varies: for *Mus musculus* and *Danio rerio*, the SWCNT-VDAC interaction is strong, but in the case of *Homo sapiens*, there is a need for *n*-Hamada index and SWCNT Molecular Weight values to decide on the strength of interactions see Figshare[48] (Fig. SM05-B). It should be noted that in the case of VDAC2-*Danio rerio*, the basic residue Lys161 is replaced by another basic residue (Arg161), with an equivalent physiological role in the ATP passage to cytosol[1]. The calculated interatomic distances relative to basic residues (Lys12, Lys20, Arg15, Arg163, Arg218, Lys109, Lys113, Lys115, Lys174, Lys256) for the SWCNT members with higher values of *n*-Hamada index and lower FEB values from pristine SWCNT and oxidized SWCNT are lower than 5 Å in most cases. The different single-walled carbon nanotubes followed the order SWCNT-COOH ~ SWCNT-OH $<$ SWCNT, according to the interatomic distance values, as shown in the radar plot in Fig. 5, and considering a cutoff value of 7 Å.

To search for the best regression NQSBR model which predicts the FEB values, linear and non-linear methodologies were implemented by using the full dataset of nanodescriptors (Pool) as input. As an initial test, regression models were obtained by excluding the expected free energy of binding (FEBexp) to check the importance of the Perturbation Theory for this type of NQSBR models. All the methods provided regression models with very low performance ($R^2_{test} < 0.50$). Thus, the importance of free energy of binding expected value (FEBexp) is confirmed for the prediction of new FEB values.

Finally, the best regression model that predicts FEB values for SWCNT-VDAC interactions based on the Pool dataset (all 19 SWCNT nanodescriptors) was provided by non-linear regression Random Forest models with $R^2_{test} = 0.833$ and $RMSE_{test} = 0.0844$. Besides, NN provided a performance of $R^2_{test}/RMSE_{test} = 0.757/0.0953$. In addition, Random Forest Recursive Feature Elimination (RF-RFE) results were between RF and NN by selecting only 2 SWCNT nanodescriptors (9 out of 10 splits): FEBexp and V02 (the same SWCNT nanodescriptors used in the classification with the minimal dataset, FS4). With only two SWCNT-nanodescriptors, RF-RFE has a good performance to classify the SWCNT-VDAC nanotoxicity docking interactions, with R^2_{test} of 0.798 and $RMSE_{test} = 0.0953$. If filters are applied in order to select optimal SWCNT nanodescriptors in RRegrs, the performance slightly decreases see Figshare[48] (Table SM06 and Table SM06-1). However, the linear methods (LM and GLM) and the parametrical models (Lasso, PLS and ENET) show very low performance ($R^2_{test} < 0.50$), whereas

the applying of non-linear methods showed an increased R^2_{test} over 0.75. See the pairwise model comparisons of R^2_{test} (A) and $RMSE_{test}$ (B) for multiple linear and non-linear regression models in Figshare[48] (Fig. SM07).

Conclusions

The Free Energy of Binding was determined using Molecular Docking Simulation with Virtual Screening Framework. The results showed that the affinity was statistically more negative for FEB values following the order (SWCNT-VDAC2-*Danio rerio*) > (SWCNT-VDAC1-*Mus musculus* > (SWCNT-VDAC1-*Homo sapiens*) ≈ (ATP-VDAC). In addition, the presence of zigzag topology and the COOH, OH functionalization are geometric, and toxicophoric SWCNT nanodescriptors are useful to describe their interactions with VDAC (order: COOH > OH > H). The FEB values of interactions based on these SWCNT nanodescriptors were shown to be stronger than the VDAC-natural substrate (ATP). However, some geometric and electronic properties, such as armchair and chiral configuration are uncorrelated with the VDAC affinity.

The broader theoretical importance of this work is not limited only to molecular docking simulation for solving nanotoxicological problems. The relevant alignments of sequences for the key functional and regulatory residues of VDAC channels from different species (represented as 3D-objects) should be relevant for the extrapolation of potential toxic effects of SWCNT to animal models, commonly used for nano-ecotoxicological studies on *Danio rerio*. Furthermore, classification and regression models able to predict strong and weak SWCNT-VDAC interactions (FEB values) were performed for the first time. Several decision trees were constructed to extract simple rules for the prediction of classes and exact values for the SWCNT-VDAC as channel nanotoxicity criteria linked to optimal SWCNT nanodescriptors, and involving interspecies comparison. The classification models demonstrated high accuracy, specificity, and sensitivity in training and validation series (73–98%) and area under receiver operating characteristic (AUROC) up to 0.978. The best regression method to predict the complex free binding energy was Random Forest with R^2_{test} of 0.833 and $RMSE_{test}$ of 0.0844. These *in silico* results pave the way for the rational designing of novel carbon nanomaterials with higher benefit-risk relationships, and for the creation of new regulatory decisions in nanotoxicology for the prediction/assessment of human health impact and environment nano-risks.

Methods

Docking simulation. To evaluate the interaction between the VDAC from three different species (VDAC1-*Mus musculus*, VDAC1-*Homo sapiens*, VDAC2-*Danio rerio*) and various types of SWCNT, a NQSBR flowchart was performed see Figshare[48] (Fig. SM08). The first step consists of preparing the VDAC macromolecule structure files (receptor), which was obtained from the *RCSB Protein Data Bank* (PDB) x-ray structures[49]. Before the molecular docking, VDAC molecular structures were optimized using the AutoDock Tools 4 software for AutoDock Vina. The algorithm includes the removal of crystallographic water molecules and all the co-crystallized VDAC ligand molecules, such as Lauryl dimethyl-amine-N-oxide (LDA) or $C_{14}H_{31}NO$ from VDAC2-*Danio rerio*.

Moreover, hydrogen atoms were added, according to appropriate hybridization geometry, to those atoms based on built-in modules to add partial charges, protonation states followed by bond orders assignment and set up rotatable bonds of the different VDAC channels.pdb x-ray structures.

In the second step, the SWCNT ligands (pristine SWCNT or SWCNT-H) structures were carefully modeled taking into account general SWCNT nanodescriptors such as semi-empirical values for [n] and [m]-Hamada indexes, calculated by H. Yorikawa and S. Muramatsu in 1995, and other SWCNT parameters such as molecular weight, no. bonds, no. atoms, radio, diameter, hexagons number/1D unit cell, metallic and/or semiconducting; SC)[42–45]. Herein, the software Nanotube Modeler (http://jcrystal.com/products/wincnt/) version 1.7.5, registered by one of the authors (J.M. Monserrat), was used. Some SWCNT-H structures were oxidized either with carboxyl (-COOH) or hydroxyl (-OH) moieties using an advanced semantic chemical editor, Avogrado (Version 1.1.1 free software). The minimization of all the SWCNT ligands was performed using the MOPAC extension for geometry optimization based on the AM1-Hamiltonian method.

An *in silico* framework was developed to configure the virtual screening (VS) experiments in order to evaluate the various parameters. This framework has a Web interface in which the user configures the docking experiment and obtains the respective Python script to automatically perform the VS steps. In the framework interface, the user provides information regarding the receptor files (VDAC channels) and the folder in which all the SWCNT structures are stored. To evaluate the SWCNT-VDAC *in silico* interactions, Autodock Vina flexible molecular docking was implemented, open source software developed by Trott & Olson (2010). The cationic cluster formed by ATP-VDAC-active binding site residues (Lys12, Lys20, Arg15, Arg163, Arg218, Lys109, Lys113, Lys115, Lys161, Lys174, Lys256, Glu280) and the VDAC phosphorylation binding site residues, experimentally determined by Martel & Brenner (2014)[9] (Ser13, Ser43, Ser102, Ser104, Ser240, Ser57, Ser215, Tyr225), obtained from *Homo sapiens-VDAC*, *Mus musculus-VDAC* and *Danio rerio-VDAC* were tested as flexible residues and the ligands (SWCNTs) were considered a rigid molecules[61]. In this context, the SWCNT-VDAC complexes of free energy of binding (FEB) from different species were calculated based on the score function which approximates the standard chemical potentials (ΔG_{bind}). The implemented ΔG scoring function combines the knowledge-based potential and empirical information obtained from experimental binding affinity measurements. The FEB optimization algorithm for SWCNT-VDAC complexes from the different species were implemented in Autodock Vina scoring function with default Amber force-field parameters. The FEB of SWCNT-VDAC complex optimization was performed with a gradient and efficient local optimization algorithm of the free energy of binding based on a quasi-Newton method, such as Broyden-Fletcher-Goldfarb-Shanno (BFGS). The algorithm is a succession of steps consisting of a mutation and a local optimization, with each step being accepted according to the Metropolis criterion. The components are the position and orientation of the SWCNT (as rigid molecules), as well as the torsions values of the VDAC-flexible residues. Conformational relaxation (flexible docking)

favors a significant gain of enthalpy of SWCNT-VDAC complexes non-associated with SWCNT intra-molecular deformation or vibrational decrease within VDAC active sites. This theoretical procedure was performed for the receptor binding cavity using Cartesian coordinates for VDAC1-*Homo sapiens* grid box size, with dimensions of X = 20 Å, Y = 22 Å, Z = 20 Å and the VDAC1- *Homo sapiens* receptor grid box center X = 28.036 Å, Y = 0.361 Å, Z = 5.176 Å. Cartesian coordinates for VDAC1-*Mus musculus* grid box size, with the average dimensions of X = 22 Å, Y = 26 Å, Z = 22 Å and the VDAC1- *Mus musculus* grid box center X = 14.826 Å, Y = 32.707 Å, Z = 13.009 Å. Finally, the Cartesian coordinates for VDAC2-*Danio rerio* grid box size, with the average dimensions of X = 24 Å, Y = 24 Å, Z = 22 Å and the VDAC2-*Danio rerio* grid box center X = -14.894 Å, Y = 20.794 Å, Z = -9.617 Å were used to evaluate the SWCNT-VDAC interaction of the three species studied, considering the ATP biophysical environment (VDAC active site) as control to evaluate the SWCNT-VDAC affinity. Several runs starting from random conformations were performed, and the number of iterations in a run was adapted according to the problem complexity. An exhaustiveness option set to 50 (average accuracy) in each docking calculation was used[61]. Furthermore, it was verified whether a high increase of the exhaustiveness docking parameter of 100 increased the simulation time keeping the same FEB results.

The docking free energy of binding output results (or FEB values) is defined by ΔG_{bind} values (affinity) for all docked poses of the formed complexes (SWCNT-VDAC) and include the internal steric energy of a given ligands (SWCNT) which can be expressed as the sum of individual molecular mechanics terms of standard-chemical potentials like: van der Waals interactions (ΔG_{vdW}), hydrogen bond ($\Delta G_{H\text{-}bond}$), electrostatic interactions ($\Delta G_{electrost}$), and intramolecular ligands interactions ($\Delta G_{internal}$) from empirically validated Autodock Vina scoring function based on default Amber force-field parameters.

In fact, the force field parameters were validated from experimental data which are molecular mechanics terms based on the scoring function to ligand-receptor conformation-dependent parameters ($SWCNT_i$-$VDAC_j$ inter-atomic interactions) and the ligand conformation-independent parameters ($SWCNT_{i\text{-}i'}$ internal interaction). These mechanistic force-field parameters included in the Autodock Vina scoring function were validated on the basis of a strong linear correlation (scoring capability) of experimental binding-affinity data (K_d, K_i, and IC_{50}-values) of the original crystallographic protein-ligand complexes (>16,000 complexes from >114,000 x-ray crystallographic structure). Besides, Autodock Vina scoring function considers optimal-linear free binding energy coefficients from experimentally determined chemical potentials ($\Delta G_{internal}$) of ligands (SWCNT). Following this idea, Autodock Vina scoring function has an optimal docking performance, which can be efficiently applied to multiple ligand-receptor affinity problems (as SWCNT-VDAC interactions). It is important to note that overall docking force field parameters are based on distance-dependent atom-pair interactions (d_{ij}) according to the general thermodynamic equations represented below:

$$FEB_{dock} \approx \Delta G_{bind} = \Delta G_{vdW} + \Delta G_{H-bond} + \Delta G_{electrost} + \Delta G_{\text{int}} \tag{3}$$

$$\begin{aligned} FEB_{dock} \approx \Delta G_{bind} = {} & \Delta G_{vdW} \sum_{SWCNT-VDAC} \left(\frac{A_{ij}}{d_{ij}^{12}} - \frac{B_{ij}}{d_{ij}^{6}} \right) + \Delta G_{H-bond} \\ & \sum_{SWCNT-VDAC} E(t) \left(\frac{C_{ij}}{d_{ij}^{12}} - \frac{D_{ij}}{d_{ij}^{10}} \right) + \Delta G_{elec} \sum_{SWCNT-VDAC} 332.0 \frac{q_i q_j}{\in (d_{ij}) d_{ij}} \\ & + \Delta G_{internal} \left\{ \sum_{SWCNT} \frac{A_{ij}}{d_{ij}^{12}} - \frac{B_{ij}}{d_{ij}^{6}} + \sum_{SWCNT} E(t) \times \left(\frac{C_{ij}}{d_{ij}^{12}} - \frac{D_{ij}}{d_{ij}^{10}} \right) \right. \\ & \left. + \sum_{SWCNT} 332.0 \frac{q_i q_j}{4 d_{ij} d_{ij}} + \sum_{SWCNT} \gamma_k (1 + \cos(\varpi_k \theta_k - \theta_{0k})) \right) \end{aligned} \tag{4}$$

$\Delta G = -RT(\ln K_i)$, R (gas constant) is 1.98 cal*(mol*K)$^{-1}$, and K_i represents the predicted inhibition constants at T = 298.15 K. The first term of a 12-6/Lennard-Jones potential (with 0.5 Å smoothing) describes the *van der Waals* interaction as A_{ij}/d_{ij}^{12} (attractive Guassian function) and B_{ij}/d_{ij}^{6} (repulsive or hyparabolic function) to represent a typical Lennard-Jones interactions (SWCNT-VDACs), provided the Gaussian term is negative and the parabolic positive, d_{ij} is the surface distance calculated as $d_{ij} = r_{ij} - R_i - R_j$, where r_{ij} is the interatomic distance and R_i and R_j are the radii of the atoms in the pair of interaction of $SWCNT_i$-$VDAC_j$ atoms. The second term is the pair consisting of an H-bond donor and an H-bond acceptor as a directional 12–10 hydrogen-bonding potential term such as B_{ij}/d_{ij}^{12} and C_{ij}/d_{ij}^{10} (H-bonding potential with Goodford directionality), where $E(t)$ is an angular weight factor which represents the directionality of the hydrogen bonds and d_{ij} follows the criteria mentioned above. The third term represents the Coulomb electrostatic potential stored in the formed complex $(SWCNT\text{-}VDAC)_{ij}$ of N charges (q_i, q_j) of pairs of charged atoms of $SWCNT_{(i)}$ and $VDAC_{(j)}$. For this instance, appropriated Gasteiger partial atomic charges of the VDAC-channels (VDAC1-*Homo sapiens*, VDAC1-*Mus musculus*, VDAC2-*Danio rerio*) were assigned. Herein, d_{ij} is the interatomic distance between the point charges as the reference positions of interaction based on distance-dependent dielectric constant. In the present study Autodock Vina based on Amber force field was parameterized with default options for the SWCNT-data set (pristine-SWCNT, SWCNT-OH and SWCNT-COOH) by summing up individual molecular mechanic contributions like: SWCNT-intra-molecular contributions, SWCNT-aromaticity criterion and the set number of active torsions moving of each SWCNT-ligand following to general preparation procedures of ligand[61]. For this instance, the fourth term of the equation (3) as ($\Delta G_{internal}$) was used to validate the internal steric energy of each SWCNT-ligand including dispersion-repulsion energy and a torsional energy through the sum of the default

Amber force field parameters (ligand conformation-independent parameters of the Autodock Vina scoring function).

By the other hand, the electrostatic components were considered and the SWCNT-partial atomic charges were properly assigned with the Gasteiger-Huckel algorithm using partial equalization of orbital electronegativities (PEOE) after the addition of polar and non-polar hydrogen atoms. These steps were empirically calibrated by default Amber force-field parameters. Furthermore, Autodock conformational search space for the ligands (SWCNT-structures) were experimentally-validated with Autodock default options which include a randomized large training dataset for ligands properties, 50 genetic algorithm runs, and 25 million evaluations in each, and also including all default structural-parameters to predict the best position and orientation of the ligand (SWCNT-docking capability) taking into consideration the coordinate systems of the receptor (VDAC-channels). It is important to note that, molecular docking dimensionality based on degree of freedom (DOF) of the each member of the SWCNT-data set (pristine-SWCNT, SWCNT-OH and SWCNT-COOH) like: SWCNT-atom position/translation (x_i, y_i, $z_i = 3$), SWCNT-atom orientation/quarternion ($q(x_i)$, $q(y_i)$, $q(z_i)$, $q(w_i) = 4$), SWCNT-number of rotable bonds/torsion (tor_1, tor_2, …, $tor_n = N_{tor}$) and SWCNT-total dimensionality (total DOF $= 3 + 4 + n$) not have a significant weight in the FEB_{dock} based on the very small intra-molecular contributions of force field parameters of the SWCNT-ligand which were considered as rigid-bodies[61] and considering the aforementioned SWCNT-geometry optimization based on the $\Delta G_{internal}$ minimization of all the SWCNT-ligands used in the present study.

Docking was found as energetically unfavorable when a FEB for SWCNT-VDAC complex ≥ 0 kcal/mol (worst crystallographic pose) shows either an extremely low or complete absence of binding affinity according to repulsive interactions. Following this criterion, SWCNT conformations with the lowest Gibbs docking free energy of binding (FEB negatives value) were obtained. The best root-mean-square deviation (RMSD) was considered as a criterion of correct docking pose accuracy for atomic positions below 2 Å[52,53]. This is comparable to the best of several knowledge-based docking scoring functions according to the equation (5).

$$RMSD(pose_{i_{swcnt}}, pose_{j_{vdac}}) = \sqrt{\frac{\sum_n (atom_{(i_{swcnt})} - atom_{(j_{vdac})})^2}{n}} \tag{5}$$

The next step consists of analyzing the results obtained from the molecular docking with respect to the final free energy of binding - FEB for the SWCNT-VDAC complex of each experiment. The minimum distances (interatomic distances) were calculated between VDAC atoms of the key amino acids of the receptor (VDAC: VDAC1-*Mus musculus*, VDAC1-*Homo sapiens*, VDAC2-*Danio rerio*) and SWCNT atoms at the best docking crystallographic binding position for ligands (SWCNT family: pristine SWCNT, SWCNT-OH, SWCNT-COOH and their respective geometric configuration like amchair, chiral and zigzag). The only considered interatomic distances were related to VDAC active binding site residues (Lys12, Lys20, Arg15, Lys 109, Lys 113, Lys115, Lys 161, Arg163, Lys174, Arg 218, Lys256) involved in the ATP transport to compare with the ATP-VDAC interatomic distances as reference control of potential ATP efflux inhibition. In addition, we calculated the interatomic distances of SWCNT related to VDAC phosphorylation binding site residues, experimentally determined by Martel & Brenner (2014)[9]: *S code letters (Ser 13, Ser 43, Ser 102, Ser 104, Ser 240, Ser 57, Ser 215) and *Y code letter (Tyr 225) from VDAC1-*Homo sapiens*, VDAC1-*Mus musculus* and VDAC2-*Danio rerio*.

Next, the Euclidean distances (d_{ij}: SWCNT-VDAC interatomic distance) were calculated from all the atoms in the SWCNT to all the atoms in the VDAC channel in each species under study. The xyz-coordinates of all atoms of a VDAC channel (*x*: VDAC, *y*: VDAC, *z*: VDAC) were taken as input, and the xyz-coordinates (*x*: SWCNT, *y*: SWCNT, *z*: SWCNT) of all atoms of a SWCNT were taken as output (or a minimum distance) between a $SWCNT_i$ atom and a $VDAC_j$ atom, according to the following equation (6):

$$d_{ij} = \sqrt{(x_{(i)swcnt} - x_{(j)vdac})^2 + (y_{(i)swcnt} - y_{(j)vdac})^2 + (z_{(i)swcnt} - z_{(j)vdac})^2} \tag{6}$$

To evaluate the $SWCNT_i$-$VDAC_j$ interaction, a cutoff value of 7 Å was used, i.e., all atoms with distances $d_{ij} \leq 7$ Å were considered as interacting atoms according to standard docking studies[52,53].

Performed molecular docking. For the docking tests, the following were used: VDAC channels from VDAC1-*Homo sapiens* (PDB ID:2JK4, resolution 4.1 Å), VDAC1-*Mus musculus* (PDB ID:3EMN, resolution 2.3 Å), VDAC2-*Danio rerio* (PDB ID:4BUM, Resolution 2.8 Å), and a combination of SWCNT ligands, such as armchair-H, armchair-COOH and armchair-OH (Hamada index $n = m$; 21 nanotubes); chiral-H, chiral-COOH and chiral-OH (no reflection symmetry; 93 nanotubes); zigzag-H, zigzag- COOH and zigzag-OH (Hamada index $m = 0$, $n > 0$; 21 nanotubes) and the ATP ligand molecule as reference control ($C_{10}\,H_{16}\,N_5\,O_{13}\,P_3$, ATP model, SDF format from PubChem CID: 5957). All docking simulations were performed using the default values for Autodock Vina parameters.

Statistical analysis. Mean values of free energy binding (FEB) from the various single-walled carbon nanotubes were compared through two-way analysis of variance in which the factors were SWCNT functionalization (-H, -OH and -COOH) and SWCNT electrotopological properties (chiral, armchair and zigzag). Normality and variance homogeneity assumptions have been previously verified. Pairwise comparisons were performed using the Newman-Keuls *post-hoc* test. In all cases, type I error was set at 0.05 ($\alpha = 5\%$). Quantitative structure-binding affinity relationships were evaluated through the use of stepwise multiple regressions, considering the FEB values of the SWCNT (SWCNT-H, SWCNT-OH and SWCNT-COOH)-VDAC complexes obtained from the different species (*Danio rerio*; *Mus musculus*; *Homo sapiens*) as dependent variables and several semi-empirical SWCNT

SWCNT nanodescriptors (V_k)	Symbol
FEB (ATP) (Kcal/mol)	−5.6
Tube Length (Å)	10
m-Hamada index	V00
n-Hamada index	V01
Molecular Weight (g/mol)	V02
No. Bonds	V03
No. Atoms	V04
Radio Rt (nm)	V05
Nanotube diameter: $d_{SWCNT\ (n;\ m)}$	V06
Highest common divisor of (n, m)	V07
Highest common divisor of (2n + m, 2 m + n)	V08
Translation vector: T(Å)	V09
Semi-empirical Homo-Lumo Bandgap E_g(eV)	V10
Chiral vector: C_h (nm)	V11
Chiral angle (θ)	V12
mod (n−m, 3)	V13
Semi-empirical V_{RBM} (cm^{-1})	V14
First van Hove Singularity Optical Transitions peak-[E_{11}] (eV)	V15
Second van Hove Singularity Optical Transitions peak-[E_{22}] (eV)	V16
No. hexagon/unit cell (N/2)	V17

Table 3. Variables used as input for the NQSBR model.

quantitative nanodescriptors (*n*, *m*-Hamada indexes, chiral angle, molecular weight, diameter, etc.) as independent variables.

VDAC channel alignments. Sequences of VDAC-1 from human *Homo sapiens* (NP_003365.1), VDAC1 from mouse *Mus musculus* (NP_035824.1) and VDAC2 from zebrafish *Danio rerio* (NP_001001404.1) were obtained from Gene Bank database (http://www.ncbi.nlm.nih.gov/genbank/). The alignments were performed on-line using the free software ClustalW2 (http://www.ebi.ac.uk/Tools/msa/clustalw2/). In addition, 3D structural alignment of VDAC from the different species tested was performed by VMD - Visual Molecular Graphics Software. Next, the PDB model X-ray structure validation from the different VDAC channels was performed by Ramachandran plots using MolProbity[51].

Model construction

Dataset. The dataset contains 19 features or SWCNT nanodescriptors (see Table 3) based on the SWCNT periodic properties[41–45] such as *m*-Hamada index (V00), *n*-Hamada index (V01), molecular weight (V02), number of bonds (V03), number of atoms (V04), CNT radio Rt in nm (V05), nanotube diameter dt in nm (V06), highest common divisor of (n, m) (V07), highest common divisor of (2n + m, 2 m + n) (V08), translation vector T in Å (V09), semi-empirical HOMO-LUMO band gap Eg in eV (V10), chiral vector in nm (V11), chiral angle θ (V12), mod(n−m, 3) (V13), estimated VRBM in cm^{-1} (V14), First van Hove Singularity Optical Transitions peak E11 in eV (V15), Second van Hove Singularity Optical Transitions peak E22 in eV (V16), and number of hexagons/unit cell (N/2) (V17). In addition, the Docking Free Energy of Binding (*FEB expected*) for the SWCNT groups (SWCNT type and SWCNT function as H, OH, COOH) was added using Perturbation Theory (PT).

Thus, 19 SWCNT nanodescriptors and 405 cases were used to build NQSBR classification and regression models that can predict whether the SWCNT-VDAC interactions are weak or strong, along with FEB values.

Performed NQSBR model based on Docking Perturbation Theory. In this section, a Nano-Quantitative Structure-Binding Relationship (PT-NQSBR model) was developed. To this end, a new prospective docking scoring function is used to predict the strength of the binding b_{ij} between the i^{th} CNT and the j^{th}-VDAC from three different species. The free energies of binding (FEB), calculated in molecular docking experiments as the measure of b_{ij}, were also employed. $b_{ij} = 1$ was considered when $FEB_{ij} < -5.6$ kcal/mol (strong binding interaction), otherwise $b_{ij} = 0$ (weak binding interaction). The cut-off FEB value was set at −5.6 kcal/mol, which represents the FEB value for the molecular docking interaction of the natural ligand substrate ATP with VDAC (calculated in this work, *vide infra*).

The re-formulation of the QSAR/QSPR approach was described, based on the Perturbation Theory (PT) to develop a new type of PT-NQSBR model for prospective classification of single-walled carbon nanotubes associated with VDAC channel nano-mitotoxicity. The main assumption of QSAR/QSPR models in general is that similar molecules have similar properties. Consequently, small changes ("*perturbations*") in the structural system should correlate linearly with small changes in the values of their properties (biological activities). PT-QSPR models are very useful for the study of complex molecular systems with simultaneous multiple experimental boundary conditions.

In this regard, the QSPR approach of the Perturbation Theory is a mathematical formalism that starts by knowing the exact solution of a problem (for instance a SWCNT physico-chemical property for VDAC interaction) and continues by adding corrections or "perturbations", according to the variations of different experimental conditions in order to predict a solution to a related problem without a known exact solution[9,30,31]. In our previous studies, Moving Average (MA) has been used to measure the deviations of the different input variables in PT models for several molecular bio-systems[18–20,31]. The PT-NQSBR model proposed herein is an additive polynomial equation expressed as follows:

$$f(FEB)_{calc} = e_0 + a_0 \cdot \left\langle f(FEB)_{expected} \right\rangle + \sum_{k=1}^{k=14} a_k \cdot \Delta V_k \quad (7)$$

$$f(FEB)_{calc} = e_0 + a_0 \cdot \left\langle f(FEB)_{expected} \right\rangle + \sum_{k=1}^{k=14} a_k \cdot [{}^{query}V_k - {}^{ref}V_k] \quad (8)$$

The first input term is the function $f(\mathrm{FEB})_{\mathrm{expected}} = <\mathrm{FEB}>$, which is the average value of FEB for a specific VDAC channel of one species for all SWCNTs of the same class with the same function (H, OH, or COOH), and the same electronic properties (metallic, semimetallic, semiconductor). It means that $<\mathrm{FEB}>$ can be considered as the expected value of FEB for the interaction of a SWCNT of the same class as the new SWCNT with the target protein VDAC (assuming a normal distribution). The second class of terms such as Vk, are values of the structural parameters (or SWCNT nanodescriptors) of the new SWCNT (or query SWCNT). Last, the difference ($\Delta V_k = {}^{query}V_k - {}^{ref}V_k$) quantifies the perturbations (changes, distortions, etc.) of the SWCNT nanodescriptors (${}^{query}V_k$) of the new SWCNT compared to those of the original reference SWCNT (${}^{ref}V_k$). Please refer to Table 1 for further details on the employed model.

The Linear Discriminant Analysis (LDA) forward-stepwise algorithms from the STATISTICA software were used to fit the values of the parameters (a0, ak, bk and e0). In the PT-NQSBR model, the output *f*(FEB)calc is a function of the value of FEB for the new SWCNT structure, which contains the SWCNT nanodescriptors (Hamada index *n* and *m*, diameter, molecular weight, number of atoms, radial breathing mode or V_{RBM} frequencies, etc).

Performed classification NQSBR models. Complex models, such as NQSBR classification models, were constructed using two types of applications: STATISTICA and Weka based on Machine Learning. With STATISTICA, the following models were calculated: Linear Discriminant Analysis (LDA), Multilayer Perceptron (MLP) and Radial basis function network (RBF). Weka provided an attribute selection tool where the process was separated into two parts: 1) Attribute Evaluator Method, through which attribute subsets were assessed and **2)** Search Method, which allows searching for the space of possible subsets of features (SWCNT nanodescriptors)[36].

Weka was used to search for models using other 12 non-linear methods grouped into classes of classifiers such as *bayes* (Bayes Network, Naïve Bayes), *functions* (Multilayer Perceptron - MLP), *lazy* (IBk, KStar or K*), *rules* (Decision Table, JRip, OneR, PART), and *trees* (J48, Random Forest, REP Tree). Thus, 14 Machine Learning[36] methods were used to compare the performance of prediction for weak or strong SWCNT-VDAC interactions.

The FEB values were transformed in two classes of SWCNT-VDAC nano-interactions: strong and weak, considering a FEB cut-off value (based on the FEB value of ATP-VDAC interaction) of −5.6 Kcal/mol, as mentioned above.

With STATISTICA, the datasets were randomly split into two subsets: training and test validation sets (75% training, 25% validation). Using Weka, the default 10-fold cross-validation (CV) was used. The performance of the classification models was measured with accuracy, specificity, and sensitivity. With Weka data mining algorithms, several variations of the initial dataset of SWCNT nanodescriptors were generated using filter methods (or feature selection, FS) to verify the influence of a high or low number of SWCNT nanodescriptors in the NQSBR model. The group of SWCNT nanodescriptors is more important to obtain a better model in order to describe the SWCNT-VDAC interaction (channel nanotoxicity) such as:

- *FS0* represents the dataset with the same SWCNT nanodescriptors of the best predictive linear NQSBR model obtained with STATISTICA (4 SWCNT nanodescriptors: FEBexp, V01, V11, V14);
- *Pool* contains all the features (SWCNT nanodescriptors: FEBexp, V00–V17);
- *FS1* was obtained by feature selection with parameters, using Evaluator (*CfsSubsetEval*) to assess subsets of SWCNT nanodescriptors that highly correlate with the class value and have low correlation with each other. In addition, Search (*Best First*) was used for 6 SWCNT nanodescriptors: FEBexp, V02, V03, V04, V10, V12) with a best-first search strategy to navigate attribute subsets which reduce training time, overfitting, and improves accuracy.
- *FS2* was obtained by feature selection with Evaluator (*Correlation Attribute Eval*) following the principle that features (SWCNT nanodescriptors) are relevant if their values vary systematically with the membership category. Search (*Ranker*) was also used, based on 8 SWCNT nanodescriptors: FEBexp, V02, V03, V04, V09, V11, V12, V14);
- *FS3* was obtained by Weka data mining feature selection using Evaluator (*Principal Components*) and Search (*Ranker*) based on 8 SWCNT nanodescriptors); the Principal Component[62] transformation was used to study the influence of dataset dimension reduction by encoding the information of 19 SWCNT nanodescriptors into only 8 linear combinations of them;
- *FS4* contains only 2 SWCNT nanodescriptors that have proven to be very important for the models (*FEB expected*, V02).

The performance of the Classification Machine Learning NQSBR models from Weka are characterized by 3 criteria: maximum AUROC[63], maximum TP Rate (true positive rate), minimum FP Rate (false positive rate), commonly used in the field of chemoinformatics[36] and currently in computational nanotoxicology. To visualize and verify the results obtained with the LDA classification NQSBR model from the external dataset, we used a set of empirical physico-chemical parameters of pristine SWCNT, not tested in our original dataset, obtained by Bachilo *et al.* (2002)[44]. In addition, to represent the multiple factors involved in VDAC channel nanotoxicity, a Two Way Joining Cluster (TWJC) analysis was performed through heat map of contingency table[64].

Performed regression NQSBR models. The Pool dataset was used with the RRegrs methodology[33,37] taking into account all the SWCNT nanodescriptos (V00–V17) to find the best regression model that predicts FEB values for the SWCNT-VDAC interactions. The initial dataset was normalized using R scripts. RRegrs is an R integrated framework that provides ten linear and non-linear regression models. The following regression methods were tested: Multiple Linear regression (LM), Generalized Linear Model with Stepwise Feature Selection (GLM), Lasso regression (Lasso), Partial Least Squares Regression (PLS), Elastic Net regression (ENET), Neural Networks regression (NN), Random Forest (RF), and Random Forest Recursive Feature Elimination (RF-RFE)[33]. Standard RRegrs parameters and methodology were applied: dataset automatically devided by RRegrs using 10 splits (train and test subsets)[33]. The selection of the best regression models used R^2_{test} (regression coefficient for test subset) and $RMSE_{test}$ (root-mean-square errors for test subset) values Figshare[48] (Fig. SM02). As an initial test, regression models were sought by excluding the FEBexp, checking the importance of the Perturbation Theory for these regression models when predicting the SWCNT-VDAC interactions.

References

1. Choudhary, O. P. *et al.* Structure-guided simulations illuminate the mechanism of ATP transport through VDAC1. *Nat. Struct. Mol. Biol.* **21**, 626–632 (2014).
2. Bayrhuber, M. *et al.* Structure of the human voltage-dependent anion channel. *Proc. Natl. Acad. Sci. USA* **105**, 15370–15375 (2008).
3. Ujwal, R. *et al.* The crystal structure of mouse VDAC1 at 2.3 A resolution reveals mechanistic insights into metabolite gating. *Proc. Natl. Acad. Sci. USA* **105**, 17742–17747 (2008).
4. Okada, S. F. *et al.* Voltage-dependent anion channel-1 (VDAC-1) contributes to ATP release and cell volume regulation in murine cells. *J. Gen. Physiol.* **124**, 513–526 (2004).
5. Crompton, M. The mitochondrial permeability transition pore and its role in cell death. *Biochem. J.* **341**(Pt 2), 233–249 (1999).
6. Scatena, R., Bottoni, P., Botta, G., Martorana, G. E. & Giardina, B. The role of mitochondria in pharmacotoxicology: a reevaluation of an old, newly emerging topic. *Am. J. Physiol. Cell Physiol.* **293**, C12–21 (2007).
7. Pi, Y., Goldenthal, M. J. & Marin-Garcia, J. Mitochondrial channelopathies in aging. *J. Mol. Med. (Berl.)* **85**, 937–951 (2007).
8. Bernardi, P. & Di Lisa, F. The mitochondrial permeability transition pore: molecular nature and role as a target in cardioprotection. *J. Mol. Cell. Cardiol.* **78**, 100–106 (2015).
9. Martel, C., Wang, Z. & Brenner, C. VDAC phosphorylation, a lipid sensor influencing the cell fate. *Mitochondrion* **19**(Pt A), 69–77 (2014).
10. Foldvari, M. & Bagonluri, M. Carbon nanotubes as functional excipients for nanomedicines: II. Drug delivery and biocompatibility issues. *Nanomed.* **4**, 183–200 (2008).
11. Shvedova, A. A., Pietroiusti, A., Fadeel, B. & Kagan, V. E. Mechanisms of carbon nanotube-induced toxicity: focus on oxidative stress. *Toxicol. Appl. Pharmacol.* **261**, 121–133 (2012).
12. Forli, S. *et al.* Computational protein-ligand docking and virtual drug screening with the AutoDock suite. *Nature Protocols* **11**, 905–919 (2016).
13. Kramer, B., Rarey, M. & Lengauer, T. CASP2 experiences with docking flexible ligands using FlexX. *Proteins* Suppl 1, 221–225 (1997).
14. Deng, Y. & Roux, B. Computations of standard binding free energies with molecular dynamics simulations. *J. Phys. Chem. B* **113**, 2234–2246 (2009).
15. Shoichet, B. K. Virtual screening of chemical libraries. *Nature* **432**, 862–865 (2004).
16. Wang, X. *et al.* Multi-walled carbon nanotubes induce apoptosis via mitochondrial pathway and scavenger receptor. *Toxicol. In Vitro* **26**, 799–806 (2012).
17. Jia, G. *et al.* Cytotoxicity of carbon nanomaterials: single-wall nanotube, multi-wall nanotube, and fullerene. *Environ. Sci. Technol.* **39**, 1378–1383 (2005).
18. Gonzalez-Durruthy, M. *et al.* Predicting the binding properties of single walled carbon nanotubes (SWCNT) with an ADP/ATP mitochondrial carrier using molecular docking, chemoinformatics, and nano-QSBR perturbation theory. *RSC Advances* **6**, 58680 (2016).
19. González-Durruthy, M. *et al.* Mitoprotective activity of oxidized carbon nanotubes against mitochondrial swelling induced in multiple experimental conditions and predictions with new expected-value perturbation theory. *RSC Adv.* **5**, 103229–103245 (2015).
20. González-Durruthy, M. *et al.* QSPR/QSAR-based Perturbation Theory approach and mechanistic electrochemical assays on carbon nanotubes with optimal properties against mitochondrial Fenton reaction experimentally induced by Fe2+-overload. 115, 312-330 (2017).
21. Toropova, A. P. *et al.* Nano-QSAR: Model of mutagenicity of fullerene as a mathematical function of different conditions. *Ecotoxicol. Environ. Saf.* **124**, 32–36 (2016).
22. Jagiello, K. *et al.* Advantages and limitations of classic and 3D QSAR approaches in nano-QSAR studies based on biological activity of fullerene derivatives. *Journal of nanoparticle research: an interdisciplinary forum for nanoscale science and technology* **18**, 256 (2016).
23. Shahbazy, M., Kompany-Zareh, M. & Najafpour, M. M. QSAR analysis for nano-sized layered manganese-calcium oxide in water oxidation: An application of chemometric methods in artificial photosynthesis. *J. Photochem. Photobiol. B.* **152**, 146–155 (2015).
24. Toropova, A. P. & Toropov, A. A. Nano-QSAR in cell biology: Model of cell viability as a mathematical function of available eclectic data. *J. Theor. Biol.* **416**, 113–118 (2017).
25. Manganelli, S. & Benfenati, E. Nano-QSAR Model for Predicting Cell Viability of Human Embryonic Kidney Cells. *Methods Mol. Biol.* **1601**, 275–290 (2017).
26. Toropova, A. P. & Toropov, A. A. Mutagenicity: QSAR - quasi-QSAR - nano-QSAR. *Mini Rev Med Chem* **15**, 608–621 (2015).
27. Sizochenko, N., Gajewicz, A., Leszczynski, J. & Puzyn, T. Causation or only correlation? Application of causal inference graphs for evaluating causality in nano-QSAR models. *Nanoscale* **8**, 7203–7208 (2016).
28. Gajewicz, A. *et al.* Towards understanding mechanisms governing cytotoxicity of metal oxides nanoparticles: hints from nano-QSAR studies. *Nanotoxicology* **9**, 313–325 (2015).
29. Puzyn, T. *et al.* Using nano-QSAR to predict the cytotoxicity of metal oxide nanoparticles. *Nature nanotechnology* **6**, 175–178 (2011).
30. Gonzalez-Diaz, H. *et al.* General theory for multiple input-output perturbations in complex molecular systems. 1. Linear QSPR electronegativity models in physical, organic, and medicinal chemistry. *Curr. Top. Med. Chem.* **13**, 1713–1741 (2013).

31. Luan, F. *et al*. Computer-aided nanotoxicology: assessing cytotoxicity of nanoparticles under diverse experimental conditions by using a novel QSTR-perturbation approach. *Nanoscale* **6**, 10623–10630 (2014).
32. Speck-Planche, A., Kleandrova, V. V., Luan, F. & Cordeiro, M. N. Computational modeling in nanomedicine: prediction of multiple antibacterial profiles of nanoparticles using a quantitative structure-activity relationship perturbation model. *Nanomedicine (Lond)* **10**, 193–204 (2015).
33. Fernandez-Lozano, C., Gestal, M., Munteanu, C. R., Dorado, J. & Pazos, A. A methodology for the design of experiments in computational intelligence with multiple regression models. *PeerJ* **4**, e2721 (2016).
34. Teixeira, A. L., Leal, J. P. & Falcao, A. O. Random forests for feature selection in QSPR Models - an application for predicting standard enthalpy of formation of hydrocarbons. *J Cheminform* **5**, 9 (2013).
35. Lavecchia, A. Machine-learning approaches in drug discovery: methods and applications. *Drug Discov. Today* **20**, 318–331 (2015).
36. Smith, T. C. & Frank, E. In Statistical Genomics: Methods and Protocols 353–378 (Springer, New York, NY; 2016).
37. Tsiliki, G. *et al*. RRegrs: an R package for computer-aided model selection with multiple regression models. *J Cheminform* **7**, 46 (2015).
38. Bishop, C. M. Neural Networks for Pattern Recognition (Oxford University Press, USA, New York; 1995).
39. Shahlaei, M. Descriptor selection methods in quantitative structure-activity relationship studies: a review study. *Chem. Rev.* **113**, 8093–8103 (2013).
40. Shao, C. Y. *et al*. Dependence of QSAR models on the selection of trial descriptor sets: a demonstration using nanotoxicity endpoints of decorated nanotubes. *J. Chem. Inf. Model.* **53**, 142–158 (2013).
41. Torrens, F. Periodic Properties of Carbon Nanotubes Based on the Chiral Vector. *Internet Electron. J. Mol. Des.* **1**, 59–81 (2005).
42. Yorikawa, H. & Muramatsu, S. Energy gaps of semiconducting nanotubules. *Phys. Rev. B* **52**, 2723 (1995).
43. Kleiner, A. & Eggert, S. Band gaps of primary metallic carbon nanotubes. *Phys Rev B.* **63**, 073408 (2001).
44. Bachilo, S. M. *et al*. Structure-assigned optical spectra of single-walled carbon nanotubes. *Science* **298**, 2361–2366 (2002).
45. Maultzsch, J., Telg, H., Reich, S. & Thomsen, C. Radial breathing mode of single-walled carbon nanotubes: Optical transition energies and chiral-index assignment. *Phys. Rev. B* **72**, 205438 (2005).
46. Xia, X. R. *et al*. Mapping the surface adsorption forces of nanomaterials in biological systems. *ACS Nano* **5**, 9074–9081 (2011).
47. Hiller, S., Abramson, J., Mannella, C., Wagner, G. & Zeth, K. The 3D structures of VDAC represent a native conformation. *Trends Biochem. Sci.* **35**, 514–521 (2010).
48. Munteanu, C.R. D., results and models for nanoQSAR & docking of SWCNT with Mitochondrial VDAC, https://doi.org/10.6084/m9.figshare.4802320.v2 (2017)
49. Berman, H. M. *et al*. The Protein Data Bank. *Nucleic Acids Res.* **28**, 235–242 (2000).
50. Ting, D. *et al*. Neighbor-dependent Ramachandran probability distributions of amino acids developed from a hierarchical Dirichlet process model. *PLoS Comput. Biol.* **6**, e1000763 (2010).
51. Davis, I. W. *et al*. MolProbity: all-atom contacts and structure validation for proteins and nucleic acids. *Nucleic Acids Res.* **35**, W375–383 (2007).
52. da Silveira, C. H. *et al*. Protein cutoff scanning: A comparative analysis of cutoff dependent and cutoff free methods for prospecting contacts in proteins. *Proteins* **74**, 727–743 (2009).
53. Xie, Z. R. & Hwang, M. J. An interaction-motif-based scoring function for protein-ligand docking. *BMC Bioinformatics* **11**, 298 (2010).
54. Park, K. H., Chhowalla, M., Iqbal, Z. & Sesti, F. Single-walled carbon nanotubes are a new class of ion channel blockers. *J. Biol. Chem.* **278**, 50212–50216 (2003).
55. Das, S., Wong, R., Rajapakse, N., Murphy, E. & Steenbergen, C. Glycogen synthase kinase 3 inhibition slows mitochondrial adenine nucleotide transport and regulates voltage-dependent anion channel phosphorylation. *Circ. Res.* **103**, 983–991 (2008).
56. Weiser, B. P., Salari, R., Eckenhoff, R. G. & Brannigan, G. Computational investigation of cholesterol binding sites on mitochondrial VDAC. *J. Phys. Chem. B* **118**, 9852–9860 (2014).
57. McCommis, K. S. & Baines, C. P. The role of VDAC in cell death: friend or foe? *Biochim. Biophys. Acta* **1818**, 1444–1450 (2012).
58. Chen, C. W. & Lee, M. H. Dependence of work function on the geometries of single-walled carbon nanotubes. *Nanotechnology* **15**, 480 (2004).
59. Latti, S., Niinivehmas, S. & Pentikainen, O. T. Rocker: Open source, easy-to-use tool for AUC and enrichment calculations and ROC visualization. *J Cheminform* **8**, 45 (2016).
60. Weisman, R. B. & Bachilo, S. M. Dependence of optical transition energies on structure for single-walled carbon nanotubes in aqueous suspension: An empirical Kataura plot. *Nano Lett.* **3**, 1235–1238 (2003).
61. Trott, O. & Olson, A. J. AutoDock Vina: improving the speed and accuracy of docking with a new scoring function, efficient optimization, and multithreading. *J. Comput. Chem.* **31**, 455–461 (2010).
62. Natarajan, R., Nirdosh, I., Basak, S. C. & Mills, D. R. QSAR modeling of flotation collectors using principal components extracted from topological indices. *J. Chem. Inf. Comput. Sci.* **42**, 1425–1430 (2002).
63. Hanley, J. A. & McNeil, B. J. The meaning and use of the area under a receiver operating characteristic (ROC) curve. *Radiology* **143**, 29–36 (1982).
64. Ciampi, A., Marcos, A. G. & Limas, M. C. Correspondence analysis and two-way clustering. *SORT* **29**, 27–42 (2005).

Acknowledgements

J.M. Monserrat is research productivity fellow from CNPq (process number PQ 308539/2016-8). A part of this study was supported by a grant from CNPq (Project number 552131/2011-3 and 454332/2014-9) offered to J.M. Monserrat. K. Machado acknowledges the support from CNPq (Process number 477462/2013-8). M. González-Durruthy is supported by a Doctoral fellowship (PEC-PG Program-Edital 062/2013) from the Brazilian Agencies CAPES and CNPq. Authors would also like to thank the support of the General Directorate of Culture, Education, and University Management of Xunta de Galicia (Ref. GRC2014/049) and the European Fund for Regional Development (FEDER) from the European Union. In addition, the work was supported by the "Galician Network for Colorectal Cancer Research (REGICC)" (Ref. R2014/039), funded by the Xunta de Galicia.

Author Contributions

M.G.D., J.M.M. performed the design and optimization of the SWCNT family as VDAC ligands. They carried out the free energy binding graphical representations, VDAC primary sequence-alignment analysis, the Ramachandran maps of the crystallographic validation from VDAC.pdb x-ray structures and developed the discussion on nanotoxicological topics. V.S., A.V.W. and K.M. implemented the Docking Simulation coupled to a Virtual Screening Framework (DS-VSF) and calculated the interatomic distance values. H.G.-D., A.P. and C.R.M. conducted the analysis of the SWCNT dataset and developed the new theoretical predictions on classification nano-Quantitative Structure-Binding Relationship models (NQSBR) based on the Perturbation Theory, machine learning and regression models. All authors discussed the results and commented on the manuscript.

Additional Information

Supplementary information accompanies this paper at doi:10.1038/s41598-017-13691-8

Competing Interests: The authors declare that they have no competing interests.

Publisher's note: Springer Nature remains neutral with regard to jurisdictional claims in published maps and institutional affiliations.

Artigo 5: Experimental−Computational Study of Carbon Nanotube E ects on Mitochondrial Respiration: In Silico Nano-QSPR Machine Learning Models Based on New Raman Spectra Transform with Markov− Shannon Entropy Invariants

JOURNAL OF CHEMICAL INFORMATION AND MODELING

Article

pubs.acs.org/jcim

Experimental−Computational Study of Carbon Nanotube Effects on Mitochondrial Respiration: In Silico Nano-QSPR Machine Learning Models Based on New Raman Spectra Transform with Markov−Shannon Entropy Invariants

Michael González-Durruthy,[†,‡] Luciane C. Alberici,[§] Carlos Curti,[§] Zeki Naal,[∥] David T. Atique-Sawazaki,[∥] José M. Vázquez-Naya,[⊥] Humberto González-Díaz,[#,○] and Cristian R. Munteanu*[,⊥,△]

[†]Institute of Biological Science (ICB) and [‡]Post-Graduate Program in Physiological Sciences, Universidade Federal do Rio Grande−FURG, 96270-900, Rio Grande, RS, Brazil

[§]Department of Physical Chemistry, Faculty of Pharmacy of Ribeirão Preto, and [∥]Department of Chemistry, Faculty of Philosophy, Sciences and Letters, University of São Paulo (USP), 14040-903 Ribeirão Preto, SP, Brazil

[⊥]RNASA-IMEDIR, Computer Science Faculty, University of A Coruna, Campus de Elviña s/n, 15071 A Coruña, Spain

[#]Department of Organic Chemistry II, Faculty of Science and Technology, University of the Basque Country UPV/EHU, 48940, Leioa, Bizkaia, Spain

[○]IKERBASQUE, Basque Foundation for Science, 48011, Bilbao, Bizkaia, Spain

[△]Instituto de Investigación Biomédica de A Coruña (INIBIC), Complexo Hospitalario Universitario de A Coruña (CHUAC), A Coruña, 15006, Spain

ABSTRACT: The study of selective toxicity of carbon nanotubes (CNTs) on mitochondria (CNT-mitotoxicity) is of major interest for future biomedical applications. In the current work, the mitochondrial oxygen consumption (E3) is measured under three experimental conditions by exposure to pristine and oxidized CNTs (hydroxylated and carboxylated). Respiratory functional assays showed that the information on the CNT Raman spectroscopy could be useful to predict structural parameters of mitotoxicity induced by CNTs. The in vitro functional assays show that the mitochondrial oxidative phosphorylation by ATP-synthase (or state V3 of respiration) was not perturbed in isolated rat-liver mitochondria. For the first time a star graph (SG) transform of the CNT Raman spectra is proposed in order to obtain the raw information for a nano-QSPR model. Box−Jenkins and perturbation theory operators are used for the SG Shannon entropies. A modified RRegrs methodology is employed to test four regression methods such as multiple linear regression (LM), partial least squares regression (PLS), neural networks regression (NN), and random forest (RF). RF provides the best models to predict the mitochondrial oxygen consumption in the presence of specific CNTs with R^2 of 0.998−0.999 and RMSE of 0.0068−0.0133 (training and test subsets). This work is aimed at demonstrating that the SG transform of Raman spectra is useful to encode CNT information, similarly to the SG transform of the blood proteome spectra in cancer or electroencephalograms in epilepsy and also as a prospective chemoinformatics tool for nanorisk assessment. All data files and R object models are available at https://dx.doi.org/10.6084/m9.figshare.3472349.

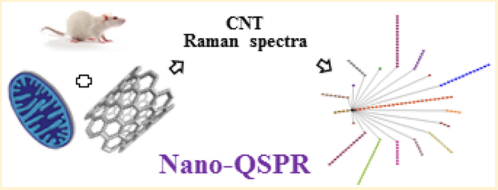

INTRODUCTION

The boom in research on carbon nanotube (CNT) shaped nanoparticles has led to the development of more powerful designs and synthesis methods.[1] Currently, several scientific reports highlight a major impact of adverse/toxic effects induced by carbon nanomaterials on critical subcellular components, mainly mitochondria, which are responsible for the maintenance of the bioenergetic balance of ADP/ATP, redox, and cellular homeostasis in all eukaryotic organisms.[2,3]

In this regard, carbon nanotubes have attracted attention for their high ability to accumulate in the mitochondrial matrix from several tissues and cells based on a peculiar mitotropic behavior. The important role of mitochondria to regulate intracellular ROS-levels based on the complete reduction of molecular oxygen by the respiratory complexes, has been extensively characterized and associated with several chronic pathological processes, such as neurodegenerative diseases (Alzheimer, Parkinson, Epilepsy), cardiovascular conditions, and cancer, which currently have high levels of morbidity and mortality, and where mitochondrial dysfunction mechanisms have been directly involved.[2,3]

Received: August 7, 2016
Published: April 17, 2017

DOI: 10.1021/acs.jcim.6b00458
J. Chem. Inf. Model. 2017, 57, 1029−1044

Mitochondrial events such as the dissipation of the membrane potential, the generation of reactive oxygen species and the release of caspase-activating proteins are closely linked to the mechanisms of cell death by apoptosis and necrosis. Lipophilic compounds such as carbon nanomaterials (single- and multiwalled CNTs (SWCNTs, MWCNTs)), with high lipid−water partition coefficients and enough access to the mitochondrial membranes could induce cell death mediated by mitochondrial mechanisms. The presence of carbon nanotubes near the respiratory chain can disrupt the normal flow of electrons along the respiratory complexes by decreasing the proton gradient and ATP synthesis. It is well-known that the mitochondria are essential elements in controlling the death or survival of the cell and they are, therefore, an important pharmacological and toxicological target that can be considered in the planning and evaluation of new carbon nanomaterials as potentially cytoprotective or cytotoxic based on their mitochondrial effects.[2,3] Consequently, a certain concern was raised about the toxicity/safety rates of these new materials with emphasis on the respiratory system.[4]

In this context, our hypothesis is that new structural information (CNT nanodescriptors) obtained from Raman spectra, based on the criteria of rational drug design and mitochondrial medicine, could improve efficient therapeutic strategies against the aforementioned diseases, considering the chemical/pharmacological modulation of mitochondrial respiratory mechanisms.

Following this idea, it is well-known that Raman spectroscopy is one of the most important experimental techniques for the characterization, detection, biological interactions, and/or toxicity of CNTs. This is due to the fact that the D band feature in the CNT Raman spectra, with a peak at approximately 1350 cm^{-1}, is commonly associated with the presence of topological defects and type of functionalization (chemical oxidation) in the carbon lattice, which is known to be able to influence the interaction properties between the CNTs and the protein complexes of the mitochondrial electron transport chain, depending on the physical−chemical characteristics of carbon nanotubes.[5]

On the other hand, polarographic mechanistic assays provide a quick and reproducible means of measuring the rate of oxygen consumption by mitochondria isolated from different tissues.[6] However, there are no precedents of this methodology applied to the evaluation of potential toxicity of CNTs. Some in vitro studies have demonstrated that CNTs exert cytotoxicity after their accumulation in the mitochondrial matrix and/or by affecting the function of mitochondrial proteins of the inner membrane.[7] Previous in vitro research on drugs and environmental pollutants using submitochondrial particles (respiratory chain complexes I, II, III, IV; ADP/ATP translocator, ATP synthase/ATPase) to predict the toxic impact of 92 different xenobiotics showed a strong correlation with toxicity in humans and pointed out that the mitochondrial area was a relevant model for studying the relative toxicity of many xenobiotics.[8] Recent efforts have been made to create a unified ontology for the annotation of data about nanomaterial safety entitled eNanoMapper.[9]

The combination of different methods proved to be a powerful tool in designing nanoscale systems such as CNTs, iron nanoparticles or micelle nanoparticles.[10] Thus, quantitative structure−property/activity relationship (QSPR/QSAR) methods have been used as complementary tools for experiments by providing theoretical nano-QSPR prediction models.[11−28] Since not all similar molecules have similar properties, the purpose is to define the *small* structural changes of molecules. In order to describe these differences, a PT-QSPR method has been proposed:[29] it combines QSPR/QSAR with perturbation theory (PT). Thus, the PT-QSPR models have been applied to complex molecular systems using a variation of multiple experimental boundary conditions: chemical reactivity, drug metabolism, vaccine peptide epitopes, metabolic networks, micelle nanoparticles,[29−32] cytotoxicity of nanoparticles,[33] ecotoxicity and cytotoxicity of uncoated and coated nanoparticles,[28,29] and antibacterial profiles of nanoparticles.[34] The classic QSPR/QSAR approach could be used with the Raman spectra descriptors and the observable output, but it limits the model information to the CNT Raman spectral data, without taking into the account the experimental conditions and time. Thus, the current study includes the information referring to the moving averages of the descriptors in specific experimental conditions, such as perturbation to the expected values of the observable output.

The design and development of novel carbon nanomaterials are currently expensive and complex processes. Thus, the new quantitative structure−activity relationship paradigm (or QSAR/QSPR tools) has become an important methodology for the prioritization/optimization of nanomaterials, as an alternative with less impact on health and environment in the nanoscience context (nanotoxicology).[35] Herein, a crucial step in QSPR is to express structural properties in a quantitative way, which is not always straightforward.[35,36] Therefore, QSPR model can be seen as a mathematical function that predicts the structure of a single or complex system using physicochemical parameters which numerically describe its essential properties. To this end, Gonzalez-Díaz et al.[29] proposed a general purpose PT-QSPR method combining a QSPR chemoinformatics approach and PT. PT-QSPR approaches are very useful for the study of complex molecular biosystems with simultaneous multiple experimental boundary conditions.

González-Díaz et al.[29] applied the PT-QSPR analysis linked to chemical reactivity studies, drug metabolism (ADME−pharmacokinetic parameters), immunotoxicity tests, metabolic networks, metal, and CNT nanoparticles. Toropova et al.[37] published a nano-QSPR model on pristine MWCNTs to study the genotoxicity under multiple experimental conditions. Recently, González-Durruthy et al.,[38] using a PT-nano-QSPR approach, have been able to predict the mitochondrial swelling inhibition (mitochondrial permeability transition pore mitoprotective activity) induced by oxidized CNT in multiple experimental conditions. The authors concluded that oxidized CNT could modulate the mitochondrial ROS-production involved in mitochondrial dysfunction.[38]

The main assumption of QSAR/QSPR approaches in general is that similar molecules have similar properties. Consequently, small structural changes ("perturbations") should correlate linearly with small changes on the values of their properties (biological activities). The QSPR perturbation model is able to find out the exact solution of a problem (physicochemical and/or biological property) and continues adding small corrections to predict a solution for a related problem, without knowing an exact solution.[39,40] In this context, currently there are no precedents for the application of this chemoinformatics methodology combining experimental and biochemical assays in isolated rat-liver mitochondria, including mechanistic explanations, to predict the potential effects of CNT on

DOI: 10.1021/acs.jcim.6b00458
J. Chem. Inf. Model. 2017, 57, 1029−1044

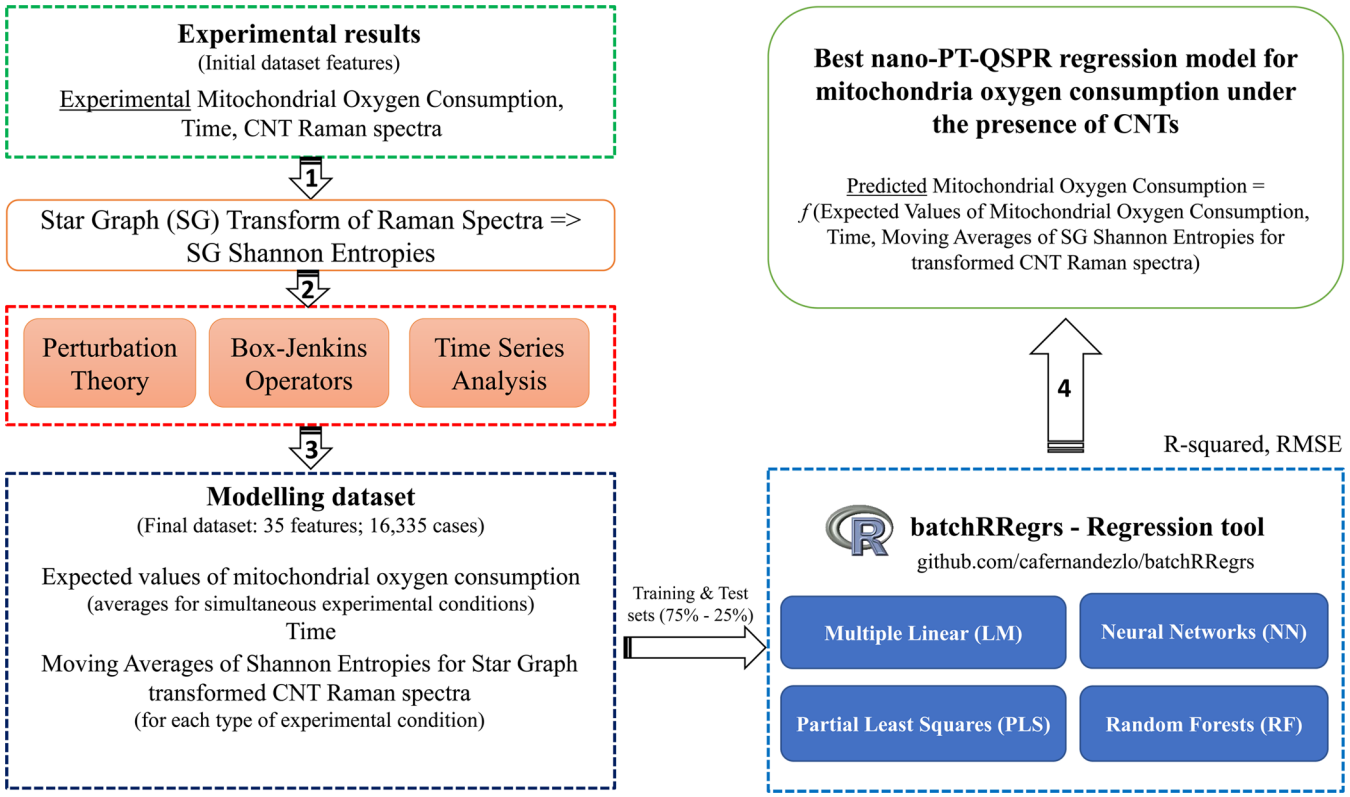

Figure 1. Methodology flowchart for nano-PT-QSPR models for mitochondrial oxygen consumption in the presence of CNTs.

mitochondrial respiration toward biomedical applications based on Raman spectroscopy structural information.

The current study proposes the use of CNT Raman spectra as the main molecular information. Raman spectroscopy is a technique that provides the chemical fingerprint of molecules as vibrational, rotational, and other low-frequency modes. Thus, it is used for the study of biomolecular systems and nanoscale structure such as DNA,[41] proteins,[42] antibodies,[43] and carbon nanotubes (CNTs).[44] The Raman spectra can be transformed into Shannon entropies of the star graph, similar to a Fourier spectra transform. The use of star graphs as a graphical method to encode molecular/signal information has been proven for protein prediction[45−47] and nucleic acid[48] function, as well as cancer prediction using blood protein mass spectra[49] and epileptic seizure prediction using electroencephalogram (EEG) signals.[50] The end point (mitochondrial respiration or E3) used in the QSPR/QSAR analyses is a predictive function of the mitochondrial oxygen consumption ($E3_{pred}$), which is the mitochondrial respiration under carbon nanotubes exposure obtained from the experimental data set as a function of Raman spectra transformed into star graph Shannon entropies indices (Sh_k) of CNT individual members of the tested CNT family. The expected values of the mitochondrial oxygen consumption ($E3_{exp}$) are the moving averages of the Raman spectra transformed into Sh_k indices under different experimental conditions and times of exposure. Points have been used as features (CNT nanodescriptors) to find the best PT-QSPR regression model that can predict the carbon nanotube effects on mitochondrial oxygen consumption in the presence of specific CNTs.

MATERIALS AND METHODS

General Workflow. The main aims of this paper are (a) development of a new transform of Raman spectra into Shannon entropy information indices (Sh_k), (b) measurement of the Raman spectra of a set of CNTs, (c) measurement of biological activity of these CNTs, and (d) use of the Sh_k values to predict the biological activity (mitochondria oxygen consumption or E3). In order to accomplish these objectives, a general workflow was proposed. The following list describes the steps of this workflow (Figure 1):

(1) Experimental measurements of the mitochondrial oxygen consumption under different experimental conditions with different types of CNTs
(2) Transformation of CNT Raman spectra into star graph Shannon entropies
(3) Use of nano-PT-QSPR methodology to calculate the expected values of the mitochondrial oxygen consumption and the moving averages of the Shannon entropies under different experimental conditions
(4) Search of regression nano-PT-QSPR models using batchRRegrs (an R tool for regressions)

Even if the RAMAN spectra need to be measured or predicted so that new CNTs could be used in the model, there is no need to measure the biological activity (E3) of CNTs in mitochondria, which is a difficult assay. In addition, it should be pointed out that the CNTs from the current study are commercial samples of CNTs. It means that the CNT samples do not contain single-molecule structures. On the contrary, each sample has many different molecules of CNTs with the same function type (H, OH, COOH) and the same percentage of this function, but in many different positions.

DOI: 10.1021/acs.jcim.6b00458
J. Chem. Inf. Model. 2017, 57, 1029−1044

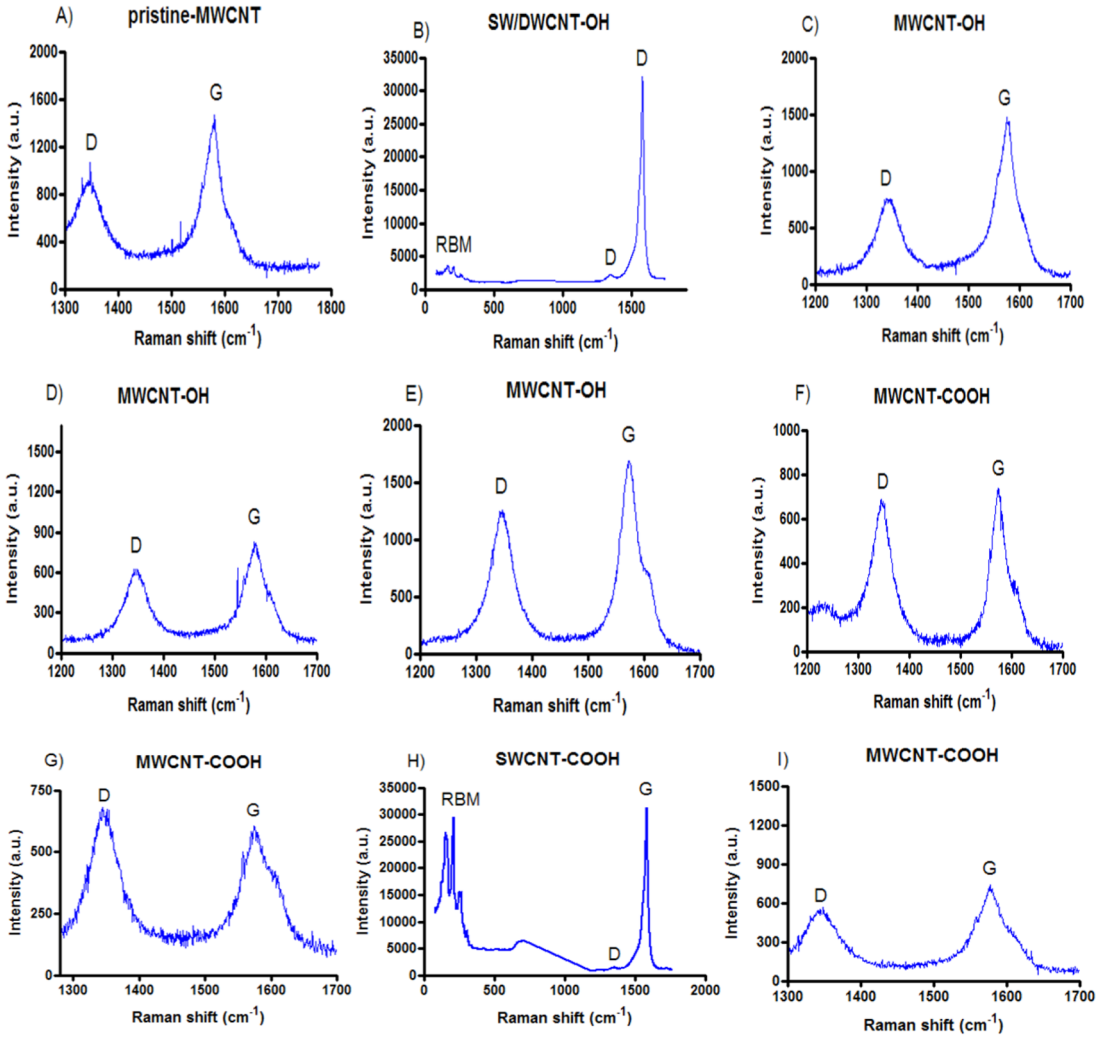

Figure 2. Raman spectra of carbon nanotubes used in this study. (A) Pristine MWCMT (CNT1), (B) SW/DWCNT−OH (CNT2), (C) MWCNT−OH (CNT3), (D) MWCNT−OH (CNT4), (E) MWCNT−OH (CNT5), (F) MWCNT−COOH (CNT6), (G) MWCNT−COOH (CNT7), (H) SWCNT−COOH (CNT8), (I) MWCNT−COOH (CNT9) (see Materials and Methods section).

Table 1. Physical−Chemical Parameters of the CNT Family

CNT properties[a]			W_i (%)		D_i (nm)				
n	type	function	min	max	min	max	L_i(μm)	P_i (%)	C_i (S/cm)
1	MWCNT				8	8	0.5−2	>95	<1.5
2	mixed SW/DWCNT	OH	0	3.96	1	4	0.5−2	>95	<1.5
3	MWCNT	OH	0	3.86	1	8	0.5−2	>95	<1.5
4	MWCNT	OH	3	4	10	20	0.5−2	>95	<1.5
5	MWCNT	OH	1	1.06	30	50	0.5−2	>95	<1.5
6	MWCNT	COOH	0	0.73	30	50	0.5−2	>95	<1.5
7	MWCNT	COOH	3	4	10	20	0.5−2	>95	<1.5
8	SWCNT	COOH	0	2.73	1	4	0.5−2	>95	<1.5
9	MWCNT	COOH	0	3.86	1	8	0.5−2	>95	<1.5

[a] W_i (%) = functional groups (OH, COOH)/carbon atoms ratio (%). The properties of the ith CNT are D_i = outer diameter, L_i = length, P_i = purity, C_i = electric conductivity.

Therefore, the calculation of merely theoretical descriptors is not applicable for the current study because it does not involve a unique CNT molecule, but a mixture of many CNT molecules with similar, but different structures. In this sense, the Raman spectra are a good solution because they capture all the variations in the structural patterns of the CNTs into a sample.

EXPERIMENTAL SECTION

Raman Spectra. Raman spectra were measured using a Renishaw Micro-Raman Spectroscopy System (Renishaw plc, Wotton-under-Edge, UK) at room temperature at a laser excitation wavelength of 514 nm (2.33 eV). All reactions were quenched to room temperature before Raman spectra were recorded in order to identify the characteristic peaks in the

DOI: 10.1021/acs.jcim.6b00458
J. Chem. Inf. Model. 2017, 57, 1029−1044

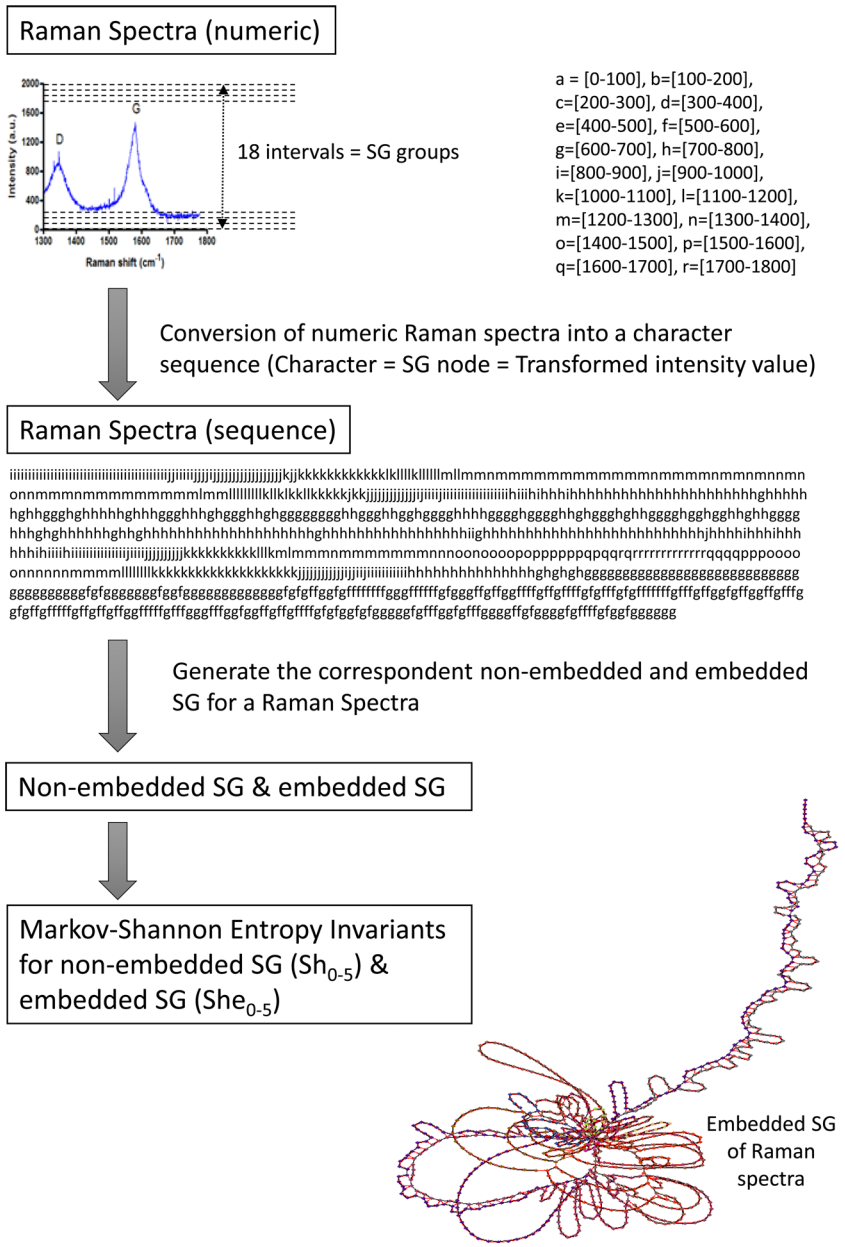

Figure 3. Transformation of the Raman spectra for Pristine MWCMT (CNT1) into SG Shannon entropies invariants using the S2SNet tool.

position of 1580 cm^{-1} (G band of graphite) and the peak in the 1350 cm^{-1} (D band of defects) approximately associated with the presence of disorder and/or vacancy defects in the CNT structure produced by chemical oxidation in the graphite structure (oxidized CNT with OH and COOH functional groups), as shown in Figure 2.

Reagents and Solutions. Sucrose, ethylene glycol-bis(β-aminoethyl)-*N*,*N*,*N*′,*N*′-tetraacetic acid (EGTA), KCL, potassium succinate (plus 2 μM rotenone), K_2HPO_4, piperazine-*N*′-2-ethanesulfonic acid (hepes-KOH). All the other reagents were commercial products of the highest purity grade available. For mitochondrial functional respiratory assays, pristine and functionalized carbon nanotubes (MWCNT, [SWCNT + DWCNT]−OH, MWCNT−OH, MWCNT−COOH, SWCNT−COOH) were dissolved in dimethyl sulfoxide (DMSO) and Milli-Q water in individual stock solutions, prepared at 1 mg/mL. The CNT family was provided by Cheaptubes Company (http://cheaptubes.com/shortohcnts.htm; see Table 1).

Animal Welfare. Male *Wistar* rats (4 months old; approximately 150 g) received food and water ad libitum. They were kept in plastic cages with wire tops in a light-controlled room (12:12 h light−dark cycle) at 22 ± 3 °C before starting the study in accordance with the animal care and experimental procedures based on the Directive 2010/63/EU of the European Parliament and of the Council on the protection of animals used for scientific purposes; these procedures were also approved by the Institutional Animal Care and Use Committee of the School of Pharmaceutical Sciences of Ribeirão Preto (CEUA-FCFRP) (license and registration number: 01.0263.2014).

Isolation of Rat Liver Mitochondria (RLM). Mitochondria were isolated by standard differential centrifugation.[51] Male *Wistar* rats weighing approximately 200 g were euthanized by decapitation; livers (10−15 g) were immediately removed,

DOI: 10.1021/acs.jcim.6b00458
J. Chem. Inf. Model. 2017, 57, 1029−1044

sliced in a medium (50 mL) consisting of 250 mM sucrose, 1 mM ethylene glycol-bis(β-aminoethyl)-*N*,*N*,*N*′,*N*′-tetraacetic acid (EGTA), and 10 mM HEPES-KOH, pH 7.2, and homogenized three times for 15 s at 1 min intervals using a Potter−Elvehjem homogenizer. Homogenates were centrifuged (2500 rpm, 5 min), and the resulting supernatant was further centrifuged (10 500 rpm, 10 min). Pellets were then suspended in a medium (10 mL) consisting of 250 mM sucrose, 0.3 mM EGTA, and 10 mM HEPES-KOH, pH 7.2, and centrifuged (6000 rpm, 15 min). The final mitochondrial pellet was suspended in a medium (1 mL) consisting of 250 mM sucrose and 10 mM HEPES-KOH, pH 7.2, and used within 3 h. Mitochondrial protein contents were determined by the Biuret reaction.

Standard Incubation Procedure. The isolated mitochondria were energized with 5 mM potassium succinate (plus 2.5 μM rotenone) in a standard incubation medium consisting of 125 mM sucrose, 65 mM KCl, 2 mM inorganic phosphate (K_2HPO_4), and 10 mM HEPES-KOH pH 7.4 at 30 °C.

Continuous-Monitoring Mitochondrial Respiration Assays. The oxygen consumption in mitochondrial suspensions was polarographically determined with a Clark-type electrode. Clark electrodes have platinum cathodes and silver chloride anodes, which are connected by a salt bridge and covered by an oxygen-permeable membrane. As oxygen diffuses across the membrane, it is reduced by a fixed voltage between the cathode and anode that generates current in proportion to the concentration of oxygen in solution. By calibrating the voltage with known oxygen concentrations, it is possible to measure the rate of oxygen consumption in a medium containing actively respiring mitochondria. Since reduction of oxygen is a critical step in the process of mitochondrial electron transport and ATP synthesis, the measurement of mitochondrial oxygen consumption provides a convenient way to assess mitochondrial function.

To this end, two different set of tools were used: (1) Oxygraph System (Hansatech Instruments Ltd., Norfolk, UK) and (2) Oroboros Instruments (Oxygraph-2k). Both methodologies were applied in a 2 mL glass chamber equipped with a magnetic stirrer. Rat liver isolated mitochondria (1 mg protein/mL) were energized with 5 mM potassium succinate (plus 2.5 μM rotenone) in a standard incubation medium consisting of 125 mM sucrose, 65 mM KCl, 2 mM inorganic phosphate (K_2HPO_4), and 10 mM HEPES-KOH pH 7.4 at 20 °C in a standard respiration medium. The experimental approach was calibrated using the oxygen content of an air-saturated medium.[51]

Theoretical Section. *Raman Spectra Transform with Markov−Shannon Entropy Invariants.* The current work proposes a new type of Raman spectra transform, similar to the Fourier transformation. This transform converts the Raman spectra values to character sequences and the corresponding star graphs (SGs) are constructed using S2SNet tool.[52] A star graph is a special type of tree with N vertices, where one has $N - 1$ degrees of freedom and the remaining $N - 1$ vertices have a single degree of freedom.[53] In the case of protein sequences, the graph is built by adding all the amino acids into 23 possible branches ("rays" corresponding to the types of amino acids). The star center is a dummy node.[54]

Thus, the Raman spectra were divided into intervals of 100 units, from 0 to 1800. As a result, the maximum number of star graph branches is 18 and corresponds to characters "a" to "r". The star graph connectivity of the transformed Raman spectra provides the information needed to calculate the Shannon entropies (Sh_k, k = 0−5) for nonembedded and embedded SG (Sh and She). The transformation of the Raman spectra of CNT1 into Shannon entropies is shown in Figure 3.

The calculation of Sh invariants is based on matrices and vectors of the SG. To calculate Sh, the starting point is the SG connectivity matrix **M** (dimension of n = number of nodes; M_{ij} = 1 if the nodes i−j are connected; 0 = if nodes i−j are not connected). In the case of nonembedded SG, the connectivity is generated by the SG rule (each node is placed into a specific branch). In the case of embedded SG, in addition to the nonembedded connectivity, the sequence connectivity is added. S2SNet has been used to calculate nonembedded and embedded Sh for each CNT Raman spectrum with the following parameters: no weights for the nodes, Markov normalization, k = 0−5. The formula of Sh invariants is described in eq 1, and the details about the SG Shannon entropy formulation are presented in ref 52.

$$Sh_k = -\sum_{i=0}^{n} {}^{k}p_i \log({}^{k}p_i) \quad (1)$$

${}^{k}p_i$ = elements of the p vector obtained by multiplying the k powered Markov normalized matrix ($n \times n$) and a vector ($n \times 1$) with elements of $1/n$. The calculated values for all the CNTs are in the Figshare file "ds3.info.xlsx", sheet "RAMAN entropies".[55]

Theoretical Details of the Nano-PT-QSPR Models. The general-purpose PT model for multiple boundaries has been proposed for chemoinformatics problems.[29] This study extends this theory to PT-QSPR models that will be able to study the effect of different CNTs on the mitochondrial respiration (oxygen consumption) under different experimental conditions. The general equation of the nano-PT-QSPR model is presented in eq 2.

$$E3_{pred} = e_0 + a_0 E3_{exp} + g_0 t + \sum_{k=0}^{5} a_k \, dSh_k + \sum_{k=0}^{5} b_k \, dShe_k \quad (2)$$

E3pred represents the predicted mitochondrial oxygen consumption. $E3_{exp}$ is the expected value of E3 in the set of three simultaneous experimental conditions (SEC). dSh_k and $dShe_k$ are the moving averages of nonembedded and embedded Shannon entropies of the CNT Raman SG transform (differences between Sh_k or She_k and their averages obtained under different experimental conditions). The coefficients e_0, g_0, a_0, a_k, and b_k are the equation optimal coefficients.

Model Data Set. The experimental data for the mitochondrial oxygen consumption (E3) in the presence of CNTs are available as a Figshare repository[55] and contain 16 335 cases (E3 measurements) with the following variables (data columns): E3, CNT label (CNT1−9), CNT type (CNT_type), type of CNT chemical modification (Function_type), type of the solvent (Solvent), and time (t). Thus, E3 was measured under three types of experimental conditions (c): CNT_type, Function_type (chemical modification of CNT), and Solvent. The codes used for CNTtypes are MWCNT, SW+DWCNT, and SWCNT. CNT type was set as 0 when the assay is a control assay with a blank solution with CNT concentration equal to 0. The values of Solvent condition are 0 and DMSO. The CNT Function types are 0 (none), COOH and OH. All the average values of the Shannon entropies under these experimental conditions are presented step by step in Figshare

DOI: 10.1021/acs.jcim.6b00458
J. Chem. Inf. Model. 2017, 57, 1029−1044

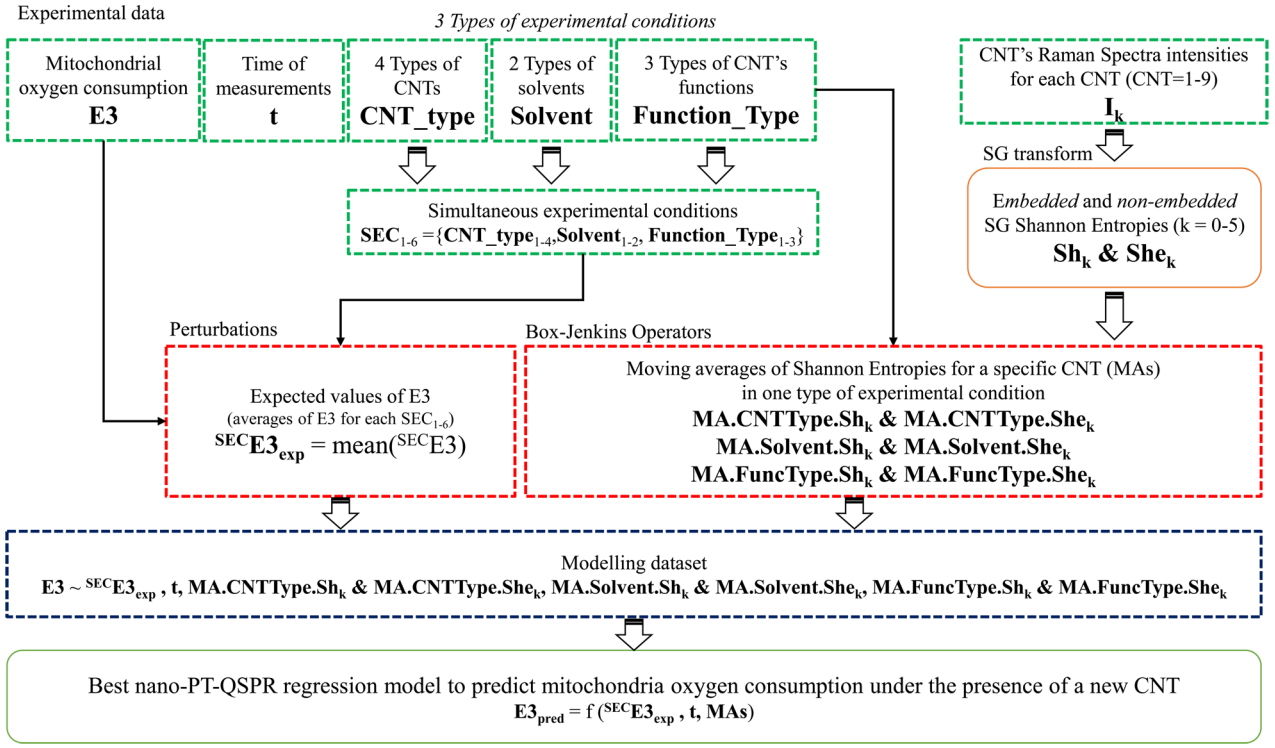

Figure 4. Methodology flowchart for nano-PT-QSPR models for mitochondrial oxygen consumption in the presence of CNTs.

repository.[55] The final data set used to find the best prediction model is made up of 16 335 cases and 35 input features. The number of cases (N) is the result of NoCNTs × TimePeriods + Replicates + CART.Blanks, where NoCNTs = 9 (different nanotubes) and TimePeriods = 1485 (min). Thus, NoCNTs× TimePeriods is 9 × 1485 = 13 365. CART.Blanks = 1485 (experiments with carboxyatractyloside (or CART as classical inhibitor of state V3 of respiration-ADP dependent at 1485 periods) were added. The remaining number of cases are replicates or blanks with H2O as solvent (see ds3.info.xlsx, sheet "Experimental Data"[55]).

The following steps were used to generate the final data set (see Figure 4 and Figshare files[55]):

(1) Calculation of 11 nonembedded and embedded SG Shannon entropies for each CNT using S2SNet (Sh_k and She_k): Sh_0, Sh_1, Sh_2, Sh_3, Sh_4, Sh_5, She_1, She_2, She_3, She_4, She_5 (the zero-value descriptors have been excluded, CNT = 9 different CNTs)

(2) Calculation of mean values for each Sh under an experimental conditions such as CNT_type = type of CNT, Solvent = type of solvent, Function_type = type of CNT chemical modification 11 CNTtypeSh_k/CNTtype-She_k, 11 FuncTypeSh_k/FuncTypeShe_k, 11 SolventSh_k/SolventShe_k; see "Experimental condition Means" in ds3.info.xlsx[55])

(3) Calculation of 33 moving averages (MAs) between the original Raman spectra SG entropies (from step 1) and their averages obtained under the experimental conditions (from step 2) and time (for each type of CNT); the resulting values have the following notation in the Figshare files: 11 MA.FuncType.Sh_k/MA.CNTtype.She_k, 11 MA.CN.FuncType.Sh_k/MA.FuncType.She_k, 11 MA.Solvent.Sh_k/MA.Solvent.She_k

(4) Calculation of the expected values of E3 ($^{SEC}E3_{exp}$) in a set of three experimental conditions (CNT type, solvent type, and CNT chemical function type; see Experimental condition Means in ds3.info.xlsx[55])

(5) The final data set of 35 features was only made up of the experimental values (E3), the expected value of E3 in a set of experimental conditions from step 4 ($E3_{exp}$), time (t) and the 33 moving averages of Sh/She under all the experimental conditions from step 3 (MA.CNTtype.Sh_k/MA.CNTtype.She_k, MA.CN.FuncType.Sh_k/MA.FuncType.She_k, MA.Solvent.Sh_k/MA.Solvent.She_k)

Therefore, the entire flow could be summarize in few ideas:

- The study is searching for the best regression model that can predict values mitochondrial oxygen consumption (E3) measured in specific experimental conditions when different CNTs are present.
- The initial data to generate this model is composed on experimental E3 values (output/predicted variable), time of the E3 measurement, three types of experimental conditions (CNT type, solvent type. and chemical function type of the CNTs), and the Raman spectra of the CNTs.
- The current model is based on the perturbation theory, and it considers that E3 measured in three simultaneous experimental conditions is the sum of the expected value of E3 ($E3_{exp}$) in these conditions and some perturbations around this value (E3 = $E3_{exp}$ + perturbations).
- Therefore, $E3_{exp}$ are obtained as mean values of E3 for three simultaneous experimental conditions (SEC). There are possible only six combinations of the three types of experimental conditions (CNT type and solvent type and chemical function type of the CNTs]. Thus, $E3_{exp}$ values are constant features for the model.
- The perturbations of E3 around $E3_{exp}$ consists in a series of moving averages (MAs) of the SG Shannon entropies for the transformed Raman spectra for each CNT type

DOI: 10.1021/acs.jcim.6b00458
J. Chem. Inf. Model. 2017, 57, 1029−1044

and for one type of experimental condition (CNT type/solvent type/chemical function type of the CNTs). Therefore, the perturbations of E3 are MAs (Box–Jenkins operators) of SG Shannon entropies for specific experimental conditions (MA = difference of the entropy with the mean entropies in specific experimental condition).
- Because the values of E3 are measured at different times (time series), the time variable was added to the model (E3 is not constant in time).
- In conclusion, the prediction of E3 is made using SG Shannon entropy MAs as perturbations around the $E3_{exp}$ (expected values of E3) and time as a time series of data.

The advantages of the PT-QSAR technique over the conventional QSAR are the following:

- The PT method uses the perturbations of the classic QSAR features around the average values of the same features in different experimental conditions (moving averages). Therefore, the PT methodology is able to compare relative values of the model features, which are much smaller compared to the absolute values of these features. PT-QSAR is based on the perturbations of the features and not on the feature values, offering information more detailed than the traditional QSAR. In the latter, if the feature values are high, the small differences between them may be undetectable by the statistical or machine learning techniques.
- The PT method averages feature values using experimental conditions (CNT type, solvent type, and CNT chemical function type). Thus, not only is molecular information included in the QSAR model but also the information about specific experimental conditions for the observed model output. The experimental conditions affect the observed variables, and therefore, including this dependent information in the future QSAR model is a big advantage.
- The introduction of the expected value of the output variable ($E3_{exp}$) is additional information added to the QSAR model. $E3_{exp}$ is the average value of the output E3 measured in a combination of experimental conditions (not only one experimental condition). This average value adds information about the measurement experiments. Thus, the predicted output $E3_{pred}$ is calculated similarly to a perturbation around the $E3_{exp}$ values for specific experimental conditions (see eq 2). The perturbations are represented by the MA of the CNT descriptors in different experimental conditions. MAs are calculated using an experimental condition, and $E3_{exp}$ was obtained using the combination of three experimental conditions (CNT type, solvent type, and CNT chemical function type).

The use of the best regression model for the prediction of E3 values (mitochondrial oxygen consumption) in the presence of a new CNT (with a new Raman spectra) consists in providing the input features for the final model such as $E3_{exp}$, time, and MAs of CNT's Shannon entropies for transformed Raman spectra: $E3_{pred} = f(^{SEC}E3_{exp}, t, MAs)$, where SEC = simultaneous experimental conditions and MAs are calculated for all types of CNTs. Thus, it is very important to specify specific experimental condition and time for the prediction of E3 values.

Let us consider the prediction of the mitochondrial oxygen consumption ($E3_{pred}$) for specific values of the experimental conditions (CNT type and solvent type and chemical function type of the CNTs) and at a specific time moment after a new CNT_x was added. Thus, the prediction is made for specific experimental conditions and, therefore, a specific value of $^{SEC}E3_{exp}$ will be used (from the six values calculated for building the regression model). It is not necessary to calculate any other value of $^{SEC}E3_{exp}$ because the model will evaluate the $E3_{pred}$ value based on the $E3_{exp}$ values obtained with the model data set. The second input feature is the time of the CNT presence in mitochondria.

After picking the time and $E3_{exp}$ is known for specific experimental conditions, only the MAs should be calculated for the new prediction. First of all, the Raman spectra of the new CNT will be transformed into SG Shannon entropies (Sh). From the model building, the averages values of the CNTs in specific experimental conditions are knows, and, therefore, the MAs of the new CNT_x will be calculated as a difference between the new Sh values and the model's averages of Sh of all the data set CNTs. Thus, the model is providing the $E3_{exp}$ values and Sh means for specific experimental conditions, but the user will choose what values to use depending on experimental conditions for the new E3 prediction.

Regression Predictors. The raw data set was normalized and the training and test subsets were obtained using 10 splits: 75% training set (train) and 25% test set (test). The raw and normalized data sets are available online with the R script for normalization and data splitting.[55] The batchRRegrs tool was used to find the best regression nano-PT-QSPR model. The models were selected using the R_{ts}^2 values (R-squared) and the $RMSE_{ts}$ (root-mean-square error) corresponding values for test subset.

RRegrs is an R integrated framework that provides ten linear and nonlinear regression models.[45,46] Due to the computational limitations, only four RRegrs methods were used: multiple linear (LM), partial least squares (PLS)[56] and neural networks (NN) regressions[57] and random forest (RF).[58] Generally, default values of parameters were used. In the case of NN and RF, the variation of the method parameters was studied. The RRegrs call is not prepared for big data sets and for some parameter variations. Thus, a modified version of RRegrs (batchRRegrs: https://github.com/cafernandezlo/batchRRegrs) was used on the BioCAI HPC platform from University of A Coruna (Spain). This version of RRegrs saves the R model objects and it leaves the door open for any type of extra calculations or graphical plots for the regression model. As an adaptation for large data sets, several features are missing in batchRRegrs: there is only one split (the user runs create each split), there is no Y-randomization, there are no output figures as PDFs and there is no automatic selection of the best model. Therefore, the current methodology is an incomplete RRegrs flow, due to the mission of the Y-randomization. The criteria to find the best model are the same as for RRegrs: maximum R_{ts}^2 and minimum $RMSE_{ts}$. The plots for the current work were obtained with R scripts. The best regression model which predicts mitochondrial oxygen consumption in the presence of CNTs is available online[55] and it can be used for future predictions.

RESULTS AND DISCUSSION

In principle, several biochemical in vitro assays may be used with different respiratory substrates, cofactors, and inhibitors in

DOI: 10.1021/acs.jcim.6b00458
J. Chem. Inf. Model. 2017, 57, 1029–1044

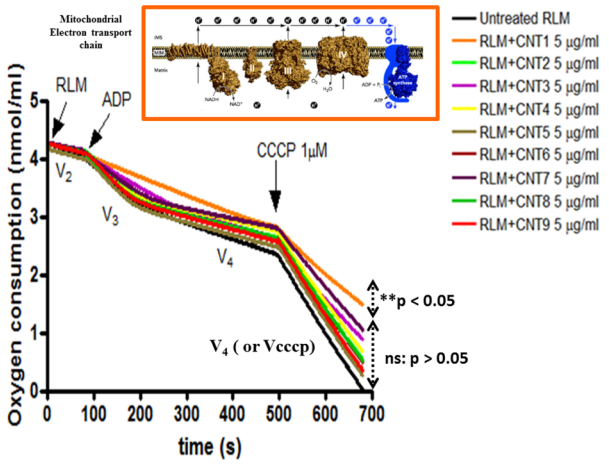

Figure 5. Profiles of mitochondrial oxygen consumption of isolated rat-liver mitochondria show the different states of mitochondrial respiration on the mitochondrial respiratory chain: V_2 state (basal respiration), V_3 state (ADP-dependent respiration), V_4 and Vcccp states (both ADP-independent respiration) in untreated-rat liver mitochondria or untreated-RLM (black line) and after the CNT exposure at 5 μg/mL (remaining colors). These results are representative of three experiments by using the two polarographic assessments of mitochondrial respiration performed with the Oxygraph System Hansatech Instruments and Oroboros Instruments (Oxygraph-2k). $^{**}p < 0.05$ is used to represent the statistical differences between CNT-1 (pristine MWCNT) (orange line) and untreated RLM (black line).

the polarographic evaluation of the effect of CNT family on the mitochondrial oxygen consumption. The rate of oxygen consumption can be measured directly using a Clark-type electrode, which consists of a probe with an exposed platinum cathode and a silver anode. When the anode and cathode are polarized, the current produced is directly proportional to the partial pressure of oxygen. The respiratory biochemical reactions are connected via an electrolyte solution, such as KCl. The cathode is typically covered by an oxygen-permeable membrane, such as a polypropylene membrane, to exclude contaminating species, ions, or samples that might interfere with the reaction.[59]

In this work, two different polarographic experiments were performed to evaluate the effects of the CNT family on the mitochondrial respiration by exposure conditions of 5 μg/mL.

In general terms, the results showed that the entire CNT family tested does not inhibit (or affect) the profiles of oxygen consumption increment after ADP addition (state V3 of ADP-dependent respiration) compared to the untreated mitochondrial control (black line), no significant differences being detected ($p > 0.05$) in this case. However, for CNT-1 (pristine MWCNT) a moderate ability to inhibit the state V3 of mitochondrial ADP-dependent respiration (orange line), compared to their similar oxidized CNT (hydroxylated-CNTs CNT2−CNT5 and carboxylated-CNTs CNT6−CNT9) was observed. The mitochondrial V3 respiratory inhibition by CNT-1 is not significant (ns: $p > 0.05$) when compared to the untreated mitochondrial control (black line) under the evaluated experimental conditions. It does not affect the oxidative phosphorylation by ATP synthase, which depends on the ADP transport by the ADP/ATP mitochondrial carrier between cytosol and the mitochondrial matrix under physiological normoxic conditions, the in vitro results suggesting lower inhibition response for isolated rat liver mitochondria based on mitochondrial V3 respiratory inhibition. Generally, a low inhibition for each member of the CNT family was observed, represented by colored lines, related to untreated mitochondrial control (black line) after the addition of CCCP 1 μM (uncoupling agent of the mitochondrial oxidative phosphorylation) in the state V4 of respiration and Vcccp (both ADP independent) shown in Figure 5. Intriguingly, it was observed that the mitochondrial respiration rate versus time of V4 (or Vcccp) stages (ADP independent) for CNT-1 (pristine MWCNT) (orange line) had the smallest decline, with significant statistical differences ($^{**}p < 0.05$) compared to their similarly oxidized CNTs (CNT2−CNT9) (the remaining colored lines) and also to the untreated mitochondrial control (black line), despite the presence of protonophore CCCP, a classic mitochondrial uncoupling agent, which represents the maximum rate of mitochondrial oxygen consumption used as control at the end of all the measurements (t = 500 s).

A physiological explanation is feasible due to the fact that carbon nanotubes can pass through phospholipid bilayers that make up the mitochondrial inner membrane. More specifically, they are accumulated similarly too many cationic amphiphilic drugs or in some cases when degraded by the oxido-reduction mechanisms that occur in the mitochondrial matrix. The effects can be observed in the interruption of the flow of electrons, decreasing the proton gradient associated with low oxygen consumption rate, uncoupling of oxidative phosphorylation and reduction of ATP synthesis, depending on the physical−chemical nature of the mitotoxic agent involved. According to this idea, it is well-known that the presence of defects such as pentagons, heptagons, vacancies, or metallic dopant are found to modify drastically the electronic properties of these nanosystems (carbon nanotubes) and, in the same vein, their properties of interaction with the biological systems, which can be expressed through biocompatibility and/or toxicity responses. In this sense, the intensity of the D band of CNT

Table 2. Training and Test R^2 and RMSE (Mean, Minimum, and Maximum Values for 10 Splits) Using RRegrs Regression Methods to Predict Mitochondrial Respiration Modifications Due to CNTs

method	R^2	mean	min	max	RMSE	mean	min	max
LM	R_{tr}^2	0.865	0.864	0.866	$RMSE_{tr}$	0.0915	0.0910	0.0922
	R_{ts}^2	0.864	0.861	0.868	$RMSE_{ts}$	0.0913	0.0891	0.0929
PLS	R_{tr}^2	0.864	0.863	0.865	$RMSE_{tr}$	0.0917	0.0912	0.0925
	R_{ts}^2	0.864	0.860	0.867	$RMSE_{ts}$	0.0916	0.0893	0.0931
NN	R_{tr}^2	0.987	0.986	0.987	$RMSE_{tr}$	0.0286	0.0283	0.0292
	R_{ts}^2	0.988	0.987	0.990	$RMSE_{ts}$	0.0271	0.0249	0.0284
RF	R_{tr}^2	**0.998**	0.998	0.998	$RMSE_{tr}$	**0.0109**	0.0102	0.0118
	R_{ts}^2	**0.998**	0.997	0.999	$RMSE_{ts}$	**0.0108**	0.0068	0.0133

DOI: 10.1021/acs.jcim.6b00458
J. Chem. Inf. Model. 2017, 57, 1029−1044

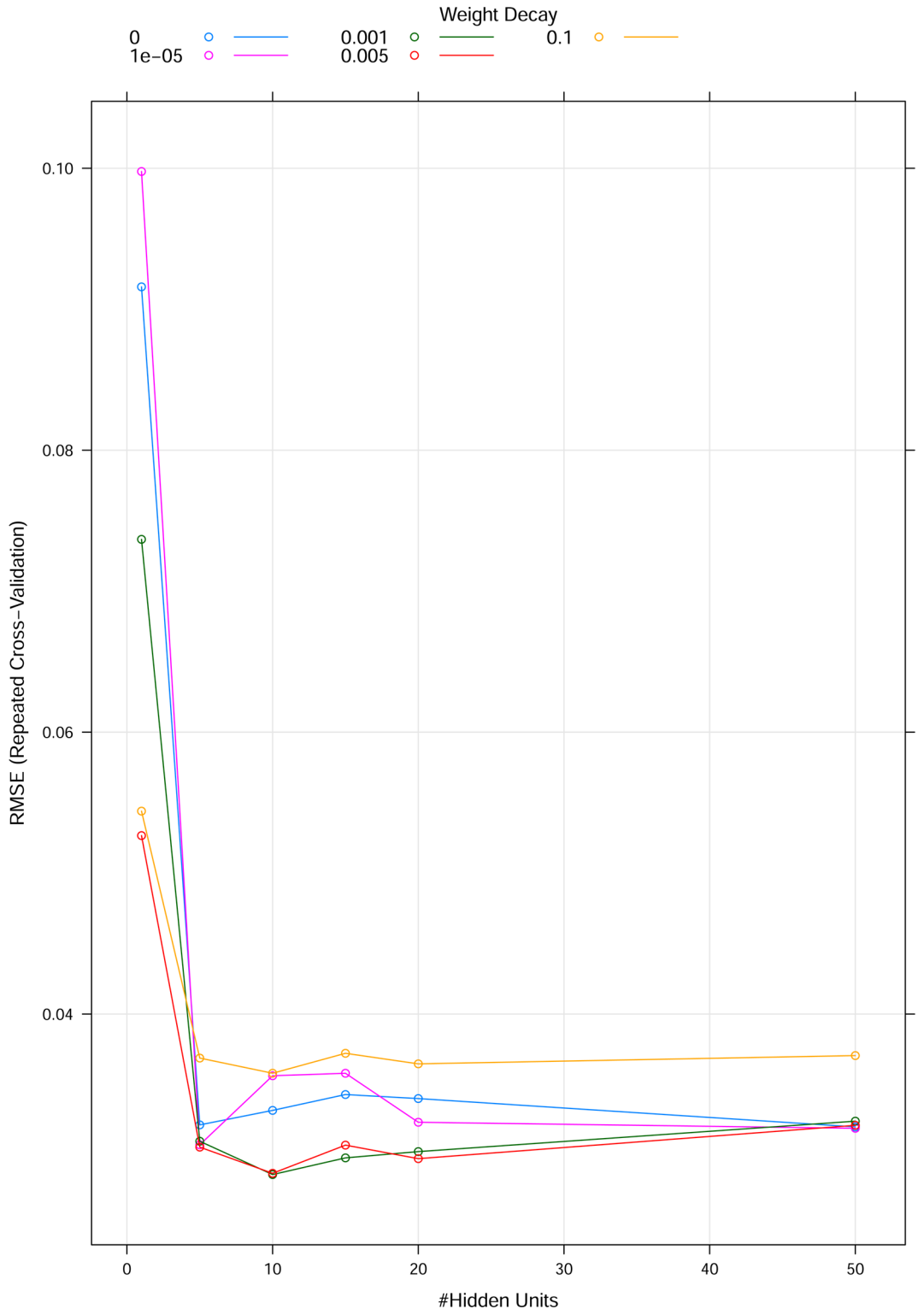

Figure 6. Parameter study for NN regression models.

tested regarding the Raman spectra with peak at approximately 1350 cm^{-1} is commonly associated with the presence of the aforementioned topological modifications in the carbon lattice of CNTs.

Thus, the presence of the CNT's oxidized groups (−OH, −COOH) with a peak at 1350 cm^{-1} can prevent inhibition of the V3 state (ADP dependent) or uncoupling effects on mitochondrial respiration state (V4), maybe associated with the oxidized CNT ability as free oxygen-radical scavenging. Since these oxygen free radicals were spontaneously formed in the mitochondrial complex I and III, perturbation can be induced in the oxidative phosphorylation of the ADP and Pi by the mitochondrial complex V wrapping. In most cases inhibition and/or uncoupling effects on mitochondrial respiration, similar to the effects observed due to the addition of CCCP or V4 (V_{cccp}) in all previous states of mitochondrial respiration (V2,

DOI: 10.1021/acs.jcim.6b00458
J. Chem. Inf. Model. 2017, 57, 1029−1044

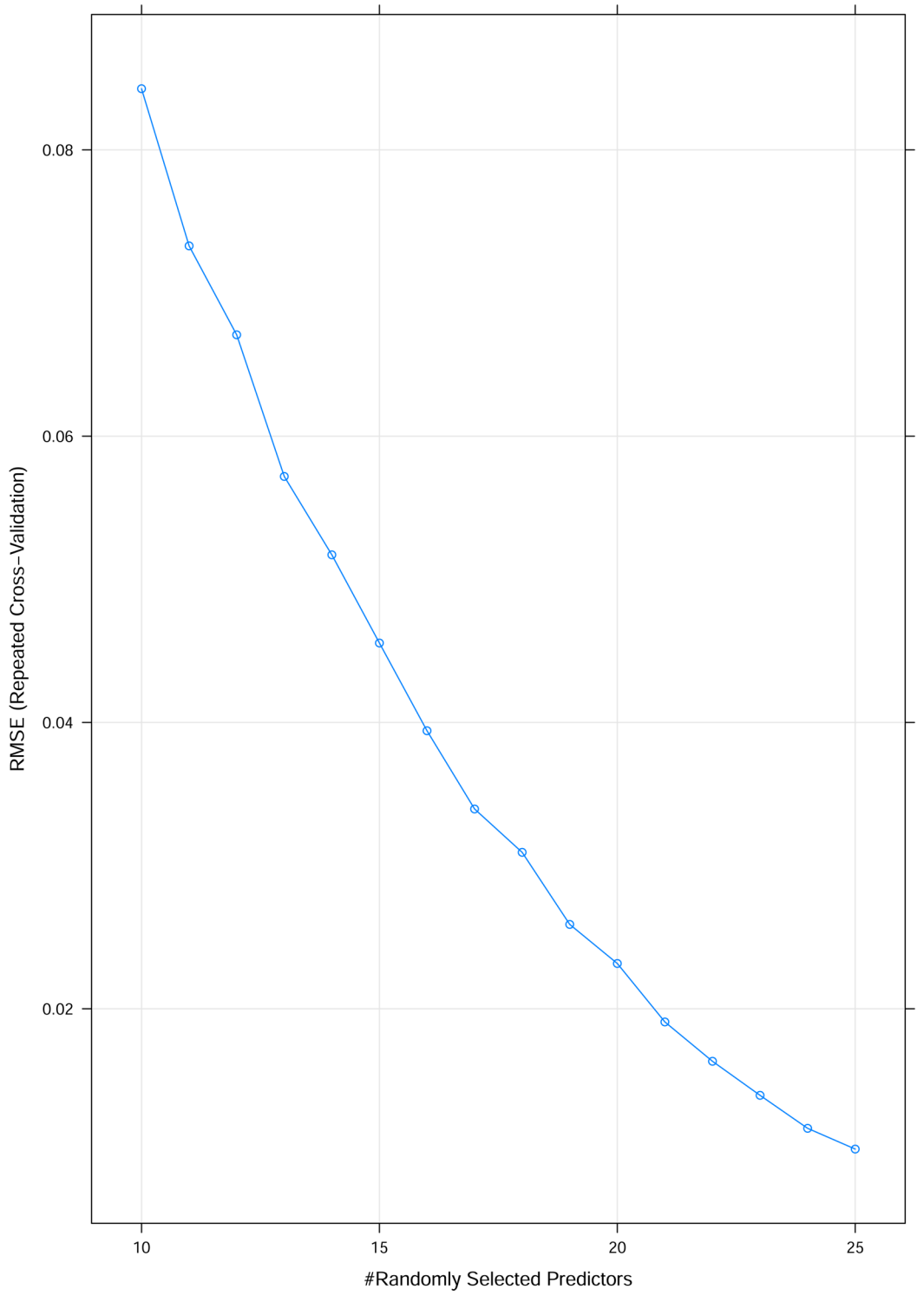

Figure 7. Parameter study for RF regression models.

V3) were not observed in the present study. Raman spectroscopy D band characterized the level of the CNT oxidation, and it has been recognized that CNT-covalent functionalization can generate different Stones−Wales defects formed by rotating a C−C bond by 90° in the sidewalls of the CNT structure with loss of sp^2-carbon hybridization or rehybridization (ability of the carbon atom to hybridize between sp^2 and sp^3). According to the theoretical results obtained by Galano et al. using semiempirical methods such as density functional theory (DFT), moderate, or high oxidation on the carbon lattice of CNT increases their oxygen free-radical scavenging activity and has no impact on mitochondrial respiration states by capturing the oxygen radical species formed in the mitochondrial complex I and III. These biochemical effects, which may involve C atoms with dangling bonds, cause a larger increase of CNT reactivity toward free radicals than the Stones−Wales and vacancy defects without C atoms with dangling bonds.[60−64] Interestingly, it was

DOI: 10.1021/acs.jcim.6b00458
J. Chem. Inf. Model. 2017, 57, 1029−1044

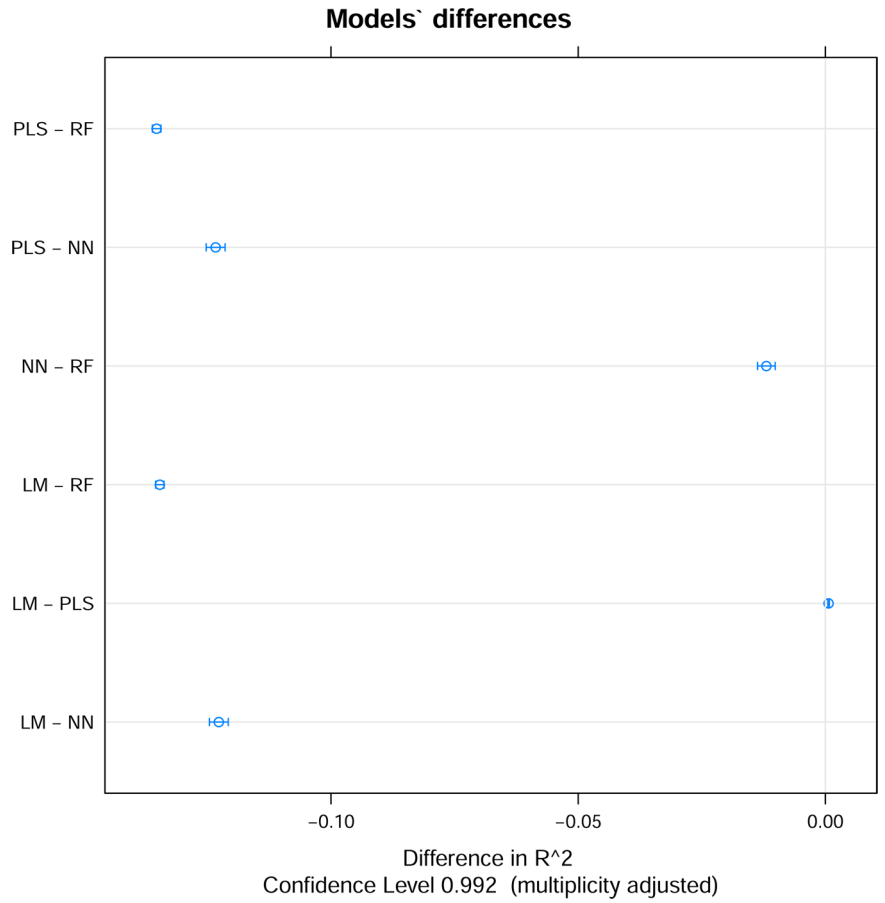

Figure 8. RRegrs pairwise model comparisons of R_{ts}^2.

demonstrated that pristine CNT (MWCNT-1) in aqueous suspension does not generate oxygen-free radicals.

On the contrary, it was observed that MWCNTs exhibit a remarkable free radical scavenging ability, when in contact with an external source of oxygen-free radicals (hydroxyl or superoxide radicals), suggesting that the multiwalls of MWCNTs can act as oxygen-free radical sponges, and therefore, they do not affect the mitochondrial respiration by removing potential oxygen radicals from the carbon lattice. Recent studies have shown that pristine SWCNT are more reactive to induce mitochondrial damage than their oxidized forms SWCNT-COOH. Our hypothesis is that OH and COOH groups from CNT family could interact with the metallic centers of Fe^{3+} and Cu^{2+} present in the respiratory complexes preventing redox change to form Fe^{2+} and Cu^{1+}, respectively. These compounds present less ability to reduce oxygen to water and promote abnormalities in mitochondrial bioenergetic processes. However, it should be emphasized the good relationship between the biocompatibility and toxicity for the oxidized-CNTs, compared to their similar pristine-CNTs (CNT-1), whose mitotoxicicity potential is greater.

In this regard, recent experiments using pristine and oxidized-CNT porin have shown the high potential as synthetic analogues of biological membrane channels with high efficiency and selectivity for transporting ions and molecules[53,54] like natural substrates (ADP, ATP). According to this idea, the tested CNT family can spontaneously insert lipid bilayers into the cellular and mitochondrial membrane to form CNT channels that exhibit a unitary conductance of 70−100 pS under physiological conditions.[65] At the same time, the attenuation of the negative charge of (COO^-) moieties of carboxylated CNT to form COOH moieties by the H^+ protons present in the intermembrane mitochondrial space, may allow the electrostatic ADP^{3-}anions passage without inducing uncoupling effects on the mitochondrial respiratory function. In addition, Tunuguntla[66] showed through molecular dynamics simulations that carbon nanotube-porins can favor the ultrafast proton transport in sub-1 nm diameter and that the transport rates in these narrow nanotube pores can also exceed those of biological channels (as respiratory complexes that form the mitochondrial electron transport chain) due to confinement in hydrophobic nanochannels. In this sense, it could be hypothesized that CNTs with diameter >1 nm, such as those used in the present study, could have lower transport rates for the H^+ influx, preventing possible mitochondrial uncoupling effects.

The structural determinants of mitochondrial mechanisms of pristine and functionalized (oxidized) CNTs remain poorly understood at present. Our suggestion is that CNT−COOH and CNT−OH should be more biocompatible compared to the pristine MWCNTs based on the influence on the respiratory mechanism under the experimental conditions tested and according to the time of exposure to the CNT assayed.

In addition, the variation in time (t) of the mitochondrial oxygen consumption in the presence of specific CNTs was modeled using nano-PT-QSPR methodology. For each type of nanotube, the corresponding star graph Shannon entropies of the Raman spectra (Sh_{0-5}/She_{0-5}; e = embedded SG) were calculated. For each set of experimental conditions, the corresponding expected values for the E (E_{exp}) and the moving

DOI: 10.1021/acs.jcim.6b00458
J. Chem. Inf. Model. 2017, 57, 1029−1044

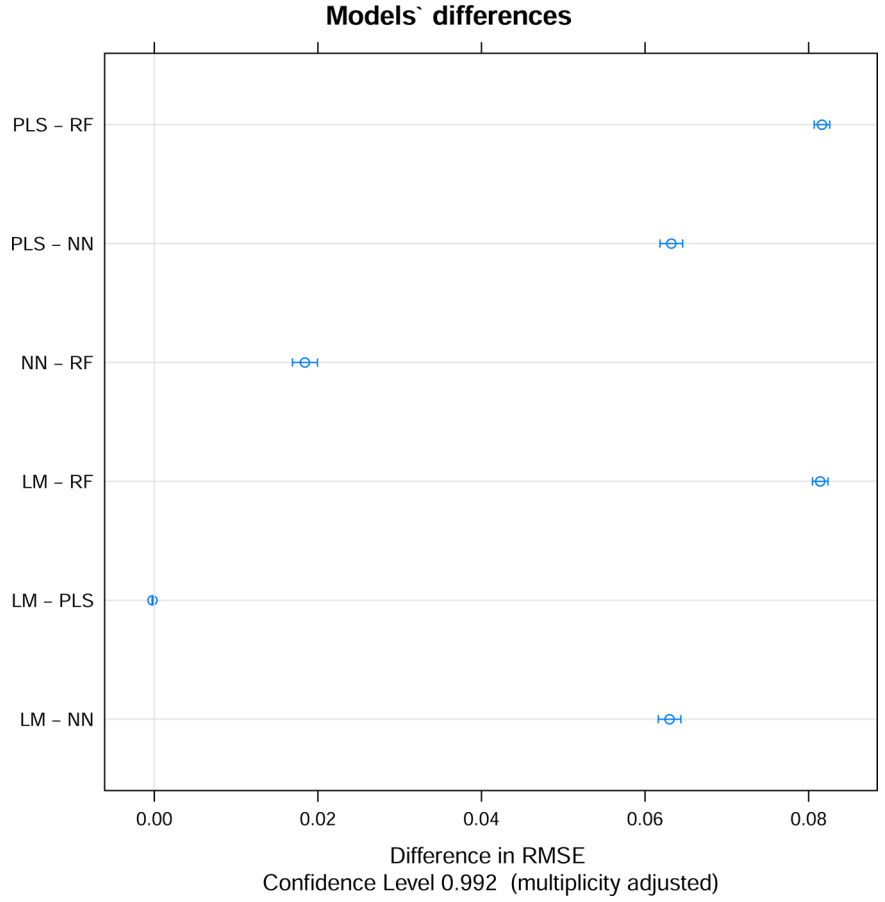

Figure 9. RRegrs pairwise model comparisons of $RMSE_{ts}$.

averages of the SG descriptors (MA.[experimental conditions].Sh_{0-5}, MA.[experimental conditions].She_{0-5}) were calculated. The final data set has 35 features: $E3_{exp}$, t, MA.CNTType.Sh_{0-5}, MA.FuncType.Sh_{0-5}, MA.Solvent.Sh_{0-5}, MA.CNTType.She_{0-5}, MA.FuncType.She_{0-5}, and MA.Solvent.-She_{0-5}. The output variable is E3, and there are 16 335 cases. A modified version of the RRegrs tool was used on an HPC cluster in order to test four types of regression methods. The purpose was to find the best prediction model for mitochondrial oxygen consumption in the presence of specific CNTs. Thus, linear and nonlinear methods were used for the feature pool: LM, PLS, NN, and RF (10 different splits and repeated cross-validation parameter). All the results are based on 35 features (pool). Table 2 shows the minimum, maximum, and mean values for the R_{tr}^2/$RMSE_{tr}$ and R_{ts}^2/$RMSE_{ts}$. The small differences between the training and test statistics demonstrated that the models are not overfitted. The statistics for 10 splits for each method could be found in the Figshare project (ds3.models.xlsx).[55] The distribution of R^2 and RMSE (tr and ts) are presented in the same file as graphics.

The results show the possibility to predict the effect of nanotubes on the mitochondrial respiration using a 35-feature linear model (LM) with a mean R_{ts}^2 value of 0.864 and a mean $RMSE_{ts}$ value of 0.0913. The MAs of the star graph Shannon entropies under different experimental conditions provide enough information for this linear regression predictor. PLS obtain results similar to those of LN, without removing any feature from the final model. Two attempts of feature selection were performed using Lasso (14 features, R_{ts}^2 = 0.865, $RMSE_{ts}$ = 0.0921) and elastic net (23 features, R_{ts}^2 = 0.864, $RMSE_{ts}$ = 0.0926) regression methods from RRegrs, but without improvements when compared to LM/PLS. The selected features included E_{exp}, t, and feature moving averages. The significant increase in the regression performance is observed when nonlinear regression methods such as NN and RF have been used. Thus, NN provides a mean R_{ts}^2 of 0.988 and a mean $RMSE_{ts}$ value of 0.0271. Thus, NN has an $RMSE_{ts}$ value over three times smaller than LM. Figure 6 shows the study of the optimal NN parameters for the final model: number of hidden neurons = [1, 5, 10, 15, 20, 50] and weight decay = [0, 0.00001, 0.005, 0.001, 0.1]. The best NN model (split 5)[55] is characterized by a single hidden layer with 10 neurons, a structure of 35−10−1 (35 inputs, 10 neurons in one hidden layer, 1 output), a weight decay of 0.001, and R_{ts}^2 of 0.990 and $RMSE_{ts}$ of 0.0249.

The RF predictor[55] is even more accurate with a mean R_{ts}^2 value of 0.998 and a mean $RMSE_{ts}$ value of 0.0108. Even if the mean R_{ts}^2 value is only 0.01, the mean $RMSE_{ts}$ value was improved over 2.5 times. The R^2/RMSE values for the 10 splits have values of 0.998−0.999/0.0068−0.0133 (training and test subsets). The RF model using the same split 5 as NN has 20 trees (parameter ntree), 25 features (from the 35 model inputs) as inputs for each tree (parameter mtry), R_{ts}^2 of 0.998, and $RMSE_{ts}$ of 0.0099. The variation of RMSE with mtry was used to choose the final RF model (see Figure 7). Thus, if the mtry value was doubled, the RMSE value decreased 4 times. The split 5 have been used to plot the pairwise model comparisons of R_{ts}^2 (Figure 8) and $RMSE_{ts}$ (Figure 9) for LN, PLS, NN, and RF. The average performance value (dot) with two-sided

DOI: 10.1021/acs.jcim.6b00458
J. Chem. Inf. Model. 2017, 57, 1029−1044

confidence limits was computed using a Student's t test with Bonferroni multiplicity correction.

Any of these models could be used for prediction due to the similar statistics. In order to help the users, one model has been exported as an R object ("RF.details.5.csv.split.1.rf.model.-RData" from the Figshare repository[55]) in order to be directly used for predictions of E3 values for a new CNT (without the necessity of recalculate the RF model). In addition, this model can be implemented in other computational tools. All the models can be obtained with the Figshare data set, batchRRegrs and the seed as the split number. The prediction of a new E3 values consists in the following steps: (1) measurement or achievement of the Raman spectra of the new CNT; (2) calculation of the SG Shannon entropies for the Raman spectra (Sh_k/She_k); (3) calculation of the new moving averages of Sh for each type of experimental condition, such as the differences between the new descriptors and the mean of Sh under different conditions from the model; (4) use of expected values from the model for a specific combination of experimental conditions (limited to the combinations in the model); (5) setting time (t) values; (6) use of the model to predict the mitochondrial oxygen consumption ($E3_{pred}$) in the presence of the new CNT, for a specific experimental condition and in a specific time scale.

CONCLUSIONS

The respiratory functional assays showed that CNT Raman spectroscopy structural nanodescriptors could be useful to evaluate toxicity criteria on mitochondrial respiration for state V3 of respiration and oxidative phosphorylation. Experimental biochemical results pointed out that encrypted information in the Raman spectra of CNT structure could be associated with canonical cellular bioenergetic mechanism to be employed for making regulatory decisions in nanotoxicology and increasing the potential biomedical application of new carbon nanomaterials. It is the first time when a star graph transform of the CNT Raman spectra is proposed in order to obtain the raw information for a nano-PT-QSPR model. Thus, Box–Jenkins and PT operators of star graph Shannon entropies under different experimental conditions and time scales were used to find the best regression predictor. A modified version of the RRegrs tool was used to test four linear and nonlinear methods such as LN, PLS, NN, and RF. The RF method provided the best models to predict the toxicity of CNTs in mitochondrial respiration with R^2 of 0.998–0.999 and RMSE of 0.0068–0.0133 for the training and test subset. As a result, this work demonstrated the SG transform power when encoding Raman spectra information, similar to the SG transform of the blood proteome spectra in cancer or electroencephalogram in epilepsy and their applicability as prospective chemoinformatics tool in nanorisk assessment.

AUTHOR INFORMATION

Corresponding Author

*E-mail: c.munteanu@udc.es. Tel.: (+34) 981 167 000 ext. 1302. Fax: (+34) 981 167 160 (C.R.M.).

ORCID

José M. Vázquez-Naya: 0000-0002-6194-5329
Humberto González-Díaz: 0000-0002-9392-2797
Cristian R. Munteanu: 0000-0002-5628-2268

Author Contributions

M.G. was involved in the Raman characterization and testing in functional biochemical respiration on isolated mitochondria. L.C.A. contributed to the polarography biochemical assays, the use of mitochondrial inhibitors, the interpretation of results, and the management of laboratory animals. Z.N. helped with the characterization of the CNTs. D.T.A.-S. was involved in the characterization of CNTs and helped with the CNT samples in the isolated mitochondria model. C.C. assisted in the interpretation of experimental results, taking into account the ethical principles regarding laboratory animals, infrastructure, and isolation techniques implemented to study mitochondria and bioenergetics. H.G.-D. applied the star graph transform of Raman spectra, and the perturbation theory and moving averages methodologies. J.M.V.-N. and C.R.M. used the machine learning techniques to find the best regression models and characterized the models employing R scripting. The manuscript was written through contributions of all authors.

Notes

The authors declare no competing financial interest.

ACKNOWLEDGMENTS

M.G.-D. acknowledges a doctoral fellowship (Postgraduate Students Program PEC-PG No.062/2013) from Brazilian Agencies CAPES-CNPq. Furthermore, M.G.-D. would like to thank to Prof. J. M. Monserrat for his valuable supervision. This work was also supported by the General Directorate of Culture, Education and University Management of Xunta de Galicia (ref GRC2014/049) and the European Regional Development Fund (FEDER). In addition, the work was supported by the "Galician Network for Colorectal Cancer Research (REGICC)" (ref R2014/039), funded by Xunta de Galicia.

ABBREVIATIONS

CNT, carbon nanotube; SWCNT, single-walled carbon nanotube; MWCNT, multiwalled carbon nanotube; SG, star graph; LM, multiple linear regression; PLS, partial least squares regression; NN, neural networks regression; RF, random forest regression; RMSE, root-mean-square error; ATP, adenosine triphosphate; ADP, adenosine diphosphate; CCCP, carbonyl cyanide m-chlorophenyl hydrazine; CART, carboxyatractyloside; QSPR/QSAR, quantitative structure–property/activity relationships; PT, perturbation theory; DFT, density functional theory; EEG, electroencephalogram; RLM, rat liver mitochondria; S2SNet, sequence to star network (software); SEC, simultaneous experimental conditions; MAs, moving averages; Sh, Shannon entropy

REFERENCES

(1) Segawa, Y.; Yagi, A.; Matsui, K.; Itami, K. Design and Synthesis of Carbon Nanotube Segments. *Angew. Chem., Int. Ed.* **2016**, *55*, 5136–58.

(2) Kroemer, G.; Reed, J. C. Mitochondrial control of cell death. *Nat. Med.* **2000**, *6*, 513–9.

(3) Kroemer, G. The Mitochondrial Permeability Transition Pore Complex as a pharmacological target. An introduction. *Curr. Med. Chem.* **2003**, *10*, 1469–72.

(4) Pacurari, M.; Lowe, K.; Tchounwou, P. B.; Kafoury, R. A Review on the Respiratory System Toxicity of Carbon Nanoparticles. *Int. J. Environ. Res. Public Health* **2016**, *13*, 325.

(5) Liu, J. H.; Yang, S. T.; Wang, H.; Liu, Y. Advances in biodistribution study and tracing methodology of carbon nanotubes. *J. Nanosci. Nanotechnol.* **2010**, *10*, 8469–81.

DOI: 10.1021/acs.jcim.6b00458
J. Chem. Inf. Model. 2017, 57, 1029–1044

(6) Li, Z.; Graham, B. H. Measurement of mitochondrial oxygen consumption using a Clark electrode. *Methods Mol. Biol.* **2012**, *837*, 63−72.
(7) Wang, X.; Guo, J.; Chen, T.; Nie, H.; Wang, H.; Zang, J.; Cui, X.; Jia, G. Multi-walled carbon nanotubes induce apoptosis via mitochondrial pathway and scavenger receptor. *Toxicol. In Vitro* **2012**, *26*, 799−806.
(8) Knobeloch, L. M.; Blondin, G. A.; Harkin, J. M. Use of submitochondrial particles for prediction of chemical toxicity in man. *Bull. Environ. Contam. Toxicol.* **1990**, *44*, 661−668.
(9) Hastings, J.; Jeliazkova, N.; Owen, G.; Tsiliki, G.; Munteanu, C. R.; Steinbeck, C.; Willighagen, E. eNanoMapper: harnessing ontologies to enable data integration for nanomaterial risk assessment. *J. Biomed Semantics* **2015**, *6*, 10.
(10) Garcia-Fuentes, M.; Gonzalez-Diaz, H.; Csaba, N. Nanocarriers & drug delivery: rational design and applications. *Curr. Top. Med. Chem.* **2014**, *14*, 1095−6.
(11) Tantra, R.; Oksel, C.; Puzyn, T.; Wang, J.; Robinson, K. N.; Wang, X. Z.; Ma, C. Y.; Wilkins, T. Nano(Q)SAR: Challenges, pitfalls and perspectives. *Nanotoxicology* **2015**, *9*, 636.
(12) Gajewicz, A.; Schaeublin, N.; Rasulev, B.; Hussain, S.; Leszczynska, D.; Puzyn, T.; Leszczynski, J. Towards understanding mechanisms governing cytotoxicity of metal oxides nanoparticles: Hints from nano-QSAR studies. *Nanotoxicology* **2015**, *9*, 313.
(13) Kar, S.; Gajewicz, A.; Puzyn, T.; Roy, K. Nano-quantitative structure-activity relationship modeling using easily computable and interpretable descriptors for uptake of magnetofluorescent engineered nanoparticles in pancreatic cancer cells. *Toxicol. In Vitro* **2014**, *28*, 600−6.
(14) Toropov, A. A.; Toropova, A. P.; Puzyn, T.; Benfenati, E.; Gini, G.; Leszczynska, D.; Leszczynski, J. QSAR as a random event: modeling of nanoparticles uptake in PaCa2 cancer cells. *Chemosphere* **2013**, *92*, 31−7.
(15) Toropov, A. A.; Toropova, A. P.; Benfenati, E.; Gini, G.; Puzyn, T.; Leszczynska, D.; Leszczynski, J. Novel application of the CORAL software to model cytotoxicity of metal oxide nanoparticles to bacteria Escherichia coli. *Chemosphere* **2012**, *89*, 1098−102.
(16) Puzyn, T.; Rasulev, B.; Gajewicz, A.; Hu, X.; Dasari, T. P.; Michalkova, A.; Hwang, H. M.; Toropov, A.; Leszczynska, D.; Leszczynski, J. Using nano-QSAR to predict the cytotoxicity of metal oxide nanoparticles. *Nat. Nanotechnol.* **2011**, *6*, 175−8.
(17) Puzyn, T.; Leszczynska, D.; Leszczynski, J. Toward the development of "nano-QSARs": advances and challenges. *Small* **2009**, *5*, 2494−509.
(18) Sizochenko, N.; Rasulev, B.; Gajewicz, A.; Kuz'min, V.; Puzyn, T.; Leszczynski, J. From basic physics to mechanisms of toxicity: the "liquid drop" approach applied to develop predictive classification models for toxicity of metal oxide nanoparticles. *Nanoscale* **2014**, *6*, 13986−93.
(19) Carbo-Dorca, R.; Besalu, E. Construction of coherent nano quantitative structure-properties relationships (nano-QSPR) models and catastrophe theory. *SAR QSAR Environ. Res.* **2011**, *22*, 661−5.
(20) Shao, C. Y.; Chen, S. Z.; Su, B. H.; Tseng, Y. J.; Esposito, E. X.; Hopfinger, A. J. Dependence of QSAR models on the selection of trial descriptor sets: a demonstration using nanotoxicity endpoints of decorated nanotubes. *J. Chem. Inf. Model.* **2013**, *53*, 142−58.
(21) Toropova, A. P.; Toropov, A. A. Mutagenicity: QSAR - Quasi-QSAR - Nano-QSAR. *Mini-Rev. Med. Chem.* **2015**, *15*, 608.
(22) Toropova, A. P.; Toropov, A. A.; Benfenati, E. A quasi-QSPR modelling for the photocatalytic decolourization rate constants and cellular viability (CV%) of nanoparticles by CORAL. *SAR QSAR Environ. Res.* **2015**, *26*, 29−40.
(23) Oksel, C.; Ma, C. Y.; Wang, X. Z. Current situation on the availability of nanostructure-biological activity data. *SAR QSAR Environ. Res.* **2015**, *26*, 79−94.
(24) Shahbazy, M.; Kompany-Zareh, M.; Najafpour, M. M. QSAR analysis for nano-sized layered manganese-calcium oxide in water oxidation: An application of chemometric methods in artificial photosynthesis. *J. Photochem. Photobiol., B* **2015**, *152*, 146.
(25) Gajewicz, A.; Cronin, M. T.; Rasulev, B.; Leszczynski, J.; Puzyn, T. Novel approach for efficient predictions properties of large pool of nanomaterials based on limited set of species: nano-read-across. *Nanotechnology* **2015**, *26*, 015701.
(26) Toropova, A. P.; Toropov, A. A.; Rallo, R.; Leszczynska, D.; Leszczynski, J. Optimal descriptor as a translator of eclectic data into prediction of cytotoxicity for metal oxide nanoparticles under different conditions. *Ecotoxicol. Environ. Saf.* **2015**, *112*, 39−45.
(27) Toropova, A. P.; Toropov, A. A.; Benfenati, E.; Korenstein, R.; Leszczynska, D.; Leszczynski, J. Optimal nano-descriptors as translators of eclectic data into prediction of the cell membrane damage by means of nano metal-oxides. *Environ. Sci. Pollut. Res.* **2015**, *22*, 745−57.
(28) Burello, E.; Worth, A. P. QSAR modeling of nanomaterials. *Wiley Interdiscip. Rev. Nanomed. Nanobiotechnol.* **2011**, *3*, 298−306.
(29) Gonzalez-Diaz, H.; Arrasate, S.; Gomez-SanJuan, A.; Sotomayor, N.; Lete, E.; Besada-Porto, L.; Ruso, J. M. General theory for multiple input-output perturbations in complex molecular systems. 1. Linear QSPR electronegativity models in physical, organic, and medicinal chemistry. *Curr. Top. Med. Chem.* **2013**, *13*, 1713−41.
(30) Gonzalez-Diaz, H.; Arrasate, S.; Juan, A. G.; Sotomayor, N.; Lete, E.; Speck-Planche, A.; Ruso, J. M.; Luan, F.; Cordeiro, M. N. Matrix trace operators: from spectral moments of molecular graphs and complex networks to perturbations in synthetic reactions, micelle nanoparticles, and drug ADME processes. *Curr. Drug Metab.* **2014**, *15*, 470−88.
(31) Vergara-Galicia, J.; Prado-Prado, F. J.; Gonzalez-Diaz, H. Galvez-Markov network transferability indices: review of classic theory and new model for perturbations in metabolic reactions. *Curr. Drug Metab.* **2014**, *15*, 557−64.
(32) Gonzalez-Diaz, H.; Perez-Montoto, L. G.; Ubeira, F. M. Model for vaccine design by prediction of B-epitopes of IEDB given perturbations in peptide sequence, in vivo process, experimental techniques, and source or host organisms. *J. Immunol. Res.* **2014**, *2014*, 768515.
(33) Luan, F.; Kleandrova, V. V.; Gonzalez-Diaz, H.; Ruso, J. M.; Melo, A.; Speck-Planche, A.; Cordeiro, M. N. Computer-aided nanotoxicology: assessing cytotoxicity of nanoparticles under diverse experimental conditions by using a novel QSTR-perturbation approach. *Nanoscale* **2014**, *6*, 10623−30.
(34) Speck-Planche, A.; Kleandrova, V. V.; Luan, F.; Ds Cordeiro, M. N. Computational modeling in nanomedicine: prediction of multiple antibacterial profiles of nanoparticles using a quantitative structure-activity relationship perturbation model. *Nanomedicine (London, U. K.)* **2015**, *10*, 193−204.
(35) Toropov, A. A.; Toropova, A. P. Quasi-QSAR for mutagenic potential of multiwalled carbon-nanotubes. *Chemosphere* **2015**, *124*, 40−46.
(36) Toropov, A. A.; Leszczynska, D.; Leszczynski, J. Predicting water solubility and octanol water partition coefficient for carbon nanotubes based on the chiral vector. *Comput. Biol. Chem.* **2007**, *31*, 127−8.
(37) Toropova, A. P.; Toropov, A. A.; Rallo, R.; Leszczynska, D.; Leszczynski, J. Nano-QSAR: genotoxicity of multi-walled carbon nanotubes. *Int. J. Environ. Res.* **2016**, *10*, 59−64.
(38) González-Durruthy, M.; Monserrat, J. M.; Alberici, L. C.; Naal, Z.; Curti, C.; González-Díaz, H. Mitoprotective activity of oxidized carbon nanotubes against mitochondrial swelling induced in multiple experimental conditions and predictions with new expected-value perturbation theory. *RSC Adv.* **2015**, *5*, 103229−103245.
(39) Poincaré, H. Sur le probléme des trois corps et les eéquations de la dynamique. *Ac. Math.* **1890**, *13*, 1−270.
(40) Bouzarth, E. L.; Brooks, A.; Camassa, R.; Jing, H.; Leiterman, T. J.; McLaughlin, R. M.; et al. Epicyclic orbits in a viscous fluid about a precessing rod: theory and experiments at the micro- and macro-scales. *Phys. Rev. E* **2007**, *76*, 016313.
(41) Urabe, H.; Sugawara, Y.; Ataka, M.; Rupprecht, A. Low-frequency Raman spectra of lysozyme crystals and oriented DNA films: dynamics of crystal water. *Biophys. J.* **1998**, *74*, 1533−40.

DOI: 10.1021/acs.jcim.6b00458
J. Chem. Inf. Model. 2017, 57, 1029−1044

(42) Chou, K. C. Identification of low-frequency modes in protein molecules. *Biochem. J.* **1983**, *215*, 465−9.
(43) Chou, K. C. The biological functions of low-frequency vibrations (phonons). VI. A possible dynamic mechanism of allosteric transition in antibody molecules. *Biopolymers* **1987**, *26*, 285−95.
(44) Hennrich, F.; Krupke, R.; Lebedkin, S.; Arnold, K.; Fischer, R.; Resasco, D. E.; Kappes, M. M. Raman spectroscopy of individual single-walled carbon nanotubes from various sources. *J. Phys. Chem. B* **2005**, *109*, 10567−73.
(45) Fernandez-Lozano, C.; Cuinas, R. F.; Seoane, J. A.; Fernandez-Blanco, E.; Dorado, J.; Munteanu, C. R. Classification of signaling proteins based on molecular star graph descriptors using Machine Learning models. *J. Theor. Biol.* **2015**, *384*, 50−8.
(46) Fernandez-Lozano, C.; Gestal, M.; Pedreira-Souto, N.; Postelnicu, L.; Dorado, J.; Munteanu, C. R. Kernel-based feature selection techniques for transport proteins based on star graph topological indices. *Curr. Top. Med. Chem.* **2013**, *13*, 1681−91.
(47) Fernandez-Blanco, E.; Aguiar-Pulido, V.; Munteanu, C. R.; Dorado, J. Random Forest classification based on star graph topological indices for antioxidant proteins. *J. Theor. Biol.* **2013**, *317*, 331−7.
(48) Perez-Bello, A.; Munteanu, C. R.; Ubeira, F. M.; De Magalhaes, A. L.; Uriarte, E.; Gonzalez-Diaz, H. Alignment-free prediction of mycobacterial DNA promoters based on pseudo-folding lattice network or star-graph topological indices. *J. Theor. Biol.* **2009**, *256*, 458−66.
(49) Vázquez, J. M.; Aguiar, V.; Seoane, J. A.; Freire, A.; Serantes, J. A.; Dorado, J.; Pazos, A.; Munteanu, C. R. Star Graphs of Protein Sequences and Proteome Mass Spectra in Cancer Prediction. *Curr. Proteomics* **2009**, *6*, 275−288.
(50) Fernandez-Blanco, E.; Rivero, D.; Rabunal, J.; Dorado, J.; Pazos, A.; Munteanu, C. R. Automatic seizure detection based on star graph topological indices. *J. Neurosci. Methods* **2012**, *209*, 410−9.
(51) Pedersen, P. L.; Greenawalt, J. W.; Reynafarje, B.; Hullihen, J.; Decker, G. L.; Soper, J. W.; Bustamente, E. Preparation and characterization of mitochondria and submitochondrial particles of rat liver and liver-derived tissues. *Methods Cell Biol.* **1978**, *20*, 411−81.
(52) Munteanu, C. R.; Magalhaes, A. L.; Duardo-Sanchez, A.; Pazos, A.; Gonzalez-Diaz, H. S2SNet: A Tool for Transforming Characters and Numeric Sequences into Star Network Topological Indices in Chemoinformatics, Bioinformatics, Biomedical, and Social-Legal Sciences. *Curr. Bioinf.* **2013**, *8*, 429−437.
(53) Harary, F. *Graph Theory*; Addison-Wesley: Reading, MA, 1969.
(54) Randić, M.; Zupan, J.; Vikic-Topic, D. On representation of proteins by star-like graphs. *J. Mol. Graphics Modell.* **2007**, *26*, 290−305.
(55) Munteanu, C. R. CNT Raman for Mitocondrial Oxygen Consumption Data Set and Regression Models. https://dx.doi.org/10.6084/m9.figshare.3472349 (accessed Jan 31, 2017).
(56) Wold, S.; Ruhe, A.; Wold, H.; Dunn, W. J., III The collinearity problem in linear regression. The partial least squares (PLS) approach to generalized inverses. *SIAM J. Sci. Stat Comput* **1984**, *5*, 735−743.
(57) Bishop, C. M. *Neural Networks for Pattern Recognition*; Oxford University Press: USA, 1995.
(58) Breiman, L. Random Forests. *Machine Learning* **2001**, *45*, 5−32.
(59) Lanza, I. R.; Nair, K. S. Functional assessment of isolated mitochondria in vitro. *Methods Enzymol.* **2009**, *457*, 349−72.
(60) Galano, A.; Francisco-Marquez, M.; Martínez, A. Influence of Point Defects on the Free-Radical Scavenging Capability of Single-Walled Carbon Nanotubes. *J. Phys. Chem. C* **2010**, *114*, 8302−8308.
(61) Francisco-Marquez, M.; Galano, A.; Martínez, A. On the Free Radical Scavenging Capability of Carboxylated Single-Walled Carbon Nanotubes. *J. Phys. Chem. C* **2010**, *114*, 6363−6370.
(62) Galano, A. Influence of Diameter, Length, and Chirality of Single-Walled Carbon Nanotubes on Their Free Radical Scavenging Capability. *J. Phys. Chem. C* **2009**, *113*, 18487−18491.
(63) Martínez, A.; Galano, A. Free Radical Scavenging Activity of Ultrashort Single-Walled Carbon Nanotubes with Different Structures through Electron Transfer Reactions. *J. Phys. Chem. C* **2010**, *114*, 8184−8191.
(64) Martínez, A.; Francisco-Marquez, M.; Galano, A. Effect of Different Functional Groups on the Free Radical Scavenging Capability of Single-Walled Carbon Nanotubes. *J. Phys. Chem. C* **2010**, *114*, 14734−14739.
(65) Geng, J.; Kim, K.; Zhang, J.; Escalada, A.; Tunuguntla, R.; Comolli, L. R.; Allen, F. I.; Shnyrova, A. V.; Cho, K. R.; Munoz, D.; et al. Stochastic transport through carbon nanotubes in lipid bilayers and live cell membranes. *Nature* **2014**, *514*, 612−5.
(66) Tunuguntla, R. H.; Allen, F. I.; Kim, K.; Belliveau, A.; Noy, A. Ultrafast proton transport in sub-1-nm diameter carbon nanotube porins. *Nat. Nanotechnol.* **2016**, *11*, 639−44.

DOI: 10.1021/acs.jcim.6b00458
J. Chem. Inf. Model. 2017, 57, 1029−1044

Artigo 6: Carbon Nanotubes' Effect on Mitochondrial Oxygen Flux Dynamics: Polarography Experimental Study and Machine Learning Models using Star Graph Trace Invariants of Raman Spectra

nanomaterials

MDPI

Article

Carbon Nanotubes' Effect on Mitochondrial Oxygen Flux Dynamics: Polarography Experimental Study and Machine Learning Models using Star Graph Trace Invariants of Raman Spectra

Michael González-Durruthy [1], Jose M. Monserrat [1,*], Bakhtiyor Rasulev [2], Gerardo M. Casañola-Martín [3], José María Barreiro Sorrivas [4], Sergio Paraíso-Medina [5], Víctor Maojo [5], Humberto González-Díaz [6,7], Alejandro Pazos [8,9] and Cristian R. Munteanu [8,9,*]

1 Institute of Biological Science (ICB), Federal University of Rio Grande, Rio Grande, RS 96270-900, Brazil; gonzalezdurruthy.furg@gmail.com
2 Department of Coatings and Polymeric Materials, North Dakota State University (NDSU), Fargo, ND 58102, USA; bakhtiyor.rasulev@ndsu.edu
3 Department of Systems and Computer Engineering, Carleton University, Ottawa, ON K1S 5B6, Canada; gmaikelc@gmail.com
4 Computer Science School (ETSIINF), Polytechnic University of Madrid (UPM), Calle de losCiruelos, Boadilla del Monte, 28660 Madrid, Spain; jmbarreiro@fi.upm.es
5 Biomedical Informatics Group, Artificial Intelligence Department, Polytechnic University of Madrid, Calle de los Ciruelos, Boadilla del Monte, 28660 Madrid, Spain; sparaiso@infomed.dia.fi.upm.es (S.P.-M.), vmaojo@fi.upm.es (V.M.)
6 Department of Organic Chemistry II, University of the Basque Country UPV/EHU, 48940 Leioa, Biscay, Spain; gonzalezdiazh@yahoo.es
7 IKERBASQUE, Basque Foundation for Science, 48011 Bilbao, Biscay, Spain
8 INIBIC Institute of Biomedical Research, CHUAC, UDC, 15006 Coruña, Spain; apazos@udc.es
9 RNASA-IMEDIR, Computer Sciences Faculty, University of Coruña, 15071 Coruña, Spain
* Correspondence: josemmonserrat@gmail.com (J.M.M.); c.munteanu@udc.es (C.R.M.); Tel.: +34-981-167-000 (ext. 1302) (C.R.M.)

Received: 7 October 2017; Accepted: 8 November 2017; Published: 11 November 2017

Abstract: This study presents the impact of carbon nanotubes (CNTs) on mitochondrial oxygen mass flux (J_m) under three experimental conditions. New experimental results and a new methodology are reported for the first time and they are based on CNT Raman spectra star graph transform (spectral moments) and perturbation theory. The experimental measures of J_m showed that no tested CNT family can inhibit the oxygen consumption profiles of mitochondria. The best model for the prediction of J_m for other CNTs was provided by random forest using eight features, obtaining test R-squared (R^2) of 0.863 and test root-mean-square error (RMSE) of 0.0461. The results demonstrate the capability of encoding CNT information into spectral moments of the Raman star graphs (SG) transform with a potential applicability as predictive tools in nanotechnology and material risk assessments.

Keywords: carbon nanotubes; cytotoxicity; mitochondria oxygen mass flux; Raman spectroscopy; graph theory; spectral moments

1. Introduction

Carbon nanotubes (CNTs) have attracted great interest for their promising applications in the fields of biomaterials and nano-biotechnology. Therefore, the evaluation of their toxicity in biological systems is a goal of major importance for the biomaterial sciences. Currently, evidence has been

accumulating regarding the CNT toxicity associated with mitochondrial dysfunction and apoptosis [1]. Some in vitro studies have demonstrated that CNTs exhibit cytotoxicity after their accumulation in the mitochondria matrix and/or by affecting the function of mitochondrial respiratory complexes of the inner membrane [2,3].

However, it is still not known which bio-energetic mechanisms (the inhibition of adenosine diphosphate/adenosine triphosphate (ADP/ATP)-transport, uncoupling effects on oxidative phosphorylation, the induction of mitochondrial permeability transition pores, etc.) are responsible for the initiation of CNT mitochondrial damage [4–9]. Particularly, the study of mitochondrial dysfunction based on perturbations of the mitochondrial oxygen mass flux induced by CNTs could be decisive for the in vitro prediction of the no-observed-adverse-effect level (NOAEL) [10] and the evaluation of the selective nanotoxicity (mitochondrial channel nanotoxicity) towards potential biomedical applications in precision medicine. Several scientific reports highlight a major impact of adverse/toxic effects induced by CNT on critical mitochondrial components due to a peculiar mitotropic behavior. Mitochondrial oxygen mass flux regulates the mitochondrial volume linked to the Ca^{2+} induction of mitochondrial permeability transition pores (MPTP) and also to the increase of the mitochondrial reactive oxygen species (ROS-levels) based on the partial reduction of molecular oxygen in the mitochondrial respiratory complexes (complex IV). The latter have been extensively characterized and associated with several chronic pathological processes, such as neurodegenerative diseases (Alzheimer, Parkinson, Epilepsy), cardiac ischemia, and cancer. These diseases have currently high levels of morbidity and mortality, and mitochondrial dysfunction based on oxygen mass flux mechanisms has been indirectly or directly involved.

On the other hand, Raman spectroscopy provides information on the chemical fingerprints of molecules, biomolecular systems and nanoscale structures: DNA [11], proteins [12], antibodies [13] and CNTs [14]. In addition, the presence of the G band (1580 cm^{-1}) in the Raman spectra of SWCNTs has been corroborated in mitochondria associated with incipient colloid–osmotic swelling or the induction of mitochondrial permeability transition pores [15]. Recent studies using Raman spectroscopy and polarographic methods have shown that CNTs alter cytochrome c electron transfer and modulate mitochondrial function at a critical concentration of 10 μg/mL [16]. Previous quantitative structure–activity relationship (QSAR) models of CNTs in terms of mitochondrial respiratory function have been reported [10]. However, there are only few studies about the relationship between a CNT's physicochemical parameters from an oxygen mass flux perspective.

In principle, the Raman spectra signals of different CNTs can be used as inputs for machine learning (ML) methods to predict a dose–effect relationship for the biological properties of CNTs. Nevertheless, the Raman spectra of CNTs have many peaks (>1000 points), making statistical analysis still possible, but somewhat difficult. A possibility for this kind of signal is to compress them into another series of numerical parameters that quantify useful structural information on all the spectra. In a previous work, the star graphs (SG) of the Raman spectra of CNTs [17] were introduced. The idea is to transform the signal into a network with star graph (SG) topology. Next, different invariants can be calculated from the adjacency matrix associated with this SG graph representation of the spectra. Afterwards, the new invariants are supposed to contain useful information, compressed and used as input in ML experiments. Last, as a result of the ML study, predictive models are obtained, which are able to connect the Raman spectra with the biological activity under study. In fact, our group have used this scheme based on SRN transforms to model biological properties from protein sequences [18–20], nucleic acid sequences [21], blood protein mass spectra [22] and electroencephalogram (EEG) signals [23]. These studies have used different matrix invariants such as Markov–Shannon entropies or matrix trace invariants Tr_k (also known as spectral moments) to compress the information from proteins, gene, etc. In a previous work, the research focused on how to use Markov–Shannon entropies to compress information from Raman spectra [17]. However, there is no report on the use of Tr_k values in this sense.

This work is aimed at combining experimental and computational techniques to provide a heuristic solution to the above-discussed problem. Firstly, high-resolution respirometry (HRR) polarographic (Oxygraph-2k) assays are used for the first time to address this issue. This methodology provides a quick and reproducible means to measure the rate of oxygen consumption by mitochondria isolated from different tissues using a sensitive Clark-type electrode. Simultaneously, the oxygen mass flux (O_2 flux) in mitochondrial suspensions can be monitored depending on the time of exposure [24–26]. Currently, there are no precedents for this methodology applied to the evaluation of the no-observed-adverse-effect level of CNTs. In addition, a new computational model is developed for the prediction of dose–effect relationships for this property for other CNTs. In doing so, the Tr_k values of the Raman spectra of CNTs are used as an input to seek a predictive model based on machine learning (ML) and perturbation theory (PT) (PTML model). PTML models are useful to predict the properties of complex molecular systems with simultaneous variations of multiple experimental boundary conditions, such as chemical reactivity, drug metabolism, vaccine peptide epitopes, metabolic networks, and micelle nanoparticles [27–30]. Figure 1 depicts a workflow scheme with the general steps of this work. The current work paves the way for the use of PTML models, polarography, and Raman spectroscopy, and for the experimental and theoretical study of other biological properties of CNTs in the future.

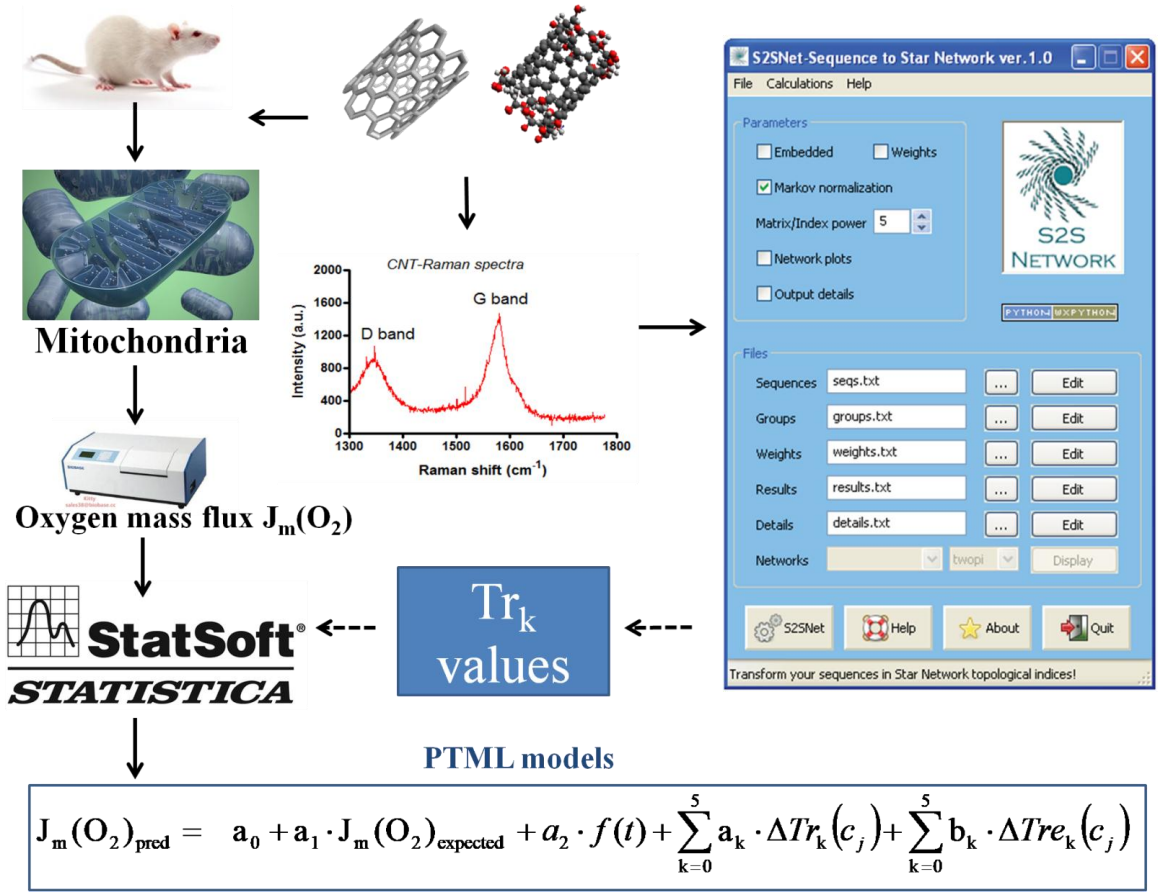

Figure 1. General workflow.

2. Results

2.1. Experimental Results

High-resolution respirometry (HRR) using Oroboros Instruments (Oxygraph-2k) was applied to evaluate the effects of the CNT family on the bioenergetic mitochondrial function through the

measurement of oxygen mass flux after exposure with different CNTs (from CNT-1 to CNT-9). A default experimental concentration of 5 µg/mL for all CNTs was established to assess the different contribution of the remaining physical–chemical parameters in the NOAEL for the oxygen mass flux response. Figure 2 shows a representative profile of the mitochondrial oxygen mass flux of isolated rat liver mitochondria, showing the small pulses of ADP-titration associated with transient increments of O_2 flux during the period of ATP synthesis or V3 state (ADP-dependent respiration) = ratio of mitochondrial ADP-flux (J_m(ADP))/(J_m(O_2)) + mitochondrial inorganic pyrophosphate Pi-flux (J_m(Pi)) for the experimental condition of untreated-rat liver mitochondria (untreated-RLM) and pre-incubation with the different CNTs (RLM + CNTs 5 µg/mL). The respiratory substrates (ADP) and the uncoupling agent carbonyl-cyanide p-trifluoromethoxyphenylhydrazone (FCCCP) were added where indicated by the arrow. In addition, in the supplementary information file, a figure that depicts a control profile of the mitochondrial oxygen mass flux of isolated RLM was included.

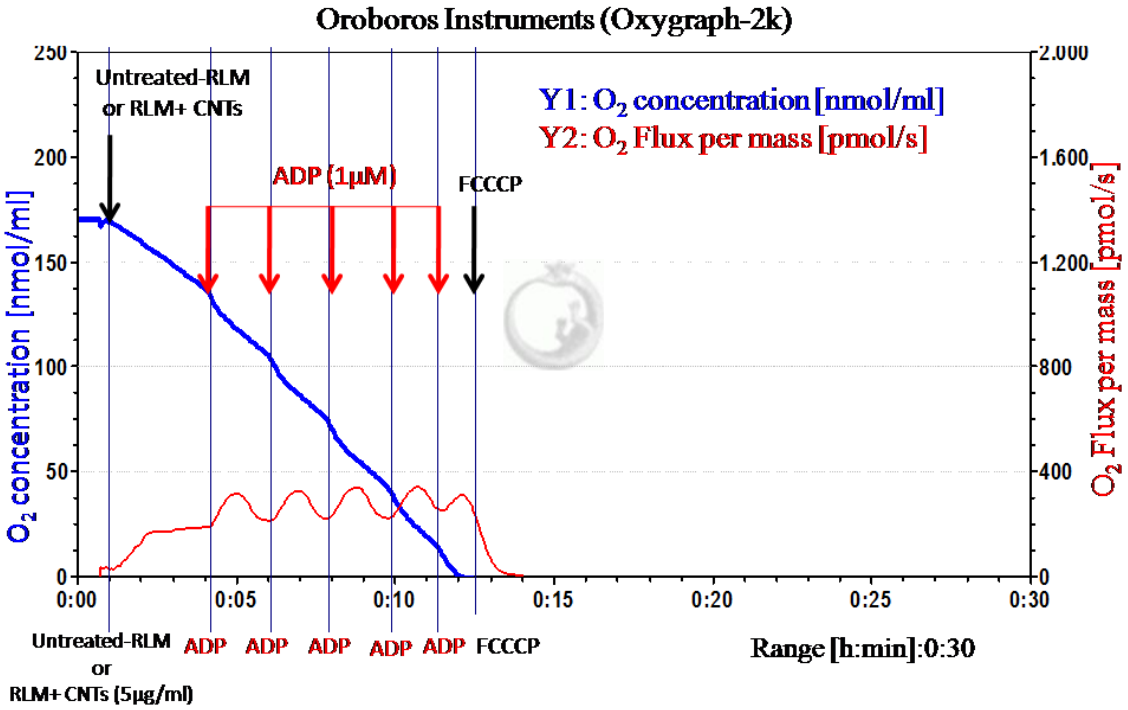

Figure 2. Representative profiles of the mitochondrial oxygen mass flux of isolated rat liver mitochondria (Y2: Red curve).

Figure 3 shows a schematic representation of mitochondrial ADP/ATP exchange and oxidative phosphorylation based on a proposed mechanism linked to the profiles of the mitochondrial oxygen mass flux of isolated rat liver mitochondria. It shows the different states of the mitochondrial respiration V2 state (basal respiration), V3 state (ADP-dependent respiration), V4 (or VFCCCP state of ADP-independent mitochondrial respiration) in untreated rat liver mitochondria or untreated RLM (black curve), CNT-treated RLM at concentration 5 µg/mL (red curves) and treated RLM with CATR (or ADP-inhibitor) (green curve). The respiratory substrates (ADP) and the uncoupling agent (FCCCP) were added where indicated by the arrow. These results are representative for the three experiments using Oroboros Instruments (Oxygraph-2k). * $p < 0.001$ to statistical differences between CATR (or ADP-inhibitor) (green curve) and CNT-treated RLM at concentration 5 µg/mL (red curves).

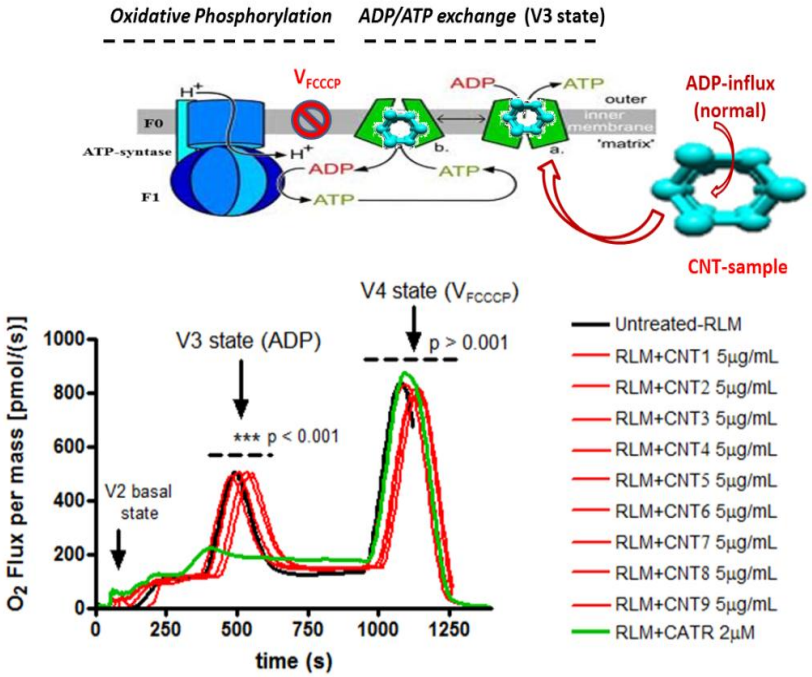

Figure 3. Representation of mitochondrial ADP/ATP exchange and oxidative phosphorylation. ***p is used to represent the significant statistical differences between V3 state-ADP-dependent mitochondrial O2 flux from the RLM + CNT treated groups (CNT1-9) and V3 state-ADP-dependent mitochondrial O2 flux from the RLM + Carboxyatractyloside (CATR, a specific inhibitor of ADP-mitochondrial transport).

2.2. Computational Results

The variation of the mitochondrial oxygen mass flux in the presence of CNTs was modeled using the PTML methodology based on the SG trace invariants of the Raman spectra ($Tr_{0–5}$) of CNT. The RRegrs tool was adapted for calculations on an High Performance Computing (HPC) cluster and was used to test three types of regression methods: Linear Multi-regression (LM), Neural Network (NN) and Random Forest (RF). The objective of the modeling was to find the best prediction model for the mitochondrial oxygen flow in the presence of CNTs. The linear and non-linear methods were used with 10 different random data splits (75% for training–25% for test) using a custom script presented in the Figshare repository (https://doi.org/10.6084/m9.figshare.3472349). This script normalizes and splits datasets in a similar way to the RRegrs tool with the parameters *CV*types = *repeatedcv* (10-cross-validations) and default number of data splits (*iSplitTimes* = 10). After the normalization and removal of the correlated features (default RRegrs methodology *cutoff* = 0.9), eight input features remain in the final dataset. Thus, the Figshare repository presents several files: "ds2.full.Tr.csv", the initial dataset without any filters (all features), and "ds2.corr.Tr.csv", the final dataset after removing correlated features and using normalization. The last dataset was used with the script "CreateNormalisedSplits.R" to create 10 random splits of data as training and test subsets to test them with regression methods.

The first two are the expected values of flux, $J_m(O_2)_{\text{expected}}$ and the duration of the experiment (t). The other six input variables are moving average (MA) operators, including at least one MA for each experimental condition. These MA operators are: ΔTr_0(rep), ΔTre_3(rep), ΔTre_0(CNTtype), ΔTre_4(Func.Type), ΔTre_0(Solvent), and ΔTre_5(Solvent). Please note that the MA operators $\Delta Tr_k(c_j) = Tr_k - \langle Tr_k(c_j)\rangle$ and $\Delta Tre_k(c_j) = Tre_k - \langle Tre_k(c_j)\rangle$ quantify the deviation of the Tr_k or Tre_k of the Raman spectra of a specific CNT from the expected values $\langle Tr_k(c_j)\rangle$ or $\langle Tre_k(c_j)\rangle$, measured for all Raman spectra and recorded for all CNTs with the specific experimental condition (c_j). The symbol Tr_k refers to traces calculated from linear graphs of the Raman spectra and the symbol Tre for graphs with recurrence information embedded. Table 1 shows the minimum, maximum, and mean values for R-squared/root mean squared error of training and test subsets (R^2_{tr}/RMSE$_{tr}$ and R^2_{ts}/RMSE$_{ts}$) for

the eight-feature dataset (10 splits). The first observation in terms of results is that the models were not over-fitted because the differences between the training and test statistics were small. Additional statistics are available online at Figshare [31] (ds2.Tr.models.xlsx).

Table 1. Predictive model based on Machine Learning and Perturbation Theory (PTML) statistics for the evaluation of mitochondrial oxygen flow modifications due to CNTs (10 random splits for each method).

Regression Method	Statistics	Training		Test	
		R^2_{tr}	$RMSE_{tr}$	R^2_{ts}	$RMSE_{ts}$
Linear Multi-regression (LM)	Mean	0.358	0.0959	0.356	0.0954
	Min	0.349	0.0954	0.340	0.0932
	Max	0.363	0.0966	0.384	0.0969
Neural Network (NN)	Mean	0.645	0.0709	0.672	0.0681
	Min	0.626	0.0697	0.620	0.0613
	Max	0.659	0.0727	0.739	0.0738
Random Forest (RF)	Mean	0.855	0.0455	0.856	0.0452
	Min	0.851	0.0451	0.853	0.0431
	Max	0.858	0.0462	0.863	0.0461

The file ds2.Tr.models.xlsx from Figshare presents the statistics for each regression model and individual data split. In addition, minimum, maximum, and average values of the statistics are presented. The final results include the best model from an individual split and its model is saved as an R object. Thus, it is possible to directly use the best model by loading it with an R script and making any prediction. Average values of R^2_{ts} and $RMSE_{ts}$ for LM, NN and RF are presented in the same file.

3. Discussion

3.1. Discussion of Experimental Results

The results showed that all the tested CNT family did not inhibit (or affect) the profiles of oxygen mass flux in isolated rat liver mitochondria after the sequential addition of ADP intermittent pulses, which characterize the state V3 of respiration (ADP-dependent) for the untreated RLM and treated RLM with CNTs (5 μg/mL) (see Figure 2, red profile of oxygen flux). Note that for this instance, no significant differences were detected in the profiles of mitochondrial oxygen mass flux, compared with the strong inhibition of the state V3 of respiration detected for mitochondrial treated with carboxyatractyloside a specific inhibitor of ADP-mitochondrial transport (CATR-treated RLM), as shown in Figure 3 (red profile of oxygen flux). Moreover, the oxidative phosphorylation was not affected by ATP synthase, which depends on the ADP transport by ADP/ATP mitochondrial carrier between the cytosol and mitochondrial matrix under physiological normoxic conditions. The in vitro results suggest a non-inhibitory biochemical response of oxygen mass flux in isolated rat liver mitochondria. Furthermore, treated RLM with CNTs maintained the normally-induced uncoupling response of state V4 (or Vfcccp) after the addition of FCCCP 2 μM (classical uncoupling agent of the mitochondrial oxidative phosphorylation) according to an increase in the oxygen mass flux state V4 of respiration between 750 and 1250 seconds for all CNTs tested, as shown in Figure 3.

According to these results, several aspects should be considered in order to explain the relevance of CNT NOAEL in terms of mitochondrial oxygen mass flux response. Covalently functionalized CNTs (oxidized-CNTs) and/or with point defects characterized by the D band of Raman spectra (with a characteristic peak at 1350 cm^{-1}) are expected to have greater biocompatibility than pristine CNTs [15]. This may be due to the ability of the OH and COOH groups of oxidized CNT or π–bond of the sp^2 of pristine CNT wall to form several adducts with the basal oxygen-free radical [32], released by the mitochondrial complex I and III at between the V2 and V3 state of mitochondrial respiration. In this context, the non-significant respiratory effects from a low CNT concentration (5 μg/mL) could be recognized as a typical pharmacodynamic criterion of NOAEL for CNTs, similar to the sub-clinical effects of traditional lipophilic agents with mitochondrial mechanisms reported in the literature.

As mentioned in the introduction of this work, CNTs can modulate mitochondrial function at a critical concentration of 10 μg/mL [25].

In this sense, it should be pointed out that the biocompatibility/toxicity relationship of the tested CNT family may be important in predicting the no-observed-adverse-effect level. This is not only limited to considerations of dosimetry in terms of concentration, but also applies to the influence of the physicochemical nanodescriptors of the tested CNTs (Raman nanodescriptors). Thus, the prediction of uncertainty factors or encrypted information in the CNT structure, such as new Raman spectra nanodescriptors, could be used to model the dosimetric criteria anticipated to be without an increased risk for CNT adverse effects [33,34].

3.2. Discussion of Computational Results

Discussion of the PTML computational study. LM produced poor results (mean R^2_{ts} = 0.356; mean $RMSE_{ts}$ = 0.0954), showing that the relationship between the input moving averages (MAs) of the CNT Raman SG spectral moment and the mitochondrial oxygen flow is not a linear one, or that these features did not include enough information to model this relationship. Starting with the non-linear methods, such as NN and RF, the performance of the regression model improved. Thus, NN provided a mean R^2_{ts} of 0.672 and a mean $RMSE_{ts}$ of 0.0681. The best NN model (split 3) was a single-hidden layer with 10 neurons, a structure of 8-10-1 (eight inputs, 10 neurons in one hidden layer, one output), a weight decay of 0.001, and an R^2_{ts} of 0.739 and an $RMSE_{ts}$ of 0.0613 [31].

The RF predictor significantly improved the regression performance for mitochondrial oxygen flow: a mean R^2_{ts} of 0.856 and a mean $RMSE_{ts}$ of 0.0452 were obtained. Compared with the NN statistics, R^2_{ts} increased by 0.184 and $RMSE_{ts}$ decreased by 36.6%. The best RF model (split 2) has 50 trees, an R^2_{ts} of 0.863 and an $RMSE_{ts}$ of 0.0461. The variation in the RF error with the number of trees is shown in Figure 4. The model could be downloaded from the free online repository [31] and it could be used for future predictions or may be included in future R applications. The use of all initial 34 features had no important improvements in the regression performance with mean values for LM, NN and RF of 0.356, 0.601 and 0.857 (see all details online [31]). This means that the other features obtained no useful information to improve the current model. In order to check the model quality, the regression receiver operator characteristic (RROC) curve [35] for the test subset is shown in Figure 5. The RROC demonstrates the performance of the RF model.

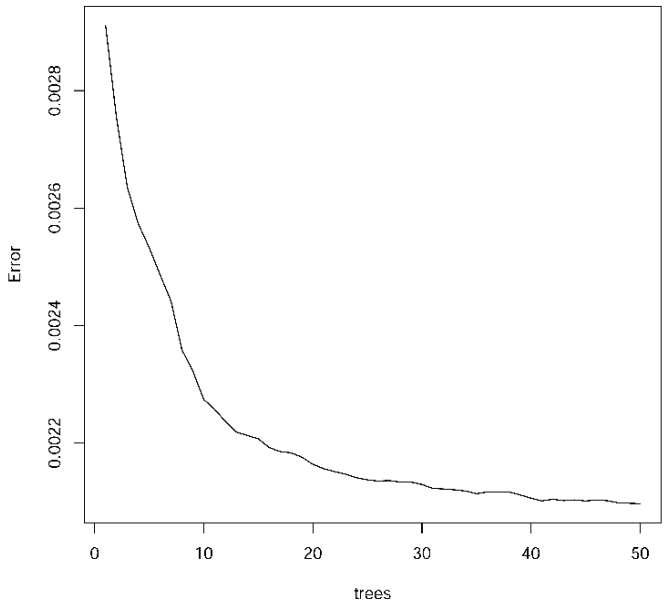

Figure 4. RF error with the number of trees for regression models.

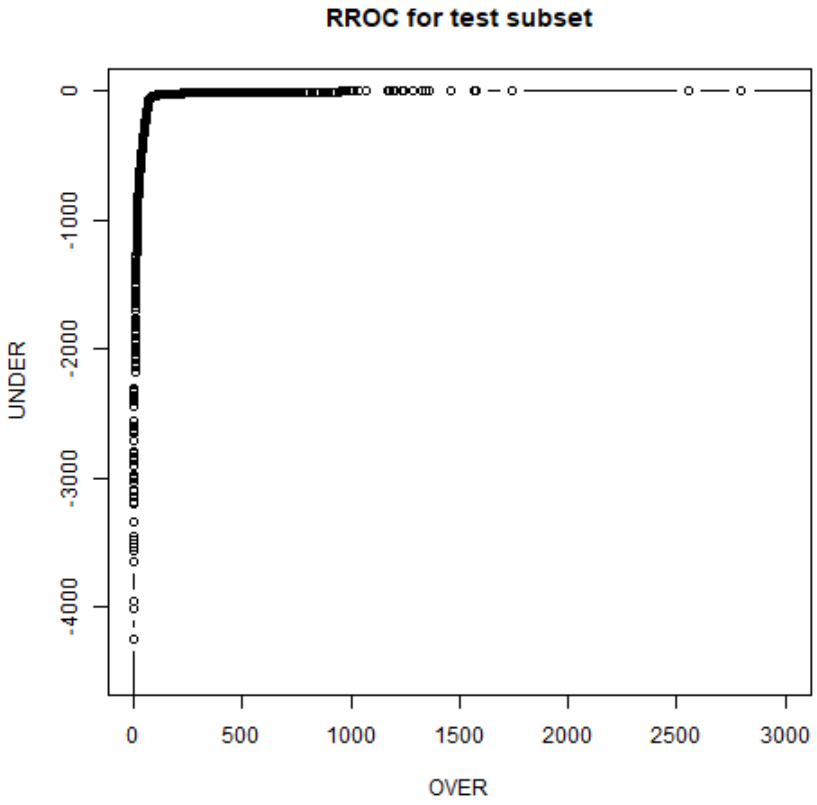

Figure 5. Regression receiver operator characteristic (RROC) curves for RF best model (test subset).

4. Materials and Methods

4.1. General Workflow

The aims of this paper are:

(a) The measurement of the CNT effect on the mitochondrial oxygen mass flux with polarography;
(b) The definition and calculation of the matrix trace invariants (Tr_k) of SG transforms of Raman spectra for a series of CNTs for the first time;
(c) The use of the Tr_k values as input to seek new PTML models able to predict CNTs' effect on mitochondrial oxygen mass flux.

Thus, the following steps were taken (see Figure 6):

(1) Experimental measurements of the mitochondria oxygen mass flux in the presence of different CNT types;
(2) Transformation of CNT's Raman spectra into SG spectral moments;
(3) Calculation of the expected values of the mitochondria oxygen mass flux and the moving averages of the SG spectral moments under different experimental conditions;
(4) Search for the best regression PTML models using the RRegrs package in R (https://github.com/enanomapper/RRegrs/).

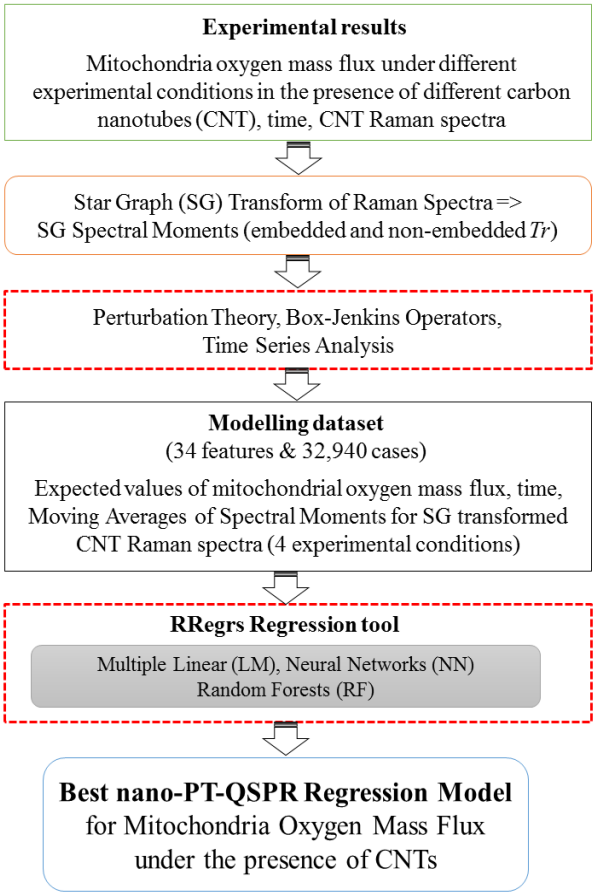

Figure 6. General workflow for the machine learning analysis.

4.2. Experimental Methods

4.2.1. General Procedures

In the Supplementary Information (SI) file, a detailed description of the following sections is included: sample preparation, reagents and solutions, Raman spectra recording, animal welfare, and isolation of rat liver mitochondria (RLM). The RLM were isolated by standard differential centrifugation according to the experimental procedures established in the literature [36].

4.2.2. Monitoring Mitochondrial Oxygen Mass

The HRR method was used, along with Oroboros Instruments, DatLab Version 4.2.1.50 (Oxygraph-2k). This methodology included the use of a 2 mL glass chamber equipped with a magnetic stirrer. Mitochondrial O_2 mass flux (pmol/seg) in the absence and presence of different carbon nanotubes (CNT-1 to CNT-9) was monitored and measured as the negative time derivative of an oxygen concentration (nmol/mL). The mitochondrial oxygen mass flux values were corrected for the small amount of back diffusion of oxygen from materials within the chamber, any leak of oxygen from outside the vessel, and oxygen consumed by the polarographic electrode [26,37,38].

With this in mind, the RLM isolated (1 mg protein/mL) were energized with 5 mM potassium succinate (plus 2.5 µM rotenone) in a standard incubation medium, consisting of 125 mM sucrose, 65 mMKCl, 2 mM inorganic phosphate (K_2HPO_4) and 10 mM potassium hydroxide-2-[4-(2-hydroxyethyl)piperazin-1-yl]ethanesulfonic acid (HEPES-KOH) pH 7.4 at 20 °C in a standard respiration medium. The experimental approach was calibrated using the oxygen content of an air saturated medium [38]. All the aforementioned steps were performed by the pre-incubation of

isolated rat liver mitochondria with 5 μg/mL for all the CNT-treated groups. This level of concentration was considered based on the NOAEL criteria mentioned in the introduction of this work. For this instance, 5 μg/mL of the CNT concentration is the corrected half value of the CNT concentration (10 μg/mL) used by Ma et al., who promoted an incipient colloid–osmotic swelling or low induction of mitochondrial permeability transition pores, noticeably detected by Raman spectroscopy [15,16]. The total number of the collected data points was 32,940. The data obtained from the mitochondrial oxygen mass study in the presence of CNTs and the CNT spectra were used to search for a theoretical model which predicts mitochondrial oxygen mass in the presence of new CNTs.

4.3. Computational Methods

4.3.1. Trace Invariants of Raman Spectra

One of the objectives of this work is to develop a mathematical model able to predict the biological effect of CNTs using as an input the information extracted from Raman spectra. Thus, a new type of parameters is proposed, calculated by the application of a Star Graph (SG) transform to the Raman spectra. The SRN transform method, which has been recently introduced and published by our group [17], uses graphs and network theory tools, and is different from a classic Fourier transformation. The transform technique used herein converts the Raman spectra values into sequences of characters and creates the corresponding SG of this signal. The SG of any sequence/signal may be constructed using the S2SNet tool [39]. To construct the SG transform of a Raman spectrum, the latter should be split into intervals of 100 units, from 0 to 1800. As a result, the maximum number of SG branches is 18 and corresponds to characters from "a" to "r". Subsequently, the adjacency matrix **A** should be constructed for this sequence of characters (spectral sequence). The matrix **A** was enriched by adding the information about the recurrence to the same type of term in the spectral sequence. After this step, the matrix $\mathbf{A_e}$ was obtained, with recurrence information embedded (**e**). As a result, different invariants from the matrices **A** and $\mathbf{A_e}$ can be calculated. In this work, the matrix trace values (Tr_k and Tre_k; k = 0–5) were calculated, also known as the spectral moments [39] of the matrices **A** and $\mathbf{A_e}$ obtained after the SG transformation of the Raman spectra. Our hypothesis is that these spectral moments encode useful structural information that can be responsible for biological activity and further predictive studies (see Figure 1).

4.3.2. PTML Model

The current section describes the application of the algorithm of PTML heuristic models [30] in order to study the effect of different CNTs on the mitochondrial oxygen mass flux under different experimental conditions. The general equation of a linear PTML heuristic model could be described by Equation (1).

$$J_m(O_2)_{pred} = a_0 + a_1 \cdot J_m(O_2)_{expected} + a_2 \cdot f(t) + \sum_{k=0}^{5} b_k \cdot \Delta Tr_k(c_j) + \sum_{k=0}^{5} c_k \cdot \Delta Tre_k(c_j) \quad (1)$$

where $J_m(O_2)_{pred}$ is the predicted mitochondrial oxygen mass flux. The term $J_m(O_2)_{expected} = \langle J_m(O_2) \rangle$ is the average value of $J_m(O_2)$ for different subsets of experimental conditions (expected value of $J_m(O_2)$). The other input values ΔTr_k and ΔTre_k are the moving average (MA) operators. The MA operators $\Delta Tr_k(c_j) = Tr_k - \langle Tr_k(c_j) \rangle$ and $\Delta Tre_k(c_j) = Tre_k - \langle Tre_k(c_j) \rangle$ quantify the deviation of Tr_k or Tre_k of the Raman spectra for a specific CNT from the expected average values $\langle Tr_k(c_j) \rangle$ or $\langle Tre_k(c_j) \rangle$ measured for all Raman spectra, recorded for all CNTs with the specific experimental condition (c_j). The symbols Tr_k refer to traces calculated from linear graphs of the Raman spectra and the symbol Tre_k for graphs with recurrence information embedded. The coefficients a_k, b_k, and c_k are the linear coefficients of the equation.

4.3.3. Model Dataset

The experimental data for the mitochondrial oxygen mass flux (J_m) in the presence of CNTs are available as a FigShare repository [31]: 32,940 cases of $J_m(O_2)$, CNT1-9, CNTtype, Replicate (rep), Function_type (chemical modification of CNT), Solvent and time (t). $J_m(O_2)$ was measured under four types of experimental conditions (c) such as Replicate (rep), CNTtype, Functiontype (chemical modification of CNT), and Solvent. Replicate (rep) has two values: 0 or 1, for non-replicated and replicated experiment. CNTtypes are multi-walled carbon nanotubes (MWCNT), mixed single walled/double-walled carbon nanotubes (SW+DWCNT), and single-walled carbon nanotube (SWCNT). CNT type is "0" when the assay is a control assay with a blank solution with a CNT concentration equal to 0. The values of the solvent condition are H_2O and dimethyl sulfoxide (DMSO). The CNT Function types could have three values: 0 (none), COOH and OH. The average of the SG spectral moments under the experimental conditions are presented on the FigShare platform [31]. The final dataset, used to find the best prediction model is made up of 32,940 cases and 34 input features.

4.3.4. PTML Regression Predictors

The raw dataset was normalized and the training and test sub-sets were obtained using 10 splits: 75% training sets (train) and 25% test sets (test) using an *R* script available online [40]. The regression PTML models were searched with RRegrs, an *R* integrated framework that provides ten linear and non-linear regression models [41,42]. The selection of the models used the criteria of the R_{ts} values (regression coefficient for test subset) and the $RMSE_{ts}$ (root-mean-square error) corresponding values.

Three types of regression methods of RRegrs were used: multiple linear regression (LM), neural networks regression (NN) [43], and random forest (RF) [44]. Thus, the correlated features were removed using the parameters of RRegrs. For NN and RF, a study of the method parameters was performed. A modified version of RRegrs (batchRRegrs: https://github.com/cafernandezlo/batchRRegrs) was used on the BioCAI HPC platform from the University of A Coruna (A Coruña, Spain). The batchRRegrs default values of parameters were generally employed (https://github.com/cafernandezlo/batchRRegrs/blob/master/batchRRegrs/batchRRegrs.R). The default optimizations used the *tuneGrid* parameter of the caret training method:

- *NNreg* function used a grid for 200, 300 and 400 neurons in the hidden layer (*.size*) and a decay of 0, 0.01, 0.2, 0.1 (*.decay*) (*method* = 'nnet');
- *RFreg* function used 1500 trees (*ntree* = 1500 for *method* = 'rf').

An additional number of neurons were tested for NN (1, 5, 10 and 15) and different decay values (0.001 and 0.005). Moreover, an additional number of trees in RF were tested: 5, 10, 20, 30, 40, 50, 100, and 500. The best RF model should use the lowest number of trees and best statistics. The results presented for NN and RF models the parameters for the best models.

The criteria to find the best model apply the RRegrs methodology: maximum R^2_{ts} and minimum $RMSE_{ts}$. The plots were obtained with custom *R* scripts. The best regression model which predicts mitochondria oxygen mass flux in the presence of CNTs is available online [31] in order to be used for future predictions. The regression receiver operator characteristic (RROC) curve was constructed using the algorithm from reference [35]. The RROC presented the over-estimation (OVER) against the under-estimation (UNDER). Thus, the curve was drawn by adjusting a shift (a constant that was added or subtracted) for the predictions. This shift is similar to the threshold in the case of classifications.

5. Conclusions

The current study presented a mixture of experimental and predictive methodologies to study the effect of different CNTs on the mitochondrial oxygen mass flux. The experimental results showing non-significant respiratory effects from low CNT concentrations (5 μg/mL) could be recognized as a typical pharmacodynamics criterion of NOAEL for CNTs. In this context, the information encrypted in

the Raman spectra of CNT structures can be used as novel nanodescriptors to model the complexity of the dosimetric criteria, as no adverse mitochondrial respiratory effect level (or normal O_2 flux) was found. The *R* object model and an *R* script are available online at https://dx.doi.org/10.6084/m9.figshare.3545561.

These results show that the SG transform of CNT Raman spectra contains important information, as new CNT nanodescriptors can be combined to provide a prediction model under the experimental conditions over time for the mitochondria oxygen mass flux under the presence of specific CNTs. These in silico results indicate that this methodology can be employed for massive, virtual-based, raw data for Raman spectroscopy in order to make regulatory decisions in the biomaterial sciences.

Supplementary Materials: The following are available online at http://www.mdpi.com/2079-4991/7/11/386/s1, Table S1. Properties of CNT families, Figure S1. Raman spectra for carbon nanotubes used in the present study, Figure S2. Control profile of mitochondrial oxygen mass flux of isolated rat liver mitochondria (Y2: Red curve).

Acknowledgments: Michael González-Durruthy acknowledges a doctoral fellowship (Postgraduate Students' Program PEC-PG No. 062/2013) from the Brazilian CAPES-CNPq Agencies. This work is supported by the "Collaborative Project on Medical Informatics (CIMED)" funded by the Carlos III Health Institute from the Spanish National plan for Scientific and Technical Research and Innovation 2013–2016 and the European Regional Development Funds (FEDER) [grant numbers PI13/02020, PI13/00280]. In addition, the work was supported by the Galician Network of Drugs R+D REGID (Xunta de Galicia R2014/025), the General Directorate of Culture, Education and University Management of Xunta de Galicia (Ref. GRC2014/049) and the Galician Network for Colorectal Cancer Research (REGICC) (Ref. R2014/039). Finally, the project was supported by the Spanish Ministry of Economy and Competitiveness (MINECO) research grants (UNLC08-1E-002, UNLC13-13-3503 and CTQ2016-74881-P) and the Basque Government (IT1045-16), Ikerbasque, Basque Foundation for Science. Jose M. Monserrat acknowledges the support of Brazilian Agency CNPq (process number 454332/2014-9) and a scientific productivity fellowship (process number 308539/2016-8).

Author Contributions: Michael González-Durruthy, Jose M. Monserrat, Bakhtiyor Rasulev, and Gerardo M. Casañola-Martín performed the experiments and analyzed the experimental results. José María Barreiro Sorrivas, Sergio Paraíso-Medina, Víctor Maojo, Humberto González-Díaz, Alejandro Pazos and Cristian R. Munteanu performed the computational study and analyzed the machine learning results. All authors wrote the manuscript.

Conflicts of Interest: The authors declare no conflict of interest.

References

1. Prato, M.; Kostarelos, K.; Bianco, A. Functionalized carbon nanotubes in drug design and discovery. *Acc. Chem. Res.* **2008**, *41*, 60–68. [CrossRef] [PubMed]
2. Toropov, A.A.; Leszczynska, D.; Leszczynski, J. Predicting water solubility and octanol water partition coefficient for carbon nanotubes based on the chiral vector. *Comput. Biol. Chem.* **2007**, *31*, 127–128. [CrossRef] [PubMed]
3. Ye, S.F.; Wu, Y.H.; Hou, Z.Q.; Zhang, Q.Q. Ros and nf-kappab are involved in upregulation of il-8 in a549 cells exposed to multi-walled carbon nanotubes. *Biochem. Biophys. Res. Commun.* **2009**, *379*, 643–648. [CrossRef] [PubMed]
4. Shvedova, A.A.; Castranova, V.; Kisin, E.R.; Schwegler-Berry, D.; Murray, A.R.; Gandelsman, V.Z.; Maynard, A.; Baron, P. Exposure to carbon nanotube material: Assessment of nanotube cytotoxicity using human keratinocyte cells. *J. Toxicol. Environ. Health A* **2003**, *66*, 1909–1926. [CrossRef] [PubMed]
5. Bottini, M.; Bruckner, S.; Nika, K.; Bottini, N.; Bellucci, S.; Magrini, A.; Bergamaschi, A.; Mustelin, T. Multi-walled carbon nanotubes induce t lymphocyte apoptosis. *Toxicol. Lett.* **2006**, *160*, 121–126. [CrossRef] [PubMed]
6. Cui, D.; Tian, F.; Ozkan, C.S.; Wang, M.; Gao, H. Effect of single wall carbon nanotubes on human HEK293 cells. *Toxicol. Lett.* **2005**, *155*, 73–85. [CrossRef] [PubMed]
7. Muller, J.; Huaux, F.; Moreau, N.; Misson, P.; Heilier, J.F.; Delos, M.; Arras, M.; Fonseca, A.; Nagy, J.B.; Lison, D. Respiratory toxicity of multi-wall carbon nanotubes. *Toxicol. Appl. Pharmacol.* **2005**, *207*, 221–231. [CrossRef] [PubMed]
8. Heller, D.A.; Baik, S.; Eurell, T.E.; Strano, M.S. Single-walled carbon nanotube spectroscopy in live cells: Towards long-term labels and optical sensors. *Adv. Mater.* **2005**, *17*, 2793–2799. [CrossRef]
9. Smart, S.K.; Cassady, A.I.; Lu, G.Q.; Martin, D.J. The biocompatibility of carbon nanotubes. *Carbon* **2006**, *44*, 1034–1047. [CrossRef]

10. Toropov, A.A.; Toropova, A.P.; Pizzo, F.; Lombardo, A.; Gadaleta, D.; Benfenati, E. Coral: Model for no observed adverse effect level (noael). *Mol. Divers.* **2015**, *19*, 563–575. [CrossRef] [PubMed]
11. Urabe, H.; Sugawara, Y.; Ataka, M.; Rupprecht, A. Low-frequency raman spectra of lysozyme crystals and oriented DNA films: Dynamics of crystal water. *Biophys. J.* **1998**, *74*, 1533–1540. [CrossRef]
12. Chou, K.C. Identification of low-frequency modes in protein molecules. *Biochem. J.* **1983**, *215*, 465–469. [CrossRef] [PubMed]
13. Piacenza, M.; Grimme, S. Van der waals interactions in aromatic systems: Structure and energetics of dimers and trimers of pyridine. *ChemPhysChem* **2005**, *6*, 1554–1558. [CrossRef] [PubMed]
14. Hennrich, F.; Krupke, R.; Lebedkin, S.; Arnold, K.; Fischer, R.; Resasco, D.E.; Kappes, M.M. Raman spectroscopy of individual single-walled carbon nanotubes from various sources. *J. Phys. Chem. B* **2005**, *109*, 10567–10573. [CrossRef] [PubMed]
15. Ma, X.; Zhang, L.H.; Wang, L.R.; Xue, X.; Sun, J.H.; Wu, Y.; Zou, G.; Wu, X.; Wang, P.C.; Wamer, W.G.; et al. Single-walled carbon nanotubes alter cytochrome c electron transfer and modulate mitochondrial function. *ACS Nano* **2012**, *6*, 10486–10496. [CrossRef] [PubMed]
16. Yang, Z.; Zhang, Y.; Yang, Y.; Sun, L.; Han, D.; Li, H.; Wang, C. Pharmacological and toxicological target organelles and safe use of single-walled carbon nanotubes as drug carriers in treating alzheimer disease. *Nanomed. Nanotechnol. Biol. Med.* **2010**, *6*, 427–441. [CrossRef] [PubMed]
17. Gonzalez-Durruthy, M.; Alberici, L.C.; Curti, C.; Naal, Z.; Atique-Sawazaki, D.T.; Vazquez-Naya, J.M.; Gonzalez-Diaz, H.; Munteanu, C.R. Experimental-computational study of carbon nanotube effects on mitochondrial respiration: In silico nano-qspr machine learning models based on new raman spectra transform with markov-shannon entropy invariants. *J. Chem. Inf. Model.* **2017**, *57*, 1029–1044. [CrossRef] [PubMed]
18. Fernandez-Lozano, C.; Cuinas, R.F.; Seoane, J.A.; Fernandez-Blanco, E.; Dorado, J.; Munteanu, C.R. Classification of signaling proteins based on molecular star graph descriptors using machine learning models. *J. Theor. Biol.* **2015**, *384*, 50–58. [CrossRef] [PubMed]
19. Fernandez-Lozano, C.; Gestal, M.; Pedreira-Souto, N.; Postelnicu, L.; Dorado, J.; Munteanu, C.R. Kernel-based feature selection techniques for transport proteins based on star graph topological indices. *Curr. Top. Med. Chem.* **2013**, *13*, 1681–1691. [CrossRef] [PubMed]
20. Fernandez-Blanco, E.; Aguiar-Pulido, V.; Munteanu, C.R.; Dorado, J. Random forest classification based on star graph topological indices for antioxidant proteins. *J. Theor. Biol.* **2012**, *317*, 331–337. [CrossRef] [PubMed]
21. Perez-Bello, A.; Munteanu, C.R.; Ubeira, F.M.; De Magalhaes, A.L.; Uriarte, E.; Gonzalez-Diaz, H. Alignment-free prediction of mycobacterial DNA promoters based on pseudo-folding lattice network or star-graph topological indices. *J. Theor. Biol.* **2009**, *256*, 458–466. [CrossRef] [PubMed]
22. Vázquez, J.M.; Aguiar, V.; Seoane, J.A.; Freire, A.; Serantes, J.A.; Dorado, J.; Pazos, A.; Munteanu, C.R. Star graphs of protein sequences and proteome mass spectra in cancer prediction. *Curr. Proteom.* **2009**, *6*, 275–288. [CrossRef]
23. Fernandez-Blanco, E.; Rivero, D.; Rabunal, J.; Dorado, J.; Pazos, A.; Munteanu, C.R. Automatic seizure detection based on star graph topological indices. *J. Neurosci. Methods* **2012**, *209*, 410–419. [CrossRef] [PubMed]
24. Wang, X.; Guo, J.; Chen, T.; Nie, H.; Wang, H.; Zang, J.; Cui, X.; Jia, G. Multi-walled carbon nanotubes induce apoptosis via mitochondrial pathway and scavenger receptor. *Toxicol. In Vitro* **2012**, *26*, 799–806. [CrossRef] [PubMed]
25. Knobeloch, L.M.; Blondin, G.A.; Harkin, J.M. Use of submitochondrial particles for prediction of chemical toxicity in man. *Bull. Environ. Contam. Toxicol.* **1990**, *44*, 661–668. [CrossRef] [PubMed]
26. Horan, M.P.; Pichaud, N.; Ballard, J.W. Review: Quantifying mitochondrial dysfunction in complex diseases of aging. *J. Gerontol. A Biol. Sci. Med. Sci.* **2012**, *67*, 1022–1035. [CrossRef] [PubMed]
27. Gonzalez-Diaz, H.; Arrasate, S.; Juan, A.G.; Sotomayor, N.; Lete, E.; Speck-Planche, A.; Ruso, J.M.; Luan, F.; Cordeiro, M.N. Matrix trace operators: From spectral moments of molecular graphs and complex networks to perturbations in synthetic reactions, micelle nanoparticles, and drug adme processes. *Curr. Drug Metab.* **2014**, *15*, 470–488. [CrossRef] [PubMed]

28. Vergara-Galicia, J.; Prado-Prado, F.J.; Gonzalez-Diaz, H. Galvez-markov network transferability indices: Review of classic theory and new model for perturbations in metabolic reactions. *Curr. Drug Metab.* **2014**, *15*, 557–564. [CrossRef] [PubMed]
29. Gonzalez-Diaz, H.; Perez-Montoto, L.G.; Ubeira, F.M. Model for vaccine design by prediction of B-epitopes of iedb given perturbations in peptide sequence, in vivo process, experimental techniques, and source or host organisms. *J. Immunol. Res.* **2014**, *2014*, 768515. [CrossRef] [PubMed]
30. Gonzalez-Diaz, H.; Arrasate, S.; Gomez-SanJuan, A.; Sotomayor, N.; Lete, E.; Besada-Porto, L.; Ruso, J.M. General theory for multiple input-output perturbations in complex molecular systems. 1. Linear qspr electronegativity models in physical, organic, and medicinal chemistry. *Curr. Top. Med. Chem.* **2013**, *13*, 1713–1741. [CrossRef] [PubMed]
31. Munteanu, C.R. Regression Models to Predict Mitochondria Oxygen Mass Flux in the preseNce of the Cnts. Figshare, 2016. Available online: Https://dx.Doi.Org/10.6084/m9.Figshare.3545561 (accessed on 7 August 2016).
32. Martínez, A.; Francisco-Marquez, M.; Galano, A. Effect of different functional groups on the free radical scavenging capability of single-walled carbon nanotubes. *J. Phys. Chem. C* **2010**, *114*, 14734–14739. [CrossRef]
33. Rivera Gil, P.; Oberdorster, G.; Elder, A.; Puntes, V.; Parak, W.J. Correlating physico-chemical with toxicological properties of nanoparticles: The present and the future. *ACS Nano* **2010**, *4*, 5527–5531. [CrossRef] [PubMed]
34. Hinderliter, P.M.; Minard, K.R.; Orr, G.; Chrisler, W.B.; Thrall, B.D.; Pounds, J.G.; Teeguarden, J.G. Isdd: A computational model of particle sedimentation, diffusion and target cell dosimetry for in vitro toxicity studies. *Part. Fibre Toxicol.* **2010**, *7*, 36. [CrossRef] [PubMed]
35. Hernández-Orallo, J. Roc curves for regression. *Pattern Recogn.* **2013**, *46*, 3395–3411. [CrossRef]
36. Pedersen, P.L.; Greenawalt, J.W.; Reynafarje, B.; Hullihen, J.; Decker, G.L.; Soper, J.W.; Bustamente, E. Preparation and characterization of mitochondria and submitochondrial particles of rat liver and liver-derived tissues. *Methods Cell Biol.* **1978**, *20*, 411–481. [PubMed]
37. Lanza, I.R.; Nair, K.S. Functional assessment of isolated mitochondria in vitro. *Methods Enzymol.* **2009**, *457*, 349–372. [PubMed]
38. Gnaiger, E. Bioenergetics at low oxygen: Dependence of respiration and phosphorylation on oxygen and adenosine diphosphate supply. *Respir. Physiol.* **2001**, *128*, 277–297. [CrossRef]
39. Munteanu, C.R.; Magalhaes, A.L.; Duardo-Sanchez, A.; Pazos, A.; Gonzalez-Diaz, H. S2Snet: A tool for transforming characters and numeric sequences into star network topological indices in chemoinformatics, bioinformatics, biomedical, and social-legal sciences. *Curr. Bioinf.* **2013**, *8*, 429–437. [CrossRef]
40. Munteanu, C.R. Cnt Raman for Mitocondrial Oxygen Consumption Data Set and Regression Models. Figshare. Available online: Https://dx.Doi.Org/10.6084/m9.Figshare.3472349 (accessed on 31 January 2017).
41. Tsiliki, G.; Munteanu, C.R.; Seoane, J.A.; Fernandez-Lozano, C.; Sarimveis, H.; Willighagen, E.L. Rregrs: An r package for computer-aided model selection with multiple regression models. *J. Cheminform.* **2015**, *7*, 46. [CrossRef] [PubMed]
42. Tsiliki, G.; Munteanu, C.R.; Seoane, J.; Fernandez-Lozano, C.; Sarimveis, H.; Willighagen, E. Using the rregrs R package for automating predictive modelling. In Proceedings of the MOL2NET International Conference on Multidisciplinary Sciences, Bizkaia, Spain, 5–15 December 2015; Volume 1, p. F009.
43. Bishop, C.M. *Neural Networks for Pattern Recognition*; Oxford University Press: New York, NY, USA, 1995.
44. Breiman, L. Random forests. *Mach. Learn.* **2001**, *45*, 5–32. [CrossRef]

4. Considerações finais

No presente trabalho foi demonstrado teórica e experimentalmente que os nanotubos de carbono de diversa natureza estrutural e propriedades físico-químicas, podem modular eficientemente mecanismos mitocondriais chaves para bioenergética celular. Este fato deve ser considerado criteriosamente desde o ponto de vista fármaco-toxicológico, com vistas a garantir seu uso seguro. Este aspecto é de fundamental importância no campo das ciências biomédicas e farmacêuticas, no desenho racional de novos candidatos com significativo potencial terapêutico em Medicina de Precisão (Nanomedicina Mitocondrial) e, desta forma, garantir um maior grau de especificidade e seletividade por mecanismos bioenergéticos sub-celulares e incrementar as relações benefício/risco destas nanopartículas o nanomateriales. Além disso, é necessário salientar que o processo de identificação e predição dos atributos estruturais (nanodescritores) de CNT orientado para alvos moleculares relevantes desde o ponto de vista farmacológico e toxicológico, é ainda pouco explorado no contexto dos estudos de Nanotoxicologia e Nanomedicina.

Além disso, e em correspondência com o nosso objetivo geral, a metodologia de estudo utilizada permitiu integrar armoniosamente abordagens *in sílico* e *in vitro* para avaliar rigorosamente os efeitos induzidos por uma família de nanotubos de carbono sobre mecanismos mitocondriais chaves na bioenergética celular. As predições das relações estrutura-atividade que subjazem aos efeitos mitocondriais utilizando novos modelos nano-QSAR para a família de CNT sob estudo, ainda não tinham sido reportados até o momento na literatura científica, e permitiram predizer os efeitos mitocondriais para outros nanotubos de carbono (CNT) não testados no nosso conjunto de dados.

É importante salientar que abordagens multidisciplinares, que incluiu o uso intensivo de técnicas de Bioinformática, foram valiosas como fonte para geração de dados relevantes à atividade biológica de CNT e para elucidar mecanismos bioquímicos complexos, associados à nanotoxicidade mitocondrial e modulação farmacológica como a atividade mitoprotetora em múltiplas circunstancias fisiopatológicas como o “swelling mitochondrial” induzido por excesso de Ca^{2+}, Fe^{2+} ou H_2O_2, as quais não obedeceram a relações lineares de doses-resposta (concentração-resposta) nas condições experimentais estabelecidas e também tendo em conta os resultados obtidos dos modelos preditivos Nano-QSAR, baseados em transformações logarítmicas negativas e não lineais da atividade mitoprotetora de CNT oxidados.

Também foi demonstrado que membros da família de CNT oxidados (CNT-OH, CNT-COOH) apresentam maior capacidade que os CNT-prístinos para prevenir a disfunção mitocondrial associada à indução da abertura do poro de transição de permeabilidade mitocondrial (MPTP) em condições de sobrecarga de íons bivalentes (Ca^{2+} e Fe^{2+}); processos que caracterizam a maioria das doenças de curso crônico como: câncer, Alzheimer, Parkinson, epilepsia, diabetes melitus e outras. Neste sentido, foi constatado que a inibição *in vitro* da indução do MPTP é baseada na habilidade dos CNT (CNT-COOH > CNT-OH > CNT-pristinos) para quelação/complexação de íons bivalentes (Ca^{2+} e Fe^{2+}), que se relaciona diretamente com a inibição da reação de Fenton-Haber-Weiss eletro-catalizada por H_2O_2 nos ensaios eletroquímicos de voltimetria cíclica, os quais mimetizam as condições de potencial redox (-0.4-0.8 E_0(V)) entre os complexos respiratórios mitocondriais (I, II, III, IV) da cadeia de transporte de elétrons e a matriz mitocondrial. Aqui é importante salientar que os CNT podem sofrer processos de oxidação na matriz mitocondrial gerando grupos oxidados (OH, COOH) com propriedades que favorecem à complexação/quelação de íons como Ca^{2+} e Fe^{2+} (indutores do MPTP), este fato é raramente discutido na literatura científica e pode modular significativamente a nanotoxicidade de nanomateriais de carbono. Neste sentido, é bem reconhecido que incrementos bioquímico-patológicos do H_2O_2 gerado na matriz mitocondrial ou concentrações experimentais toxicológicamente relevantes e consideradas mitotóxicas de H_2O_2 (300µM), como a utilizada para induzir a reação de Fenton associada à indução do MPTP, podem gerar condições marcadamente pro-oxidantes. Neste contexto, o H_2O_2 pode interagir com os CNT (CNT-pristino e CNT-oxidados) induzindo oxidação com formação de agrupamentos oxidados nas pontas e/ou paredes dos CNT. Específicamente, para CNT-prístinos a inibição da reação de Fenton-Haber-Weiss observada pode ser explicada através da interação do radical hidroxila ($HO^{\cdot}$) com as paredes dos CNT, fato que pode acarretar a geração de defeitos topológicos da rede hexagonal do carbono (vacâncias), gerando pontos de defeitos altamente reativos com capacidade sequestradora do radical hidroxila ($HO^{\cdot}$) ou através inserção de grupos oxidados (OH, COOH), como previamente mencionado.

Estes novos grupos oxidados ainda conservam a habilidade dos CNT-oxidados (CNT-COOH > CNT-OH > CNT-pristinos) para quelação/complexação de íons bivalentes (Ca^{2+} e Fe^{2+}), frente à reação de Fenton-Haber-Weiss induzida experimentalmente. Além disso, as evidencias *in vitro* são confirmadas pelos resultados dos modelos preditivos nano-QSPR/QSAR,

apontando ao fato de que os grupos oxidados (COOH e OH) estão fortemente correlacionados experimental ($R^2 > 0.90$) e teoricamente com a capacidade dos CNT-oxidados de inibir a reação de Fenton-Haber-Weiss induzida experimentalmente por sobrecarga de Ca^{2+} e Fe^{2+} em mitocôndrias isoladas. Isto pode ser corroborado baseado nos resultados da validação externa ($Q^2_{(adj.)}$, Q^2_{F1}, Q^2_{F2}, Q^2_{F3}, > 0.90) para o melhor modelo nano-QSPR/QSAR, o qual permitiu extrapolar apropriadamente as predições *in sílico* sobre a inibição da reação de Fenton-Haber-Weiss e inibição da indução do MPTP para CNT não testados no nosso conjunto de dados original (CNT1-CNT9).

Em adição, foi comprovado que parâmetros estruturais dos CNT (diâmetro, tipo e grau de funcionalização) e parâmetros de exposição *in vitro* (concentração e tempo de exposição), podem ser eficientemente usados como nanodescritores para o desenvolvimento de modelos preditivos (nano-QSAR) de um determinado mecanismo ou resposta mitocondrial (inibição do MPTP, inibição da reação de Fenton, respiração mitocondrial, fluxo de oxigênio mitocondrial e outros). Além do mais, o tipo e grau de funcionalização dos CNT-oxidados (OH, COOH) são nanodescritores chaves para explicar relações quantitativas estrutura-atividade, baseadas na modulação destes mecanismos mitocondriais. Outra consideração a ser salientada no trabalho, é que as técnicas experimentais como Microscopia Electrónica de Transmissão (TEM), Microscopia Electrónica de Varredura (SEM), Espectroscopia Raman, Espectroscopia Infravermelho por transformada de Fourier e outras, constituem poderosas ferramentas para caracterização das propriedades físico-químicas dos CNT e ainda como fonte para a obtenção/geração de novos nanodescriptores de CNT, para a aplicação bem sucedida da abordagem *in sílico* nano-QSAR e representação direta da relação estrutura-atividade de nanomateriais de carbono através de CNT-nanodescritores. Específicamente, a Espectroscopia Raman foi de grande utilidade para modelagem teórica de novos nanodescriptores baseado no espectro Raman dos CNT testados como as: “Markov−Shannon entropy invariants” e “Star-Graph Trace invariants” que permitiram investigar e predizer ausência de efeitos inibitórios sob a respiração e fluxo de oxigênio mitocondrial para os CNT-oxidados (CNT-OH, CNT-COOH) em comparação com o único CNT-prístino e ainda associado aos defeitos topológicos induzidos pela oxidação e caracterizados pela intensidade da banda (D ~1350 cm^{-1}) no espectro Raman.

Em concordância com o anterior, os nanotubos de carbono oxidados, não induziram dissipação do potencial de membrana mitocondrial, apesar da presença de condições *in vitro* pro-

oxidantes (Fe^{2+} 20 µM, Fe^{2+} 20 µM + H_2O_2 300 µM, Fe^{2+} 20µM + Vit C 100 µM), sugerindo potencial mitoprotetor associado a estas condições experimentais. Também diminuiu a geração de H_2O_2 mitocondrial utilizando a técnica de Amplex red, o qual foi associado diretamente com a diminuição significativa da geração do radical hidroxila ($HO^{\cdot}$), como observado nos resultados de voltimetria cíclica para inibição da reação de Fenton mencionada previamente.

Os estudos *in silico* baseados em docagem molecular de CNT (SWCNT, SWCNT-OH, SWCNT-COOH) com transportadores mitocondriais chave (ADP/ATP-carrier e VDAC), foram cruciais para compreender relações críticas em termos mecanísticos e sobre o vínculo existente entre a estrutura e atividade (nanotoxicidade mitocondrial) de SWCNT considerando o fato de que o transportador mitocondrial de ADP/ATP e a VDAC são componentes críticos da estrutura e função do MPTP.

Neste sentido, é importante salientar que paralelamente com o desenvolvimento dos estudos *in vitro* foi desenvolvida uma plataforma *in sílico* de Nanotoxicología, baseadas em ferramentas de Docagem Molecular (do inglês, "Molecular Docking"), que permitiram modelar múltiplas interações dos nanotubos de carbono (SWCNT, SWCNT-COOH, SWCNT-OH) com proteínas mitocondriais chaves na bioenergética e fisiologia celular.

Assim, as ferramentas de Docagem Molecular usadas no nosso estudo, permitiram realizar aproximações realistas validadas sobre a base experimental da cristalografia de proteínas alvos, conhecimentos sobre os sítios críticos de interação, inibidores específicos dos mecanismos mitocondriais estudados e substratos nativos, os quais foram usados como controles teóricos da especificidade e força das interações. Isto facilitou a tomada de decisões sobre nanotoxicidade mitocondrial induzida por SWCNT, com base na determinação de interações fortes e fracas (FEB, do inglês *free energy of binding*) para os complexos de interação formados entre os SWCNT e os sítios ativos das proteínas mitocondriais alvos (ADP/ATP-carrier e VDAC), que conformam o MPTP. Estas metodologias também permitiram a redução significativa do tempo e custos dos nossos estudos tendo em vista a rapidez de execução dos ensaios com alta precisão e reprodutibilidade dos resultados obtidos, garantindo assim a qualidade das informações obtidas e permitindo otimizar as relações beneficio/risco tóxico associado a exposição de CNT, com vistas a garantir seu uso seguro e potenciais aplicações terapêuticas com refinamento estrutural da reatividade tóxica (ex: topologia zig-zag e presença de agrupamentos oxidados OH e COOH).

Particularmente, desde o ponto de vista da relação estrutura-atividade (modelos nano-QSBR) derivada dos estudos de Docagem Molecular, os resultados obtidos sugerem um incremento da nanotoxicidade consistentes com valores de FEB significativamente mais negativos ($p<0.05$) para os SWCNT-COOH > SWCNT-OH > pristine-SWCNT e com excelente correlação ($R^2 > 0.90$) com a nanotoxicidade mitocondrial (FEB) e o parâmetro [n-Hamada index] e com maior força das interações para nanotubos de topologia zig-zag ($n > 0$; $m = 0$) > quiral (($n \neq m$) > 0) > armchair ($n = m$), indicando que os arranjos geométricos ou topologia zig-zag, a carga e natureza química dos grupos polares (COOH; OH), são atributos importantes (nanodescritores) para a interação (ancoragem) dos CNT com as proteínas mitocondriais alvos (ADP/ATP-carrier e VDAC) e também para sítios de fosforilação reguladores da permeabilidade destes transportadores mitocondriais, que formam o MPTP.

È importante salientar que estes parâmetros estruturais: índices de Hamada (*n*, *m*), apresentam relação direta com o diâmetro dos nanotubos de carbono o qual, como já foi dito anteriormente, constitui um nanodescritor crítico correlacionado com a inibição *in vitro* do MPTP e predita pelos modelos nano-QSAR para os testes de inibição de inchamento mitocondrial e inibição da reação de Fenton-Haber-Weiss. Porém, resulta extremadamente complexo a determinação experimental (*in vitro*) da influência dos índices de Hamada (*n*, *m*), devido a sua difícil caracterização (quantificação) através de espectroscopia Raman, a qual tem sido usada para esta finalidade, com escassas referências na literatura científica, fato que salienta a importância dos estudos teóricos de docagem molecular apresentados nesta Tese.

Outra importante consideração derivada dos resultados de Docagem Molecular é a possibilidade de fazer inferências sobre efeitos semelhantes induzidos por CNT em outras espécies animais, com independência do grupo filogenético avaliado. Devido ao alto grau de conservação dos sítios ativos e de fosforilação dos transportadores mitocondriais (ADP/ATP-carrier e VDAC), os quais são alvo para ação dos nanotubos de carbono de diversa natureza estrutural (quiralidade e funcionalização), esta visão comparada permitiu aumentar a percepção do risco tóxico derivado da exposição à nanomateriais de carbono, assim como a generalização dos resultados para aplicações na saúde e meio ambiente, considerando que em circunstâncias patológicas a abertura do MPTP formado pelos transportadores mitocondriais (ADP/ATP-carrier e VDAC) está diretamente envolvida em diversas doenças de alta prevalência e mortalidade como câncer, Alzheimer, Parkinson, Epilepsia, Diabetes e também pode ser observada em

modelos animais comumente usados em ecotoxicologia como o peixe *Danio rerio* e também no camarão *Litopenaeus vannamei*). Além do mais, desde o ponto de vista metodológico, teórico e experimental, o estudo da modulação de mecanismos mitocondriais induzida por CNT poderia ser uma abordagem crítica na compreensão dos mecanismos que governam a nanotoxicidade. Devido a que os mecanismos mitocondriais são altamente conservados nas células eucariotas e ainda considerando o rol bioenergético decisivo da mitocôndria nos mecanismos de sobrevivência e morte celular.

Como perspectivas do nosso trabalho poderíamos considerar a execução de outros estudos termodinâmicos quantificando experimentalmente a energia livre de interação (FEB) dos CNT com os transportadores mitocondriais (ANT e VDAC) usando calorimetria diferencial de barrido que permitiria realizar comparações com os valores teóricos de FEB obtidas pelos ensaios *in silico* de docagem molecular. Desenvolver experimentos de dinâmica molecular que permitam estudar os efeitos da solvatação com moléculas de água e fatores temporais que determinam a formação dos complexos entre os CNT e os transportadores mitocondriais. Considerar estudos *in silico* e *in vitro* sobre outros componentes do MPTP como: HK, Bcl2, PBR também visando relações quantitativas estrutura-atividade (Nano-QSAR) dos CNT estudados. Além disso considerar estas metodologias num nível de complexidade maior usando células hepáticas (HepG2) acompanhado de modelos preditivos para múltiplos alvos. Aprofundar no estudo da influência do diâmetro dos CNT associado à reatividade superficial e disposição geométrica dos átomos (índices de Hamada n, m) nas interações *in silico* e *in vitro*. Implementar esta abordagem considerando efeitos mitocondriais induzidos por CNT sobre modelos relevantes para ecotoxicologia.

Finalmente, o presente trabalho apresenta uma contribuição inédita para a abordagem teórica-experimental e predição dos efeitos seletivos dos nanomateriais de carbono (CNT) sobre a bioenergética mitocondrial com vistas a garantir o uso seguro e desenvolvimento sustentável das nanotecnologias, reduzir o número de animais na experimentação animal e potenciar o surgimento de áreas emergentes como o Desenho Racional de Nanomateriais de Carbono e a Nanomedicina e Nanotoxicologia Mitocondrial.

Conclusões

- Os membros oxidados da família de CNT oxidados (CNT-COOH, CNT-OH) apresentam maior capacidade que os CNT-prístinos para prevenir a indução do poro de transição de permeabilidade mitocondrial (MPTP) em condições de sobrecarga Ca^{2+}, Fe^{2+} e H_2O_2.
- Os CNT estudados foram capazes de inibir a reação de Fenton mitocondrial electro-induzida em condições de sobrecarga dos íons Fe^{2+} e baseado em mecanismos de quelação/complexação dos íons Fe^{2+} na matriz mitocondrial.
- Os membros oxidados da família de CNT não afetaram a respiração mitocondrial, fluxo de oxigênio e não induziram dissipação do potencial de membrana mitocondrial em condições de sobrecarga Fe^{2+}.
- Parâmetros físico-químicos dos CNT como: quiralidade zig-zag, diâmetro, presença de grupos oxidados (COOH > OH) e parâmetros de exposição como: concentração e tempo de exposição que podem ser nanodescritotes relevantes para predizer interações críticas de docagem molecular e correlações *in sílico* estrutura-atividade (modelos nano-QSAR).

Referências

1. Sahoo, S.K, Parveen, S Panda. The present and future of nanotechnology in human health care. *Nanomed: Nanotec, Biol and Med*, 2007. **3**: 20-31.
2. Oberdörster G. Safety assessment for nanotechnology and nanomedicine: concepts of nanotoxicology. *J Intern Med*, 2010. **67**:89-105.
3. Neus F, Bengt F. Nanotoxicology: no small matter. *Journ Nanosc*, 2010. **2**: 2514–2520
4. Feynman RP. There's a plenty room at the bottom. *Eng Sci*, 1960. **23**:22-36.
5. Ramos, B. G. Z, Pasa, T. B. O desenvolvimento da nanotecnologia: cenário mundial e nacional de investimentos. *Rev. Bras. Farm*, 2008. **89**: 95-101.
6. Li, K.C Pandit S.D, Guccione, S Bednarski, Molecular imaging applications in nanomedicine. *Biomed Micro Devices*, 2004. **6**:113–116.
7. Foldvari, M. and Bagonluri, M. (2008). Carbon nanotubes as functional excipients for nanomedicines: II. Drug delivery and biocompatibility issues. *Nanomed: Nanotech Biol Med*, 2008. **4**:183–200.
8. Harald F.K, Peter W. Nanotoxicology: An Interdisciplinary Challenge. *Angew. Chem. Int*. Ed, 2011. **50**:1260 – 1278.
9. Iijima S. Helical microtubules of graphitic carbon. *Nature*, 1991. **354**:56–58.
10. Iijima S. Carbon nanotubes: past, present, and future. *Physica B*, 2002. **323**:1–5.
11. Hamada, N., Sawada, S., Oshiyama, A. New one-dimensional conductors: Graphitic microtubes. *Phys Rev Let*, 1992. **68**:1579.
12. Thomsen C., Telg H., Maultzsch J., and Reich S. Chirality assignments in carbon nanotubes based on resonant Raman scattering. *Phys Stat Sol B*, 2005. **242**:1802–1806.
13. Duffin, R., Cloute, A., Brown, D.M., et al. The importance of surface area and specific reactivity in the acute pulmonary inflammatory response to particles. *Ann Occup Hyg*, 2002. **46**:242–245.
14. Shane D.B. New Solvents for Nanotubes: Approaching the Dispersibility of Surfactants. *J Phys Chem C*, 2010. **114**: 231–237.
15. Michael G.D et al. QSPR/QSAR-Based Perturbation Theory Approach and Mechanistic Electrochemical Assays on Carbon Nanotubes with Optimal Properties Against Mitochondrial Fenton Reaction Experimentally Induced by Fe2+-overload. *Carbon*, 2017. **115**: 312-330.
16. Sebastian K., Alberto B., Mounir T., and Christophe R. Insertion of Short Amino-Functionalized Single-Walled Carbon Nanotubes into Phospholipid Bilayer Occurs by Passive Diffusion. *Plos One Journ*, 2012. **7**: E40707.
17. Chistyakov V.A et al. Physical consequences of the mitochondrial targeting of single-walled carbon nanotubes probed computationally. *Phys E*, 2015. **70**: 198-202.
18. Yang Z., Zhang Y., Yang Y., Sun L., Han D., Pharmacological and toxicological target organelles and safe use of single-walled carbon nanotubes as drug carriers in treating Alzheimer disease. *Nanomedicine*, 2010. **6**:427-41.
19. M. González-Durruthy *et al*., Mitoprotective activity of oxidized carbon nanotubes against mitochondrial swelling induced in multipe experimental conditions and

predictions with new expected-value perturbation theory. *RSC adv*, 2015. **5**: 103229-103245.
20. OECD Principles for the validation, for regulatory purposes of (Quantitative) Structure Activity Relationship Model. http:www.oecd.org/(accessed 9/03/2016).

21. ISO/TC 229 *Nanotech*., 2011.
22. Natalie B *et al*. The 3Rs as a framework to support a 21st century approach for nanosafety assessment. *Nano today*, 2017. **12**: 10-13.
23. Toropov AA, Toropova AP, Quasi-QSAR for mutagenic potential of multi-walled carbon-nanotubes. *Chemosphere* 2015; **124**:40–46.
24. González-Díaz H, Arrasate S, Gómez-San Juan A, Sotomayor N, Lete E, Besada-Porto L et al. General Theory for Multiple Input-Output Perturbations in Complex Molecular Systems. 1. Linear QSPR Electronegativity Models in Physical,Organic, and Medicinal Chemistry. *Curr Top Med Chem;* 2013, **13***:* 1713-1741.
25. Roy K, Das RN, Ambure P, Aher RB, Be aware of error measures. Further studies on validation of predictive QSAR models. *Chemom Intell Lab Sys* 2016; **152:** 18-33.
26. Toropov AA, Leszczynska D, Leszczynski J. Predicting water solubility and octanol water partition coefficient for carbon nanotubes based on the chiral vector. *Comput Biol Chem* 2007; **31**: 127–128.
27. Toropova AP, Toropov AA, Rallo R, Leszczynska D, Leszczynski J. Nano-QSAR: Genotoxicity of multi-walled carbon nanotubes. *Int. J. Environ. Res 2016*, **10**:59-64.
28. OECD Document. Guidance Document on the Validation of (Quantitative) 1226 Structure Activity Relationships (Q)SARs Models, ENV/JM/MONO(2007)2; 2007.
29. Trott, O. & Arthur J.O. AutoDock Vina: improving the speed and accuracy of docking with a new scoring function, efficient optimization, and multithreading. *J. Comput. Chem*, 2010. **31:** 455-461.
30. Stefano F., Ruth H., Michael E.P., Michel F.S., David S.G and Arthur J.O. Computational protein–ligand docking and virtual drug screening with the AutoDock suite. *Nat Prot*, 2016. **11**: 905-917.